MHD MODE CONVERSION OF FAST AND SLOW MAGNETOACOUSTIC WAVES IN THE SOLAR CORONA

A. M. Dee McDougall-Bagnall

A Thesis Submitted for the Degree of PhD
at the
University of St. Andrews

2010

MHD Mode Conversion of Fast and Slow Magnetoacoustic Waves in the Solar Corona

A. M. Dee McDougall-Bagnall

Thesis submitted for the degree of Doctor of Philosophy

of the University of St Andrews

7 April 2010

Abstract

There are three main wave types present in the Sun's atmosphere: Alfvén waves and fast and slow magnetoacoustic waves. Alfvén waves are purely magnetic and would not exist if it was not for the Sun's magnetic field. The fast and slow magnetoacoustic waves are so named due to their relative phase speeds. As the magnetic field tends to zero, the slow wave goes to zero as the fast wave becomes the sound wave. When a resonance occurs energy may be transferred between the different modes, causing one to increase in amplitude whilst the other decreases. This is known as mode conversion. Mode conversion of fast and slow magnetoacoustic waves takes place when the characteristic wave speeds, the sound and Alfvén speeds, are equal. This occurs in regions where the ratio of the gas pressure to the magnetic pressure, known as the plasma β, is approximately unity.

In this thesis we investigate the conversion of fast and slow magnetoacoustic waves as they propagate from low- to high-β plasma. This investigation uses a combination of analytical and numerical techniques to gain a full understanding of the process. The MacCormack finite-difference method is used to model a wave as it undergoes mode conversion. Complementing this analytical techniques are employed to find the wave behaviour at, and distant from, the mode-conversion region. These methods are described in Chapter 2.

The simple, one-dimensional model of an isothermal atmosphere permeated by a uniform magnetic field is studied in Chapter 3. Gravitational acceleration is included to ensure that mode conversion takes place. Driving a slow magnetoacoustic wave on the upper boundary conversion takes place as the wave passes from low- to high-β plasma. This is expanded upon in Chapter 4 where the effects of a non-isothermal temperature profile are examined. A $\tanh$ profile is selected to mimic the steep temperature gradient found in the transition region. In Chapter 5 the complexity is increased by allowing for a two-dimensional model. For this purpose we choose a radially-expanding magnetic field which is representative of a coronal hole. In this instance the slow magnetoacoustic wave is driven upwards from the surface, again travelling from low to high β. Finally, in Chapter 6 we investigate mode conversion near a two-dimensional, magnetic null point. At the null the plasma β becomes infinitely large and a wave propagating towards the null point will experience mode conversion.

The methods used allow conversion of fast and slow waves to be described in the various model atmospheres. The amount of transmission and conversion are calculated and matched across the mode-conversion layer giving a full description of the wave behaviour.

Declarations

I, Dee McDougall-Bagnall, hereby certify that this thesis, which is approximately 55 000 words in length, has been written by me, that it is the record of work carried out by me and that it has not been submitted in any previous application for a higher degree.

I was admitted as a research student in September 2005 and as a candidate for the degree of Doctor of Philosophy in September 2006; the higher study for which this is a record was carried out in the University of St Andrews between 2005 and 2010.

Date: ________ Signature of Candidate: ______________________________.

I hereby certify that the candidate has fulfilled the conditions of the Resolution and Regulations appropriate for the degree of Doctor of Philosophy in the University of St Andrews and that the candidate is qualified to submit this thesis in application for that degree.

Date: ________ Signature of Supervisor: ______________________________.

In submitting this thesis to the University of St Andrews we understand that we are giving permission for it to be made available for use in accordance with the regulations of the University Library for the time being in force, subject to any copyright vested in the work not being affected thereby. We also understand that the title and the abstract will be published, and that a copy of the work may be made and supplied to any bona fide library or research worker, that my thesis will be electronically accessible for personal or research use unless exempt by award of an embargo as requested below, and that the library has the right to migrate my thesis into new electronic forms as required to ensure continued access to the thesis. We have obtained any third-party copyright permissions that may be required in order to allow such access and migration, or have requested the appropriate embargo below.

The following is an agreed request by candidate and supervisor regarding the electronic publication of this thesis:

Access to Printed copy and electronic publication of thesis through the University of St Andrews.

Date: ________ Signature of Candidate: ____________ Signature of Supervisor: ____________.

Acknowledgements

I would like to mention a few people who have contributed in various ways to this thesis.

My supervisor, Alan: I was inspired to do a Ph.D. under your supervision during my undergraduate Summer and Honours projects; your endless enthusiasm and support have always kept me going, even through the tough times.

The Carnegie Trust for the Universities of Scotland for financial support during the first three years, and for additional support to attend a number of enjoyable conferences - especially the ones in sunnier climes! I would also like to thank the Registry for finding me plenty of part-time work after my funding ran out, and more recently for providing the opportunity for me to work for the University on a full-time basis.

All of my office mates, but in particular Mike, Ricki, Lynsey and Ruth. Most of you were friends before I started my Ph.D. and spending time with you was always fun - both in and out of the office! Also to those outwith the maths department: Aoife, Lorna, Emma and others, both in St Andrews and further afield, you always provided a welcome distraction from work when it was needed.

Last, but by no means least, Jon. During my Ph.D. you have gone from my boyfriend to my husband, and you have been nothing but supportive every step along the way. I couldn't have done it without you.

Publications

The following published papers include material from this thesis:

- A. M. D. McDougall and A. W. Hood. A New Look at Mode Conversion in a Stratified Isothermal Atmosphere. *Sol. Phys.*, 246:259 – 271, 2007.
- A. M. D. McDougall and A. W. Hood. MHD Mode Conversion in a Stratified Atmosphere. In R. Erdélyi and C. A. Mendoza-Briceño, editors, *Proceedings of the International Astronomical Union, Waves & Oscillations in the Solar Atmosphere: Heating and Magneto-Seismology*, volume 247, pages 296 – 302, 2008.
- A. M. D. McDougall and A. W. Hood. MHD Mode Conversion around a 2D Magnetic Null Point. In *15th Cambridge Workshop on Cool Stars, Stellar Systems, and the Sun*, volume 1094, pages 752 – 755, 2009.

Contents

List of Figures

Chapter 1

Introduction

1.1 The Sun

This thesis aims to investigate waves in the Sun's atmosphere. On Earth acoustic waves are important in the lower atmosphere. The presence of a magnetic field modifies the acoustic waves in the solar atmosphere giving slow and fast magnetoacoustic waves, named according to their relative speeds of propagation. We investigate how energy may transfer from one wave mode to another through a process called mode conversion. Before this is examined in more detail we first look at some of the Sun's basic properties.

The Sun has been studied for many centuries. As long ago as 2000 BC eclipses were studied by the Chinese, who recorded them and predicted subsequent events. The Greeks also studied these phenomena from around 600 BC. It was a Greek, Theophrastus, a pupil of Aristotle, who observed sunspots with the naked eye in 350 BC. Sunspots were then systematically observed by the Chinese from 23 BC right through to the Middle Ages. In the West Galileo was among the first to have observed sunspots, using the newly invented telescope in the early 1600s. In 1666 the law of gravitation was devised by Newton, who then applied it to the motion of the planets around the Sun. The theory that the planets revolve around the Sun in concentric circles had first been put forward by Copernicus in 1530.

The Sun is our closest star at a distance of approximately 93 million miles, or 150 million kilometres, from the Earth. This distance is given the name of one astronomical unit, or 1 AU, and was given correctly by Euler in 1770. It takes 8 minutes for light from the Sun to traverse this distance to the Earth. The age of the Sun is about 4.5 billion years old, it has a mass $M_{\odot} = 1.99 \times 10^{30}$ kg and radius $R_{\odot} = 6.96 \times 10^{8}$ m. These values are 330 000 and 109 times larger than the Earth's mass and radius respectively. At a value of 1.4×10^{3} kg m^{-3} the Sun's mean density is roughly equivalent to the mean density of the Earth. The surface pressure, however, is much smaller - only 0.2 of the Earth's pressure at sea level. The gravity at the surface of the Sun, $g_{\odot} = 274$ m s^{-2}, is 27 times that of the Earth. These facts may be found in Priest (1982), Golub and Pasachoff (2001), Lang (2001) and Goedbloed and Poedts (2004) for example, and are summarised in Section 1.1.4.

The Sun is made up of a giant ball of plasma. In fact most matter in the Universe exists in a plasma state; the Earth and its lower atmosphere is one exception. A plasma is a gas in which many of the electrons are no longer bound to the nuclei. There are enough of these free charged particles in a plasma that the dynamics are dominated by electromagnetic forces (Boyd and Sanderson, 2003). This is true of the Sun where much of the observed structure is due to the presence of the magnetic field. The magnetic field influences the plasma in many ways. It can exert a force which may support prominence material against gravity or propel

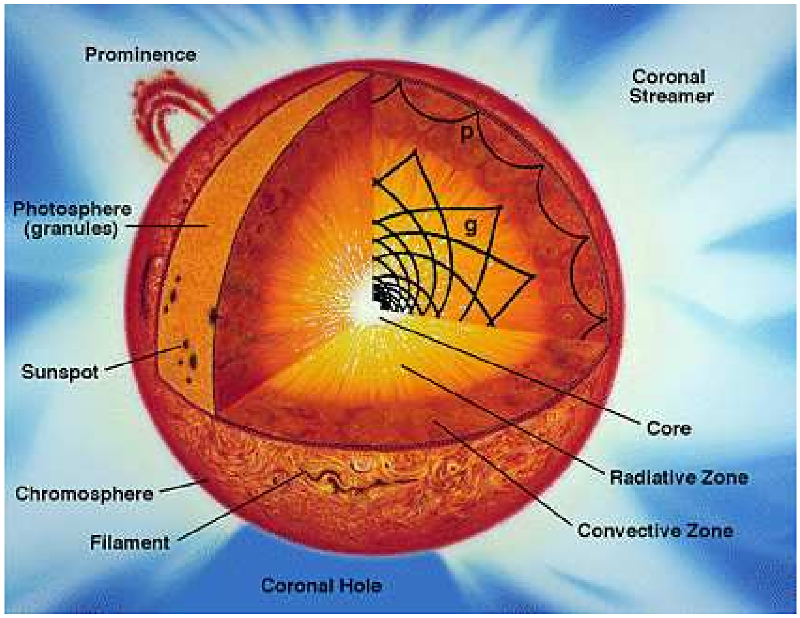

Figure 1.1: This cartoon shows the many layers of the Sun from the core, through the radiative zone to the convective zone, and out into the atmosphere. Some of the features which may be observed at different heights in the atmosphere are also shown.
Credit: SOHO (ESA & NASA).

material from the Sun at high speeds, for example. It may store energy; this could provide a source of heating or be released explosively as a solar flare. The magnetic field also provides thermal insulation allowing cool plasma to exist alongside hotter material, *i.e.* in prominences or cool loop cores. The plasma in the Sun is composed of approximately 90% hydrogen, 10% helium and 0.1% carbon, nitrogen, oxygen and heavier elements (iron, for example, is responsible for much of the coronal emissions) held together and compressed under its own gravitational attraction.

Many distinct regions are present in the Sun, as shown in Figure 1.1. The interior of the Sun is made up of the core, the radiative zone, and the convection zone; the latter two layers named after the mode of energy transport present. Then moving up into the atmosphere, where the magnetic field is dominant, there is the photosphere, the chromosphere and the corona, which extends out to the Earth and beyond. We now go on to describe the processes and features that are present in each of these layers.

1.1.1 Solar Interior

At the centre of the Sun lies the core which extends out to about $0.25\ R_\odot$. The temperature of 1.6×10^7 K and density of 1.6×10^5 kg m^{-3} are high enough for thermonuclear reactions to take place. This involves the fusion of hydrogen into helium, and the energy produced is the source of the Sun's luminosity and all of the physics of the outer layers. Most of the energy passes out into space; although the photons are absorbed and re-emitted so many times that it takes them 10^7 years to travel from the core to the surface (Lang, 2001). The collisions during this process increase the wavelength from gamma rays in the core to visible

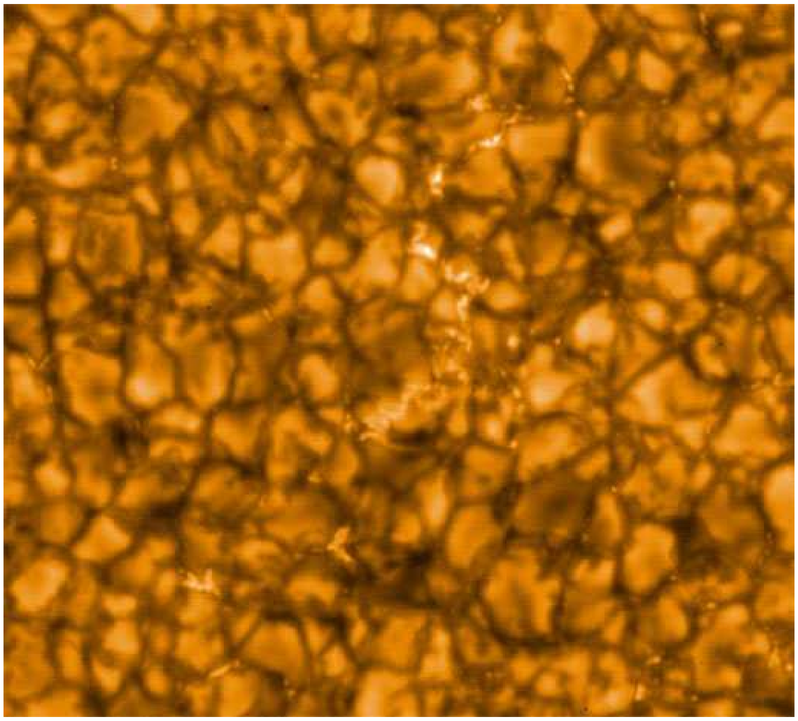

Figure 1.2: This image taken by Hinode's Solar Optical Telescope shows the solar surface. Energy is transported to the solar surface by convection and it is these motions that make the granular structure seen at the surface. The lighter areas are where plasma is rising from below and the darker lanes show where it sinks back downwards.
Credit: Hinode JAXA/NASA/PPARC.

light at the solar surface.

The radiative zone extends out to $0.7\ R_\odot$ and the temperature drops to approximately 5×10^5 K at this point. Beyond this radius electrons recombining with other particles allow photons to be absorbed more easily, decreasing the radiative conductivity and increasing the opacity. This causes an increase in the temperature gradient which becomes so large that the convective instability sets in. This marks the start of the convection zone where turbulent motions are dominant through to the lower photosphere. At this point the opacity decreases and the material becomes convectively stable again. Figure 1.2 shows the photosphere where the top of these convection cells can be seen. The brighter centres mark the upward-flowing, hotter material and the dark boundaries are where the cooler material is descending. These motions are highly dynamic and granular cells have a typical lifetime of 10 minutes.

1.1.2 Solar Atmosphere

The solar atmosphere is characterised by its magnetic nature. Its lowest layer is the photosphere. Across this layer the material changes from being completely opaque to radiation to being transparent, allowing energy to escape into space. This is the visible surface of the Sun as it emits photons in the visible spectrum. This layer is very thin, with a thickness of about 500 km. As mentioned above and shown in Figure 1.2, the

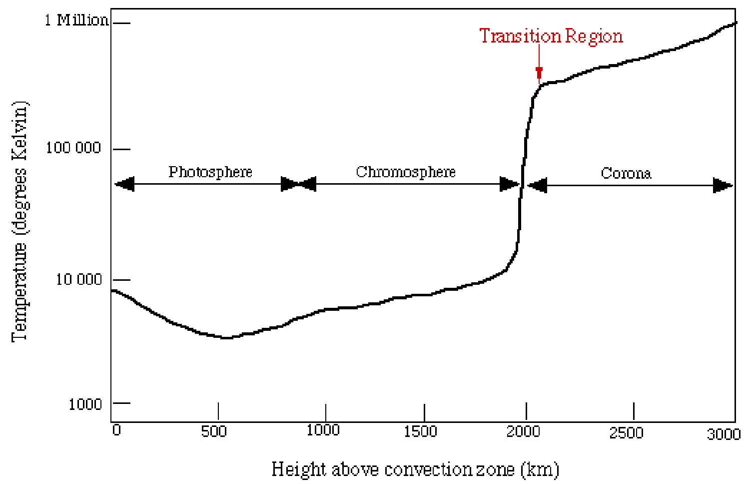

Figure 1.3: The changing temperature from the solar surface out into the corona. A minimum of about 4300 K is reached in the photosphere. The temperature then rises to about 20 000 K at the top of the chromosphere, before surging to over a million degrees in the corona.
Credit: MSU.

surface of the photosphere is covered by the top of the granular cells which extend up from the convection zone. There are also larger cells, called supergranulation cells, which are approximately 30 000 km across and have a lifetime of 1 – 2 days. As the material flows upwards in the centre of the cells and outwards towards the boundaries it drags the magnetic field with it. Thus the magnetic field is weak at the centre of the supergranule cells and is concentrated at the boundaries.

The photospheric magnetic field is made up of different regions. In addition to the supergranulation fields there are also sunspots (as in Figure 1.6), plage regions, large scale unipolar areas, and ephemeral regions. In ephemeral regions numerous tiny bipoles are present giving a salt and pepper effect on solar magnetograms. These newly emerging regions of magnetic flux last for about four to six hours on average. As suggested by the name large scale unipolar areas contain elements of predominantly one polarity. These can extend over hundreds of kilometres in both longitude and latitude and are remarkably long lived, with a lifetime of a year or more. The polar field is believed to lie above these unipolar regions. Next there are sunspots where the magnetic field is highly concentrated. These are examined in more detail in Section 1.1.3. There are then the plage regions which are made up of the part of an active region found outside of sunspots, where the mean magnetic field has values of a few hundred gauss.

The temperature in the photosphere falls to a minimum of 4300 K where it unexpectedly begins to rise again, marking the boundary between the photosphere and the chromosphere. The temperature rises monotonically in the chromosphere with rapid increases at the boundary between the photosphere and chromosphere, and again at the transition region between the chromosphere and the corona. This dramatic change in temperature is depicted in Figure 1.3. The height at which these temperature gradients lie is highly variable. The chromosphere may be viewed in Hα which shows up the network of supergranulation boundaries. The chromosphere may also be observed at the limb of the Sun as plasma jets known as spicules.

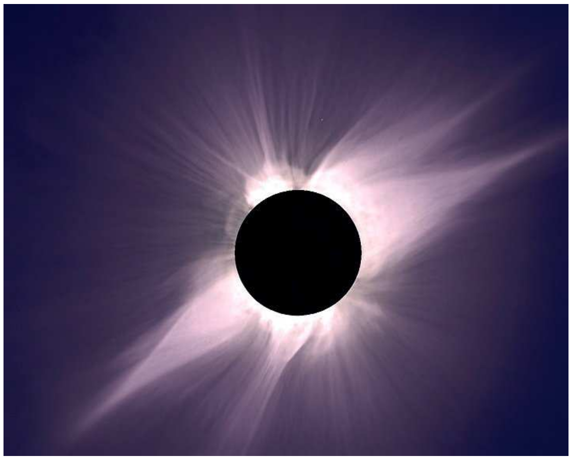

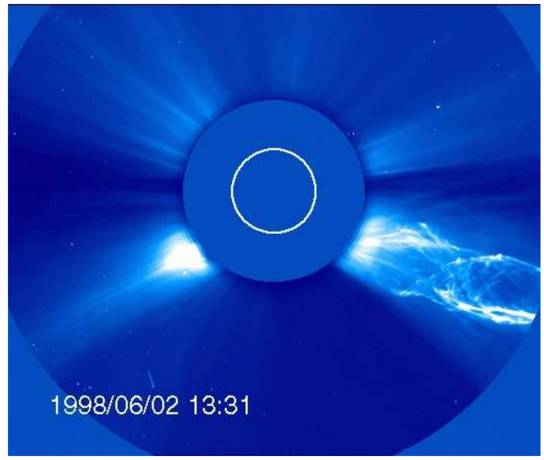

Figure 1.4: *Left:* The solar corona viewed from the top of Mauna Kea, Hawaii during a total solar eclipse in 1991. The corona can be seen streaming out as the solar wind from the coronal holes, with helmet streamers on either side.
Credit: NASA Astronomy Picture of the Day Collection. HAO & NCAR.
Right: The solar corona as viewed by the LASCO C2 coronagraph on board SOHO on 2 June 1998 at 13:31 UT. In this image a bright CME is present with an enormous erupting prominence.
Credit: Courtesy of SOHO/LASCO consortium. SOHO is a project of international cooperation between ESA and NASA.

The solar corona extends out from the top of the transition region where the temperature jumps to 1 – 2 million degrees. The question of how the corona is heated is one of the biggest mysteries in solar physics. Some of the proposed heating mechanisms suggest that the corona is heated by reconnection (Sweet, 1958; Parker, 1963; Priest and Forbes, 1986) causing flares which transport energy out through the corona. Others suggest that waves are the dominant heating mechanism; for example, by the dissipation of shear Alfvén waves (Heyvaerts and Priest, 1983) or by the damping of slow magnetoacoustic waves or high-frequency fast magnetoacoustic waves (Porter et al., 1994). Despite many years of research on this topic the true cause of coronal heating is still under debate. In the outer corona the temperature slowly falls as the corona expands out as the solar wind. This is also true of the density which is of the order 10^{14} m^{-3} in quiet regions, but between 5 – 20 times larger within coronal loops.

The corona only used to be visible as a faint halo during a solar eclipse (left-hand image, Figure 1.4) as it is normally masked by the brightness of the photosphere which is a million times brighter. But with the invention of the coronagraph by Lyot at the Pic du Midi Observatory in 1930, the corona could be viewed at any time. The coronagraph is a telescope which eliminates the glare of the photosphere with an occulting disc, illustrated in the right-hand image of Figure 1.4. The corona may also be viewed in soft X-rays as it emits thermally at this wavelength; any contribution from the lower atmosphere is negligible. The shape of the corona varies greatly during the solar cycle. During solar maximum streamers extend out in all directions, whereas during minimum these tend to be confined to the equatorial regions with polar plumes fanning out from the poles.

Coronal streamers are roughly radial features which extend from a height of 0.5 – 1 $R_\odot$ to 10 $R_\odot$ and have a density enhancement of between 3 and 10 times that of the surrounding plasma. They are named

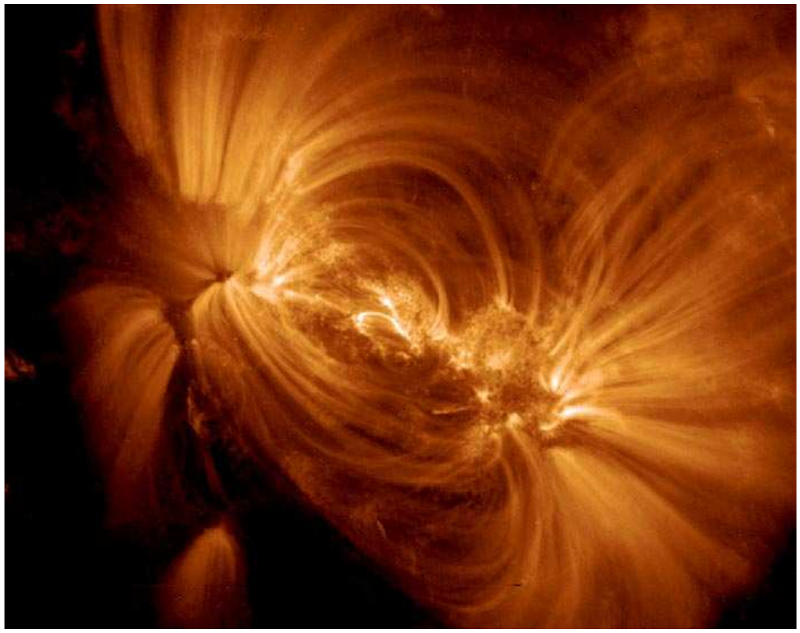

Figure 1.5: An active region seen by the satellite TRACE in the 171 Å bandpass on 19 May 1998. The image shows coronal loops connecting two active regions, which show up due to the plasma lying along the magnetic field lines.
Credit: The Transition and Coronal Region Explorer, TRACE, is a mission of the Stanford-Lockheed Institute for Space Research (a joint program of the Lockheed-Martin Technology Centre's Solar and Astrophysics Laboratory and Stanford's Solar Observatory's Group) and part of the NASA Small Explorer Program.

depending on the type of structure which they lie above; helmet streamers lie above prominences and active region streamers above active regions. A streamer consists of an arcade of closed field lines surrounded by a blade of open field lines. Polar plumes are ray-like structures found near the poles and in coronal holes. These are especially noticeable at solar minimum.

There are two distinct types of region in the corona (Aschwanden, 2004). Where the field lines are predominantly open the corona appears dark; these regions are known as coronal holes. They have a density 3 times lower than the background corona and are also at a lower temperature. The corona continually expands outwards from these regions giving the solar wind (Parker, 1958). Most of this outflow comes from the coronal holes, especially those at the poles, but it may also originate from areas of open field above active regions. The flow speed increases as the solar wind flows out from the corona reaching speeds of $400-800$ km s^{-1} near the Earth. The high speed streams tend to originate from coronal holes and are more uniform than the slower streams which come from open fields above active regions. Where the magnetic field is mainly closed many coronal loops can be observed, as in Figure 1.5. The complex structure of these features is created by the magnetic field. In fact coronal loops are made up of plasma outlining the magnetic field lines. There are numerous types of coronal loop. Between active regions (described in Section 1.1.3) interconnecting loops are found, these may be up to 700 000 km long and tend to be rooted in strong magnetic field at the edges of active regions. Quiet region loops do not connect active regions, and are much cooler at a temperature of $1.5-2.1\times10^6$ K compared to $2-3\times10^6$ K. Loops may also be

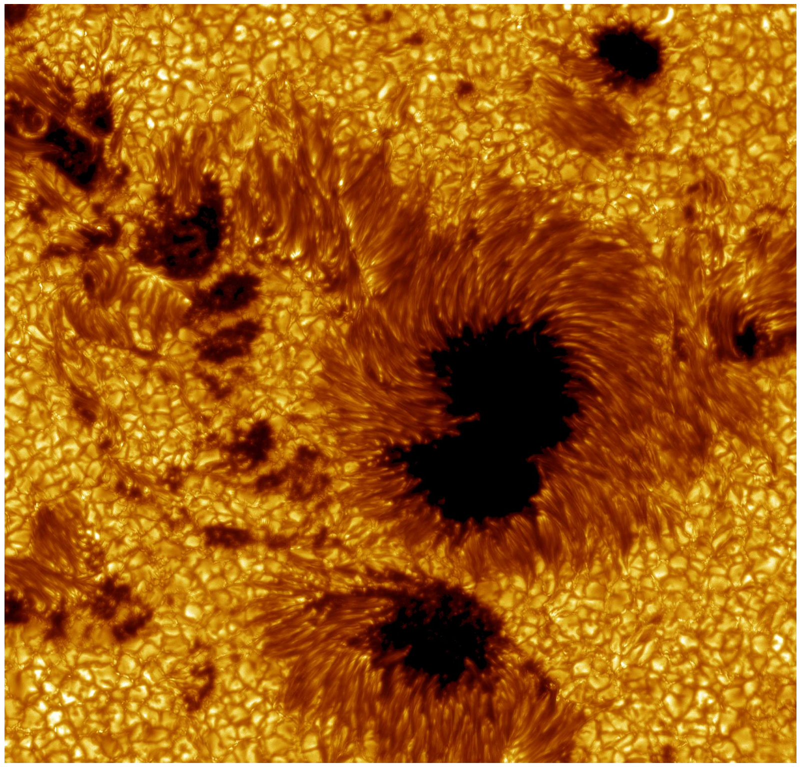

Figure 1.6: This image of a sunspot group was taken by the Swedish 1 m Solar Telescope on the 15 July 2002. The SST is the largest optical solar telescope in Europe and can observe details as small as 70 km on the solar surface. In this image we can see the tops of the granular cells that cover the photosphere and a sunspot group, in which the dark umbra and surrounding penumbra are clearly visible.
Credit: Göran Scharmer, ISP. Image processing: Mats Löfdahl, ISP; Royal Swedish Academy of Sciences.

found within active regions; these tend to be smaller with lengths from tens to hundreds of thousands of kilometres and a wide range of different temperatures.

1.1.3 Solar Features

There are many other features that exist on the Sun and a selection are described here. All of these features are different ways that the Sun's magnetic field influences the solar plasma. Active regions typically consist of a pair of sunspots appearing within $\pm 30^\circ$ of the equator connected by a system of loops which expand out into the corona. After a few days an active region can be seen with a bright Hα plage, below this will lie the sunspot group surrounded by photospheric faculae and above there will be an X-ray enhancement. It takes 10 to 15 days for the maximum activity to be reached, but the decay is much slower and is marked by the dispersal of magnetic flux until the active region eventually disappears.

Sunspots appear as dark regions in the photosphere because they are cooler than the surrounding plasma. The observed light comes from a greater depth because the sunspot is more transparent than the surrounding plasma. In November and December 1769, whilst observing a large sunspot, Wilson found that a sunspot is a saucer-like depression extending 500 to 700 km below the photosphere (Wilson and Maskelyne, 1774);

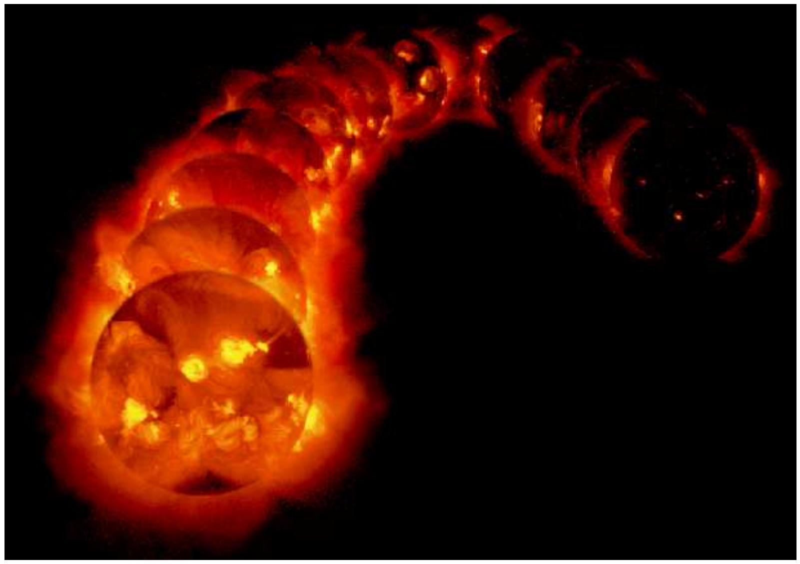

Figure 1.7: The changing Sun from solar maximum to solar minimum. These X-ray images of the solar corona were taken by Yohkoh at 120 day increments between 1991 and 1995. As the solar cycle wanes from maximum to minimum we can see the corona change from having a complex structure to a more simple configuration with an overall decrease in brightness by 100 times.
Credit: G.L. Slater and G.A. Linford. The solar X-ray images are taken from the Yohkoh mission of ISAS, Japan. The X-ray telescope was prepared by the Lockheed Palo Alto Research Laboratory, the National Astronomical Observatory of Japan, and the University of Tokyo with the support of NASA and ISAS.

this is known as the Wilson effect. Most sunspots will disappear within a few days, but larger sunspots may last much longer decaying over a period of a few months (Bray and Loughhead, 1964). A nice example of a sunspot is shown in Figure 1.6. The dark central part is known as the umbra and has typical sizes ranging from 10 000 – 20 000 km. The magnetic field in the umbra has a strength of 2 000 – 3 000 G and the field lines are vertical in the centre and begin to fan outwards towards the penumbra. The penumbra is the region surrounding the umbra consisting of light and dark radial filaments (Muller, 1973). These take the form of a comb of vertical and horizontal magnetic field lines respectively. Radial motions in these filaments were discovered by Evershed (1909). There is a continuous outward flow along the dark filaments with speeds of 6 to 7 km s^{-1}. A slower inflow is also present in the bright penumbral filaments. Higher in the atmosphere the Evershed outflow slows until it reverses direction in the chromosphere.

As mentioned previously sunspots appear within a belt surrounding the equator. The average latitude at which they appear depends on the solar cycle. Early in the cycle sunspots emerge at higher latitudes and as the cycle progresses this emergence latitude decreases. The cycle has an approximate 11 year period discovered by Schwabe (1843) through observations of sunspots. The solar cycle is variable; the rise from maximum is generally steeper than the subsequent decline, and sometimes it may disappear altogether. This occurred in 1645, a time known as the Maunder Minimum, when no sunspots were observed for 70 years. Sunspots are governed by certain rules. Sunspot groups are tilted with the leading spot lying closer to the equator than the following spots (Hale et al., 1919). During the solar cycle the polarity of all leading sunspots in the northern hemisphere is the same. Those in the southern hemisphere will have the opposite polarity to those in the north. These polarities will reverse at the onset of the new solar cycle (Hale and Nicholson, 1925). The Sun thus takes two cycles to return to the same magnetic state; this 22 year periodicity is known as the Hale Cycle. The dramatic change in the Sun between solar maximum and minimum is demonstrated by Figure 1.7 where a huge decrease in activity is apparent.

Other phenomena that exist on the Sun include solar prominences. These are large, cool and dense structures which are located in the solar corona. Their temperature is 100 times lower than coronal values and their density between 100 and 1000 times greater (Tandberg-Hanssen, 1974). Prominences appear as bright structures on the limb of the Sun, as shown in Figure 1.8. Against the disk prominences appear as thin, dark ribbons and are referred to as filaments. There are two main types of prominence: quiescent and active prominences. Quiescent prominences have a magnetic field of strength of $5-10$ G which makes a small angle to their long axis. Their active equivalents are about 100 G with the field approximately aligned with the prominence. Quiescent prominences are highly stable and may last for many months. They start out along a polarity inversion line, perhaps between active regions or at the edge of an active region. As the active region disperses the prominence will grow longer and thicker, all the while moving polewards. A typical quiescent prominence may have a length of 200 000 km, a height of 50 000 km, and a width of 6 000 km. Active region prominences tend to be three or four times smaller than this and as suggested by the name are located within active regions. These are more dynamic than the quiescent prominences, lasting only minutes or hours, and when they erupt are often associated with flares.

Both active and quiescent prominences may exhibit large-scale motions. The prominence can become lighter or darker (depending on whether it is viewed on the limb or against the disk) and grow larger. This behaviour may simply fade away or it can lead to an eruption. In this case the prominence will ascend and eventually disappear, with some material escaping from the Sun and the rest descending into the chromosphere. The cause of these eruptions is unknown, but is sometimes associated with a disturbance from an emerging flux region or a solar flare. A solar flare consists of a rapid brightening in Hα accompanied by a simultaneous ejection of high energy particles and plasma into the solar wind. There are two main stages to this process: the flash phase when the increase in intensity takes place (lasting 5 minutes), and the main phase during which this intensity slowly declines over about an hour. The energy released by these solar flares can heat overlying coronal loops to tens of millions of degrees. Although this will contribute to coronal heating, it is not the only factor.

1.1.4 Solar Facts

Here we summarise some general properties of the Sun.

Age	4.5×10^9 years,
Mass	$M_\odot = 1.99 \times 10^{30}$ kg,
Radius	$R_\odot = 696$ Mm,
Mean Density	1.4×10^3 kg m^{-3},
Mean Distance from Earth	1 AU = 1.5×10^{11} m = 215 $R_\odot$,
Surface Gravity	$g_\odot = 274$ m s^{-2},
Equatorial Rotation Period	26 days,
Effective Temperature	5785 K.

Table 1.1: Solar facts (Priest, 1982).

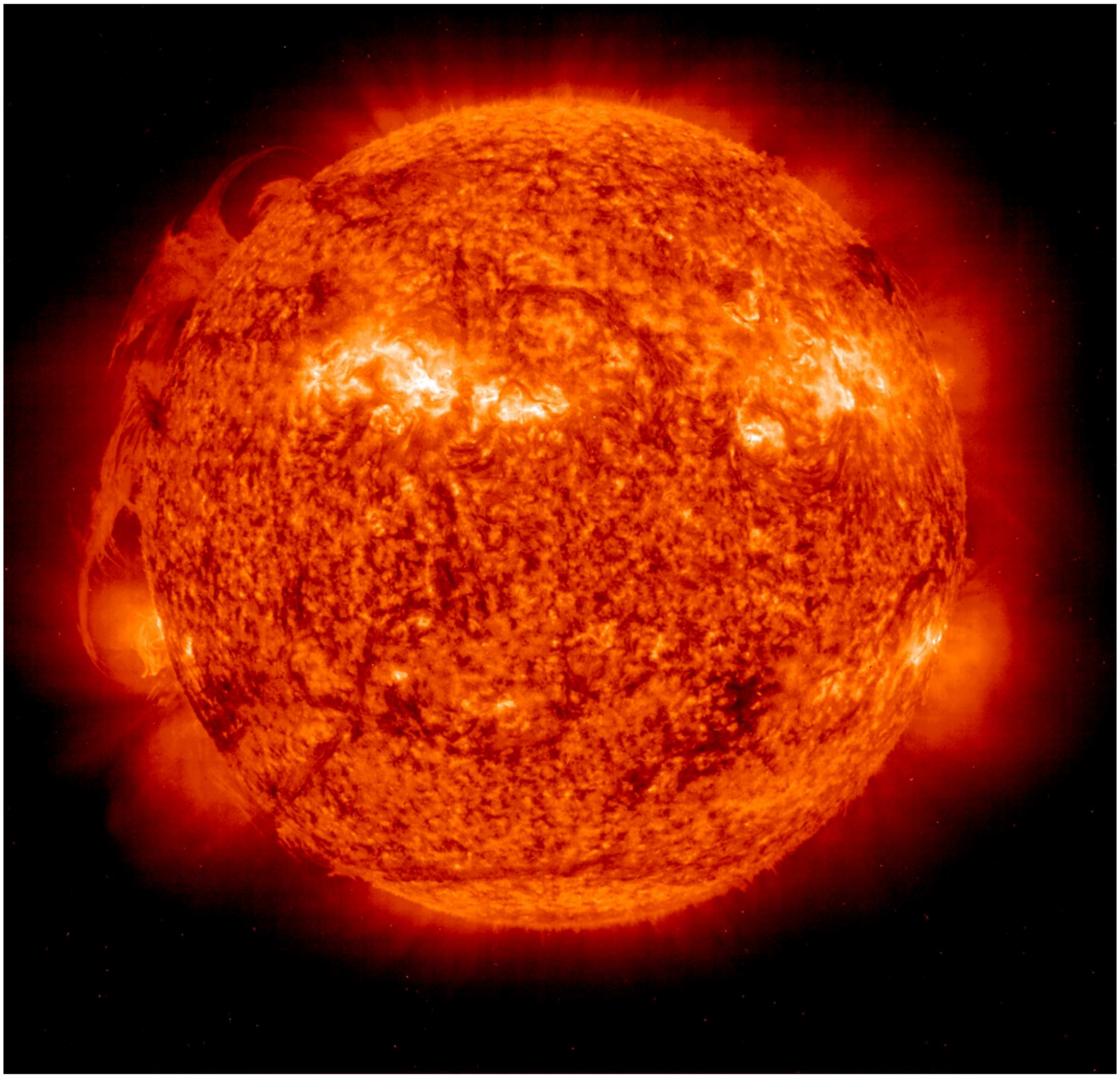

Figure 1.8: This image was taken by SOHO's EIT instrument in the 304 Å passband on 5 December 1998. It shows the upper chromosphere at a temperature of 60 000 K and some elongated prominences may be seen in the upper left-hand corner.
Credit: Courtesy of SOHO/EIT consortium. SOHO is a project of international cooperation between ESA and NASA.

1.2 MHD Equations

The Magnetohydrodynamic (MHD) equations are used to model the Sun, where the ionised gas is treated as a continuous plasma. The electric and magnetic fields are determined by Maxwell's equations, which combined with Ohm's Law and the equations of fluid mechanics describe the plasma behaviour. These equations may be derived from the Boltzmann equations for electrons and protons by taking moments as described in Boyd and Sanderson (1969). The equations of continuity, momentum and energy for each species are found from the zeroth, first and second velocity moments respectively. However, we shall start with the equations in a single fluid format (Priest, 1982).

1.2.1 Maxwell's Equations

Maxwell's equations describe how the magnetic field ($\mathbf{B}$) and the electric field ($\mathbf{E}$) vary due to the presence of electric currents ($\mathbf{j}$) and the density of charges (ρ_c).

$$\nabla \times \mathbf{B} = \mu \mathbf{j} + \frac{1}{c^2}\frac{\partial \mathbf{E}}{\partial t}, \tag{1.1}$$

$$\nabla \cdot \mathbf{B} = 0, \tag{1.2}$$

$$\nabla \times \mathbf{E} = -\frac{\partial \mathbf{B}}{\partial t}, \tag{1.3}$$

$$\nabla \cdot \mathbf{E} = \frac{\rho_c}{\epsilon}, \tag{1.4}$$

where for a vacuum or a low-density plasma

$$\mathbf{j} = \sigma \left(\mathbf{E} + \mathbf{v} \times \mathbf{B} \right). \tag{1.5}$$

The speed of light in a vacuum is given by $c = (\mu_0 \epsilon_0)^{-1/2}$ where $\mu_0 = 4\pi \times 10^{-7}$ H m^{-1} and $\epsilon_0 \approx 8.854 \times 10^{-12}$ F m^{-1} are the vacuum values of the magnetic permeability (μ) and the permittivity of free space (ϵ), and σ is the electrical conductivity.

Equation (1.1) is known as Ampére's Law and states that magnetic fields may be produced by electric currents or time-varying electric fields, Equation (1.2) is the Solenoidal Condition which implies that there are no magnetic monopoles, Equation (1.3) is Faraday's Law of Induction and Equation (1.4) is Gauss's Law which states that charge is conserved. Equations (1.3) and (1.4) also imply that either time-varying magnetic fields or electric charges may give rise to an electric field. Equation (1.5) is Ohm's Law. The right-hand side of Equation (1.4) may be set to zero if the plasma is assumed to be quasi-neutral, so

$$\nabla \cdot \mathbf{E} = 0. \tag{1.6}$$

This is not generally used in MHD as $\nabla \cdot \mathbf{E}$ can be found by taking the divergence of Ohm's Law (1.5).

If we carry out a dimensional analysis on Equations (1.1) – (1.4) where $v_0 = l_0/t_0$ is a characteristic plasma speed, with l_0 and t_0 giving a typical lengthscale and timescale, then Faraday's Law (1.3) suggests

$$\frac{E_0}{l_0} \approx \frac{B_0}{t_0}, \tag{1.7}$$

where E_0 and B_0 are typical values of E and B. Now considering Ampére's Law (1.1) the final term may be approximated as

$$\frac{E_0}{c^2 t_0} \approx \frac{B_0 l_0}{c^2 t_0^2} = \frac{v_0^2}{c^2}\frac{B_0}{l_0}. \tag{1.8}$$

Since one of the fundamental assumptions of MHD states that motions are non-relativistic, so $v_0 << c$, this term may then be neglected in comparison with the left-hand side of Ampére's Law to give

$$\mathbf{j} = \frac{1}{\mu}\left(\nabla \times \mathbf{B}\right). \tag{1.9}$$

N.B. It is possible to use relativistic MHD but it is not considered here.

In solar MHD the primary variables are generally considered to be $\mathbf{v}$ and $\mathbf{B}$. We eliminate $\mathbf{E}$ and $\mathbf{j}$ by combining Equations (1.9), (1.3) and (1.5)

$$\frac{\partial \mathbf{B}}{\partial t} = \nabla \times \left(\mathbf{v} \times \mathbf{B}\right) - \eta \nabla \times \left(\nabla \times \mathbf{B}\right), \tag{1.10}$$

where we have assumed that the magnetic diffusivity $\eta = 1/\left(\mu\sigma\right)$ is uniform. This is the Induction equation. We may then use the vector identity

$$\nabla \times \left(\nabla \times \mathbf{B}\right) = \nabla\left(\nabla \cdot \mathbf{B}\right) - \left(\nabla \cdot \nabla\right)\mathbf{B} = -\nabla^2 \mathbf{B}, \tag{1.11}$$

to find

$$\frac{\partial \mathbf{B}}{\partial t} = \nabla \times \left(\mathbf{v} \times \mathbf{B}\right) + \eta \nabla^2 \mathbf{B}, \tag{1.12}$$

which is the form of the Induction equation we use.

Thus, if $\mathbf{v}$ is known we may find $\mathbf{B}$ subject to Equation (1.2). It is worth noting that if we take the divergence of Equation (1.10) we obtain

$$\frac{\partial}{\partial t}\left(\nabla \cdot \mathbf{B}\right) = 0, \tag{1.13}$$

since the divergence of a curl is automatically zero. Thus if Equation (1.2) is satisfied initially it will remain true for all time. The current density and the electric field follow from Ampére's Law

$$\mathbf{j} = \frac{1}{\mu}\left(\nabla \times \mathbf{B}\right), \tag{1.14}$$

and Ohm's Law

$$\mathbf{E} = -\mathbf{v} \times \mathbf{B} + \frac{\mathbf{j}}{\sigma}. \tag{1.15}$$

If we take a closer look at the MHD Induction equation (1.12), then we may see that the first term on the right-hand side represents changes of $\mathbf{B}$ in time due to advective motions and the second term due to diffusion. Taking the ratio of these terms we obtain a dimensionless parameter known as the magnetic Reynolds number

$$R_m = \frac{l_0 v_0}{\eta}. \tag{1.16}$$

If $R_m << 1$ then the advective term may be neglected in comparison with the diffusive term and the Induction equation becomes

$$\frac{\partial \mathbf{B}}{\partial t} = \eta \nabla^2 \mathbf{B}. \tag{1.17}$$

This has the form of a simple diffusion equation, and describes how the magnetic field may slip through the plasma. This occurs only for some very small-scale phenomena in the solar atmosphere such as thin current sheets. If $R_m >> 1$, as is the case for the majority of the solar atmosphere, then the induction equation may be approximated by

$$\frac{\partial \mathbf{B}}{\partial t} = \nabla \times (\mathbf{v} \times \mathbf{B}). \tag{1.18}$$

In this limit Alfvén's frozen flux theorem applies (Alfvén, 1943) which tells us that: *In a perfectly conducting fluid ($R_m \to \infty$), magnetic field lines move with the fluid: the field lines are 'frozen' into the plasma.* A textbook version of this proof is given in Priest (1982). We assume that we are working with a perfectly conducting fluid throughout.

1.2.2 Equations of Fluid Mechanics

The velocity $\mathbf{v}$, the gas density ρ and the pressure p evolve according to the equations of fluid mechanics.

$$\rho \left(\frac{\partial}{\partial t} + \mathbf{v} \cdot \nabla \right) \mathbf{v} = -\nabla p + \rho \mathbf{g} + \nu \nabla^2 \mathbf{v}, \tag{1.19}$$

$$\frac{\partial \rho}{\partial t} + \nabla \cdot (\rho \mathbf{v}) = 0, \tag{1.20}$$

$$p = R\rho \frac{T}{\widetilde{\mu}}, \tag{1.21}$$

where $|\mathbf{g}| = 274$ m s^{-2} is the surface gravitational acceleration, ν is the coefficient of kinematic viscosity, R is the universal gas constant, and $\widetilde{\mu}$ is the mean molecular weight (this takes the value 0.5 in a fully ionised hydrogen plasma, and 0.6 in the solar corona due to the contribution from helium ions). Equation (1.19) is known as the Equation of Motion, Equation (1.20) is the Continuity Equation and Equation (1.21) is the Ideal Gas Law which is a good approximation for high temperature, low density gases. We consider viscosity to be negligible and this term is therefore neglected from the Equation of Motion.

Because we are dealing with an ionised plasma an additional magnetic force $\mathbf{j} \times \mathbf{B}$ per unit volume will be experienced. This is known as the Lorenz Force. The Equation of Motion (1.19) thus becomes

$$\rho \left(\frac{\partial}{\partial t} + \mathbf{v} \cdot \nabla \right) \mathbf{v} = -\nabla p + \mathbf{j} \times \mathbf{B} + \rho \mathbf{g}. \tag{1.22}$$

Now the Lorenz Force may be written

$$\mathbf{j} \times \mathbf{B} = \frac{1}{\mu} \left(\nabla \times \mathbf{B} \right) \times \mathbf{B}, \tag{1.23}$$

using the triple vector product this reduces to

$$\mathbf{j} \times \mathbf{B} = \frac{1}{\mu} \left(\mathbf{B} \cdot \nabla \right) \mathbf{B} - \nabla \left(\frac{B^2}{2\mu} \right). \tag{1.24}$$

The first term in this equation represents a magnetic tension acting parallel to the magnetic field with magnitude B^2/μ. This will only have an effect when the field lines are curved. The second term gives a magnetic pressure force when the magnetic field varies with position. In contrast to the magnetic tension force this acts in all directions.

To complete this set of equations we also require an energy equation.

$$\frac{\rho^\gamma}{\gamma - 1} \frac{\mathrm{D}}{\mathrm{D}t} \left(\frac{p}{\rho^\gamma} \right) = -\mathcal{L}, \tag{1.25}$$

where γ is the ratio of specific heats (generally $\gamma = 5/3$ in the corona) and $\mathcal{L}$ is the energy loss function which represents the net effect of all sinks and sources of energy. We consider an adiabatic energy equation so that the loss function vanishes, *i.e.* $\mathcal{L} = 0$, as the effects of thermal conduction, radiative cooling and ohmic heating are neglected. This has the consequence that entropy ($S = C_v \log \left(p/\rho^\gamma \right) +$ const, where C_v is the specific heat at a constant volume) is conserved. The Energy Equation is then

$$\frac{\mathrm{D}}{\mathrm{D}t} \left(\frac{p}{\rho^\gamma} \right) = 0, \tag{1.26}$$

or alternatively

$$\frac{\partial p}{\partial t} + \left(\mathbf{v} \cdot \nabla \right) p = \frac{\gamma p}{\rho} \left(\frac{\partial \rho}{\partial t} + \left(\mathbf{v} \cdot \nabla \right) \rho \right) = -\gamma p \left(\nabla \cdot \mathbf{v} \right). \tag{1.27}$$

1.2.3 Summary of MHD Equations and Assumptions

The fundamental MHD equations we use throughout this thesis are then:

The Equation of Mass Continuity

$$\frac{\partial \rho}{\partial t} + \nabla \cdot (\rho \mathbf{v}) = 0. \tag{1.28}$$

The Equation of Motion

$$\rho \left(\frac{\partial}{\partial t} + \mathbf{v} \cdot \nabla \right) \mathbf{v} = -\nabla p + \mathbf{j} \times \mathbf{B} + \rho \mathbf{g}. \tag{1.29}$$

The Induction Equation

$$\frac{\partial \mathbf{B}}{\partial t} = \nabla \times (\mathbf{v} \times \mathbf{B}). \tag{1.30}$$

The Adiabatic Energy Equation

$$\frac{\partial p}{\partial t} + (\mathbf{v} \cdot \nabla) p = \frac{\gamma p}{\rho} \left(\frac{\partial \rho}{\partial t} + (\mathbf{v} \cdot \nabla) \rho \right). \tag{1.31}$$

The Ideal Gas Law

$$p = R\rho \frac{T}{\widetilde{\mu}}. \tag{1.32}$$

These equations are generally coupled together, and can be solved to determine $\mathbf{v}$, $\mathbf{B}$, p, ρ and T. Additionally, the secondary variables $\mathbf{j}$ and $\mathbf{E}$ may be calculated from Ampére's Law

$$\mathbf{j} = \frac{1}{\mu} (\nabla \times \mathbf{B}), \tag{1.33}$$

and Ohm's Law

$$\mathbf{E} = -\mathbf{v} \times \mathbf{B} + \frac{\mathbf{j}}{\sigma}. \tag{1.34}$$

Finally $\mathbf{B}$ must also satisfy the Solenoidal Condition

$$\nabla \cdot \mathbf{B} = 0. \tag{1.35}$$

In this form we have already assumed that viscous and diffusive terms are negligible, and variations in p, ρ and T take place on a timescale much smaller than that of radiation, conduction or heating.

More generally the MHD equations must satisfy the following assumptions (Priest, 1982; Boyd and Sanderson, 1969, 2003). The plasma is assumed to be collisional which means it may be treated as a continuum. This is valid provided that the collision timescale (τ_c) is very much shorter than the typical plasma timescale (t_0), $\tau_c << t_0$. This allows the particle distribution function to relax to a Maxwellian. It is also required that the mean free path of the ions and electrons (λ_c) is very small compared to hydrodynamic lengthscales $\lambda_c << l_0$, and that the ion Larmor radius (r_L) is very much smaller than the mean free path $r_L << \lambda_c$. This means that the gyro-motions of particles may be neglected. In the solar corona a magnetic field of $B = 10$ G, temperature $T = 10^6$ K, and density $n = 10^{15}$ m^{-3} give a Larmor radius $r_L = 9.47 \times 10^3$ m, a collision time $\tau_c = 0.836$ s, and a mean free path $\lambda_c = 7.6 \times 10^4$ m. The mean free path will increase for higher temperature, lower density plasmas. Taking the coronal scale height as a typical lengthscale $l_0 = 60$ Mm, and a typical timescale for wave motions $t_0 = 60$ s the above constraints are satisfied. The plasma is also assumed to satisfy the condition of quasi-neutrality, $n_i - n_e << n$, which states that the number density of the ions (n_i) minus that of the electrons (n_e) is very much smaller than the total number density (n). In other words the number of ions and electrons is approximately equal. Finally it is assumed that the plasma motions are non-relativistic, *i.e.* the typical plasma velocity is much smaller than the speed of light $v_0 << c$.

1.3 MHD Waves

The magnetised plasma of the solar atmosphere may support a variety of waves. As an analogy for this we investigate the simple example of a wave propagating along a string, and then examine the complexities added by introducing a magnetic field.

1.3.1 General Wave Properties

If we consider perturbing a one-dimensional string from its equilibrium we would expect to see a transverse wave, either standing or propagating along the string. The behaviour of this wave would be described by the wave equation

$$\frac{\partial^2 y}{\partial t^2} = c^2 \frac{\partial^2 y}{\partial x^2}, \tag{1.36}$$

where the wave speed is given by

$$c = \sqrt{\frac{\text{Tension}}{\text{Density}}}, \tag{1.37}$$

and x and y are the horizontal and vertical direction and t is the time.

We may then take Fourier components by setting

$$y = Ae^{i(kx - \omega t)}, \tag{1.38}$$

where k is the wavenumber and ω is the frequency of the disturbance. These contain information about the wave properties as the wavelength is given by $\lambda = 2\pi/k$ and the period is $2\pi/\omega$. Substituting Equation (1.38) into Equation (1.36) allows a dispersion relation to be found relating ω to k

$$\omega^2 = k^2 c^2. \tag{1.39}$$

From the dispersion relation we may determine the phase speed

$$c_{\text{ph}} = \frac{\omega}{k}, \tag{1.40}$$

and the group velocity

$$\mathbf{c}_{\text{g}} = \frac{\mathrm{d}\omega}{\mathrm{d}\mathbf{k}}. \tag{1.41}$$

The phase speed is the speed at which a wave specified by a single wavenumber (or component of a wave train) will travel in the direction of the wavenumber $\mathbf{k}$, whereas the group velocity tells us the speed and direction of a group or packet of waves which may have a range of wavenumbers. The phase and group velocities are generally different and it is at the group velocity that energy is transmitted. For this problem it turns out that the phase speed and group velocity are the same with a value of $\pm c$. We now return to solar applications, beginning with the MHD equations.

1.3.2 Equilibrium

Before considering small amplitude waves we must discuss the equilibrium. If we consider an equilibrium, *i.e.* $\partial/\partial t = 0$ and $\mathbf{v} = 0$, then the MHD Equations (1.28) – (1.32) are greatly reduced leaving only the equilibrium Equation of Motion and the Ideal Gas Law

$$\nabla p_0 = \frac{1}{\mu} \left(\nabla \times \mathbf{B}_0\right) \times \mathbf{B}_0 + \rho_0 \mathbf{g}, \tag{1.42}$$

$$p_0 = R\rho_0 \frac{T_0}{\widetilde{\mu}}, \tag{1.43}$$

where the zero subscripts signify that we are dealing with equilibrium quantities, and gravity acts vertically downwards, opposite to the z-axis. The MHD equations may then be linearised about the equilibrium.

1.3.3 Linearised MHD Equations

We may linearise Equations (1.28) – (1.35) for general equilibria (given by setting $\partial/\partial t = 0$ and $\mathbf{v}_0 = 0$) by taking each term and adding a small perturbation (denoted by subscript 1)

$$\begin{aligned} \mathbf{B} = \mathbf{B}_0 + \mathbf{B}_1 \left(x, z, t\right), \quad \mathbf{v} = \mathbf{v}_1 \left(x, z, t\right), \quad p = p_0 + p_1 \left(x, z, t\right), \\ \rho = \rho_0 + \rho_1 \left(x, z, t\right), \quad T = T_0 + T_1 \left(x, z, t\right), \end{aligned} \tag{1.44}$$

where the equilibrium quantities (denoted by subscript 0) may vary with x and z. For the sake of our investigation all quantities are assumed to be invariant in y. These are then substituted back into the MHD equations; to complete the linearisation products of perturbed quantities and squares are neglected. This process yields the Linearised MHD equations:

$$\frac{\partial \rho_1}{\partial t} + \nabla \cdot \left(\rho_0 \mathbf{v}_1\right) = 0, \tag{1.45}$$

$$\rho_0 \frac{\partial \mathbf{v}_1}{\partial t} = -\nabla p_1 + \frac{1}{\mu}\left(\nabla \times \mathbf{B}_1\right) \times \mathbf{B}_0 + \frac{1}{\mu}\left(\nabla \times \mathbf{B}_0\right) \times \mathbf{B}_1 + \rho_1 \mathbf{g}, \tag{1.46}$$

$$\frac{\partial \mathbf{B}_1}{\partial t} = \nabla \times \left(\mathbf{v}_1 \times \mathbf{B}_0\right), \tag{1.47}$$

$$\frac{\partial p_1}{\partial t} + \left(\mathbf{v}_1 \cdot \nabla\right) p_0 = \frac{\gamma p_0}{\rho_0}\left(\frac{\partial \rho_1}{\partial t} + \left(\mathbf{v}_1 \cdot \nabla\right)\rho_0\right), \tag{1.48}$$

$$\frac{p_1}{p_0} = \frac{\rho_1}{\rho_0} + \frac{T_1}{T_0}, \tag{1.49}$$

$$\nabla \cdot \mathbf{B}_1 = 0. \tag{1.50}$$

Henceforth the subscripts on perturbed variables are dropped and it is assumed that we are working with the Linearised MHD equations. Here the equations are in their most general form but they may be applied to specific equilibria; say a constant, vertical background magnetic field directed along the z-axis.

$$\mathbf{B}_0 = \left(0, 0, B_0\right), \quad \mathbf{v}_0 = 0. \tag{1.51}$$

Applying the equilibrium values (1.51) to the Linearised MHD Equations (1.45) – (1.48) we obtain

$$\frac{\partial \rho}{\partial t} + \nabla \cdot \left(\rho_0 \mathbf{v}\right) = 0, \tag{1.52}$$

$$\rho_0 \frac{\partial \mathbf{v}}{\partial t} = -\nabla p + \frac{1}{\mu}\left(\nabla \times \mathbf{B}\right) \times \mathbf{B}_0 + \rho \mathbf{g}, \tag{1.53}$$

$$\frac{\partial \mathbf{B}}{\partial t} = \nabla \times \left(\mathbf{v} \times \mathbf{B}_0\right), \tag{1.54}$$

$$\frac{\partial p}{\partial t} = -\left(\mathbf{v} \cdot \nabla\right) p_0 - \gamma p_0 \left(\nabla \cdot \mathbf{v}\right). \tag{1.55}$$

Equations (1.52) – (1.55) can be manipulated into a pair of wave equations. First we differentiate the Equation of Motion (1.53) with respect to t to give

$$\rho_0 \frac{\partial^2 \mathbf{v}}{\partial t^2} = -\nabla \frac{\partial p}{\partial t} + \frac{1}{\mu}\left(\nabla \times \frac{\partial \mathbf{B}}{\partial t}\right) \times \mathbf{B}_0 + \frac{\partial \rho}{\partial t}\mathbf{g}, \tag{1.56}$$

we may then substitute for $\partial p/\partial t$ and $\partial \mathbf{B}/\partial t$ from Equations (1.55) and (1.54) respectively to obtain

$$\rho_0 \frac{\partial^2 \mathbf{v}}{\partial t^2} = \nabla\left(\mathbf{v} \cdot \nabla\right) p_0 + \gamma \nabla\left(p_0 \left(\nabla \cdot \mathbf{v}\right)\right) + \frac{1}{\mu}\left(\nabla \times \left(\nabla \times \left(\mathbf{v} \times \mathbf{B}_0\right)\right)\right) \times \mathbf{B}_0 + \frac{\partial \rho}{\partial t}\mathbf{g}. \tag{1.57}$$

Finally we can substitute for $\partial \rho/\partial t$ from the Mass Continuity Equation (1.52)

$$\rho_0 \frac{\partial^2 \mathbf{v}}{\partial t^2} = \nabla\left(\mathbf{v} \cdot \nabla\right) p_0 + \gamma \nabla\left(p_0 \left(\nabla \cdot \mathbf{v}\right)\right) + \frac{1}{\mu}\left(\nabla \times \left(\nabla \times \left(\mathbf{v} \times \mathbf{B}_0\right)\right)\right) \times \mathbf{B}_0 - \nabla \cdot \left(\rho_0 \mathbf{v}\right)\mathbf{g}. \tag{1.58}$$

This is the general form of the wave equation.

1.3.4 Sound Waves (Zero B)

To obtain an equation for pure sound waves we must neglect both the magnetic field and the gravitational acceleration. Taking the equilibrium pressure and density to be constant the Linearised MHD equations reduce to

$$\frac{\partial \rho}{\partial t} + \rho_0 \left(\nabla \cdot \mathbf{v}\right) = 0, \tag{1.59}$$

$$\rho_0 \frac{\partial \mathbf{v}}{\partial t} = -\nabla p, \tag{1.60}$$

and the Energy Equation may be written

$$p = c_s^2 \rho, \tag{1.61}$$

where $c_s = \sqrt{\gamma p_0/\rho_0}$ is the sound speed. In the solar corona the sound speed will typically take a value of approximately 150 km s^{-1}.

We may then eliminate $\mathbf{v}$ and p to obtain a wave equation in ρ. If we first differentiate Equation (1.59) with respect to t,

$$\frac{\partial^2 \rho}{\partial t^2} = -\rho_0 \left(\nabla \cdot \frac{\partial \mathbf{v}}{\partial t}\right), \tag{1.62}$$

then substitute from Equations (1.60) and (1.61) we find the wave equation

$$\frac{\partial^2 \rho}{\partial t^2} = c_s^2 \nabla^2 \rho. \tag{1.63}$$

Taking the Fourier component

$$\rho = A e^{i(\mathbf{k}\cdot\mathbf{r} - \omega t)}, \tag{1.64}$$

where $\mathbf{k} = (k_x, k_y, k_z)$ and $\mathbf{r} = (x, y, z)$ we obtain the dispersion relation

$$\omega^2 = k^2 c_s^2, \tag{1.65}$$

where $k^2 = k_x^2 + k_y^2 + k_z^2$. From this we can see that disturbances travel at the sound speed c_s. This is a purely acoustic wave which we can see is compressible in nature ($\nabla \cdot \mathbf{v} \neq 0$) as it will cause compressions and rarefactions in the plasma as it propagates.

1.3.5 Alfvén Waves (Zero β)

Remembering back to the Lorenz Force (1.24) there is a magnetic tension force. So if we consider the magnetic field lines to act like strings, then in analogy with Section 1.3.1 we expect to see waves propagating transverse to the magnetic field. From Equation (1.37) we would then expect such disturbances to travel at a speed

$$v_A = \sqrt{\frac{B_0^2/\mu}{\rho_0}} = \frac{B_0}{\sqrt{\mu\rho_0}}. \tag{1.66}$$

This is known as the Alfvén speed and is named after Hannes Alfvén who first predicted the existence of these waves in 1942. A typical value for the Alfvén speed in the solar corona is 1000 km s^{-1}. The dispersion equation for these waves can be derived as follows.

The equilibrium pressure is set to zero, $p_0 = 0$, in order to avoid the complication of including sound waves. Additionally we take $\mathbf{g} = 0$, a uniform magnetic field $\mathbf{B}_0 = (0, 0, B_0)$, and assume that there are no variations in pressure or density. From the Continuity Equation (1.52) we have

$$\nabla \cdot \mathbf{v} = 0, \tag{1.67}$$

which means that the plasma is incompressible.

Applying the equilibrium conditions to the general wave equation (1.58) gives

$$\rho_0 \frac{\partial^2 \mathbf{v}}{\partial t^2} = \frac{1}{\mu} \left[\nabla \times (\nabla \times (\mathbf{v} \times \mathbf{B}_0))\right] \times \mathbf{B}_0. \tag{1.68}$$

Taking the Fourier component

$$\mathbf{v} = \widetilde{\mathbf{v}} e^{i(\mathbf{k}\cdot\mathbf{r} - \omega t)}, \tag{1.69}$$

the wave equation reduces to

$$\rho_0 \omega^2 \mathbf{v} = \frac{1}{\mu} \left[\mathbf{k} \times (\mathbf{k} \times (\mathbf{v} \times \mathbf{B}_0))\right] \times \mathbf{B}_0. \tag{1.70}$$

Note that we have $\nabla \cdot \mathbf{v} = 0$ and from the above equation $\mathbf{v} \cdot \mathbf{B}_0 = 0$. This tells us that the wave motions are perpendicular to both the direction of propagation and the equilibrium magnetic field, so Alfvén waves are transverse waves. Using vector identities we see that

$$\rho_0 \omega^2 \mathbf{v} = \frac{1}{\mu} \left(\mathbf{k} \cdot \mathbf{B}_0\right)^2 \mathbf{v}, \tag{1.71}$$

giving the dispersion relation

$$\omega^2 = k_z^2 v_A^2 = k^2 v_A^2 \cos^2\theta, \tag{1.72}$$

where θ is the angle between the wave vector ($\mathbf{k}$) and the magnetic field ($\mathbf{B}_0$) which is orientated parallel to the z-axis. From this we may calculate the phase speed

$$c_{\text{ph}} = \pm v_A \cos\theta, \tag{1.73}$$

and the group velocity

$$\mathbf{c}_\mathrm{g} = \pm v_A \hat{\mathbf{z}}. \tag{1.74}$$

These are both shown on the polar plots in Figure 1.9. As we can see Alfvén waves cannot propagate across the magnetic field lines and energy flows along the field at the Alfvén speed. We shall not discuss Alfvén waves any further here as these are not studied in this thesis.

1.3.6 General Uniform Medium

Next we look at a uniform, isothermal medium by taking the equilibrium given by (1.51) with the additional constraint of taking the gravitational acceleration to be zero.

$$\mathbf{B}_0 = (0, 0, B_0)\,, \quad \mathbf{v}_0 = 0, \quad p_0 = p_0, \quad \rho_0 = \rho_0, \quad \mathbf{g} = 0. \tag{1.75}$$

Applying these equilibrium values (1.75) to the Linearised MHD Equations (1.45) – (1.48) they become

$$\frac{\partial \rho}{\partial t} + \rho_0 \left(\nabla \cdot \mathbf{v}\right) = 0, \tag{1.76}$$

$$\rho_0 \frac{\partial \mathbf{v}}{\partial t} = -\nabla p + \frac{1}{\mu}\left(\nabla \times \mathbf{B}\right) \times \mathbf{B}_0, \tag{1.77}$$

$$\frac{\partial \mathbf{B}}{\partial t} = \nabla \times \left(\mathbf{v} \times \mathbf{B}_0\right), \tag{1.78}$$

$$\frac{\partial p}{\partial t} = \frac{\gamma p_0}{\rho_0}\frac{\partial \rho}{\partial t}. \tag{1.79}$$

We may then follow the method used in Section 1.3.3 to obtain a wave equation.

$$\rho_0 \frac{\partial^2 \mathbf{v}}{\partial t^2} = \rho_0 c_s^2 \nabla \left(\nabla \cdot \mathbf{v}\right) + \frac{1}{\mu}\left(\nabla \times \left(\nabla \times \left(\mathbf{v} \times \mathbf{B}_0\right)\right)\right) \times \mathbf{B}_0. \tag{1.80}$$

As the magnetic field is only in the z-direction and the variables are all invariant in y, it is fairly easy to show that

$$\left(\nabla \times \left(\nabla \times \left(\mathbf{v} \times \mathbf{B}_0\right)\right)\right) \times \mathbf{B}_0 = B_0^2 \nabla^2 v_x \hat{\mathbf{x}}, \tag{1.81}$$

and so we can separate Equation (1.58) into its x and z components

$$\frac{\partial^2 v_x}{\partial t^2} = \left(c_s^2 + v_A^2\right)\frac{\partial^2 v_x}{\partial x^2} + c_s^2 \frac{\partial^2 v_z}{\partial x \partial z} + v_A^2 \frac{\partial^2 v_x}{\partial z^2}, \tag{1.82}$$

$$\frac{\partial^2 v_z}{\partial t^2} = c_s^2 \left(\frac{\partial^2 v_x}{\partial x \partial z} + \frac{\partial^2 v_z}{\partial z^2}\right). \tag{1.83}$$

The variables v_x and v_z denote different components of the same wave mode in each equation.

If we take Fourier components so that

$$v_x\left(x,z,t\right)=v_{x0}e^{i(\omega t+k_x x+k_z z)}, \tag{1.84}$$

$$v_z\left(x,z,t\right)=v_{z0}e^{i(\omega t+k_x x+k_z z)}, \tag{1.85}$$

Equations (1.82) and (1.83) reduce down to

$$\left(\omega^2-\left(c_s^2+v_A^2\right)k_x^2-v_A^2k_z^2\right)v_{x0}=c_s^2k_xk_zv_{z0}, \tag{1.86}$$

$$\left(\omega^2-c_s^2k_z^2\right)v_{z0}=c_s^2k_xk_zv_{x0}. \tag{1.87}$$

Equations (1.86) and (1.87) may then be combined to obtain the dispersion relation for magnetoacoustic waves as discussed by Roberts (1985)

$$\omega^4-\left(c_s^2+v_A^2\right)k^2\omega^2+c_s^2v_A^2k_z^2k^2=0, \tag{1.88}$$

where $k=\sqrt{k_x^2+k_z^2}$ is the magnitude of the wave vector $\mathbf{k}=(k_x,0,k_z)$. This is a quadratic in ω^2 and has two solutions

$$\omega^2=\frac{k^2}{2}\left[\left(c_s^2+v_A^2\right)\pm\sqrt{\left(c_s^2+v_A^2\right)^2-4c_s^2v_A^2\cos^2\theta}\right], \tag{1.89}$$

where the plus sign gives the higher frequency fast wave solution and the minus sign the lower frequency slow wave. These wave modes are named fast and slow waves due to their relative speeds. These waves are driven by both tension and pressure forces.

For the fast wave the phase speed is given by

$$\frac{\omega}{k}=\sqrt{\frac{1}{2}\left[\left(c_s^2+v_A^2\right)+\sqrt{\left(c_s^2+v_A^2\right)^2-4c_s^2v_A^2\cos^2\theta}\right]}. \tag{1.90}$$

If $\theta=0$ then the phase speed depends on the relative sizes of the sound and Alfvén speeds.

$$\frac{\omega}{k}=\begin{cases} v_A & \text{if } c_s<v_A, \\ c_s & \text{if } c_s>v_A. \end{cases} \tag{1.91}$$

However, if $\theta=\pi/2$ then the phase speed takes only one value

$$\frac{\omega}{k}=\left(c_s^2+v_A^2\right)^{1/2}=c_f, \tag{1.92}$$

where c_f is the fast speed.

The group velocity may be written in terms of its components $\left(\frac{\partial\omega}{\partial k_x}, 0, \frac{\partial\omega}{\partial k_z}\right)$

$$\frac{\partial\omega}{\partial k_x} = \frac{\sin\theta\left(c_s^2+v_A^2+\frac{\left[\left(c_s^2+v_A^2\right)^2-2c_s^2v_A^2\cos^2\theta\right]}{\sqrt{\left(c_s^2+v_A^2\right)^2-4c_s^2v_A^2\cos^2\theta}}\right)}{2\sqrt{\frac{1}{2}\left[\left(c_s^2+v_A^2\right)+\sqrt{\left(c_s^2+v_A^2\right)^2-4c_s^2v_A^2\cos^2\theta}\right]}}, \tag{1.93}$$

$$\frac{\partial\omega}{\partial k_z} = \frac{\cos\theta\left(c_s^2+v_A^2+\frac{\left[\left(c_s^2+v_A^2\right)^2-2c_s^2v_A^2\sin^2\theta-4c_s^2v_A^2\cos^2\theta\right]}{\sqrt{\left(c_s^2+v_A^2\right)^2-4c_s^2v_A^2\cos^2\theta}}\right)}{2\sqrt{\frac{1}{2}\left[\left(c_s^2+v_A^2\right)+\sqrt{\left(c_s^2+v_A^2\right)^2-4c_s^2v_A^2\cos^2\theta}\right]}}. \tag{1.94}$$

Now, when $\theta = 0$ we have

$$\frac{\partial\omega}{\partial k_x} = 0, \tag{1.95}$$

$$\frac{\partial\omega}{\partial k_z} = \begin{cases} v_A & \text{if } c_s < v_A, \\ c_s & \text{if } c_s > v_A. \end{cases} \tag{1.96}$$

If $\theta = \pi/2$ the group speed is given by

$$\frac{\partial\omega}{\partial k_x} = c_f, \tag{1.97}$$

$$\frac{\partial\omega}{\partial k_z} = 0. \tag{1.98}$$

These results are clearly depicted in Figure 1.9.

We may carry out a similar analysis for the slow wave. The phase speed is given by

$$\frac{\omega}{k} = \sqrt{\frac{1}{2}\left[\left(c_s^2+v_A^2\right)-\sqrt{\left(c_s^2+v_A^2\right)^2-4c_s^2v_A^2\cos^2\theta}\right]}. \tag{1.99}$$

If $\theta = 0$ then

$$\frac{\omega}{k} = \begin{cases} c_s & \text{if } c_s < v_A, \\ v_A & \text{if } c_s > v_A. \end{cases} \tag{1.100}$$

If $\theta = \pi/2$ then

$$\frac{\omega}{k} = 0. \tag{1.101}$$

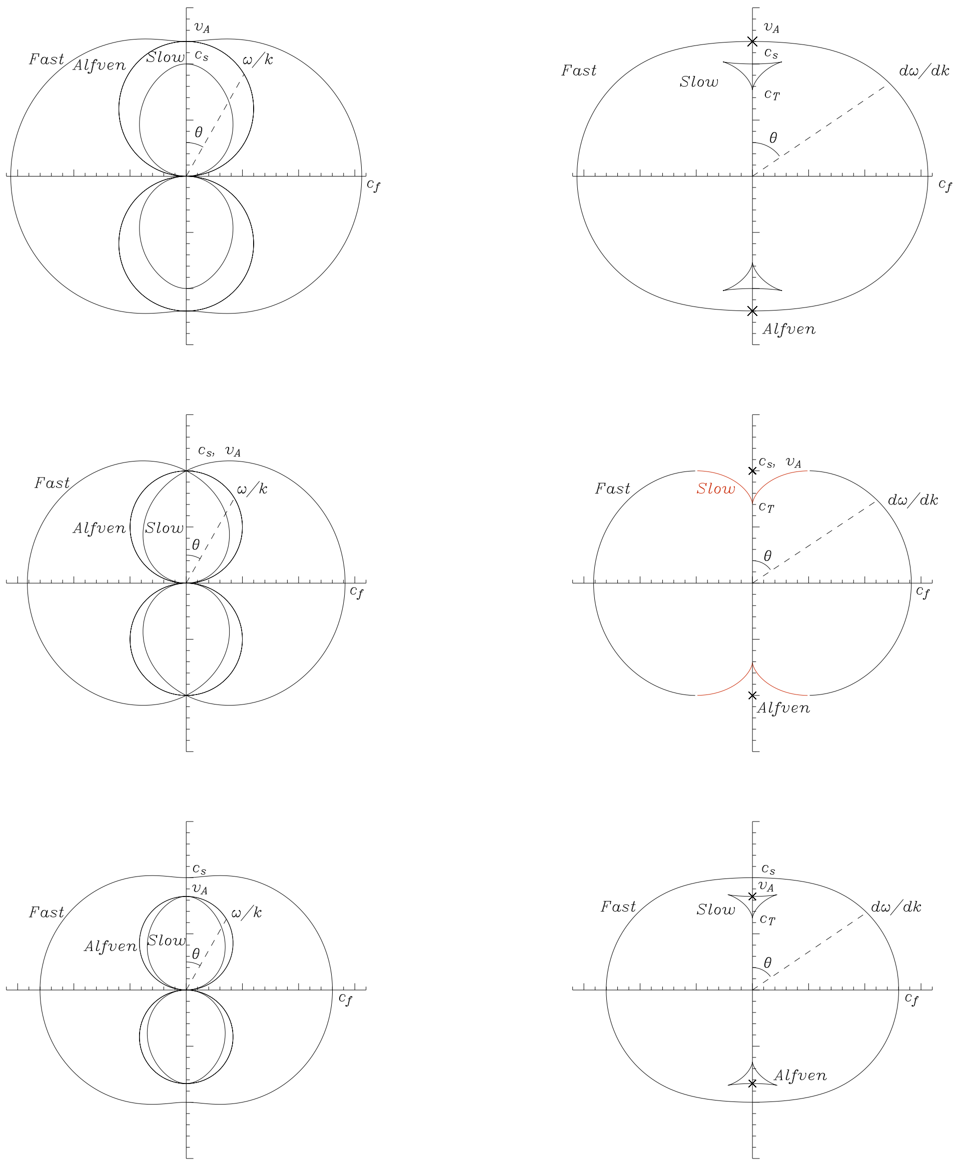

Figure 1.9: *Left:* The phase speeds for the Alfvén wave and the fast and slow magnetoacoustic waves. *Right:* The group velocities for the Alfvén wave and the fast and slow magnetoacoustic waves.
The top row have $c_s < v_A$, the middle row $c_s = v_A$, and the bottom row $c_s > v_A$. In all cases the magnetic field is aligned with the vertical direction, the horizontal axis gives the x-direction, and the vertical axis the z-direction.

The group velocity may again be given by its component parts; although this time we must take the binomial expansion of the terms inside the larger square root

$$\sqrt{\frac{1}{2}\left[(c_s^2+v_A^2)-\sqrt{\left(c_s^2+v_A^2\right)^2-4c_s^2v_A^2\cos^2\theta}\right]}\approx\frac{c_s v_A\cos\theta}{\left(c_s^2+v_A^2\right)^{1/2}}, \tag{1.102}$$

otherwise the solution cannot be evaluated in the limit $\theta\rightarrow\pi/2$.

So we obtain

$$\frac{\partial\omega}{\partial k_x}=\sin\theta\sqrt{\frac{1}{2}\left[(c_s^2+v_A^2)-\sqrt{\left(c_s^2+v_A^2\right)^2-4c_s^2v_A^2\cos^2\theta}\right]}- \\ -\sin 2\theta\frac{c_s v_A\left(c_s^2+v_A^2\right)^{1/2}}{2\sqrt{\left(c_s^2+v_A^2\right)^2-4c_s^2v_A^2\cos^2\theta}}, \tag{1.103}$$

$$\frac{\partial\omega}{\partial k_z}=\cos\theta\sqrt{\frac{1}{2}\left[(c_s^2+v_A^2)-\sqrt{\left(c_s^2+v_A^2\right)^2-4c_s^2v_A^2\cos^2\theta}\right]}+ \\ +\sin^2\theta\frac{c_s v_A\left(c_s^2+v_A^2\right)^{1/2}}{\sqrt{\left(c_s^2+v_A^2\right)^2-4c_s^2v_A^2\cos^2\theta}}. \tag{1.104}$$

If $\theta=0$ then

$$\frac{\partial\omega}{\partial k_x}=0, \tag{1.105}$$

$$\frac{\partial\omega}{\partial k_z}=\begin{cases} c_s & \text{if } c_s<v_A, \\ v_A & \text{if } c_s>v_A. \end{cases} \tag{1.106}$$

If $\theta=\pi/2$ then

$$\frac{\partial\omega}{\partial k_x}=0, \tag{1.107}$$

$$\frac{\partial\omega}{\partial k_z}=\frac{c_s v_A}{\left(c_s^2+v_A^2\right)^{1/2}}=c_T, \tag{1.108}$$

where c_T is the tube speed (see Roberts and Webb (1978)). The characteristic speeds are ordered such that $c_T<c_s,\ v_A<c_f$.

We can see these results for the phase and group velocities of the various MHD modes in Figure 1.9. From these plots it is clear that both the slow and Alfvén waves are unable to propagate across the magnetic field. While the Alfvén wave may only carry energy along the field, the group velocity plots show that for the slow wave energy flow is confined to close to the magnetic field. In contrast, the fast wave is roughly isotropic although it does travel slightly faster across the magnetic field.

1.3.7 Acoustic-Gravity Case

A slightly more complicated case includes gravitational acceleration in the isothermal atmosphere, but the magnetic field ($\mathbf{B}_0$) is taken to be zero and so the Alfvén speed is also zero. It can be seen from the equilibrium that the pressure and density now vary with z

$$\frac{\mathrm{d}p_0}{\mathrm{d}z} = -\rho_0 g. \tag{1.109}$$

This can be solved using the Ideal Gas Law (1.50) with T constant to give

$$p_0\left(z\right) = p_0\left(0\right) e^{-z/H}, \quad \rho_0\left(z\right) = \rho_0\left(0\right) e^{-z/H}, \tag{1.110}$$

where $H = p_0/\left(\rho_0 g\right)$ is the scale height. This tells us the typical scale over which gravity has a significant effect. If the typical lengthscales in a problem are very much smaller than the scale height then gravity may be neglected.

As in the uniform case we may substitute the equilibrium variables (1.110) into the Linearised MHD equations to obtain

$$\frac{\partial \rho}{\partial t} + \nabla \cdot \left(\rho_0 \mathbf{v}\right) = 0, \tag{1.111}$$

$$\rho_0 \frac{\partial \mathbf{v}}{\partial t} = -\nabla p + \rho \mathbf{g}, \tag{1.112}$$

$$\frac{\partial p}{\partial t} + \left(\mathbf{v} \cdot \nabla\right) p_0 = \frac{\gamma p_0}{\rho_0} \left(\frac{\partial \rho}{\partial t} + \left(\mathbf{v} \cdot \nabla\right) \rho_0\right). \tag{1.113}$$

As before these equations may be combined to form a pair of wave equations:

$$\frac{\partial^2 v_x}{\partial t^2} = c_s^2 \left(\frac{\partial^2 v_x}{\partial x^2} + \frac{\partial^2 v_z}{\partial x \partial z}\right) - g \frac{\partial v_z}{\partial x}, \tag{1.114}$$

$$\frac{\partial^2 v_z}{\partial t^2} = c_s^2 \left(\frac{\partial^2 v_x}{\partial x \partial z} + \frac{\partial^2 v_z}{\partial z^2}\right) - \left(\gamma - 1\right) g \frac{\partial v_x}{\partial x} - \gamma g \frac{\partial v_z}{\partial z}. \tag{1.115}$$

Since the coefficients are constant in space we may repeat the method used for the uniform case and take Fourier components in Equations (1.114) and (1.115) to obtain

$$\left(\omega^2 - c_s^2 k_x^2\right) v_{x0} = \left(c_s^2 k_x k_z + i k_x g\right) v_{z0}, \tag{1.116}$$

$$\left(\omega^2 - c_s^2 k_z^2 - i k_z \gamma g\right) v_{z0} = \left(c_s^2 k_x k_z + i k_x \left(\gamma - 1\right) g\right) v_{x0}, \tag{1.117}$$

which may then be combined to find the dispersion relation

$$\omega^4 - \left(c_s^2 k^2 + i k_z \gamma g\right) \omega^2 + k_x^2 \left(\gamma - 1\right) g^2 = 0. \tag{1.118}$$

As before we have a quadratic in ω^2, but if we wish ω to be real we must allow k_z to be imaginary. Substituting $k_z = k_{zr} + ik_{zi}$ the dispersion relation becomes

$$\omega^4 - \left(c_s^2\left(k_x^2 + k_{zr}^2\right) - k_{zi}\left(c_s^2 k_{zi} + \gamma g\right) + i\left(2c_s^2 k_{zi} + \gamma g\right)k_{zr}\right)\omega^2 + k_x^2\left(\gamma - 1\right)g^2 = 0. \quad (1.119)$$

For this to be entirely real we must choose

$$k_{zi} = -\frac{\gamma g}{2c_s^2}, \quad (1.120)$$

and the dispersion relation takes the form

$$\omega^4 - \left(c_s^2 k^2 + \frac{\gamma^2 g^2}{4c_s^2}\right)\omega^2 + k_x^2\left(\gamma - 1\right)g^2 = 0, \quad (1.121)$$

where we have set $k^2 = k_x^2 + k_{zr}^2$. This is in agreement with the dispersion relation found in Roberts (1985) although a slightly different technique has been used. This may be solved to give

$$\omega^2 = \frac{1}{2}\left[\left(c_s^2 k^2 + \frac{\gamma^2 g^2}{4c_s^2}\right) \pm \sqrt{\left(c_s^2 k^2 + \frac{\gamma^2 g^2}{4c_s^2}\right)^2 - 4k_x^2\left(\gamma - 1\right)g^2}\right]. \quad (1.122)$$

The plus and minus signs give solutions for the fast and slow acoustic-gravity waves respectively. As $\mathbf{g} \to 0$ the plus root gives the sound wave, $\omega^2 = k^2 c_s^2$, and the negative root gives the buoyancy wave, $\omega^2 = N^2 k_x^2 / k^2$, where $N = \left(\gamma - 1\right)^{1/2} g/c_s$ is the Brunt-Väisälä frequency.

Note that by setting $v_A = 0$ in the uniform case and neglecting gravity in the acoustic-gravity case, Equations (1.82) and (1.83) and Equations (1.114) and (1.115) reduce down to the same pair of equations.

1.4 MHD Mode Conversion

MHD mode conversion in the solar atmosphere has been a problem of interest for many years; however, it is still not well understood. The process involves the conversion of one wave mode into another as it propagates through the mode-conversion region. This occurs where the sound and Alfvén speeds are of equal magnitude, or equivalently where the plasma β (the ratio of gas pressure to magnetic pressure) is approximately unity. Both of these descriptions are used to identify where mode conversion occurs. Away from this complex region (*i.e.* in the low-β plasma high in the atmosphere, and the high-β plasma low down in the atmosphere) the fast and slow waves are effectively decoupled. When this is the case one mode will behave like an acoustic wave and the other will display a strongly magnetic nature. A good understanding of the mode-conversion process will be highly useful in many areas of solar physics, for example, in the chromospheric network and inter-network, in sunspot atmospheres, and in the vicinity of magnetic null points. Although evidence of mode conversion has been observed by way of decreased wavelet durations above the magnetic canopy, indicating a loss of wave energy (Bloomfield et al., 2006) most work in the area has been done analytically or numerically.

1.4.1 Analytical Studies

A full and detailed study of mode conversion was presented by Stein (1971). In this model, gravity is neglected and mode conversion occurs due to propagation across a density step. The reflection, transmission and conversion coefficients were found for fast, slow and Alfvén waves using the dispersion relations and boundary conditions. The different ways in which these modes are coupled to each other was then described.

Zhugzhda and Dzhalilov wrote a series of papers through the late seventies to the eighties analytically investigating mode conversion of magneto-acoustic-gravity waves. In this case mode conversion is a result of the inclusion of gravitational stratification. These papers began by investigating wave propagation in an isothermal atmosphere with a uniform, vertical magnetic field (Zhugzhda, 1979) where a solution was found in terms of Hypergeometric ${}_2F_3$ functions, and the equivalent Meijer-G functions. An asymptotic solution was also given in the limit of a weak field (*i.e.* a high-β plasma). This study was extended in Zhugzhda and Dzhalilov (1981) where an asymptotic solution was found for the strong field (low β) limit. With these solutions reflection, transmission and conversion coefficients were found for all wave modes. It was also discovered that the extent of mode conversion is dependent on the inclination of the wavefront to the magnetic field, often referred to as the *attack angle*. The authors then moved on to consider the effect of tunnelling through the region in which the geometric-optics conditions are violated (Zhugzhda and Dzhalilov, 1982a,b) again with transmission and conversion coefficients calculated. This work was extended by Cally (2001) who noted that the Hypergeometric ${}_2F_3$ functions are much easier to work with than the equivalent Meijer-G functions. Using this form an additional set of conversion coefficients was found to those listed in Zhugzhda and Dzhalilov (1982a).

Having carried out a complete study with a vertical magnetic field Zhugzhda and Dzhalilov then relaxed their model to include an oblique magnetic field (Zhugzhda and Dzhalilov, 1983, 1984a,b). In this case propagation was assumed to be from high- to low-β plasma, representative of waves travelling upwards from a sunspot atmosphere. Similarly to their previous papers, the solutions in terms of the Meijer-G functions were used to find conversion coefficients. This theory was then used to model running penumbral waves (Zhugzhda and Dzhalilov, 1984c) finding that they are the result of the conversion of trapped 5-minute waves from the convection zone in a near horizontal magnetic field. The problem of a fully horizontal magnetic field (Zhugzhda and Dzhalilov, 1986) was the last to be investigated in this series of papers. More recently, Zhugzhda has looked at a model consisting of four isothermal layers taking into account linear and nonlinear effects. It was found that the spectrum of oscillations seen in the chromosphere and transition region of sunspot atmospheres is due to a combination of chromospheric resonance, the cutoff frequency at the temperature minimum, and nonlinear antireflection of the sunspot atmosphere (Zhugzhda, 2007).

Another way of studying mode-conversion problems is through wave mechanical and ray tracing theory. These methods have been utilised by Cally (2005, 2006) and Schunker and Cally (2006) to study the propagation and transmission of acoustic fast waves as they propagate up from the surface through active regions. It was argued that the method of wave tracing is preferable to the WKB method in the case of mode-conversion problems (Cally, 2005). Cally then went on to show that there is no reflection associated with the *equipartition depth*, where the sound and Alfvén speeds are equal, and that transmission is likely to be strong in regions of strong magnetic field but the amount of transmission will decrease with decreasing frequency. This was extended in Cally (2006) where the effect of a strong magnetic field in the conversion region was investigated for a two-dimensional adiabatic polytrope. The dispersion diagrams showed two types of avoided crossing, which identify where conversion occurs; one at the equipartition depth and another higher up occurring due to the acoustic cutoff frequency. It was noted that this splitting of the acoustic wave may cause defocusing of images, and should thus be taken into account in both time-distance helioseismology and acoustic holography. This theory was then applied to a more realistic model of the solar atmosphere (Schunker and Cally, 2006). A two-dimensional version of the Model S atmosphere, modified to include a magnetic field, was used to model an active region. The attack angle at the equipartition depth was found to influence the transmission of acoustic waves into the atmosphere, with a small range of fairly weak angles greatly enhancing conversion. It was suggested that this will affect the acoustic signals transmitted up to observable heights in the atmosphere.

1.4.2 Numerical Investigations

The work mentioned previously was purely analytical, however many numerical studies have also been carried out on this topic in various areas of solar physics. Cally and Bogdan (1997) investigated the interaction of f- and p-modes within a vertical slab of sunspot strength. The simulations were run in a two-dimensional geometry using a Lax-Wendroff style finite difference scheme. Strong evidence of mode conversion within sunspot atmospheres was found, with both f- and p-modes being converted into slow magnetoacoustic gravity waves and carried away from the convection zone. The p-modes were also seen to partially mix with f-modes of similar frequency as they exit the magnetic flux concentration. Numerical modelling of MHD mode conversion and refraction has also been carried out by Khomenko and Collados (2006). A thick flux tube in two-and-a-half dimensions with the magnetic field inclined to the vertical was used as a sunspot model. The modes seen were found to depend not only on the sound and Alfvén speeds being equal but also on the inclination of the magnetic field, *i.e.* the attack angle, similar to Zhugzhda and Dzhalilov (1981) and Schunker and Cally (2006). Above the region where the sound and Alfvén speeds are equal the fast waves were refracted back down towards the photosphere, whereas the slow waves were channelled upwards along the magnetic field into the chromosphere.

Moving up in the atmosphere conversion has also been studied in the chromospheric network and internetwork. Rosenthal et al. (2002) solved the two-dimensional, nonlinear, compressible MHD equations to study wave propagation in a gravitationally stratified atmosphere. Various magnetic structures were considered. Magnetic fields that are significantly inclined to the vertical were found to result in the total internal reflection of waves at a surface highly variable with altitude. In near vertical magnetic fields the waves were seen to continue upwards, guided by the field, but otherwise unaffected by it. This study was continued by Bogdan et al. (2003) in which the *magnetic canopy*, defined as the area where the sound and Alfvén speeds are of comparable magnitude, was found to be the region where mode conversion occurs. It was concluded that the wave behaviour is complex and sensitive not only to the orientation of the magnetic canopy but also to its location. Carlsson and Bogdan (2006) took this investigation up to three dimensions simulating acoustic waves, generated by convective motions, as they pass through the magnetic canopy.

Realistic configurations were used in which the wavelength of the waves is similar to the lengthscales of the magnetic field. This system was found to be highly dependent on the attack angle. For an angle under 30° the fast wave was transmitted as a slow wave along the magnetic field lines. At larger angles the majority of the fast wave was either refracted or totally internally reflected, causing complex interference patterns between the upward and downward propagating waves. The complexity seen, even for this simple configuration, suggests that more realistic models will be highly difficult to interpret.

MHD wave propagation in the vicinity of two-dimensional magnetic null points has been studied in detail by McLaughlin and Hood (2004, 2005) and by Fruit and Craig (2006) who looked at Alfvén wave dissipation in the same topology. In moving from zero- to finite-β plasma it was found that mode conversion is introduced into the problem (McLaughlin and Hood, 2006). The non-zero sound speed has no effect on the Alfvén speed, and so the coupling takes place between the fast and slow magnetoacoustic modes. In this case a fast wave was considered to be travelling through low-β plasma towards the null. As before conversion occurs as the wave passes through the layer where the sound and Alfvén speeds are equal. The converted part of the wave continues through the null point as a high-β fast wave, and the transmitted part is now a high-β slow wave which spreads out along the separatrices.

1.5 Outline of Thesis

This thesis aims to further the understanding of mode conversion in the solar corona. The focus is on the conversion between slow and fast magnetoacoustic waves in an MHD regime. In all of the research chapters a combination of analytical and numerical techniques are used to investigate mode conversion; these are outlined in Chapter 2. The analytical approximations described are the WKB method, Charpit's method, and a method developed specifically for mode conversion by Cairns and Lashmore-Davies (1983). Section 2.3 gives an introduction to finite difference schemes, stability, and initial and boundary conditions. Examples are then given for specific schemes including the MacCormack method which is used throughout the thesis.

We begin our investigation of mode conversion with a simple model in Chapter 3. A one-dimensional model is used with a vertical, background magnetic field in a gravitationally-stratified, isothermal atmosphere. A slow magnetoacoustic wave is driven downwards passing from low- to high-β plasma triggering mode conversion in the process. A range of analytical techniques is used to find the wave behaviour as the wave propagates across the mode-conversion region. This allows coefficients to be calculated which describe the proportion of the incident wave that is transmitted and converted. Coupled with the results of the WKB method this gives a complete description of the wave behaviour across the domain. The analytical results are supported by the numerical simulations.

In Chapter 4 the model described above is extended to allow for the inclusion of a non-isothermal temperature profile. The temperature profile chosen has a $\tanh$ profile. This is chosen to mimic the steep temperature gradient which is found at the transition region. As before a slow wave is driven on the upper boundary. Using the same analytical and numerical techniques as the previous chapter we investigate the effect of this temperature profile, if any, on the mode-conversion process.

A more complex topology is examined in Chapter 5 as the model is extended to two dimensions. A radially-expanding magnetic field is used to represent a coronal hole. Due to the geometry of the model spherical polar coordinates are used throughout this chapter. The investigation neglects gravitational effects. A slow wave is driven on the lower boundary propagating upwards from low- to high-β plasma. The same techniques are used as before to try and give a description of the wave behaviour as it propagates across the mode-conversion region.

In Chapter 6 we investigate mode conversion around a two-dimensional magnetic null point. As before we examine propagation from low- to high-β plasma by driving both a slow wave and a fast wave towards the null point. As has been done throughout the thesis a combination of analytical and numerical techniques are used to describe the mode conversion.

Finally we summarise our findings in Chapter 7, looking at how mode conversion is affected by various magnetic topologies and other such complexities. Possible extensions of the work are also considered.

Chapter 2

Analytical Approximations and Numerical Techniques

2.1 Introduction

The MHD equations are highly complex and it is not possible to solve them exactly, except in very special cases. This is true even after they have been simplified by neglecting more complex terms and non-linear effects. This is a common problem in applied mathematics. In order to progress approximations may be used, giving an approximate solution to the problem. These approximations may be either analytical, using known analytical functions, or numerical, using finite difference schemes to solve the differential equations for example. We use both analytical and numerical techniques.

2.2 Analytical Approximations

A number of analytical approximations are employed in this thesis. We go over some of these in detail here showing how they work in general terms. We begin by going over the WKB method and Charpit's equations. Then we look at a method developed by Cairns and Lashmore-Davies (1983) specifically for mode-conversion problems.

2.2.1 WKB Method

The WKB method is named after Wentzel, Kramers and Brillouin who popularised it in the field of quantum mechanics around 1926. The theory has actually been around for much longer and was developed by Liouville (1837), Green (1837), Rayleigh (1912) and Jeffreys (1924). The WKB method is useful for solving problems which cannot be solved by matched asymptotic expansions or similar methods because they are globally singular. A good description of this technique is given in White (2005) and Nayfeh (1981), for example.

Consider a second-order, linear, ordinary differential equation with a large parameter λ

$$\frac{\mathrm{d}^2 y}{\mathrm{d}x^2} + \lambda^2 G_0\left(x\right) y = 0, \tag{2.1}$$

for $\lambda \equiv 1/\sqrt{\epsilon} \to \infty$ as $\epsilon \to 0$. As $\lambda \to \infty$ the equation becomes

$$G_0\left(x\right)y = 0, \tag{2.2}$$

which yields the trivial solution. This is why the equation cannot be solved using a series expansion.

Letting

$$y = e^{\lambda Y(x;\lambda)}, \tag{2.3}$$

so

$$\frac{\mathrm{d}y}{\mathrm{d}x} = \lambda e^{\lambda Y}\frac{\mathrm{d}Y}{\mathrm{d}x}, \tag{2.4}$$

and

$$\frac{\mathrm{d}^2 y}{\mathrm{d}x^2} = \lambda^2 e^{\lambda Y}\left(\frac{\mathrm{d}Y}{\mathrm{d}x}\right)^2 + \lambda e^{\lambda Y}\frac{\mathrm{d}^2 Y}{\mathrm{d}x^2}. \tag{2.5}$$

Equation (2.1) thus becomes

$$\frac{1}{\lambda}\frac{\mathrm{d}^2 Y}{\mathrm{d}x^2} + \left(\frac{\mathrm{d}Y}{\mathrm{d}x}\right)^2 + G_0\left(x\right) = 0, \tag{2.6}$$

as $\lambda \to \infty$.

We may then expand the new variable Y in inverse powers of λ

$$Y = Y_0 + \frac{1}{\lambda}Y_1 + \ldots, \tag{2.7}$$

which is valid for $\lambda^{-1} \to 0$. Substituting this expansion into Equation (2.6) gives

$$\frac{1}{\lambda}\left\{\frac{\mathrm{d}^2 Y_0}{\mathrm{d}x^2} + \frac{1}{\lambda}\frac{\mathrm{d}^2 Y_1}{\mathrm{d}x^2} + \ldots\right\} + \left\{\left(\frac{\mathrm{d}Y_0}{\mathrm{d}x}\right)^2 + \frac{2}{\lambda}\frac{\mathrm{d}Y_0}{\mathrm{d}x}\frac{\mathrm{d}Y_1}{\mathrm{d}x} + \ldots\right\} + G_0\left(x\right) = 0. \tag{2.8}$$

To obtain a solution, we collect together powers of λ^{-1} to give a series of differential equations. The leading order terms give

$$\left(\frac{\mathrm{d}Y_0}{\mathrm{d}x}\right)^2 + G_0\left(x\right) = 0, \tag{2.9}$$

which can be solved to give

$$\frac{\mathrm{d}Y_0}{\mathrm{d}x} = \begin{cases} \pm i G_0^{1/2} & \text{if } G_0 > 0, \\ \pm\left(-G_0\right)^{1/2} & \text{if } G_0 < 0. \end{cases} \tag{2.10}$$

There are two possible solutions depending on whether G_0 is positive or negative. There are also two possible solutions given by the plus and minus signs as we would expect for a second-order, linear differential equation. Integrating we find

$$Y_0 = \begin{cases} \pm i \int G_0^{1/2} \mathrm{d}x & \text{if } G_0 > 0, \\ \pm \int (-G_0)^{1/2} \,\mathrm{d}x & \text{if } G_0 < 0. \end{cases} \tag{2.11}$$

We may neglect constants of integration here as they would simply modify the arbitrary constants later on. If convenient, it is also possible to include a constant in the limit of the integration without altering the final solution.

To find the solution for Y_1 we turn to the first order equation $\mathcal{O}\left(1/\lambda\right)$

$$\frac{\mathrm{d}^2 Y_0}{\mathrm{d}x^2} + 2\frac{\mathrm{d}Y_0}{\mathrm{d}x}\frac{\mathrm{d}Y_1}{\mathrm{d}x} = 0, \tag{2.12}$$

or

$$\frac{\mathrm{d}Y_1}{\mathrm{d}x} = -\frac{\mathrm{d}^2 Y_0/\mathrm{d}x^2}{2\mathrm{d}Y_0/\mathrm{d}x}. \tag{2.13}$$

Integrating

$$Y_1 = -\frac{1}{2}\ln\left\{\frac{\mathrm{d}Y_0}{\mathrm{d}x}\right\} = \ln\left\{\left(\frac{\mathrm{d}Y_0}{\mathrm{d}x}\right)^{-1/2}\right\}. \tag{2.14}$$

Finally we can substitute from Equation (2.10) to give

$$Y_1 = \begin{cases} \ln\left\{G_0^{-1/4}\right\} & \text{if } G_0 > 0, \\ \ln\left\{(-G_0)^{-1/4}\right\} & \text{if } G_0 < 0. \end{cases} \tag{2.15}$$

To find further terms in the expansion we need only look at higher order terms.

So the WKB approximation to Equation 2.1 is given by

$$y = e^{\lambda Y} = e^{\lambda Y_0 + Y_1 + \mathcal{O}(1/\lambda)} = e^{\lambda Y_0} e^{Y_1} e^{\mathcal{O}(1/\lambda)}. \tag{2.16}$$

For $G_0 > 0$

$$y = \frac{A}{G_0^{1/4}} \exp\left(i\lambda \int G_0^{1/2} \mathrm{d}x\right) + \frac{B}{G_0^{1/4}} \exp\left(-i\lambda \int G_0^{1/2} \mathrm{d}x\right) + \mathcal{O}\left(1/\lambda\right), \tag{2.17}$$

alternatively this may be written in terms of trigonometric functions

$$y = \frac{A}{G_0^{1/4}} \cos\left(\lambda \int G_0^{1/2} \mathrm{d}x\right) + \frac{B}{G_0^{1/4}} \sin\left(\lambda \int G_0^{1/2} \mathrm{d}x\right) + \mathcal{O}\left(1/\lambda\right). \tag{2.18}$$

For $G_0 < 0$

$$y = \frac{C}{\left(-G_0\right)^{1/4}} \exp\left(\lambda \int \left(-G_0\right)^{1/2} \mathrm{d}x\right) + \frac{D}{\left(-G_0\right)^{1/4}} \exp\left(-\lambda \int \left(-G_0\right)^{1/2} \mathrm{d}x\right) + \mathcal{O}\left(1/\lambda\right), \tag{2.19}$$

and we have growing and decaying exponentials rather than trigonometric functions.

It is worth noting that the WKB approximations are local solutions as they are not valid in the vicinity of a zero of G_0. These regions where the approximation breaks down are known as turning or transition points, and they mark a change between oscillatory and exponential behaviour. It is necessary to match the solutions across layers such as these in terms of Airy functions.

Note that Equation (2.1) does not have a first derivative term. If the equation in question is not already in this form the first derivative term can always be eliminated. Consider the equation

$$\frac{\mathrm{d}^2 y}{\mathrm{d}x^2} + a\left(x;a\right)\frac{\mathrm{d}y}{\mathrm{d}x} + b\left(x;a\right)y = 0. \tag{2.20}$$

This may be reduced to standard form by making a simple transformation

$$y\left(x\right) = u\left(x\right)z\left(x\right), \tag{2.21}$$

where u is chosen to eliminate the first derivative term in z. It can be shown that

$$\ln u = -\frac{1}{2}\int a\mathrm{d}x, \tag{2.22}$$

and the full equation reduces to the form

$$\frac{\mathrm{d}^2 z}{\mathrm{d}x^2} + \left\{\frac{1}{u}\frac{\mathrm{d}^2 u}{\mathrm{d}x^2} - \frac{a^2}{2} + b\right\}z = 0. \tag{2.23}$$

From this point the WKB approximation may be implemented.

2.2.2 Charpit's Method

When we are dealing with a first-order, partial differential equation which has two independent variables a solution can be found using Charpit's method, outlined in Piaggio (1942) and Chester (1971). This technique is partly due to Lagrange but it was Charpit who perfected it. The work was presented at the Paris Academy of Sciences in 1784, but Charpit died soon afterwards and his memoir was never published.

We start with the first-order, partial differential equation which in its most general form may be written

$$F\left(x,z,u,p,q\right) = 0, \tag{2.24}$$

where the dependent variable $u = u\left(x,z\right)$, and $p = \partial u/\partial x = u_x$ and $q = \partial u/\partial z = u_z$.

Assuming that the variables depend on an independent parameter s such that

$$\frac{\mathrm{d}x}{\mathrm{d}s} = F_p, \tag{2.25}$$

$$\frac{\mathrm{d}z}{\mathrm{d}s} = F_q, \tag{2.26}$$

we have the equation

$$p\frac{\mathrm{d}x}{\mathrm{d}s} + q\frac{\mathrm{d}z}{\mathrm{d}s} = \frac{\mathrm{d}u}{\mathrm{d}s}. \tag{2.27}$$

This yields the characteristic equations

$$\frac{\mathrm{d}x}{F_p} = \frac{\mathrm{d}z}{F_q} = \frac{\mathrm{d}u}{pF_p + qF_q} = \mathrm{d}s, \tag{2.28}$$

which can be written

$$\frac{\mathrm{d}x}{\mathrm{d}s} = F_p, \tag{2.29}$$

$$\frac{\mathrm{d}z}{\mathrm{d}s} = F_q, \tag{2.30}$$

$$\frac{\mathrm{d}u}{\mathrm{d}s} = pF_p + qF_q. \tag{2.31}$$

Equations (2.29) – (2.31) describe the characteristic curves of Equation (2.24). Along these characteristics F is constant; this will not necessarily be the same constant on different characteristic curves. Here we have only three equations but five unknowns. We need two more equations to complete the set, and it is natural to look for $\mathrm{d}p/\mathrm{d}s$ and $\mathrm{d}q/\mathrm{d}s$. Remembering that $p = p(x, z)$ and $q = q(x, z)$, we have

$$\frac{\mathrm{d}p}{\mathrm{d}s} = p_x\frac{\mathrm{d}x}{\mathrm{d}s} + p_z\frac{\mathrm{d}z}{\mathrm{d}s} = p_xF_p + p_zF_q, \tag{2.32}$$

and

$$\frac{\mathrm{d}q}{\mathrm{d}s} = q_x\frac{\mathrm{d}x}{\mathrm{d}s} + q_z\frac{\mathrm{d}z}{\mathrm{d}s} = q_xF_p + q_zF_q. \tag{2.33}$$

Differentiating Equation (2.24) with respect to x and z respectively we find

$$F_x + pF_u + p_xF_p + q_xF_q = 0, \tag{2.34}$$

$$F_z + qF_u + p_zF_p + q_zF_q = 0. \tag{2.35}$$

Noting that $p_z = q_x$ and $p_x = q_z$ we obtain the equations we are looking for

$$\frac{\mathrm{d}p}{\mathrm{d}s} = -F_x - pF_u, \tag{2.36}$$

$$\frac{\mathrm{d}q}{\mathrm{d}s} = -F_z - qF_u. \tag{2.37}$$

There are now five ordinary differential equations for five unknown functions, x, z, u, p and q, summarised below.

$$\frac{\mathrm{d}x}{\mathrm{d}s} = F_p, \tag{2.38}$$

$$\frac{\mathrm{d}z}{\mathrm{d}s} = F_q, \tag{2.39}$$

$$\frac{\mathrm{d}u}{\mathrm{d}s} = pF_p + qF_q, \tag{2.40}$$

$$\frac{\mathrm{d}p}{\mathrm{d}s} = -F_x - pF_u, \tag{2.41}$$

$$\frac{\mathrm{d}q}{\mathrm{d}s} = -F_z - qF_u. \tag{2.42}$$

Alternatively these may be written in ratio form

$$\frac{\mathrm{d}x}{F_p} = \frac{\mathrm{d}z}{F_q} = \frac{\mathrm{d}u}{pF_p + qF_q} = \frac{\mathrm{d}p}{-F_x - pF_u} = \frac{\mathrm{d}q}{-F_z - qF_u}. \tag{2.43}$$

Charpit's method allows a complete integral of Equation (2.24) to be found and this is usually sufficient to find a solution. Suppose that we can find an integral of the Characteristic Equations (2.43)

$$\Phi\left(x, z, u, p, q\right) = \alpha. \tag{2.44}$$

Furthermore, suppose that we can solve Equation (2.44) and the given Partial Differential Equation (2.24) for p and q in terms of x, z, u and α, say $p = P(x, z, u, \alpha)$ and $q = Q(x, z, u, \alpha)$. It can be shown that

$$\mathrm{d}u = P\mathrm{d}x + Q\mathrm{d}z, \tag{2.45}$$

is exact, and integration of this expression will yield a second constant β. The result is a solution $u(x, z, \alpha, \beta)$ which is a complete integral as it depends only upon two parameters.

2.2.3 Cairns and Lashmore-Davies Method

Mode conversion is a problem which arises in many different forms and in many different areas. For example, problems in ion and electron cyclotron regimes in plasma physics and wave transformation in magnetohydrodynamics. It is this last problem in which we are interested; specifically the conversion between fast and slow magnetoacoustic waves which is discussed in detail in this thesis. All of these problems are treated by varied methods which are often very mathematically complex.

The paper by Cairns and Lashmore-Davies (1983) discusses a method which can be applied to all of these different problems. It works by using the dispersion relation at the mode-conversion region to find differential equations describing the coupled mode amplitudes. These differential equations give the energy conservation in the absence of any damping. Solving the equations analytically gives a solution for the transmission and conversion coefficients. This solution is in terms of parameters which govern the behaviour of the local dispersion relation.

Here we describe the method applicable to general mode-conversion problems, as outlined in Cairns and Lashmore-Davies (1983). Imagine that the dispersion relation around the mode-conversion region is given by

$$(\omega - \omega_1)(\omega - \omega_2) = \eta, \tag{2.46}$$

where ω_1 and ω_2, both functions of the wavenumber k_x and x, are the frequencies of the two uncoupled modes. The parameter η is significant only in the neighbourhood of the mode-conversion region. If a wave of frequency ω_0 propagates through the plasma then coupling will take place at x_0, where for the appropriate $k_x = k_0$, $\omega_0 = \omega_1(k_0, x_0) = \omega_2(k_0, x_0)$ and there is a resonance. We expand about this point by writing

$$k_x = k_0 + \delta, \qquad x = x_0 + \xi, \tag{2.47}$$

and letting

$$\omega_1 = \omega_0 + a\delta + b\xi, \qquad \omega_2 = \omega_0 + f\delta + g\xi, \tag{2.48}$$

where a, b, f and g are the appropriate partial derivatives of ω_1 and ω_2. Considering Equation (2.46) around (k_0, x_0) gives

$$(\omega_0 - \omega_1)(\omega_0 - \omega_2) = \eta_0, \tag{2.49}$$

and substituting from Equations(2.47) and (2.48) this becomes

$$(ak_x - ak_0 + b\xi)(fk_x - fk_0 + g\xi) = \eta_0, \tag{2.50}$$

where η_0 is simply the value of η evaluated at (k_0, x_0).

The next step is to associate this dispersion relation, valid at the mode-conversion region, with a differential equation. To do this we set

$$k_x = -i\frac{\mathrm{d}}{\mathrm{d}\xi}, \tag{2.51}$$

and substituting this into Equation (2.50) gives

$$\left(\frac{\mathrm{d}}{\mathrm{d}\xi} - i\left(k_0 - \frac{b}{a}\xi\right)\right)\left(\frac{\mathrm{d}}{\mathrm{d}\xi} - i\left(k_0 - \frac{g}{f}\xi\right)\right) = -\frac{\eta_0}{af}. \tag{2.52}$$

As we are considering two coupled wave modes we introduce two wave amplitudes ϕ_1 and ϕ_2. These are then described by the first-order differential equations

$$\frac{\mathrm{d}\phi_1}{\mathrm{d}\xi} - i\left(k_0 - \frac{b}{a}\xi\right)\phi_1 = i\lambda\phi_2, \tag{2.53}$$

$$\frac{\mathrm{d}\phi_2}{\mathrm{d}\xi} - i\left(k_0 - \frac{g}{f}\xi\right)\phi_2 = i\lambda\phi_1, \tag{2.54}$$

where $\lambda = (\eta_0/af)^{1/2}$.

At this point we show that energy is conserved. Multiplying Equation (2.53) by its complex conjugate we obtain

$$\bar{\phi}_1\frac{\mathrm{d}\phi_1}{\mathrm{d}\xi} - i\left(k_0 - \frac{b}{a}\xi\right)\bar{\phi}_1\phi_1 = i\lambda\bar{\phi}_1\phi_2, \tag{2.55}$$

and taking the complex conjugate of this gives

$$\phi_1\frac{\mathrm{d}\bar{\phi}_1}{\mathrm{d}\xi} + i\left(k_0 - \frac{b}{a}\xi\right)\phi_1\bar{\phi}_1 = -i\lambda\phi_1\bar{\phi}_2. \tag{2.56}$$

Adding Equations (2.55) and (2.56) we find

$$\frac{\mathrm{d}}{\mathrm{d}\xi}\left(|\phi_1|^2\right) = i\lambda\left(\bar{\phi}_1\phi_2 - \phi_1\bar{\phi}_2\right). \tag{2.57}$$

Performing a similar analysis on Equation (2.54) gives Equations (2.58) and (2.59)

$$\bar{\phi}_2\frac{\mathrm{d}\phi_2}{\mathrm{d}\xi} - i\left(k_0 - \frac{g}{f}\xi\right)\bar{\phi}_2\phi_2 = -\lambda\bar{\phi}_2\phi_2, \tag{2.58}$$

$$\phi_2\frac{\mathrm{d}\bar{\phi}_2}{\mathrm{d}\xi} + i\left(k_0 - \frac{g}{f}\xi\right)\phi_2\bar{\phi}_2 = -i\lambda\phi_2\bar{\phi}_1, \tag{2.59}$$

which may be added to obtain

$$\frac{\mathrm{d}}{\mathrm{d}\xi}\left(|\phi_2|^2\right) = i\lambda\left(\phi_1\bar{\phi}_2 - \bar{\phi}_1\phi_2\right). \tag{2.60}$$

Adding together Equations (2.57) and (2.60) we find

$$\frac{\mathrm{d}}{\mathrm{d}\xi}\left(|\phi_1|^2 + |\phi_2|^2\right) = 0, \tag{2.61}$$

and so energy is conserved.

Returning to Equations (2.53) and (2.54), these may be combined to give a second-order differential equation in terms of ϕ_1

$$\frac{\mathrm{d}^2\phi_1}{\mathrm{d}\xi^2} - 2\left(ik_0 - \frac{i}{2}\frac{b}{a}\xi - \frac{i}{2}\frac{g}{f}\xi\right)\frac{\mathrm{d}\phi_1}{\mathrm{d}\xi} + \left(\frac{ib}{a} - k_0^2 + \frac{b}{a}k_0\xi + \frac{g}{f}k_0\xi - \frac{bg}{af}\xi^2 + \lambda^2\right)\phi_1 = 0. \tag{2.62}$$

To progress from this point the following transformation is made

$$\phi_1(\xi) = \exp\left(ik_0\xi - \frac{i}{4}\frac{b}{a}\xi^2 - \frac{i}{4}\frac{g}{f}\xi^2\right)\psi(\xi), \tag{2.63}$$

and upon substitution into Equation (2.62) we find

$$\frac{\mathrm{d}^2\psi}{\mathrm{d}\xi^2} + \left(\frac{\eta_0}{af} - \frac{i}{2}\left(\frac{ag-bf}{af}\right) + \frac{1}{4}\left(\frac{ag-bf}{af}\right)^2\xi^2\right)\psi = 0. \tag{2.64}$$

Finally we make the transformation

$$\zeta = \left(\frac{ag-bf}{af}\right)^{1/2}\xi\exp\left(\frac{3i\pi}{4}\right), \tag{2.65}$$

so that

$$\xi^2 = i\left(\frac{af}{ag-bf}\right)\zeta^2, \qquad \mathrm{d}\xi^2 = i\left(\frac{af}{ag-bf}\right)\mathrm{d}\zeta^2. \tag{2.66}$$

Assuming that $(ag-bf)/af > 0$, this results in the equation

$$\frac{\mathrm{d}^2\psi}{\mathrm{d}\zeta^2} + \left(\frac{i\eta_0}{ag-bf} + \frac{1}{2} - \frac{1}{4}\zeta^2\right)\psi = 0, \tag{2.67}$$

which is an exact result. The case $(ag-bf)/af < 0$ is not considered in this thesis. The solution to this equation is given by the parabolic cylinder function $D_n(\zeta)$. The asymptotic solution for ϕ_1 depends on ξ. For $\xi < 0$ it is

$$\phi_1(\xi) \sim \left(\frac{ag-bf}{af}\right)^{i\beta/2}\exp\left(\frac{\pi\beta}{4}\right)|\xi|^{i\beta}\exp\left(ik_0\xi - \frac{i}{2}\frac{b}{a}\xi^2\right), \tag{2.68}$$

and for $\xi > 0$ we have

$$\begin{aligned}\phi_1(\xi) \sim \left(\frac{ag-bf}{af}\right)^{i\beta/2}\exp\left(-\frac{3\pi\beta}{4}\right)\xi^{i\beta}\exp\left(ik_0\xi - \frac{i}{2}\frac{b}{a}\xi^2\right) - \\ -\frac{(2\pi)^{1/2}}{\Gamma(-i\beta)}\exp\left(-\frac{\pi\beta}{4}\right)\left(\frac{ag-bf}{af}\right)^{-i\beta/2-1/2}\xi^{-i\beta-1}\exp\left(ik_0\xi - \frac{i}{2}\frac{g}{f}\xi^2 - \frac{3i\pi}{4}\right),\end{aligned} \tag{2.69}$$

where $\beta = \eta_0/(ag-bf)$.

Equation (2.69) contains terms arising both from the coupled and uncoupled modes, and the equation for ϕ_2 is of a similar form. To interpret Equations (2.68) and (2.69) we consider what is happening away from the mode-conversion region. By setting the right-hand side of Equations (2.53) and (2.54) to zero we find a first approximation to ϕ_1 and ϕ_2

$$\phi_1 = A\exp\left(ik_0\xi - \frac{ib\xi^2}{2a}\right), \tag{2.70}$$

$$\phi_2 = B\exp\left(ik_0\xi - \frac{ig\xi^2}{2f}\right). \tag{2.71}$$

To obtain a correction to these approximations they can be substituted back into the original equations.

$$\frac{\mathrm{d}\phi_1}{\mathrm{d}\xi} - i\left(k_0 - \frac{b}{a}\xi\right)\phi_1 = i\lambda B\exp\left\{ik_0\xi - \frac{i}{2}\frac{g}{f}\xi^2\right\}, \tag{2.72}$$

has an integration factor

$$\exp\left\{-ik_0\xi + \frac{i}{2}\frac{b}{a}\xi^2\right\}, \tag{2.73}$$

and may be written

$$\frac{\mathrm{d}}{\mathrm{d}\xi}\left(\phi_1\exp\left\{-ik_0\xi + \frac{i}{2}\frac{b}{a}\xi^2\right\}\right) = i\lambda B\exp\left\{-\frac{i}{2}\left(\frac{ag-bf}{af}\right)\xi^2\right\}. \tag{2.74}$$

This may be solved to give

$$\phi_1 = -\frac{\lambda af}{(ag-bf)}\frac{B}{\xi}\exp\left\{ik_0\xi - \frac{i}{2}\frac{g}{f}\xi^2\right\} + \mathcal{O}\left(\frac{1}{\xi^2}\right). \tag{2.75}$$

Performing the same steps on Equation (2.54) gives

$$\phi_2 = \frac{\lambda af}{(ag-bf)}\frac{A}{\xi}\exp\left\{ik_0\xi - \frac{i}{2}\frac{b}{a}\xi^2\right\} + \mathcal{O}\left(\frac{1}{\xi^2}\right). \tag{2.76}$$

These approximations of ϕ_1 and ϕ_2 can again be substituted into Equations (2.53) and (2.54) to find a more accurate solution. The equation for ϕ_1 then becomes

$$\frac{\mathrm{d}\phi_1}{\mathrm{d}\xi} - i\left(k_0 - \frac{b}{a}\xi\right)\phi_1 = \frac{i\lambda^2 af}{(ag-bf)}\frac{A}{\xi}\exp\left\{ik_0\xi - \frac{i}{2}\frac{b}{a}\xi^2\right\}. \tag{2.77}$$

This has the integration factor

$$\exp\left\{-ik_0\xi + \frac{i}{2}\frac{b}{a}\xi^2\right\}, \tag{2.78}$$

which reduces the equation to

$$\frac{\mathrm{d}}{\mathrm{d}\xi}\left(\phi_1\exp\left\{-ik_0\xi + \frac{i}{2}\frac{b}{a}\xi^2\right\}\right) = \frac{i\lambda^2 af}{(ag-bf)}\frac{A}{\xi}. \tag{2.79}$$

Solving this equation,

$$\phi_1 \approx A\xi^{i\beta}\exp\left\{ik_0\xi - \frac{i}{2}\frac{b}{a}\xi^2\right\}, \tag{2.80}$$

and we have a correction to the amplitude A found in Equation (2.70). Doing the same for ϕ_2 we find

$$\phi_2 \approx B\xi^{-i\beta}\exp\left\{ik_0\xi - \frac{i}{2}\frac{g}{f}\xi^2\right\}. \tag{2.81}$$

Substituting this back into Equation (2.53) a final time gives us ϕ_1 to the accuracy we need.

$$\frac{\mathrm{d}\phi_1}{\mathrm{d}\xi} - i\left(k_0 - \frac{b}{a}\xi\right)\phi_1 = i\lambda B\xi^{-i\beta}\exp\left\{ik_0\xi - \frac{i}{2}\frac{g}{f}\xi^2\right\}, \tag{2.82}$$

may be written

$$\frac{\mathrm{d}}{\mathrm{d}\xi}\left(\phi_1\exp\left\{-ik_0\xi + \frac{i}{2}\frac{b}{a}\xi^2\right\}\right) = i\lambda B\xi^{-i\beta}\exp\left\{-\frac{i}{2}\left(\frac{ag-bf}{af}\right)\xi^2\right\}. \tag{2.83}$$

The solution to this is

$$\phi_1 = -\frac{\lambda af}{(ag-bf)}B\xi^{-i\beta-1}\exp\left\{ik_0\xi - \frac{i}{2}\frac{g}{f}\xi^2\right\}. \tag{2.84}$$

We now have two linearly independent solutions to the ordinary differential equation. These may be added together to give

$$\phi_1 = A\xi^{i\beta}\exp\left\{ik_0\xi - \frac{i}{2}\frac{b}{a}\xi^2\right\} - \frac{\lambda af}{(ag-bf)}B\xi^{-i\beta-1}\exp\left\{ik_0\xi - \frac{i}{2}\frac{g}{f}\xi^2\right\}, \tag{2.85}$$

which is correct to $\mathcal{O}\left(1/\xi^2\right)$. This solution corresponds to that found from the parabolic cylinder function solution, and comparison of these two equations yields amplitudes A and B of the transmitted and converted waves. Specifically we must first divide Equation (2.69) by the factor $\exp\left(\pi\beta/4\right)$ which comes from Equation (2.68) to give

$$\begin{aligned}\phi_1 \sim \left(\frac{ag-bf}{af}\right)^{i\beta/2}\exp\left(-\pi\beta\right)\xi^{i\beta}\exp\left(ik_0\xi - \frac{i}{2}\frac{b}{a}\xi^2\right) - \\ -\frac{(2\pi)^{1/2}}{\Gamma\left(-i\beta\right)}\exp\left(-\frac{\pi\beta}{2}\right)\left(\frac{ag-bf}{af}\right)^{-i\beta/2-1/2}\xi^{-i\beta-1}\exp\left(ik_0\xi - \frac{i}{2}\frac{g}{f}\xi^2 - \frac{3i\pi}{4}\right).\end{aligned} \tag{2.86}$$

This may then be compared directly to Equation (2.85) to give

$$A = \exp\left(-\pi\beta\right), \tag{2.87}$$

$$B = \frac{(2\pi)^{1/2}}{\beta^{1/2}}\exp\left(-\frac{\pi\beta}{2}\right)\frac{1}{\Gamma\left(-i\beta\right)}. \tag{2.88}$$

Noting that

$$\left|\Gamma\left(-i\beta\right)\right|^2 = \frac{\pi}{\beta\sinh\left(\pi\beta\right)}, \tag{2.89}$$

the formula for B reduces to

$$B = \sqrt{1-\exp\left(-2\pi\beta\right)}. \tag{2.90}$$

At this point we may also note that

$$A^2 + B^2 = 1, \tag{2.91}$$

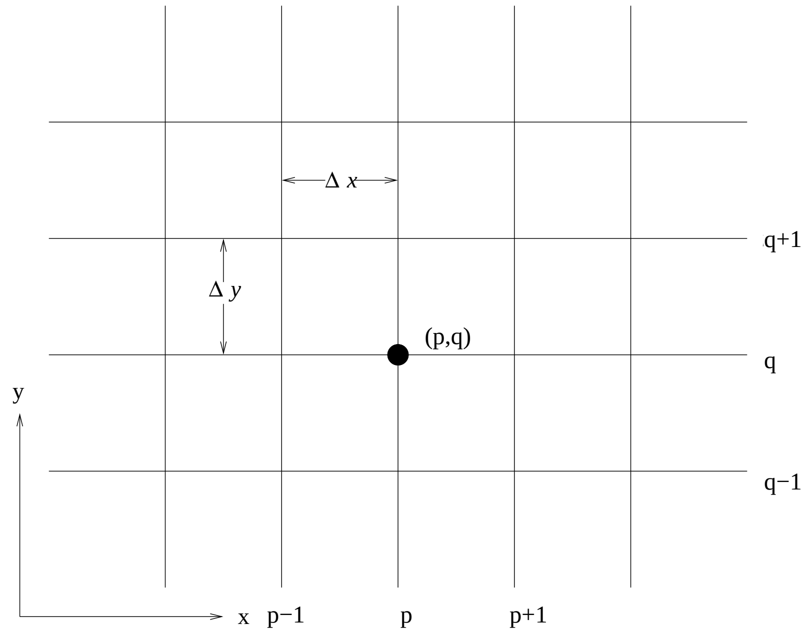

Figure 2.1: This figure shows how a domain may be broken down into a Cartesian grid for solution by a suitable finite difference scheme. The subscripts p and q refer the x and y indices respectively, and the values Δx and Δy are the distances between cell boundaries.

illustrating the conservation of energy.

Here we have shown step by step how the Cairns and Lashmore-Davies method for mode conversion is derived. The two coefficients obtained at the end tell us how much of the incident wave will be transmitted across the conversion region, and how much will be converted to another mode. This solution can be linked with a WKB analysis of the regions away from the conversion point, giving a complete picture of the problem.

2.3 Numerical Techniques

Not all problems can be solved easily using analytical approximations. In this case one can look for a numerical solution instead. It is most useful to use numerical simulations alongside analytical approximations or observations in order to verify the results. Numerical simulations also have the advantage that the parameters are easily varied, and so it is simple to test the sensitivity of the solution to the parameters in the model. Here we concentrate on the use of finite difference methods which work by replacing the derivatives by ratios of finite differences. Imagine a regularly spaced Cartesian grid, as shown in Figure 2.1, where subscripts p and q refer to the x, y indices and superscripts n refer to the time steps. We solve the finite-difference equation at each point on the grid, and if the grid spacing is small enough this will be a good approximation to a smooth function. The method used often depends on the type of partial differential equation so next we look at how these may be classified.

2.3.1 Classification of Partial Differential Equations

The classification of a partial differential equation depends only on the value of the highest derivatives. Given a second-order, partial differential equation

$$A\frac{\partial^2 u}{\partial x^2} + B\frac{\partial^2 u}{\partial x \partial y} + C\frac{\partial^2 u}{\partial y^2} = f, \tag{2.92}$$

where A, B, C and f may themselves be functions of x, y, u, u_x and u_y, a classification may be made by noting that with

$$\mathrm{d}\left(u_x\right) = u_{xx}\mathrm{d}x + u_{xy}\mathrm{d}y, \tag{2.93}$$

$$\mathrm{d}\left(u_y\right) = u_{xy}\mathrm{d}x + u_{yy}\mathrm{d}y, \tag{2.94}$$

we have the linear system

$$\left(\begin{array}{ccc} A & B & C \\ \mathrm{d}x & \mathrm{d}y & 0 \\ 0 & \mathrm{d}x & \mathrm{d}y \end{array} \right) \left(\begin{array}{c} u_{xx} \\ u_{xy} \\ u_{yy} \end{array} \right) = \left(\begin{array}{c} f \\ \mathrm{d}\left(u_x\right) \\ \mathrm{d}\left(u_y\right) \end{array} \right). \tag{2.95}$$

This matrix equation will have a unique solution, except in the case when its determinant is equal to zero

$$A\left(\mathrm{d}y\right)^2 - B\mathrm{d}x\mathrm{d}y + C\left(\mathrm{d}x\right)^2 = 0, \tag{2.96}$$

which defines the characteristics of the partial differential equation. It is the roots of the characteristic equation that will allow the equation to be classified.

$$\begin{array}{lcl} B^2 - 4AC > 0 & \text{Two Real Roots} & \text{Hyperbolic Equation}, \\ B^2 - 4AC = 0 & \text{Single Real Repeated Root} & \text{Parabolic Equation}, \\ B^2 - 4AC < 0 & \text{Complex Conjugate Roots} & \text{Elliptic Equation}. \end{array} \tag{2.97}$$

In addition to this it is also possible to classify systems of first-order partial differential equations. Following Hoffman and Chiang (1993) we consider the model equation

$$A\frac{\partial \phi}{\partial x} + B\frac{\partial \phi}{\partial y} = 0, \tag{2.98}$$

where ϕ is a vector containing the unknown variables, and A and B are matrices containing the coefficients. As before these may be functions of x and y with

$$\phi = \left(\begin{array}{c} u \\ v \end{array} \right), \qquad A = \left(\begin{array}{cc} a_1 & a_2 \\ b_1 & b_2 \end{array} \right), \qquad B = \left(\begin{array}{cc} a_3 & a_4 \\ b_3 & b_4 \end{array} \right). \tag{2.99}$$

If we consider $\mathbf{n}$ to represent the normal to the characteristic surfaces, for two-dimensional Cartesian problems

$$\mathbf{n} = n_x\mathbf{i} + n_y\mathbf{j}. \tag{2.100}$$

A solution may be obtained for the system if

$$|T| = 0, \tag{2.101}$$

where

$$T = An_x + Bn_y, \tag{2.102}$$

or

$$T = \begin{pmatrix} a_1n_x & a_2n_x \\ b_1n_x & b_2n_x \end{pmatrix} + \begin{pmatrix} a_3n_y & a_4n_y \\ b_3n_y & b_4n_y \end{pmatrix} = \begin{pmatrix} a_1n_x + a_3n_y & a_2n_x + a_4n_y \\ b_1n_x + b_3n_y & b_2n_x + b_4n_y \end{pmatrix}. \tag{2.103}$$

The determinant is then given by

$$|T| = (a_3b_4 - b_3a_4)\, n_y^2 + (a_1b_2 - a_2b_1)\, n_x^2 + (a_1b_4 + a_3b_2 - a_2b_3 - b_1a_4)\, n_xn_y = 0. \tag{2.104}$$

Dividing by n_x^2 we obtain

$$(a_3b_4 - b_3a_4)\left(\frac{n_y}{n_x}\right)^2 + (a_1b_4 + a_3b_2 - a_2b_3 - b_1a_4)\left(\frac{n_y}{n_x}\right) + (a_1b_2 - a_2b_1) = 0. \tag{2.105}$$

Writing this as

$$Q\left(\frac{n_y}{n_x}\right)^2 + R\left(\frac{n_y}{n_x}\right) + P = 0, \tag{2.106}$$

we can solve to get

$$\left(\frac{n_y}{n_x}\right) = \frac{-R \pm \sqrt{R^2 - 4PQ}}{2Q}. \tag{2.107}$$

This gives a similar set of conditions to those we had previously

$$\begin{array}{lcl} R^2 - 4PQ > 0 & \text{Two Real Roots} & \text{Hyperbolic Equation,} \\ R^2 - 4PQ = 0 & \text{Single Real Repeated Root} & \text{Parabolic Equation,} \\ R^2 - 4PQ < 0 & \text{Complex Conjugate Roots} & \text{Elliptic Equation.} \end{array} \tag{2.108}$$

This method will also work when the system of equations is greater than two (quadratic goes up to cubic etc.).

2.3.2 Derivation of Finite Difference Formulae via Taylor Expansion

There are a number of methods for finding finite difference equations, such as polynomial fitting and integral methods, but we concentrate here on the use of Taylor series expansion (Roache, 1998). Starting with a function u the first derivative can be derived by expanding

$$u_{p+1,q} = u_{p,q} + \left.\frac{\partial u}{\partial x}\right|_{p,q} (x_{p+1,q} - x_{p,q}) + \frac{1}{2}\left.\frac{\partial^2 u}{\partial x^2}\right|_{p,q} (x_{p+1,q} - x_{p,q})^2 + \ldots, \tag{2.109}$$

which may equivalently be written

$$u_{p+1,q} = u_{p,q} + \left.\frac{\partial u}{\partial x}\right|_{p,q} \Delta x + \frac{1}{2}\left.\frac{\partial^2 u}{\partial x^2}\right|_{p,q} \Delta x^2 + \ldots. \tag{2.110}$$

Denoting the finite-difference form of $\partial u/\partial x$ by $\delta u/\delta x$, the forward difference approximation is given by

$$\left.\frac{\delta u}{\delta x}\right|_{p,q} = \frac{u_{p+1,q} - u_{p,q}}{\Delta x}, \tag{2.111}$$

and has a truncation error of order Δx. This is therefore a first-order accurate term. In the same way it is possible to find a backward-difference approximation

$$\left.\frac{\delta u}{\delta x}\right|_{p,q} = \frac{u_{p,q} - u_{p-1,q}}{\Delta x}. \tag{2.112}$$

A centred-difference approximation may be found by subtracting Equation (2.112) from Equation (2.111) to obtain

$$u_{p+1,q} - u_{p-1,q} = 2\left.\frac{\partial u}{\partial x}\right|_{p,q} \Delta x + \frac{1}{3}\left.\frac{\partial^3 u}{\partial x^3}\right|_{p,q} \Delta x^3 + \ldots, \tag{2.113}$$

which can be solved to give

$$\left.\frac{\delta u}{\delta x}\right|_{p,q} = \frac{u_{p+1,q} - u_{p-1,q}}{2\Delta x}. \tag{2.114}$$

In contrast to the forward- and backward-difference approximations this is second order accurate. This means that the solution will improve in accuracy much faster as the grid size decreases. Note that adding Equations (2.111) and (2.112) gives a centred-difference approximation to $\delta^2 u/\delta x^2$

$$\left.\frac{\delta^2 u}{\delta x^2}\right|_{p,q} = \frac{u_{p+1,q} - 2u_{p,q} + u_{p-1,q}}{\Delta x^2}, \tag{2.115}$$

which is also second-order accurate. If required approximations with a higher accuracy may be derived in a similar manner.

Taking a partial differential equation, a finite difference equation is simply found by using combinations of these finite difference expressions for the partial derivatives. There are certain conditions which must be met to ensure that the finite difference scheme will converge to the desired solution. It must be consistent, meaning that the finite difference equation reduces to the partial differential equation as the grid size approaches zero. Secondly it must be stable, meaning that any error introduced in the finite difference equation does not grow with the solution of that finite difference equation. Finally it must be convergent, meaning that the solution of the finite difference equation approaches that of the partial differential equation as the grid size approaches zero. Conveniently it is only required to check the first two conditions, as the Lax equivalence theorem states that for a finite difference equation that approximates a well-posed, linear, initial value problem the necessary and sufficient condition for convergence is that the finite difference equation must be stable and consistent (Lax and Richtmyer, 1956). One method for checking stability is the von Neumann stability analysis.

2.3.3 The von Neumann Stability Analysis

This method was developed by John von Neumann at the Los Alamos National Laboratory in the 1940s. It was first published by Crank and Nicolson in 1947, and later by von Neumann himself (Charney et al., 1950); it is now the most commonly used method for stability analysis. The idea behind the method is to use a finite Fourier series expansion on the finite difference equation, and then consider the decay or amplification of each mode separately in order to determine whether or not the method is stable.

As an example consider Euler's FTCS method when applied to the first order wave equation

$$\frac{\partial u}{\partial t} = -a\frac{\partial u}{\partial x} \qquad\qquad a > 0, \tag{2.116}$$

which is a linear equation for constant a. Euler's FTCS method uses forward differencing for the time derivative and central differencing for the spatial derivative (hence the name) giving the finite difference equation

$$\frac{u_p^{n+1} - u_p^n}{\Delta t} = -a\frac{u_{p+1}^n - u_{p-1}^n}{2\Delta x}, \tag{2.117}$$

which is first-order accurate in time, and second-order accurate in space. To perform the stability analysis each Fourier component is written

$$u_p^n = V^n e^{ik_x(p\Delta x)}, \tag{2.118}$$

where V^n is the amplitude at time-step n of the component, whose wavenumber is k_x, and $i = \sqrt{-1}$. Boundary effects are not included as the spatial domain is considered to be infinite. Defining the phase angle as $\theta = k_x\Delta x$, the Fourier components are given by

$$u_p^n = V^n e^{ip\theta}. \tag{2.119}$$

Substituting this into Equation (2.116) gives

$$V^{n+1}e^{ip\theta} = V^n e^{ip\theta} - \frac{c}{2}V^n\left(e^{i(p+1)\theta} - e^{i(p-1)\theta}\right), \tag{2.120}$$

where $c = a\Delta t/\Delta x$ is the Courant number, named after Richard Courant (1888 – 1972) whose work in the analysis of numerical methods and nonlinear partial differential equations laid much of the groundwork for modern computational fluid dynamics. Dividing through by $e^{ip\theta}$ gives

$$V^{n+1} = V^n \left(1 - ic\sin\theta\right). \tag{2.121}$$

We may write this as

$$V^{n+1} = GV^n, \tag{2.122}$$

where G is the amplification factor. This will generally depend on θ, and so will vary for each individual Fourier component. If we wish the solution to remain bounded then we require

$$\begin{array}{lll} G \text{ Real} & |G| \le 1 & \forall\theta, \\ G \text{ Complex} & |G|^2 \le 1 & \forall\theta. \end{array} \tag{2.123}$$

In this case the stability requirement is given by

$$|1 - ic\sin\theta|^2 \le 1, \tag{2.124}$$

or

$$1 + c^2\sin^2\theta \le 1. \tag{2.125}$$

This condition is false for all c and so this method is unconditionally unstable.

For more general finite difference equations involving three or more time levels the amplification factor takes a matrix form. The stability condition is then applied to the eigenvalues, λ, and must be satisfied for the largest of these

$$\begin{array}{ll} \lambda \text{ Real} & |\lambda| \le 1, \\ \lambda \text{ Complex} & |\lambda|^2 \le 1. \end{array} \tag{2.126}$$

There are some standard values that are used for determining the stability criteria for one-dimensional problems which hold for the majority of explicit formulations

$$\begin{array}{rl} \text{Courant Number} & c \le 1, \\ \text{Diffusion Number} & d \le 0.5, \end{array} \tag{2.127}$$

where the diffusion number is defined as $d = a\Delta t/\Delta x^2$. The von Neumann stability analysis can also be easily applied to systems of linear, partial differential equations and multi-dimensional problems. If the latter of these have equal grid spacing in all directions then the standard values for stability are usually adjusted by dividing by the number of dimensions. This may be demonstrated by considering the linearised, constant coefficient, two-dimensional transport equation

$$\frac{\partial u}{\partial t} = -a\frac{\partial u}{\partial x} - b\frac{\partial u}{\partial y} + \alpha\triangle^2 u, \tag{2.128}$$

which may be discretised as

$$\begin{aligned}\frac{u_{p,q}^{n+1}-u_{p,q}^{n}}{\Delta t} &= -a\frac{u_{p+1,q}^{n}-u_{p-1,q}^{n}}{2\Delta x}-b\frac{u_{p,q+1}^{n}-u_{p,q-1}^{n}}{2\Delta y}+\\ &+ \alpha\left(\frac{u_{p+1,q}^{n}-2u_{p,q}^{n}+u_{p-1,q}^{n}}{\Delta x^{2}}+\frac{u_{p,q+1}^{n}-2u_{p,q}^{n}+u_{p,q-1}^{n}}{\Delta y^{2}}\right).\end{aligned} \tag{2.129}$$

In two-dimensions the Fourier components are given by

$$u_{p,q}^{n}=V^{n}e^{i(k_x p\Delta x+k_y q\Delta y)}, \tag{2.130}$$

and as before V^n is the amplitude function at time-step n of the component whose x and y wavenumbers are given by k_x and k_y respectively and $i=\sqrt{-1}$. Defining the x and y phase angles to be $\theta_x=k_x\Delta x$ and $\theta_y=k_y\Delta y$ we have

$$u_{p,q}^{n}=V^{n}e^{i(p\theta_x+q\theta_y)}. \tag{2.131}$$

Furthermore we define the dimensional counterparts of the Courant number as

$$c_x=\frac{a\Delta t}{\Delta x},\qquad c_y=\frac{b\Delta t}{\Delta y}, \tag{2.132}$$

and the counterparts of the diffusion number as

$$d_x=\frac{\alpha\Delta t}{\Delta x^2},\qquad d_y=\frac{\alpha\Delta t}{\Delta y^2}. \tag{2.133}$$

Substituting all of these values into Equation (2.129) we find that the amplification factor is given by

$$G=1-2\left(d_x+d_y\right)+2d_x\cos\theta_x+2d_y\cos\theta_y-i\left(c_x\sin\theta_x+c_y\sin\theta_y\right). \tag{2.134}$$

The necessary conditions for $|G|^2\leq 1$ are then

$$d_x+d_y\leq\frac{1}{2},\qquad c_x+c_y\leq 1, \tag{2.135}$$

and it is easy to see that for the special case where $d_x=d_y=d$ we require $d\leq 1/4$, and similarly for $c_x=c_y=c$ we need $c\leq 1/2$. So as stated above, the conditions are twice as restrictive as for the one-dimensional case.

2.3.4 Initial and Boundary Conditions

In addition to a convergent, finite difference equation a set of supplementary equations is needed to find a unique solution to the partial differential equation. These are needed to determine the arbitrary functions which result from integration of the partial differential equation. Such equations are known as boundary or initial conditions. As suggested by the name, an initial condition gives the value of the dependent variable at some initial time. A boundary condition specifies the value of the dependent variable or its derivative,

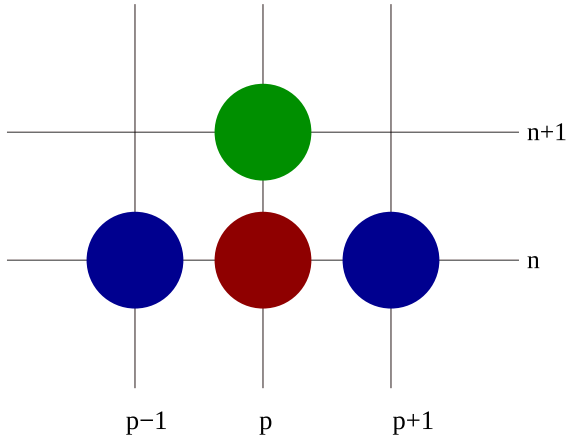

Figure 2.2: Numerical stencil for the Lax and Lax-Wendroff methods. The red dot indicates the point that we start from (which is not used in the Lax method) and the green that for which we are trying to find the value. The blue spots indicate the other nodes that are required in the calculation of this value.

but on the boundary of the domain of the partial differential equation.

There are a number of different types of boundary condition. If the dependent variable itself is specified along the boundary then it is described as a Dirichlet type condition. If it is the normal gradient of the dependent variable which is given it is a Neumann boundary condition. It is possible to have a linear combination of Dirichlet and Neumann type boundary conditions, which is known as a Robin boundary condition. In a more complex situation the boundary condition may take on different characteristics on different parts of the boundary calling for a mixed boundary condition. Having looked at the general theory behind finite difference methods let us now look at some specific techniques and their application to the one-dimensional wave equation, as outlined in Hoffman and Chiang (1993).

2.3.5 The Lax Method

The Lax method (Lax, 1954) is related to Euler's FTCS method (Equation (2.117)) which we used to demonstrate the von Neumann stability analysis. The difference is that this method uses an average value of u_p^n, giving

$$u_p^{n+1} = \frac{1}{2}\left(u_{p+1}^n + u_{p-1}^n\right) - \frac{c}{2}\left(u_{p+1}^n - u_{p-1}^n\right). \tag{2.136}$$

Figure 2.2 shows the numerical stencil for this method. This graphically illustrates the points that are necessary to progress with each step of the numerical solution. So this method requires information from the point in question and those on either side. Performing the von Neumann stability analysis on this equation gives

$$G = \cos\theta - ic\sin\theta, \tag{2.137}$$

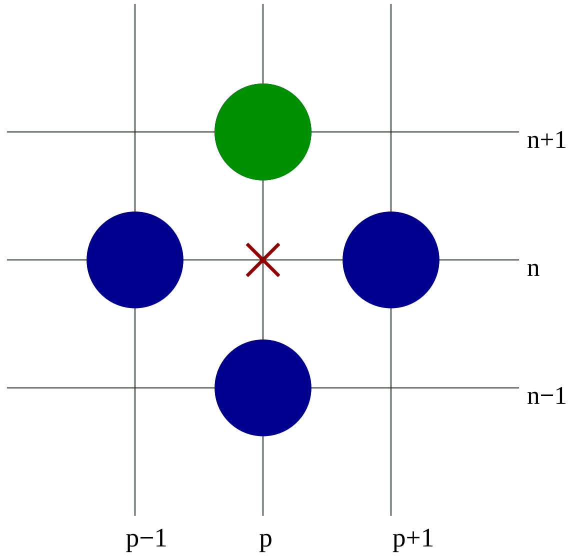

Figure 2.3: Numerical stencil for the Midpoint Leapfrog method. The red cross shows the starting point, there is no dot as it is not part of the calculation. The green dot is the point that we are trying to find a value for and the blues are all the points that are needed to get to the solution.

yielding the stability criterion

$$c \leq 1. \tag{2.138}$$

Therefore, unlike Euler's FTCS method which was unconditionally unstable, this method is of practical use. It is, however, still only first-order accurate.

2.3.6 The Midpoint Leapfrog Method

A more accurate method is given by the Midpoint Leapfrog method which uses central differencing of the second order for both the time and space derivatives. Applied to Equation (2.116) it gives

$$\frac{u_p^{n+1} - u_p^{n-1}}{2\Delta t} = -a\frac{u_{p+1}^n - u_{p-1}^n}{2\Delta x}. \tag{2.139}$$

This is shown pictorially in Figure 2.3 which demonstrates that the method skips over the point we are sitting at and uses those surrounding it to calculate the value at the next time step. Hence the name *leapfrog*. The values of the dependent variable are required at time steps n and $n-1$ in order to calculate the value at $n+1$. This means that two initial conditions are required to get the method started. A starter solution can be used for this, in which case another method is used for the initial time step. However, this will affect the accuracy of the method.

Performing a stability analysis we find

$$V^{n+1} = -2ic\sin\theta V^n + V^{n-1}, \tag{2.140}$$

and letting

$$V^n = V^n + (0)\, V^{n-1}, \tag{2.141}$$

gives the matrix equation

$$\begin{pmatrix} V^{n+1} \\ V^n \end{pmatrix} = \begin{pmatrix} -2ic\sin\theta & 1 \\ 1 & 0 \end{pmatrix} \begin{pmatrix} V^n \\ V^{n-1} \end{pmatrix}. \tag{2.142}$$

The amplification factor is then given by the matrix

$$G = \begin{pmatrix} -2ic\sin\theta & 1 \\ 1 & 0 \end{pmatrix}, \tag{2.143}$$

whose eigenvalues are given by

$$\lambda_{1,2} = -ic\sin\theta \pm \sqrt{1 - c^2\sin^2\theta}. \tag{2.144}$$

Note that these eigenvalues may also be found by multiplying Equation (2.140) through by V^{1-n} giving a quadratic equation in V.

Now, if $c^2\sin^2\theta \leq 1$ then

$$|\lambda_{1,2}|^2 = c^2\sin^2\theta + \left(1 - c^2\sin^2\theta\right) = 1, \tag{2.145}$$

and the stability requirement is satisfied. The most restrictive constraint occurs when $\sin^2\theta = 1$ giving $c \leq 1$. If $c^2\sin^2\theta > 1$ then

$$|\lambda_{1,2}|^2 = 2c^2\sin^2\theta \pm 2c\sin\theta\sqrt{c^2\sin^2\theta - 1} - 1. \tag{2.146}$$

Taking the positive root the condition $|\lambda_{1,2}|^2 \leq 1$ cannot be satisfied. Thus the stability condition is given by $c \leq 1$.

2.3.7 The Lax-Wendroff Method

The Lax-Wendroff method is also second-order accurate in time and space, but has the advantage that it does not need a starter solution (Lax and Wendroff, 1960). It may be derived from the Taylor series expansion of the dependent variable as follows

$$u_p^{n+1} = u_p^n + \frac{\partial u}{\partial t}\Delta t + \frac{\partial^2 u}{\partial t^2}\frac{(\Delta t)^2}{2} + \mathcal{O}\left(\Delta t\right)^3. \tag{2.147}$$

Taking the derivative of the first-order wave equation with respect to t we obtain

$$\frac{\partial^2 u}{\partial t^2} = a^2\frac{\partial^2 u}{\partial x^2}. \tag{2.148}$$

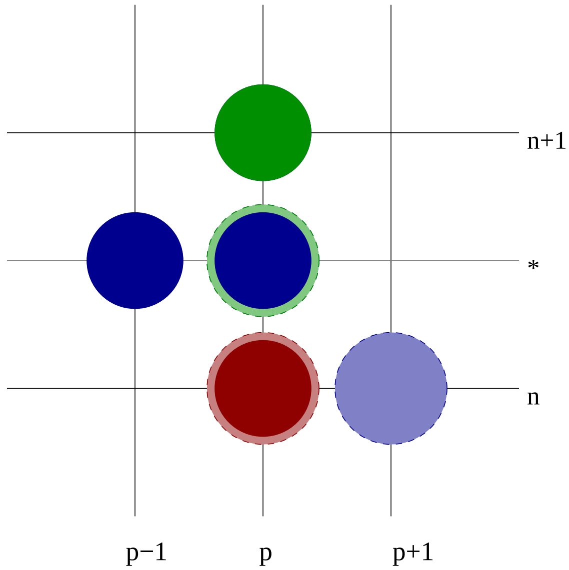

Figure 2.4: The numerical stencil for the MacCormack method. The shaded dots denote the stencil for the predictor method, and the solid dots are those for the corrector step. The red dots show the starting point, the green dots the finishing point, and the blue dots the points needed along the way.

Substituting this into the Taylor series expansion gives

$$u_p^{n+1} = u_p^n - a\Delta t\frac{\partial u}{\partial x} + \frac{a^2\left(\Delta t\right)^2}{2}\frac{\partial^2 u}{\partial x^2}. \tag{2.149}$$

Using central differencing of the second order for the spatial derivatives we obtain the finite difference equation

$$u_p^{n+1} = u_p^n - \frac{c}{2}\left(u_{p+1}^n - u_{p-1}^n\right) + \frac{c^2}{2}\left(u_{p+1}^n - 2u_p^n + u_{p-1}^n\right). \tag{2.150}$$

The stencil for this method is the same as that for the Lax method, shown in Figure 2.2, but this method has a higher order of accuracy.

The von Neumann stability analysis shows this method to have an amplification factor of

$$G = 1 - c^2\left(1 - \cos\theta\right) - ic\sin\theta, \tag{2.151}$$

and the method is stable for $c \leq 1$.

2.3.8 The MacCormack Method

The final method which we demonstrate here is the MacCormack method (MacCormack, 1969) which is the method we utilise throughout this thesis. This is a multi-step method which uses a predictor and corrector step. These have the advantage that unlike the methods discussed previously, they work well with nonlinear hyperbolic problems. The first step calculates a temporary value for the dependent variable, which is corrected in the second step to provide the final value for the dependent variable.

This method uses forward differencing for the initial step. For the first-order wave equation this gives

$$\frac{u_p^* - u_p^n}{\Delta t} = -a\frac{u_{p+1}^n - u_p^n}{\Delta x}, \tag{2.152}$$

where * represents a temporary prediction for the dependent variable at time step $n+1$. The corrector step uses backward differencing

$$\frac{u_p^{n+1} - u_p^{n+\frac{1}{2}}}{\frac{1}{2}\Delta t} = -a\frac{u_p^* - u_{p-1}^*}{\Delta x}. \tag{2.153}$$

The value of $u_p^{n+\frac{1}{2}}$ is then replaced by an average

$$u_p^{n+\frac{1}{2}} = \frac{1}{2}\left(u_p^n + u_p^*\right), \tag{2.154}$$

to give

$$\begin{array}{ll} \text{Predictor Step} & u_p^* = u_p^n - c\left(u_{p+1}^n - u_p^n\right), \\ \text{Corrector Step} & u_p^{n+1} = \frac{1}{2}\left[\left(u_p^n + u_p^*\right) - c\left(u_p^* - u_{p-1}^*\right)\right]. \end{array} \tag{2.155}$$

This is illustrated in Figure 2.4, in which the predictor step is shown by the shaded dots and the corrector step by the solid dots. It is also possible to reverse the order of differencing at each step, *i.e.* forward/backward, backward/forward. This method is second order accurate in both time and space and has the standard stability condition $c \leq 1$. Note that this method is related to the Lax-Wendroff method as it reduces to this form for linear equations.

2.4 Summary

In the first half of this chapter we have summarised some of the analytical techniques which are employed throughout this thesis, from the WKB method and Charpit's equations to a method for quantifying mode conversion - a problem central to this thesis. In the remaining chapters we shall demonstrate how using a combination of these techniques we can fully examine mode conversion in different atmospheric and topological situations.

The analytical approximations are combined with the use of numerical simulations. These are carried out using the MacCormack finite-difference scheme. This style of numerical technique is described in detail in the latter part of this chapter, looking at how these methods may be derived and how to test for the stability of a finite difference equation. Finally some specific methods were detailed, building up from Lax's method, through the Midpoint Leapfrog and Lax-Wendroff methods, to the MacCormack method. The numerical simulations run using this method can be used alongside the results of the analytical approximations to gain real insight into the mode-conversion problem.

Chapter 3

MHD Mode Conversion in a Stratified Isothermal Atmosphere

3.1 Introduction

In this chapter we examine mode conversion in an isothermal atmosphere. The model we have chosen and the basic equations are described in Section 3.2. In Section 3.3 we describe the numerical simulations which are supported by the analytical approximations detailed in Section 3.4. Finally we summarise our findings in Section 3.5. The results of this chapter have been published in McDougall and Hood (2007).

3.2 Isothermal Model

We begin the investigation into mode conversion by looking at a very simple one-dimensional model consisting of a uniform vertical magnetic field within a gravitationally stratified, isothermal atmosphere as shown in Figure 3.1. A slow wave is sent in from above which then propagates from low- to high-β plasma passing through the mode-conversion region as it does so. We choose such a simple model with the hope of gaining a deeper understanding of the complex physical processes involved in mode conversion. Previous more complicated models have included too many factors to truly and clearly determine exactly what is occurring. It is much easier to see how mode conversion occurs in this simple model.

3.2.1 Ideal MHD Equations

We shall be using the ideal form of the MHD equations throughout so the field lines are assumed frozen in to the plasma, with resistivity and viscosity neglected. These are given by (Equations (1.28) – (1.33) and (1.35)):

$$\frac{\partial \rho}{\partial t} + \nabla \cdot (\rho \mathbf{v}) = 0, \tag{3.1}$$

$$\rho \left(\frac{\partial}{\partial t} + \mathbf{v} \cdot \nabla \right) \mathbf{v} = -\nabla p + \mathbf{j} \times \mathbf{B} + \rho \mathbf{g}, \tag{3.2}$$

$$\frac{\partial \mathbf{B}}{\partial t} = \nabla \times (\mathbf{v} \times \mathbf{B}), \tag{3.3}$$

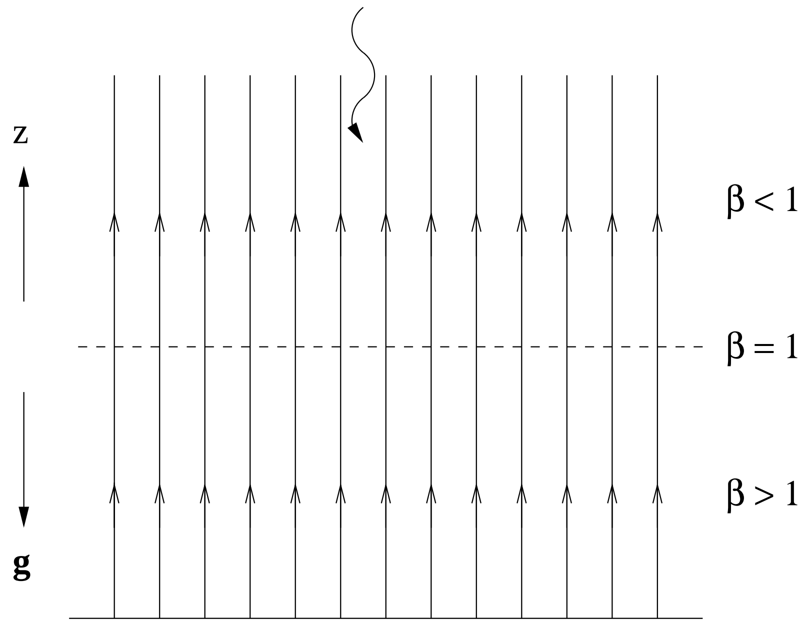

Figure 3.1: Cartoon of the model atmosphere with uniform vertical magnetic field. The z-axis points upwards (opposite to gravity) and a slow wave is driven on the upper boundary travelling down towards the mode-conversion layer at $\beta \approx 1$.

$$\left(\frac{\partial}{\partial t} + \mathbf{v}\cdot\nabla\right) p = \frac{\gamma p}{\rho}\left(\frac{\partial}{\partial t} + \mathbf{v}\cdot\nabla\right)\rho, \tag{3.4}$$

$$p = R\rho\frac{T}{\widetilde{\mu}}, \tag{3.5}$$

$$\mathbf{j} = \frac{1}{\mu}\left(\nabla \times \mathbf{B}\right), \tag{3.6}$$

$$\nabla\cdot\mathbf{B} = 0. \tag{3.7}$$

In these equations ρ is the mass density, $\mathbf{v}$ the fluid velocity, p the gas pressure, j the current density, $\mathbf{B}$ the magnetic induction, $\mathbf{g}$ the gravitational acceleration, and T the temperature.

3.2.2 Linearised MHD Equations

Under the equilibrium condition of a uniform, vertical magnetic field Equations (3.1) – (3.7) give

$$\nabla p_0 = \rho_0\mathbf{g}, \tag{3.8}$$

and

$$p_0 = R\rho_0\frac{T_0}{\widetilde{\mu}}. \tag{3.9}$$

By setting $\mathbf{B} = \mathbf{B}_0 + \mathbf{B}_1(x,z,t)$, $\mathbf{v} = \mathbf{v}_1(x,z,t)$, $p = p_0 + p_1(x,z,t)$, $\rho = \rho_0 + \rho_1(x,z,t)$ and $T = T_0 + T_1(x,z,t)$ and neglecting small quantities we obtain the Linearised MHD equations.

$$\frac{\partial \rho_1}{\partial t} + \nabla \cdot (\rho_0 \mathbf{v}_1) = 0, \tag{3.10}$$

$$\rho_0 \frac{\partial \mathbf{v}_1}{\partial t} = -\nabla p_1 + \frac{1}{\mu}(\nabla \times \mathbf{B}_1) \times \mathbf{B}_0 + \rho_1 \mathbf{g}, \tag{3.11}$$

$$\frac{\partial \mathbf{B}_1}{\partial t} = \nabla \times (\mathbf{v}_1 \times \mathbf{B}_0), \tag{3.12}$$

$$\frac{\partial p_1}{\partial t} + (\mathbf{v}_1 \cdot \nabla) p_0 = \frac{\gamma p_0}{\rho_0}\left(\frac{\partial \rho_1}{\partial t} + (\mathbf{v}_1 \cdot \nabla)\rho_0\right), \tag{3.13}$$

$$\frac{p_1}{p_0} = \frac{\rho_1}{\rho_0} + \frac{T_1}{T_0}, \tag{3.14}$$

$$\nabla \cdot \mathbf{B}_1 = 0. \tag{3.15}$$

Henceforth the subscripts on perturbed variables are dropped and it is assumed that we are working with the Linearised MHD equations. We may now apply equilibrium conditions specific to the problem.

3.2.3 Uniform Medium Stratified by Gravity

The equilibrium state consists of a gravitationally stratified, isothermal atmosphere permeated by a uniform vertical magnetic field (Figure 3.1). Examining the Momentum Equation (3.11) under these conditions, with the use of the equilibrium Gas Law (3.9), we obtain the same equilibrium condition as we found for the acoustic-gravity case (1.109), so we have

$$p_0(z) = p_0(0)\, e^{-z/H}, \quad \rho_0(z) = \rho_0(0)\, e^{-z/H}. \tag{3.16}$$

The plasma β is defined as the ratio of the gas pressure to the magnetic pressure,

$$\beta = \frac{2\mu p_0}{B_0^2} = \frac{2c_s^2}{\gamma v_A^2}. \tag{3.17}$$

The effect of including gravitational stratification in the model is that it causes the plasma β to be dependent on z. This ensures that the waves will propagate across the region where $c_s^2 = v_A^2$, the layer that we wish to investigate.

We may combine the full Linearised MHD Equations (3.10) – (3.13) into a pair of wave equations with a little manipulation

$$\frac{\partial^2 v_x}{\partial t^2} = \left(c_s^2 + v_A^2\right)\frac{\partial^2 v_x}{\partial x^2} + c_s^2 \frac{\partial^2 v_z}{\partial x \partial z} + v_A^2 \frac{\partial^2 v_x}{\partial z^2} - g\frac{\partial v_z}{\partial x}, \tag{3.18}$$

$$\frac{\partial^2 v_z}{\partial t^2} = c_s^2\left(\frac{\partial^2 v_x}{\partial x \partial z} + \frac{\partial^2 v_z}{\partial z^2}\right) - (\gamma - 1)\, g\frac{\partial v_x}{\partial x} - \gamma g\frac{\partial v_z}{\partial z}. \tag{3.19}$$

These wave equations are in agreement with Ferraro and Plumpton (1958) and are valid for general temperature $T(z)$, in which case both the sound and Alfvén speeds will vary with height. Note that we are working with an isothermal atmosphere so in this case only the Alfvén speed varies with height. There are a number of additional checks that we may perform to ensure that no errors have been made in the calculation of these equations. First of all it is easy to see that the equations have the correct dimensions. Next we should check that the equations correctly reduce down to the uniform and acoustic gravity cases under the correct conditions. Setting $\mathbf{g} = 0$ the equations do indeed reduce down to Equations (1.82) and (1.83) of the uniform case. Finally by setting $v_A = 0$, Equations (3.18) and (3.19) become Equations (1.114) and (1.115) of the acoustic gravity case.

3.2.3.1 x-Dependence

Equations (3.18) and (3.19) depend on both x and z and are thus two dimensional. To reduce this down to one dimension, as we have in the model (Figure 3.1), we must make some assumption about the form of x-dependence for the variables. We choose an oscillatory dependence given by trigonometric functions of $k_x x$, where k_x is the horizontal wavenumber.

$$\begin{aligned}
\mathbf{v} &= (v_x(z,t)\sin k_x x,\ 0,\ v_z(z,t)\cos k_x x)\,,\\
\mathbf{B} &= (B_x(z,t)\sin k_x x,\ 0,\ B_z(z,t)\cos k_x x)\,,\\
\rho &= \rho(z,t)\cos k_x x,\\
p &= p(z,t)\cos k_x x.
\end{aligned} \tag{3.20}$$

Under this assumption the Linearised MHD equations take the form

$$\rho_0\frac{\partial v_x}{\partial t} - \frac{B_0}{\mu}\frac{\partial B_x}{\partial z} = k_x p + \frac{B_0 k_x}{\mu}B_z, \tag{3.21}$$

$$\rho_0\frac{\partial v_z}{\partial t} + \frac{\partial p}{\partial z} = -\rho g, \tag{3.22}$$

$$\frac{\partial B_x}{\partial t} - B_0\frac{\partial v_x}{\partial z} = 0, \tag{3.23}$$

$$\frac{\partial B_z}{\partial t} = -k_x B_0 v_x, \tag{3.24}$$

$$\frac{\partial \rho}{\partial t} + \rho_0\frac{\partial v_z}{\partial z} = \frac{\rho_0}{H}v_z - k_x\rho_0 v_x, \tag{3.25}$$

$$\frac{\partial p}{\partial t} + \gamma p_0\frac{\partial v_z}{\partial z} = \rho_0 g v_z - \gamma p_0 k_x v_x. \tag{3.26}$$

The wave equations (3.18) and (3.19) then become

$$\frac{\partial^2 v_x}{\partial t^2} = v_A^2\frac{\partial^2 v_x}{\partial z^2} - k_x c_s^2\frac{\partial v_z}{\partial z} - k_x^2\left(c_s^2 + v_A^2\right)v_x + k_x g v_z, \tag{3.27}$$

$$\frac{\partial^2 v_z}{\partial t^2} = c_s^2\frac{\partial^2 v_z}{\partial z^2} + k_x c_s^2\frac{\partial v_x}{\partial z} - \gamma g\frac{\partial v_z}{\partial z} - k_x(\gamma-1)g v_x, \tag{3.28}$$

which are dependent only on z and t.

3.2.3.2 Non-Dimensionalisation

In order to simplify the numerical side of the modelling we non-dimensionalise the variables by setting $\mathbf{v} = v_0\bar{\mathbf{v}}$, $\mathbf{B} = B_0\bar{\mathbf{B}}$, $p = p_{00}\bar{p}$, $\rho = \rho_{00}\bar{\rho}$, $p_0 = p_{00}\bar{p}_0$, $\rho_0 = \rho_{00}\bar{\rho}_0$, $z = L\bar{z}$, $t = \tau\bar{t}$, and $k_x = \bar{k}_x/L$, where a bar denotes a dimensionless quantity and v_0, B_0, p_{00}, ρ_{00}, L and τ are constants with the dimensions of the variable they are scaling.

Under this system we may choose $p_{00} = p_0\left(0\right)$ and $\rho_{00} = \rho_0\left(0\right)$ so

$$\bar{p}_0 = \bar{\rho}_0 = e^{-L\bar{z}/H}. \tag{3.29}$$

The sound and Alfvén speeds may also be non-dimensionalised, *i.e.* $c_s^2 = c_{s0}^2\bar{c}_s^2$ and $v_A^2 = v_0^2\bar{v}_A^2$ where $\bar{c}_s^2 = 1$ and $\bar{v}_A^2 = 1/\bar{\rho}_0$, and the plasma β may be written $\beta = \beta_0\bar{\beta}$ where $\bar{\beta} = \bar{p}_0$ and

$$\beta_0 = \frac{2c_{s0}^2}{\gamma v_0^2}. \tag{3.30}$$

We are then free to set $c_{s0}^2 = v_0^2 = 1$ so we have $c_s^2 = v_A^2$ at $z = 0$, and from Equation (3.30) $\beta_0 = 2/\gamma = 1.2$. If $v_0 = L/\tau$ then the speed is measured in units of v_0, which represents a constant background Alfvén speed. Under these scalings $\bar{t} = 1$ (for example) refers to $t = \tau = L/v_0$; *i.e.* the time taken for a wave to travel a distance L at the reference background Alfvén speed. Note that we can write $g = c_s^2/\left(\gamma H\right)$. The bar on quantities is now dropped and it is understood that we are working with dimensionless values.

The dimensionless Linearised MHD equations are

$$\frac{1}{v_A^2}\frac{\partial v_x}{\partial t} - \frac{\partial B_x}{\partial z} = \frac{k_x c_s^2}{\gamma}p + k_x B_z, \tag{3.31}$$

$$\frac{1}{v_A^2}\frac{\partial v_z}{\partial t} + \frac{c_s^2}{\gamma}\frac{\partial p}{\partial z} = -\frac{Lc_s^2}{\gamma H}\rho, \tag{3.32}$$

$$\frac{\partial B_x}{\partial t} - \frac{\partial v_x}{\partial z} = 0, \tag{3.33}$$

$$\frac{\partial B_z}{\partial t} = -k_x v_x, \tag{3.34}$$

$$v_A^2\frac{\partial \rho}{\partial t} + \frac{\partial v_z}{\partial z} = \frac{L}{H}v_z - k_x v_x, \tag{3.35}$$

$$v_A^2\frac{\partial p}{\partial t} + \gamma\frac{\partial v_z}{\partial z} = \frac{L}{H}v_z - \gamma k_x v_x. \tag{3.36}$$

These give rise to the wave equations

$$\left(v_A^2\frac{\partial^2}{\partial z^2} - \left(c_s^2 + v_A^2\right)k_x^2 - \frac{\partial^2}{\partial t^2}\right)v_x = k_x c_s^2\left(\frac{\partial}{\partial z} - \frac{L}{\gamma H}\right)v_z, \tag{3.37}$$

$$\left(c_s^2\frac{\partial^2}{\partial z^2}-\frac{Lc_s^2}{H}\frac{\partial}{\partial z}-\frac{\partial^2}{\partial t^2}\right)v_z=-k_xc_s^2\left(\frac{\partial}{\partial z}-\frac{L}{\gamma H}\left(\gamma-1\right)\right)v_x. \tag{3.38}$$

When written in this form the equations are much easier to analyse using the WKB method (Section 3.4.3).

3.3 Numerical Simulations

We solve Equations (3.31) – (3.36) numerically using the MacCormack method. This is a finite difference scheme which uses two steps to solve the equations at each time step. The first of these is a predictor step giving the solution at half a time step, the second step corrects the solution at the full time step; this gives the method its name of a predictor-corrector method. This scheme is second-order accurate in both time and space and, for linear harmonic waves, not strongly affected by numerical dispersion or diffusion. We have selected to use backward differencing for the predictor steps and forward differencing for the corrector steps (although this may be reversed). By doing it this way we are using the more accurate corrected values on the upper boundary where we are driving a wave into the system. The lower boundary is less important as we terminate the simulation before the wavefront reaches this point to eliminate reflection effects. The conditions specified on the boundaries are:

$$B_x=-\frac{1}{k_x}\frac{\partial B_z}{\partial z},\quad \frac{\partial B_z}{\partial t}=-k_xv_x,\quad \frac{\partial p}{\partial z}=0,\quad \frac{\partial \rho}{\partial z}=0. \tag{3.39}$$

In addition to these we have the conditions on the velocity which differ on the upper and lower boundaries

$$\text{Upper Boundary:}\quad v_x=0,\quad v_z=\sin\omega t. \tag{3.40}$$

$$\text{Lower Boundary:}\quad \frac{\partial v_x}{\partial z}=0,\quad v_z=0. \tag{3.41}$$

Imposing v_z on the upper boundary means that we are predominantly driving a slow wave. Since the slow wave also has a small component of v_x the condition $v_x = 0$ means that there is a small component of the fast mode generated; however this mode is evanescent and does not propagate into the computational domain. The simulations are run for $-8 \le z \le 6$ and $0 \le t \le 13.5$ where $\delta z = 0.003$ and $\delta t = 0.0002$; as mentioned above the end time is chosen just before the wavefront reaches the lower boundary. In all simulations we choose L equal to the coronal scale height (H) so that $z = 1$ corresponds to one coronal scale height ≈ 60 Mm. Having set this value, we are left with two free parameters: the driving frequency (ω) and the wavenumber in the x-direction (k_x). By altering these parameters we can make comparisons between the results and different analytical models. In this chapter we use $\omega = 2\pi$, $2\pi\sqrt{6}$, and $4\pi\sqrt{6}$ which correspond in real terms to frequencies of 0.1 s^{-1}, 0.26 s^{-1} and 0.51 s^{-1} and periods of 60 s, 24.5 s and 12.3 s respectively. In the corona the acoustic cutoff frequency is given by $\Omega_{ac} = 0.001$ s^{-1} with a corresponding period $P_{ac} = 91.7$ minutes (Roberts, 2004). This acoustic cutoff frequency is much smaller than those driven on the upper boundary and so does not affect the simulations.

	High β	Low β
Slow Wave	Speed $\approx v_A$ Transverse Wave	Speed $\approx c_s$ Longitudinal Wave
Fast Wave	Speed $\approx c_s$ Longitudinal Wave	Speed $\approx v_A$ Transverse Wave

Table 3.1: Speed and preferential direction of propagation for magnetoacoustic waves in high- and low-β plasma.

3.3.1 Wave Properties

We wish to investigate the wave behaviour across the $\beta \approx 1$ layer but it is also important to know the properties of waves away from this region. Table 3.1 shows the typical speed and direction of propagation for slow and fast magnetoacoustic waves in high- and low-β plasma. From this table it is clear that the high-β slow wave shares its properties with the low-β fast wave, and similarly the low-β slow wave and high-β fast wave have common properties. So an uncoupled slow magnetoacoustic wave ($k_x = 0$ limit) propagating through low-β plasma will change its behaviour to that of a fast magnetoacoustic wave as it passes into high-β plasma. Similarly an uncoupled fast wave will change its behaviour to that of a slow wave as it travels from low- to high-β plasma. Despite this change in terminology the wave mode is the same - no mode conversion has occurred. Thus, when we discuss mode conversion the slow wave driven on the upper boundary retains the properties of a slow wave as it propagates down into high-β plasma. We do not see any evidence of upward-propagating fast waves from the mode-conversion region. The transmitted component of the incident slow wave will continue into the high-β plasma as a fast wave.

In the numerical simulation it is clear that something is happening to the wave as it crosses the region where $c_s = v_A$ (Figure 3.2) especially in the horizontal velocity, and the horizontal and vertical magnetic field. This change displays itself as a change in the phase and the behaviour of the amplitude. It is not easy to pick out what is happening, however, as all of the plots display a strong exponential nature which is disguising other underlying effects. We can uncover these by making a simple transformation: $v_x \rightarrow \tilde{v}_x e^{-z/2}$, $v_z \rightarrow \tilde{v}_z e^{z/2}$, $B_x \rightarrow \tilde{B}_x e^{-z/2}$, $B_z \rightarrow \tilde{B}_z e^{-z/2}$, $p \rightarrow \tilde{p} e^{-z/2}$, and $\rho \rightarrow \tilde{\rho} e^{-z/2}$. The data resulting from this transformation is shown in Figure 3.3. In the low-β plasma to the right of the dashed red line only one wave mode is present - this is the slow mode which we are driving. To the left of the red dashed line both the fast and slow modes are present. The converted slow mode is clearly visible in the plots of the horizontal velocity and the horizontal and vertical magnetic field, where we can see that the wavefront has slowed right down. The transmitted fast mode is apparent in the plots of the vertical velocity, pressure and density, where we can see it has almost reached the edge of the computational domain. The slow mode is also present in these plots and can be seen as interference with the fast mode just to the left of the red dashed line.

It is possible to predict the position of these different modes at any given time. The position of the acoustic mode (slow in low β, fast in high β) may be found from

$$\frac{\mathrm{d}z}{\mathrm{d}t} = -c_s, \tag{3.42}$$

$$z = 6 - c_s t, \tag{3.43}$$

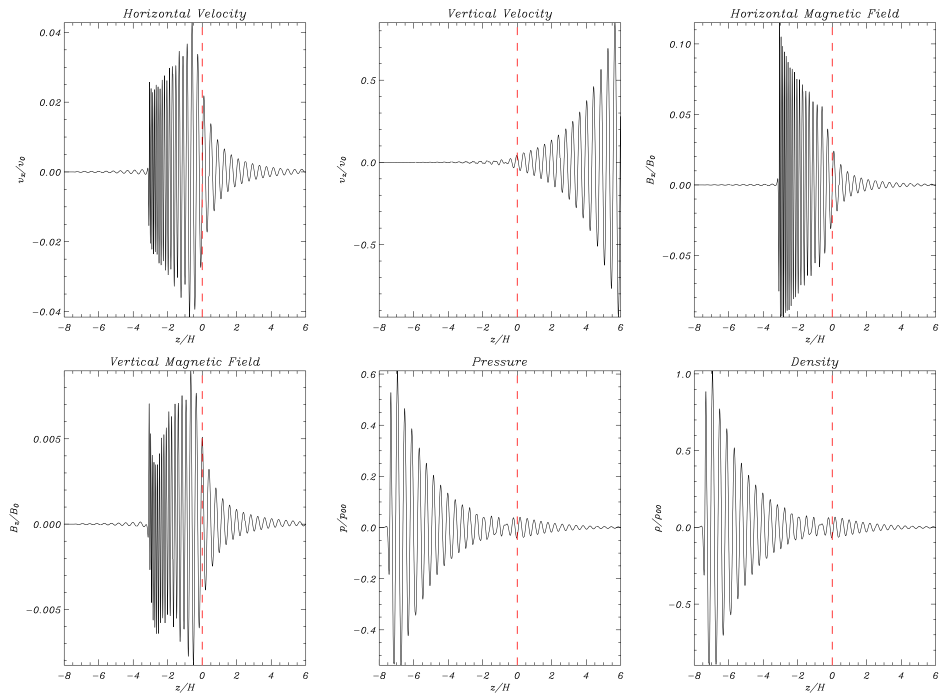

Figure 3.2: Results of the numerical simulation with $\omega = 2\pi\sqrt{6}$ and $k_x = \pi$ at $t = 13.5$ Alfvén times. The plots show the horizontal and vertical velocity, the horizontal and vertical magnetic field, pressure and density respectively from top left to bottom right. The red dashed line indicates where $c_s = v_A$.

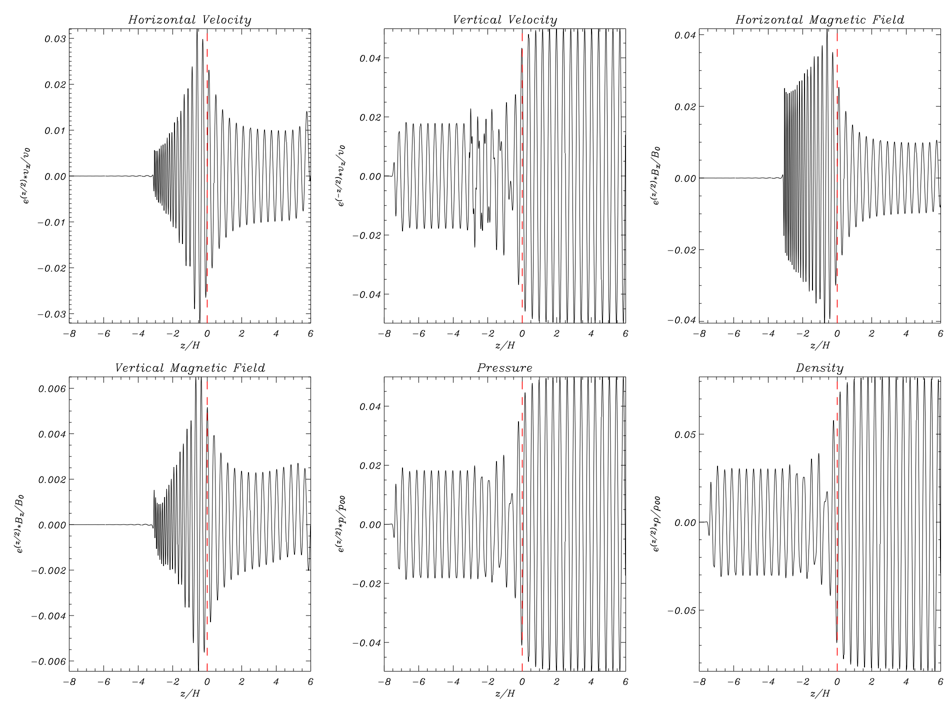

Figure 3.3: Results of the numerical simulation with $\omega = 2\pi\sqrt{6}$ and $k_x = \pi$ at $t = 13.5$ Alfvén times. The plots show a transformation of the horizontal and vertical velocity, the horizontal and vertical magnetic field, pressure and density respectively from top left to bottom right. The red dashed line indicates where $c_s = v_A$.

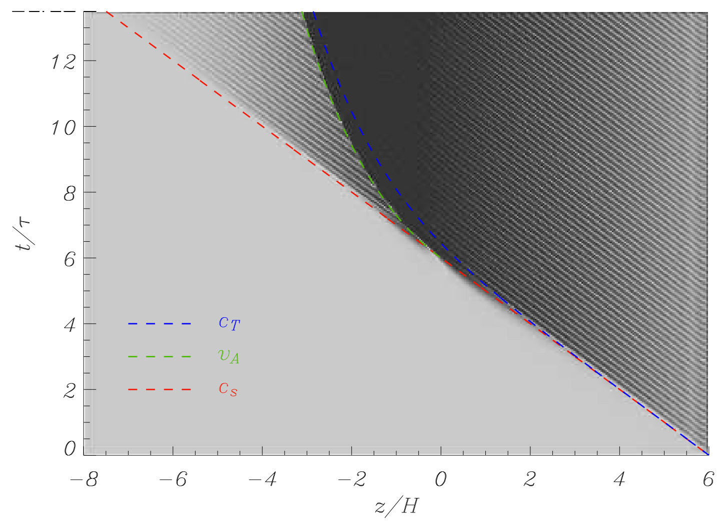

Figure 3.4: Surface plot of the horizontal velocity for $\omega = 2\pi\sqrt{6}$ and $k_x = \pi$. The red dashed line shows the position of the acoustic mode, the green dashed line the position of the magnetic mode, and the blue dashed line the position of the slow mode.

which tells us that at $t = 13.5$ Alfvén times the fast wave should have reached $z \approx -7.5$. Similarly the position of the magnetic mode (the slow wave in high β) may be found from

$$\frac{\mathrm{d}z}{\mathrm{d}t} = -v_A, \tag{3.44}$$

$$z = -2\ln\left(\frac{t}{2} + 1 - \frac{3}{c_s}\right), \tag{3.45}$$

so the slow mode will have reached $z \approx -3.1$ at $t = 13.5$ Alfvén times. This is in agreement with the simulations shown in Figure 3.3. We may also use the equation

$$\frac{\mathrm{d}z}{\mathrm{d}t} = -c_T, \tag{3.46}$$

where $c_T = c_s v_A / \sqrt{c_s^2 + v_A^2}$ is the tube speed. This is easier to solve in terms of t

$$t = 2\left(\frac{1}{c_T} - \frac{1}{c_T\,(6)}\right) + \frac{1}{c_s}\ln\left|\frac{(c_s - c_T)\,(c_s + c_T\,(6))}{(c_s + c_T)\,(c_s - c_T\,(6))}\right|. \tag{3.47}$$

This equation models the behaviour of the slow mode throughout the computational domain, following the incident slow wave in the low-β plasma and the converted slow wave in the high-β plasma. Figure 3.4 shows the horizontal velocity viewed from above, overplotted on this are the paths predicted by Equations (3.43), (3.45) and (3.47). The path of the acoustic mode is modelled well by Equation (3.43) and the path of the magnetic mode (given by Equation (3.45)) also agrees after $z = 0$, which is unsurprising as the magnetic mode is not present before the conversion point. Equation (3.47) does not seem to agree as well with the simulations as the others; but as the magnitude of k_x is increased in comparison to ω, it turns out that this prediction improves and that given by Equation (3.45) actually worsens.

3.3.2 Effect of Varying the Model Parameters

We have already noted that there are two free parameters in the model setup - the horizontal wavenumber and the driving frequency. We now investigate the effect of varying these parameters on mode conversion.

3.3.2.1 Varying the Wavenumber

Firstly we consider the effect of varying the wavenumber on the simulations. To do this we fix the value of ω so that the effects seen are purely due to the variations in k_x. The driving frequency we have chosen, $\omega = 2\pi\sqrt{6}$, corresponds to driving a wave with a period of approximately 0.4 Alfvén times, or 24.5 s. Figure 3.5 shows the transformed vertical velocity ($\tilde{v}_z$) for a range of values for k_x. We know from the wave equations (3.37) and (3.38) that when $k_x = 0$ the fast and slow magnetoacoustic modes are completely decoupled. It is therefore no surprise that we do not see a change in the amplitude of the slow wave as it travels across the domain for $k_x = 0$. Even for very small values of k_x, such as $k_x = 0.25$ and $k_x = \pi/10$, the mode conversion is so insignificant that it is not at all visible in the plots. It is only for $k_x = 1$ that we begin to see a change in amplitude as the wavefront crosses $c_s = v_A$ (denoted by the red dashed line). This change in amplitude becomes more significant as the value of k_x increases, with more and more of the incident wave being converted into a slow wave. The plots of $k_x = 5$ and $k_x = 7$ show the slow wave quite clearly, as the amplitude of the transmitted fast wave has significantly decreased. This allows us to observe that the wavelength of the converted slow wave is decreasing as the wave progresses.

3.3.2.2 Varying the Driving Frequency

We have already seen that the amount of conversion increases with increasing k_x. Next we look at what happens if we fix the wavenumber at $k_x = \pi$ and vary the driving frequency ω. We have three different values of the frequency, $\omega = 2\pi$, $2\pi\sqrt{6}$ and $4\pi\sqrt{6}$, corresponding to periods of 60 s, 24.5 s and 12.3 s respectively. Figure 3.6 shows the transformed vertical velocity ($\tilde{v}_x$) at these frequencies. It is easy to see from these plots that as ω increases, the transmission increases and so the conversion is decreasing; this is in agreement with Cally (2005). Thus the amount of mode conversion increases with increasing k_x but decreases with increasing ω.

3.4 Analytical Approximations

Using the numerical solution we have described qualitatively what is occurring. For the remainder of this investigation we try to quantify what is happening by calculating the amplitudes of the transmitted and converted waves and finding the change in phase as the incident slow mode undergoes conversion. We plan to do this using analytical techniques and approximations.

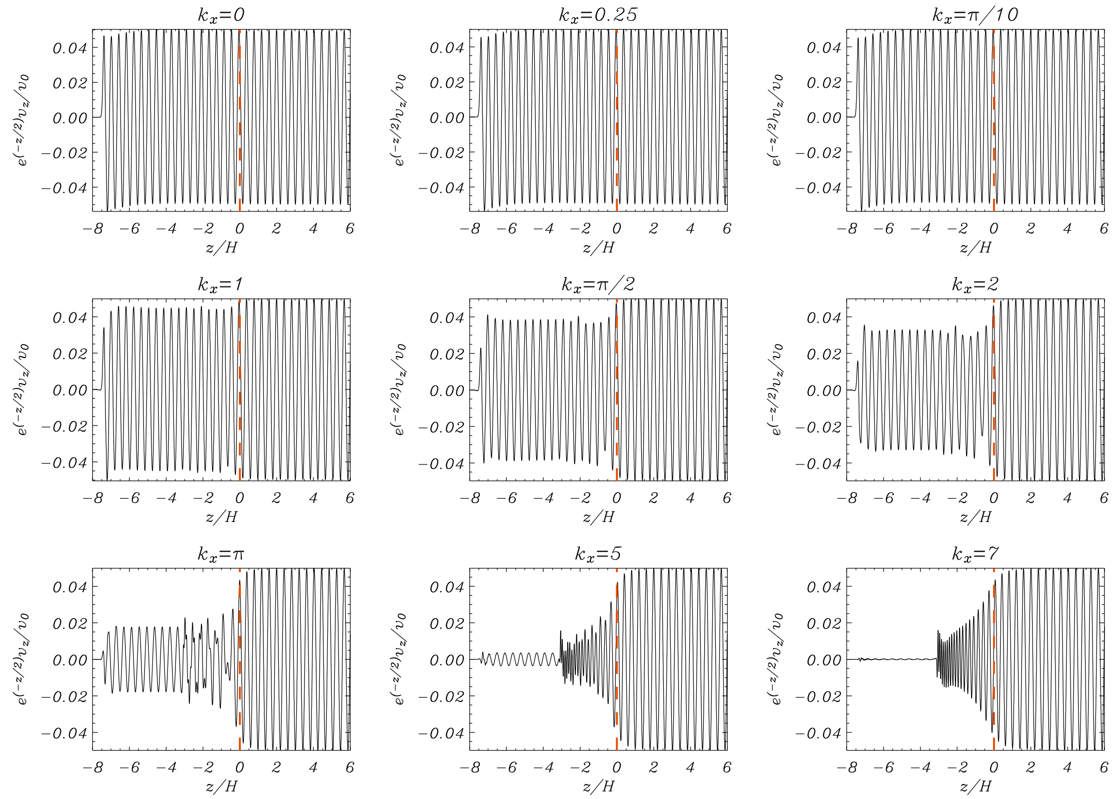

Figure 3.5: Transformed vertical velocity for $\omega = 2\pi\sqrt{6}$ at $t = 13.5$ Alfvén times. The plots show the results for $k_x = 0$, 0.25, $\pi/10$, 1, $\pi/2$, 2, π, 5 and 7 respectively from top left to bottom right. The dashed red line indicates where $c_s = v_A$.

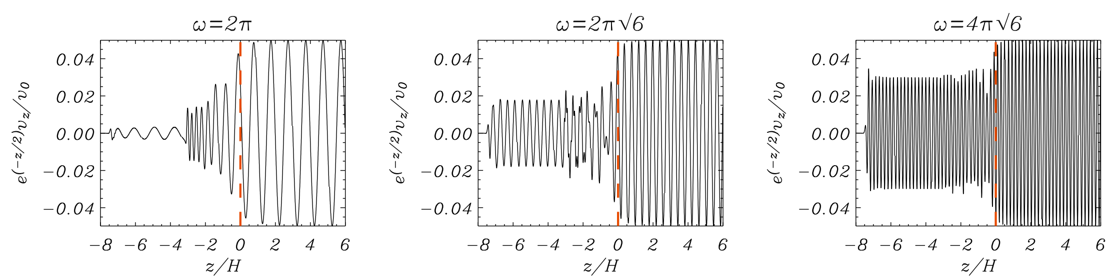

Figure 3.6: Transformed vertical velocity for $k_x = \pi$ at $t = 13.5$ Alfvén times. The plots show the results for $\omega = 2\pi$, $2\pi\sqrt{6}$ and $4\pi\sqrt{6}$ respectively from left to right. The dashed red line indicates where $c_s = v_A$.

3.4.1 Small k_x Limit

Much of the literature concerning mode conversion may be found in the field of plasma physics, particularly relating to ion cyclotron heating in tokamaks. In this area Cairns and Lashmore-Davies (1983, 1986) and Cairns and Fuchs (1989) developed a method of solving mode-conversion problems. Firstly they derived differential equations describing the coupled mode amplitudes from the local dispersion relation. These equations could then be solved analytically to find the transmission and conversion coefficients. In relation to the simulations this method can be applied when k_x is small, and ω sufficiently large in comparison to k_x ($\omega \gg k_x c_s$).

Starting with the wave equations (3.37) and (3.38) we may assume that the time variation behaves as $e^{i\omega t}$ so that $\partial/\partial t = i\omega$

$$\left(v_A^2 \frac{\mathrm{d}^2}{\mathrm{d}z^2} - \left(c_s^2 + v_A^2\right) k_x^2 + \omega^2\right) v_x = k_x c_s^2 \left(\frac{\mathrm{d}}{\mathrm{d}z} - \frac{1}{\gamma}\right) v_z, \tag{3.48}$$

$$\left(c_s^2 \frac{\mathrm{d}^2}{\mathrm{d}z^2} - c_s^2 \frac{\mathrm{d}}{\mathrm{d}z} + \omega^2\right) v_z = -k_x c_s^2 \left(\frac{\mathrm{d}}{\mathrm{d}z} - \frac{1}{\gamma}\left(\gamma - 1\right)\right) v_x. \tag{3.49}$$

Making the substitution $v_z = ie^{z/2} V_z / c_s$ removes the first derivative on the left-hand side of Equation (3.49). We may then neglect terms involving k_x in comparison to those involving ω; also, as k_x is small we may neglect v_x and v_z in comparison to their first derivatives with respect to z, and so on. Thus Equations (3.48) and (3.49) reduce down to

$$\left(v_A^2 \frac{\mathrm{d}^2}{\mathrm{d}z^2} + \omega^2\right) v_x = i k_x c_s v_A \frac{\mathrm{d}V_z}{\mathrm{d}z}, \tag{3.50}$$

$$\left(c_s^2 \frac{\mathrm{d}^2}{\mathrm{d}z^2} + \omega^2\right) V_z = \frac{i k_x c_s^3}{v_A} \frac{\mathrm{d}v_x}{\mathrm{d}z}. \tag{3.51}$$

These equations may be written as

$$\left(\frac{\mathrm{d}}{\mathrm{d}z} + \frac{i\omega}{v_A}\right)\left(\frac{\mathrm{d}}{\mathrm{d}z} - \frac{i\omega}{v_A}\right) v_x = \frac{i k_x c_s}{v_A} \frac{\mathrm{d}V_z}{\mathrm{d}z}, \tag{3.52}$$

$$\left(\frac{\mathrm{d}}{\mathrm{d}z} + \frac{i\omega}{c_s}\right)\left(\frac{\mathrm{d}}{\mathrm{d}z} - \frac{i\omega}{c_s}\right) V_z = \frac{i k_x c_s}{v_A} \frac{\mathrm{d}v_x}{\mathrm{d}z}, \tag{3.53}$$

so that the coefficients multiplying the derivative on the right-hand side of each equation are now identical and the pair of brackets on the left-hand side represent two waves, one travelling upwards and the other downwards for each equation. The equation for v_x is driven by the V_z that is driven on the upper boundary. This inhomogeneous term has a wavenumber in z given by ω/c_s and at z_c, where $v_A\left(z_c\right) = c_s$, there is a resonance between the downward travelling waves and the amplitude of v_x increases rapidly while the amplitude of V_z is reduced. This is mode conversion.

Expanding $z = z_c + \xi$ around the mode-conversion region (*i.e.* for the downward propagating waves described by the brackets containing minus signs) we have $\mathrm{d}/\mathrm{d}z = \mathrm{d}/\mathrm{d}\xi$ and

$$v_A = e^{z_c/2} e^{\xi/2} = c_s e^{\xi/2}. \tag{3.54}$$

Using the Taylor expansion of the exponential term this becomes

$$v_A = c_s \left(1 + \frac{\xi}{2} + \dots \right), \tag{3.55}$$

where we may take as many terms as we require. For the remaining terms we may replace $\mathrm{d}/\mathrm{d}z$ by $i\omega/c_s$. The equations may thus be written

$$\frac{\mathrm{d}v_x}{\mathrm{d}\xi} - i\left(\frac{\omega}{c_s} - \frac{\omega}{2c_s}\xi\right) v_x = \frac{ik_x}{2} V_z, \tag{3.56}$$

$$\frac{\mathrm{d}V_z}{\mathrm{d}\xi} - \frac{i\omega}{c_s} V_z = \frac{ik_x}{2} v_x. \tag{3.57}$$

Using Equations (3.56) and (3.57) we may show that energy is conserved in this system. If we begin with Equation (3.56) and multiply through by its complex conjugate $\bar{v_x}$ we obtain

$$\bar{v_x}\frac{\mathrm{d}v_x}{\mathrm{d}\xi} - i\left(\frac{\omega}{c_s} - \frac{\omega}{2c_s}\xi\right) \bar{v_x} v_x = \frac{ik_x}{2} \bar{v_x} V_z, \tag{3.58}$$

and taking the complex conjugate

$$v_x\frac{\mathrm{d}\bar{v_x}}{\mathrm{d}\xi} + i\left(\frac{\omega}{c_s} - \frac{\omega}{2c_s}\xi\right) v_x \bar{v_x} = -\frac{ik_x}{2} v_x \bar{V_z}. \tag{3.59}$$

Adding Equations (3.58) and (3.59) we find

$$\frac{\mathrm{d}}{\mathrm{d}\xi}\left(|v_x|^2\right) = \frac{ik_x}{2}\left(\bar{v_x} V_z - v_x \bar{V_z}\right). \tag{3.60}$$

Performing a similar analysis on Equation (3.57) we may add Equations (3.61) and (3.62)

$$\bar{V_z}\frac{\mathrm{d}V_z}{\mathrm{d}\xi} - \frac{i\omega}{c_s}\bar{V_z} V_z = \frac{ik_x}{2}\bar{V_z} v_x, \tag{3.61}$$

$$V_z\frac{\mathrm{d}\bar{V_z}}{\mathrm{d}\xi} + \frac{i\omega}{c_s} V_z \bar{V_z} = -\frac{ik_x}{2} V_z \bar{v_x}, \tag{3.62}$$

to obtain

$$\frac{\mathrm{d}}{\mathrm{d}\xi}\left(|V_z|^2\right) = -\frac{ik_x}{2}\left(\bar{v_x} V_z - v_x \bar{V_z}\right). \tag{3.63}$$

If we then add Equations (3.60) and (3.63) we find

$$\frac{\mathrm{d}}{\mathrm{d}\xi}\left(|v_x|^2 + |V_z|^2\right) = 0, \tag{3.64}$$

and so energy is conserved.

Returning to Equation (3.56) we may eliminate v_x using Equation (3.57) to find a second order differential equation for V_z

$$\frac{\mathrm{d}^2 V_z}{\mathrm{d}\xi^2} + \frac{i\omega}{c_s}\left(\frac{\xi}{2} - 2\right)\frac{\mathrm{d}V_z}{\mathrm{d}\xi} + \left(\frac{\omega^2}{c_s^2}\left(\frac{\xi}{2} - 1\right) + \frac{k_x^2}{4}\right)V_z = 0. \tag{3.65}$$

By making the substitution

$$V_z\left(\xi\right) = \exp\left(\frac{i\omega}{c_s}\xi - \frac{i\omega}{8c_s}\xi^2\right)\psi\left(\xi\right), \tag{3.66}$$

the first derivative term in Equation (3.65) drops out to leave

$$\frac{\mathrm{d}^2\psi}{\mathrm{d}\xi^2} + \left(\frac{\omega^2}{16c_s^2}\xi^2 - \frac{i\omega}{4c_s} + \frac{k_x^2}{4}\right)\psi = 0. \tag{3.67}$$

Finally we make the substitution

$$\zeta = \left(\frac{\omega}{2c_s}\right)^{1/2} e^{3i\pi/4}\xi, \tag{3.68}$$

to obtain

$$\frac{\mathrm{d}^2\psi}{\mathrm{d}\zeta^2} - \left(\frac{\zeta^2}{4} - \frac{1}{2} - \frac{ik_x^2 c_s}{2\omega}\right)\psi = 0. \tag{3.69}$$

The advantage of writing Equation (3.65) in this form is that the solution is known in terms of the Parabolic Cylinder function $U\left(a,\zeta\right)$ where

$$a = -\frac{1}{2} - \frac{ik_x^2 c_s}{2\omega}. \tag{3.70}$$

The asymptotic behaviour of these functions is described in detail in Abramowitz and Stegun (1964). Taking the asymptotic solutions used in Cairns and Lashmore-Davies (1983), in low-β plasma ($\xi > 0$)

$$V_z\left(\xi\right) \sim \left(\frac{\omega}{2c_s}\right)^{ik_x^2 c_s/(4\omega)} \exp\left(\frac{\pi k_x^2 c_s}{8\omega}\right)\left|\xi\right|^{ik_x^2 c_s/(2\omega)} \exp\left(\frac{i\omega}{c_s}\xi\right), \tag{3.71}$$

and in high-β plasma ($\xi < 0$)

$$\begin{aligned} V_z\left(\xi\right) \sim& \left(\frac{\omega}{2c_s}\right)^{ik_x^2 c_s/(4\omega)} \exp\left(-\frac{3\pi k_x^2 c_s}{8\omega}\right)\xi^{ik_x c_s/(2\omega)} \exp\left(\frac{i\omega}{c_s}\xi\right) - \frac{\left(2\pi\right)^{1/2}}{\Gamma\left(-ik_x^2 c_s/\left(2\omega\right)\right)} \times \\ &\times \exp\left(-\frac{\pi k_x^2 c_s}{8\omega}\right)\left(\frac{\omega}{2c_s}\right)^{-\left(ik_x^2 c_s/(4\omega)\right)-1/2} \xi^{-\left(ik_x^2 c_s/(2\omega)\right)-1} \exp\left(\frac{i\omega}{c_s}\xi - \frac{i\omega}{4c_s}\xi^2 - \frac{3i\pi}{4}\right). \end{aligned} \tag{3.72}$$

Remembering the assumption that $\omega \gg k_x c_s$ we may utilise the WKB method to find approximations to the transmitted and converted components of V_z. To find an expression for the transmitted wave we may assume that v_x is small in comparison to V_z so

$$v_x = \frac{V_{x0}}{\omega} \exp\left(\omega\phi_0 + \frac{\phi_1}{\omega}\right), \tag{3.73}$$

$$V_z = B \exp\left(\omega\phi_0 + \frac{\phi_1}{\omega}\right), \tag{3.74}$$

where $\omega\phi_0 \gg \phi_1/\omega,\ V_{x0}/\omega$.

Substituting these expansions into Equations (3.56) and (3.57) we obtain the expressions

$$V_{x0}\phi_0' + \frac{V_{x0}'}{\omega} + \frac{V_{x0}}{\omega^2}\phi_1' - \frac{i}{c_s}V_{x0} + \frac{i}{2c_s}\xi V_{x0} = \frac{ik_x}{2}B, \tag{3.75}$$

$$B\omega\phi_0' + \frac{B\phi_1'}{\omega} - \frac{Bi\omega}{c_s} = \frac{ik_x}{2\omega}V_{x0}. \tag{3.76}$$

Equating the various powers of ω we find that

$$\phi_0 = \frac{i}{c_s}\xi, \qquad V_{x0} = \frac{Bk_xc_s}{\xi}, \qquad \phi_1 = \frac{ik_x^2c_s}{2}\ln\xi. \tag{3.77}$$

Substituting these values back into Equation (3.74) we have an expression for the transmitted component of V_z

$$V_z = B\xi^{ik_x^2c_s/(2\omega)} \exp\left(\frac{i\omega}{c_s}\xi\right). \tag{3.78}$$

To find the converted portion of V_z we may follow the same process, this time assuming that V_z is small in comparison to v_x

$$v_x = A \exp\left(\omega\phi_0 + \frac{\phi_1}{\omega}\right), \tag{3.79}$$

$$V_z = \frac{V_{z0}}{\omega} \exp\left(\omega\phi_0 + \frac{\phi_1}{\omega}\right), \tag{3.80}$$

where $\omega\phi_0 \gg \phi_1/\omega,\ V_{z0}/\omega$. Substituting these into Equations (3.56) and (3.57) we find

$$A\omega\phi_0' + \frac{A\phi_1'}{\omega} - \frac{Ai\omega}{c_s} + \frac{Ai\omega}{2c_s}\xi = \frac{ik_x}{2\omega}V_{z0}, \tag{3.81}$$

$$V_{z0}\phi_0' + \frac{V_{z0}'}{\omega} + \frac{V_{z0}}{\omega^2}\phi_1' - \frac{i}{c_s}V_{z0} = \frac{Aik_x}{2}. \tag{3.82}$$

Again examining the powers of ω we find values for the unknown coefficients

$$\phi_0 = \frac{i}{c_s}\xi - \frac{i}{4c_s}\xi^2, \qquad V_{z0} = -\frac{Ak_xc_s}{\xi}, \qquad \phi_1 = -\frac{ik_x^2c_s}{2}\ln\xi. \tag{3.83}$$

Substituting these values back into Equation (3.80) we have an expression for the converted part of V_z

$$V_z = -\frac{k_x c_s}{\omega} A \xi^{-\left(i k_x^2 c_s/(2\omega)\right)-1} \exp\left(\frac{i\omega}{c_s}\xi - \frac{i\omega}{4c_s}\xi^2\right). \tag{3.84}$$

As Equations (3.78) and (3.84) are both solutions to the same linear, ordinary differential equation they may be added together, so

$$V_z \sim B \xi^{i k_x^2 c_s/(2\omega)} \exp\left(\frac{i\omega}{c_s}\xi\right) - \frac{k_x c_s}{\omega} A \xi^{-\left(i k_x^2 c_s/(2\omega)\right)-1} \exp\left(\frac{i\omega}{c_s}\xi - \frac{i\omega}{4c_s}\xi^2\right) + \mathcal{O}\left(\frac{1}{\xi^2}\right), \tag{3.85}$$

which corresponds to the asymptotic expansion found from the Parabolic Cylinder function solution.

We may compare Equations (3.71), (3.72) and (3.85) to find the values of A and B, which give the amplitude of the converted wave and the transmitted wave in comparison to the incident wave respectively. If we take the coefficient multiplying the $\xi^{i k_x^2 c_s/(2\omega)} \exp\left(i\omega\xi/c_s\right)$ term in Equations (3.71) and (3.72) and divide the high-β equation by the low-β one, then B must take the value

$$B = \exp\left(-\frac{\pi k_x^2 c_s}{2\omega}\right). \tag{3.86}$$

Similarly by comparing the relevant terms in Equations (3.72), (3.71) and (3.85) we find

$$A = \frac{2\left(2\pi\right)^{1/2}}{k_x \Gamma\left(-i k_x^2 c_s/\left(2\omega\right)\right)} \exp\left(-\frac{\pi k_x^2 c_s}{4\omega}\right)\left(\frac{\omega}{2c_s}\right)^{1/2} \exp\left(-\frac{3i\pi}{4}\right)\left(\frac{\omega}{2c_s}\right)^{-i k_x^2 c_s/(2\omega)}. \tag{3.87}$$

Since we are interested only in the amplitude at this point, the last two imaginary terms may be neglected as they only effect the phase. We may then note that (Gradshteyn and Ryzhik, 1981)

$$\left|\Gamma\left(iy\right)\right|^2 = \left|\Gamma\left(-iy\right)\right|^2 = \frac{\pi}{y \sinh\left(\pi y\right)}, \tag{3.88}$$

so the equation may be solved to give

$$A = \sqrt{1 - \exp\left(-\frac{\pi k_x^2 c_s}{\omega}\right)}. \tag{3.89}$$

Thus if we know the amplitude of the incident wave then we may calculate the amplitude of the transmitted and converted waves after the mode-conversion region. Substituting Equations (3.86) and (3.89) into Equation (3.85) we may calculate V_z for any ω and k_x. Figure 3.7 shows V_z as a function of z given for $\omega = 4\pi\sqrt{6}$ and $k = \pi$, and is in good agreement with the numerical simulations. More rigorously, if we take the ratio of the transmitted wave (dashed line to the left of $z = 0$) to the incident wave (dashed line to the right of $z = 0$) for numerical simulations with various values of k_x we may determine how well the predicted transmitted wave ratios correspond to the numerical data (Figure 3.8).

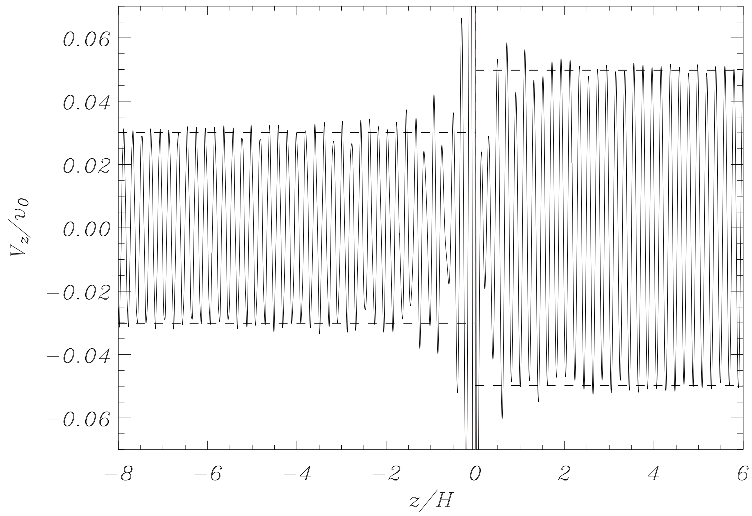

Figure 3.7: Vertical velocity as predicted by Equation (3.85) with $\omega = 4\pi\sqrt{6}$ and $k_x = \pi$. The vertical red dashed line denotes where $c_s = v_A$; the horizontal dashed line to the right of this shows the predicted amplitude of the incident wave and to the left the predicted amplitude of the transmitted wave.

Figure 3.8 shows the agreement between the predicted amplitude ratio of the transmitted fast wave to the incident slow wave (solid line) and the numerical data (stars) for $\omega = 4\pi\sqrt{6}$. The plot on the left demonstrates near perfect agreement; however, in the right hand plot, we can see by taking the logarithm of the ratios that as k_x becomes large in comparison to ω the data do not agree so well with the prediction. This is hardly surprising as it violates the assumption that $\omega \gg k_x c_s$ in the calculation of Equation (3.86). Thus, in the limit of small k_x, we have found a highly accurate prediction for the amplitude of the transmitted wave. It is more difficult to perform such a comparison for the converted slow wave as we cannot get rid of the interference due to the fast wave, but we may assume that Equation (3.89) also gives a good amplitude prediction.

In support of Section 3.3.2 Figure 3.9 shows that as k_x increases, conversion increases and transmission decreases, and as ω increases, conversion decreases and transmission increases. We may also note that the change with ω is much more gradual than that with k_x, so the horizontal wavenumber has the stronger effect as we would expect from Equations (3.86) and (3.89).

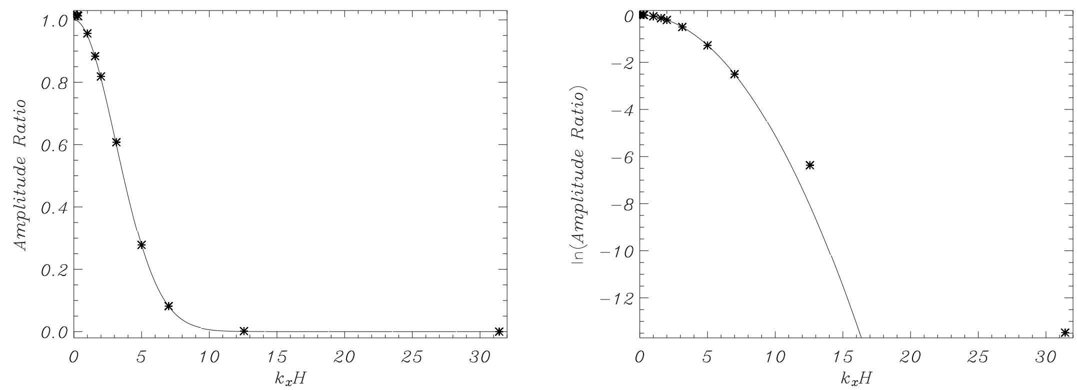

Figure 3.8: *Left:* Ratio of the transmitted and incident wave amplitudes.
Right: Logarithm of the ratio of the transmitted and incident wave amplitudes.
In both cases $\omega = 4\pi\sqrt{6}$ and the solid line is that predicted by Equation (3.86) and the stars are the values calculated from the numerical data.

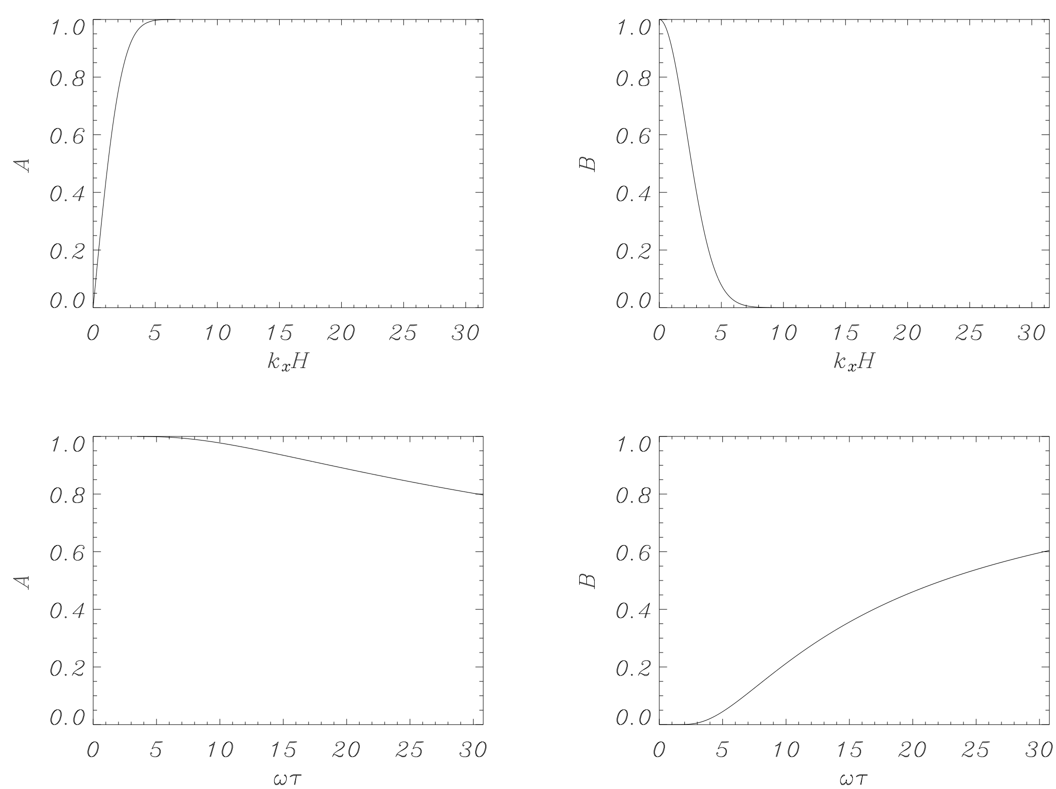

Figure 3.9: *Top Left:* The variation of A with k_x for $\omega = 2\pi\sqrt{6}$.
Top Right: The variation of B with k_x for $\omega = 2\pi\sqrt{6}$.
Bottom Left: The variation of A with ω for $k_x = \pi$.
Bottom Right: The variation of B with ω for $k_x = \pi$.

3.4.2 Large k_x Limit

For large k_x we may compare the numerical simulations with an analytical approximation derived by Roberts (2006). In that paper the slow mode was extracted from the MHD equations by scaling the variables, allowing a description of the slow mode to be found in terms of the Klein-Gordon equation. Starting with the wave equations (3.37) and (3.38)

$$\left(v_A^2\frac{\partial^2}{\partial z^2}-\left(c_s^2+v_A^2\right)k_x^2-\frac{\partial^2}{\partial t^2}\right)v_x=k_xc_s^2\left(\frac{\partial}{\partial z}-\frac{1}{\gamma}\right)v_z, \tag{3.90}$$

$$\left(c_s^2\frac{\partial^2}{\partial z^2}-c_s^2\frac{\partial}{\partial z}-\frac{\partial^2}{\partial t^2}\right)v_z=-k_xc_s^2\left(\frac{\partial}{\partial z}-\frac{1}{\gamma}\left(\gamma-1\right)\right)v_x, \tag{3.91}$$

we may assume that k_x is large so Equation (3.90) reduces down to

$$\left(c_s^2+v_A^2\right)k_xv_x+k_xc_s^2\left(\frac{\partial}{\partial z}-\frac{1}{\gamma}\right)v_z=0. \tag{3.92}$$

This may then be used to eliminate v_x from Equation (3.91) which reduces to

$$\frac{\partial^2 v_z}{\partial t^2}-c_T^2\frac{\partial^2 v_z}{\partial z^2}+\frac{c_T^4}{c_s^2}\frac{\partial v_z}{\partial z}+\frac{c_s^2c_T^2}{\gamma v_A^2}\left(\frac{c_T^2}{c_s^2}-\left(\frac{1}{\gamma}-1\right)\right)v_z=0, \tag{3.93}$$

after a little manipulation. If we introduce

$$Q\left(z,t\right)=\left(\frac{\rho_0c_T^2}{\rho_0\left(0\right)c_T^2\left(0\right)}\right)^{1/2}v_z\left(z,t\right), \tag{3.94}$$

then the first derivative drops out and Equation (3.93) may be written in the form of the Klein-Gordon equation

$$\frac{\partial^2 Q}{\partial t^2}-c_T^2\frac{\partial^2 Q}{\partial z^2}+\Omega^2Q=0, \tag{3.95}$$

where

$$\Omega^2=c_T^2\left\{\frac{1}{4}\frac{c_T^4}{c_s^4}-\frac{c_T^4}{2c_s^2v_A^2}+\frac{c_s^2}{\gamma v_A^2}\left(\frac{c_T^2}{c_s^2}-\left(\frac{1}{\gamma}-1\right)\right)\right\}, \tag{3.96}$$

is a cutoff frequency.

As we can see from Figure 3.10 the maximum value of the cutoff frequency is $\Omega\approx 0.5235$, so as long as the driving frequency we choose is much larger than this the term involving Ω may be neglected. Assuming that this is the case we may solve Equation (3.95) using the formal WKB method (as described in Bender and Orszag (1978)) to find a leading order solution for $Q\left(z,t\right)$ valid for large ω to get

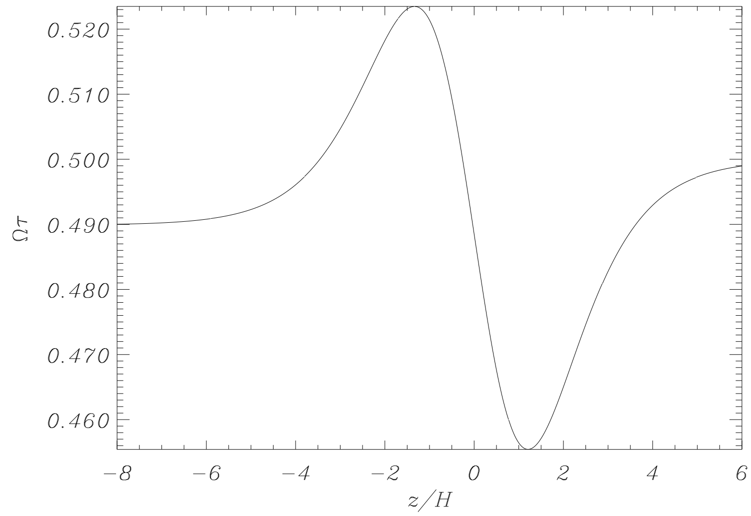

Figure 3.10: The cutoff frequency Ω shown across the computational domain z.

$$Q(z,t) \sim C_1 \left(-\frac{1}{c_T^2}\right)^{-1/4} \exp\left\{\omega\left[it + \int_{z_m}^{z}\left(-\frac{1}{c_T^2}\right)^{1/2}\mathrm{d}\hat{z}\right]\right\} + \\ + C_2 \left(-\frac{1}{c_T^2}\right)^{-1/4} \exp\left\{-\omega\left[it + \int_{z_m}^{z}\left(-\frac{1}{c_T^2}\right)^{1/2}\mathrm{d}\hat{z}\right]\right\}, \tag{3.97}$$

where C_1 and C_2 are arbitrary constants which may be determined from the initial or boundary conditions and z_m is the maximum value of z. It is fairly easy to show that

$$\left(-\frac{1}{c_T^2}\right)^{-1/4} = i^{-1/2} c_T^{1/2}, \tag{3.98}$$

and

$$\int_{z_m}^{z}\left(-\frac{1}{c_T^2}\right)^{1/2}\mathrm{d}\hat{z} = \pm i \int_{z_m}^{z} \frac{1}{c_T}\mathrm{d}\hat{z}. \tag{3.99}$$

Using Equations (3.98) and (3.99) we may rewrite Equation (3.97) in the form

$$Q(z,t) \sim C c_T^{1/2} \sin\left\{\omega\left[t + \int_{z_m}^{z}\frac{1}{c_T}\mathrm{d}\hat{z}\right]\right\}, \tag{3.100}$$

where C is a new arbitrary constant. It makes sense to write the equation in this form as we drive a sine wave in v_z on the upper boundary. Performing the necessary integration we find that

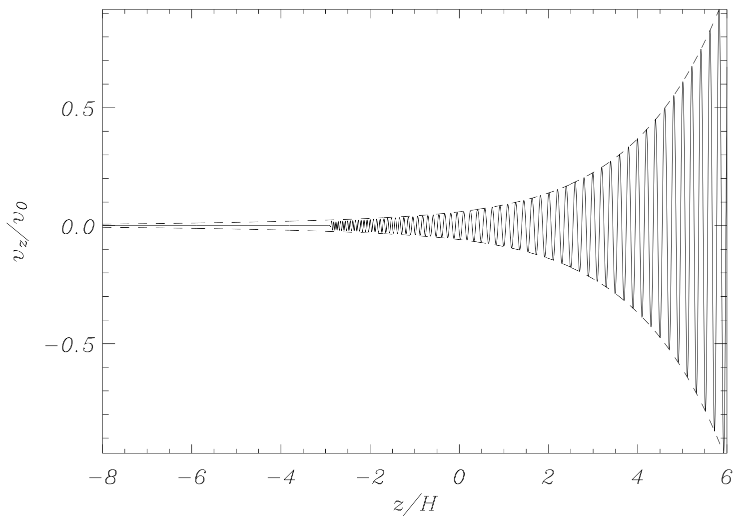

Figure 3.11: Vertical velocity for driving frequency $\omega = 4\pi\sqrt{6}$ and wavenumber $k_x = 40\pi$ at $t = 13.5$ Alfvén times. The solid line shows the numerical simulation and the dashed line the amplitude predicted by Equation (3.102).

$$Q(z,t) \sim C c_T^{1/2} \sin\left\{\omega\left[t + \frac{1}{c_s}\ln\left|\frac{(c_T + c_s)(c_T(z_m) - c_s)}{(c_T - c_s)(c_T(z_m) + c_s)}\right| - 2\left(\frac{1}{c_T} - \frac{1}{c_T(z_m)}\right)\right]\right\}. \tag{3.101}$$

Using Equation (3.94) and the upper boundary condition on v_z (3.40) we obtain an expression for v_z

$$v_z(z,t) = \frac{c_T^{1/2}(z_m)\, v_A}{v_A(z_m)\, c_T^{1/2}} \sin\left\{\omega\left[t + \frac{1}{c_s}\ln\left|\frac{(c_T + c_s)(c_T(z_m) - c_s)}{(c_T - c_s)(c_T(z_m) + c_s)}\right| - 2\left(\frac{1}{c_T} - \frac{1}{c_T(z_m)}\right)\right]\right\}. \tag{3.102}$$

Figure 3.11 shows the amplitude predicted by Equation (3.102) overplotted on the results of the numerical simulations. By eye these seem to be in prefect agreement. We may then use Equation (3.92) along with Equation (3.102) to find an analytical approximation to v_x. The amplitude predicted from this approximation is shown in Figure 3.12 in comparison to the numerical data. At the top end of the domain the two seem to be in good agreement; however as z decreases, particularly once we pass $z = 0$, the analytical approximation deviates from the numerical solution. This is surprising considering how well the approximation for v_z performed, at least until we look at the transformed vertical velocity (Figure 3.13). We can then see that the analytical approximation to v_z also deviates from the numerical solution as z decreases - previously it was masked by the strong exponential nature of the velocity. This discrepancy between the analytical and numerical data does decrease with increasing k_x, but it seems that k_x must be much, much larger than ω in order to obtain a high level of agreement. This is due to the fact that the second z derivative

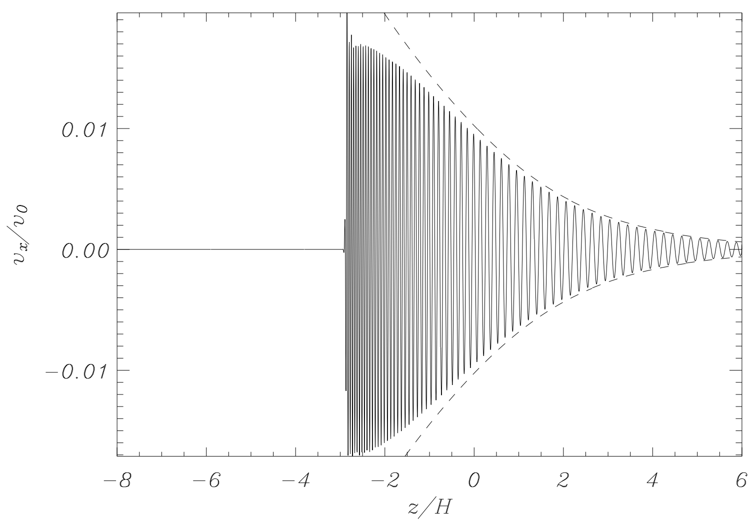

Figure 3.12: Horizontal velocity for driving frequency $\omega = 4\pi\sqrt{6}$ and wavenumber $k_x = 40\pi$ at $t = 13.5$ Alfvén times. The solid line shows the numerical simulation and the dashed line the amplitude predicted by Equations (3.92) and (3.102).

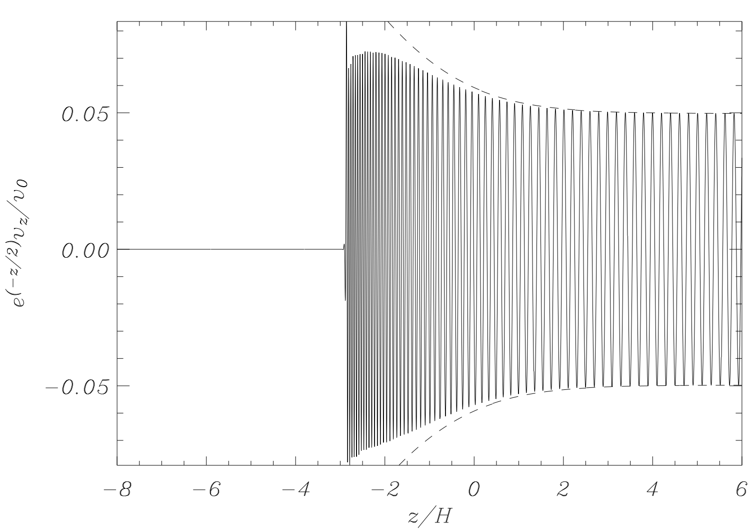

Figure 3.13: Transformed vertical velocity, $\tilde{v}_z$, for driving frequency $\omega = 4\pi\sqrt{6}$ and wavenumber $k_x = 40\pi$ at $t = 13.5$ Alfvén times. The solid line shows the numerical simulation and the dashed line the amplitude predicted by Equation (3.102).

in Equation (3.90) becomes large as $z \to -\infty$ and it is no longer negligible.

3.4.3 WKB Analysis away from the Conversion Region

Having looked in detail at what is occurring around the mode-conversion region where $\beta \approx 1$, we move on to consider the behaviour of the system in high- and low-β plasma. We do this using a WKB style analysis which is valid for large ω.

We begin with the wave equations (3.37) and (3.38) with $\partial/\partial t = i\omega$

$$\left(v_A^2 \frac{\mathrm{d}^2}{\mathrm{d}z^2} - \left(c_s^2 + v_A^2\right) k_x^2 + \omega^2\right) v_x = k_x c_s^2 \left(\frac{\mathrm{d}}{\mathrm{d}z} - \frac{1}{\gamma}\right) v_z, \tag{3.103}$$

$$\left(c_s^2 \frac{\mathrm{d}^2}{\mathrm{d}z^2} - c_s^2 \frac{\mathrm{d}}{\mathrm{d}z} + \omega^2\right) v_z = -k_x c_s^2 \left(\frac{\mathrm{d}}{\mathrm{d}z} - \frac{1}{\gamma}\left(\gamma - 1\right)\right) v_x. \tag{3.104}$$

Then under the assumption that $\omega \gg k_x c_s$ we expand v_x and v_z in inverse powers of ω. To find equations which will model the incident and transmitted waves we make the assumption that v_x is small compared to v_z

$$v_x = \frac{V_{x0}}{\omega} \exp\left(\omega\phi_0 + \phi_1 + \phi_2/\omega\right), \tag{3.105}$$

$$v_z = \exp\left(\omega\phi_0 + \phi_1 + \phi_2/\omega\right), \tag{3.106}$$

where $\omega\phi_0 \gg \phi_1 \gg \phi_2/\omega, V_{x0}/\omega$.

Substituting these back into the wave equations we obtain

$$\omega\left(1 + v_A^2 \left(\phi_0'\right)^2\right) V_{x0} = \omega k_x c_s^2 \phi_0' + \mathcal{O}\left(1\right), \tag{3.107}$$

and

$$\omega^2\left(1 + c_s^2\left(\phi_0'\right)^2\right) + \omega c_s^2\left(\phi_0'' + 2\phi_0'\phi_1' - \phi_0'\right) + c_s^2\left(\phi_1'' + \left(\phi_1'\right)^2 + 2\phi_0'\phi_2' - \phi_1'\right) = \\ = -k c_s^2 \phi_0' V_{x0} + \mathcal{O}\left(\frac{1}{\omega}\right), \tag{3.108}$$

where $' = \mathrm{d}/\mathrm{d}z$.

From the $\mathcal{O}\left(\omega^2\right)$ terms in Equation (3.108) we have $\phi_0' = i/c_s$ so $\phi_0 = iz/c_s$ and $\phi_0'' = 0$. We may substitute these back into the $\mathcal{O}\left(\omega\right)$ equations to find

$$\phi_1 = \frac{z}{2}, \tag{3.109}$$

$$V_{x0} = -\frac{i k_x c_s^3}{\left(v_A^2 - c_s^2\right)}. \tag{3.110}$$

These may then be substituted into the $\mathcal{O}(1)$ equation from which we obtain

$$\phi_2 = \frac{ik_x^2 c_s}{2} \ln\left|\frac{v_A^2 - c_s^2}{v_A^2}\right| - \frac{ic_s}{8} z. \tag{3.111}$$

Returning to Equations (3.105) and (3.106) we have

$$v_x = -\frac{ik_x c_s^3 e^{z/2}}{\omega\left(v_A^2 - c_s^2\right)} \exp\left(\frac{i\omega}{c_s} z + \frac{i}{\omega}\left(\frac{k_x^2 c_s}{2} \ln\left|1 - \frac{c_s^2}{v_A^2}\right| - \frac{c_s}{8} z\right)\right), \tag{3.112}$$

$$v_z = e^{z/2} \exp\left(\frac{i\omega}{c_s} z + \frac{i}{\omega}\left(\frac{k_x^2 c_s}{2} \ln\left|1 - \frac{c_s^2}{v_A^2}\right| - \frac{c_s}{8} z\right)\right), \tag{3.113}$$

which may also be written in the form

$$v_x = -\frac{k_x c_s^3 e^{z/2}}{\omega\left(v_A^2 - c_s^2\right)} \cos\left(\frac{\omega z}{c_s} + \frac{1}{\omega}\left(\frac{k_x^2 c_s}{2} \ln\left|1 - \frac{c_s^2}{v_A^2}\right| - \frac{c_s}{8} z\right)\right), \tag{3.114}$$

$$v_z = e^{z/2} \sin\left(\frac{\omega z}{c_s} + \frac{1}{\omega}\left(\frac{k_x^2 c_s}{2} \ln\left|1 - \frac{c_s^2}{v_A^2}\right| - \frac{c_s}{8} z\right)\right). \tag{3.115}$$

In low-β plasma Equations (3.114) and (3.115) represent the incident slow wave and in high-β plasma they represent the transmitted fast wave. Depending on whether we are considering the incident or transmitted wave there will be a different constant amplitude multiplying the equations which may be calculated from Equation (3.86).

Now to find an equation which gives the behaviour of the converted wave we must assume that v_z is small in comparison to v_x

$$v_x = \exp\left(\omega\phi_0 + \phi_1 + \phi_2/\omega\right), \tag{3.116}$$

$$v_z = \frac{V_{z0}}{\omega} \exp\left(\omega\phi_0 + \phi_1 + \phi_2/\omega\right), \tag{3.117}$$

where $\omega\phi_0 \gg \phi_1 \gg \phi_2/\omega, V_{z0}/\omega$.

As before, these may be substituted back into Equations (3.103) and (3.104) to find

$$\omega^2\left(1 + v_A^2\left(\phi_0'\right)^2\right) + \omega v_A^2\left(\phi_0'' + 2\phi_0'\phi_1'\right) + \left(v_A^2\phi_1'' + v_A^2\left(\phi_1'\right)^2 + 2v_A^2\phi_0'\phi_2' - \right.$$
$$\left. - \left(c_s^2 + v_A^2\right)k_x^2\right) = k_x c_s^2 \phi_0' V_{z0} + \mathcal{O}\left(\frac{1}{\omega}\right), \tag{3.118}$$

and

$$\omega\left(1 + c_s^2\left(\phi_0'\right)^2\right) V_{z0} = -\omega k_x c_s^2 \phi_0' + \mathcal{O}(1). \tag{3.119}$$

The $\mathcal{O}\left(\omega^2\right)$ equation tells us that $\phi_0' = i/v_A$. So we have $\phi_0'' = -i/\left(2v_A\right)$ and, integrating between 0 and z, $\phi_0 = 2i/c_s - 2i/v_A$. We may substitute these back into the $\mathcal{O}\left(\omega\right)$ equations to find

$$\phi_1 = \frac{z}{4}, \tag{3.120}$$

$$V_{z0} = -\frac{ik_x c_s^2 v_A}{\left(v_A^2 - c_s^2\right)}. \tag{3.121}$$

These may then be substituted into the $\mathcal{O}\left(1\right)$ equation from which we obtain

$$\phi_2 = ik_x^2 c_s \tanh^{-1}\left(\frac{v_A}{c_s}\right) + \frac{iv_A}{16} - ik_x^2 v_A. \tag{3.122}$$

Returning to Equations (3.116) and (3.117) we have

$$v_x = e^{z/4}\exp\left(\frac{2i\omega}{c_s} - \frac{2i\omega}{v_A} + \frac{i}{\omega}\left(k_x^2 c_s \tanh^{-1}\left(\frac{v_A}{c_s}\right) + \frac{v_A}{16} - k_x^2 v_A\right)\right), \tag{3.123}$$

$$v_z = -\frac{ik_x c_s^2 v_A e^{z/4}}{\omega\left(v_A^2 - c_s^2\right)}\exp\left(\frac{2i\omega}{c_s} - \frac{2i\omega}{v_A} + \frac{i}{\omega}\left(k_x^2 c_s \tanh^{-1}\left(\frac{v_A}{c_s}\right) + \frac{v_A}{16} - k_x^2 v_A\right)\right), \tag{3.124}$$

which may also be written in the form

$$v_x = e^{z/4}\cos\left(\frac{2\omega}{c_s} - \frac{2\omega}{v_A} + \frac{1}{\omega}\left(k_x^2 c_s \tanh^{-1}\left(\frac{v_A}{c_s}\right) + \frac{v_A}{16} - k_x^2 v_A\right)\right), \tag{3.125}$$

$$v_z = -\frac{k_x c_s^2 v_A e^{z/4}}{\omega\left(v_A^2 - c_s^2\right)}\sin\left(\frac{2\omega}{c_s} - \frac{2\omega}{v_A} + \frac{1}{\omega}\left(k_x^2 c_s \tanh^{-1}\left(\frac{v_A}{c_s}\right) + \frac{v_A}{16} - k_x^2 v_A\right)\right). \tag{3.126}$$

In this case v_x and v_z are both zero in the low-β plasma as the fast wave is evanescent there. In the high-β plasma Equations (3.125) and (3.126) represent the converted slow wave, which will again have a constant coefficient multiplying both equations; this can be calculated from Equation (3.89).

To summarise we have:

$$\begin{aligned}
\text{Low } \beta\text{:}\quad \text{Inc.}\quad & v_x = -a\frac{k_x c_s^3 e^{z/2}}{\omega\left(v_A^2 - c_s^2\right)}\cos\left(\frac{\omega z}{c_s} + \frac{1}{\omega}\left(\frac{k_x^2 c_s}{2}\ln\left|1 - \frac{c_s^2}{v_A^2}\right| - \frac{c_s}{8}z\right)\right), \\
& v_z = ae^{z/2}\sin\left(\frac{\omega z}{c_s} + \frac{1}{\omega}\left(\frac{k_x^2 c_s}{2}\ln\left|1 - \frac{c_s^2}{v_A^2}\right| - \frac{c_s}{8}z\right)\right), \\
\text{High } \beta\text{:}\quad \text{Trans.}\quad & v_x = -aB\frac{k_x c_s^3 e^{z/2}}{\omega\left(v_A^2 - c_s^2\right)}\cos\left(\frac{\omega z}{c_s} + \frac{1}{\omega}\left(\frac{k_x^2 c_s}{2}\ln\left|1 - \frac{c_s^2}{v_A^2}\right| - \frac{c_s}{8}z\right)\right), \\
& v_z = aBe^{z/2}\sin\left(\frac{\omega z}{c_s} + \frac{1}{\omega}\left(\frac{k_x^2 c_s}{2}\ln\left|1 - \frac{c_s^2}{v_A^2}\right| - \frac{c_s}{8}z\right)\right), \\
\text{Conv.}\quad & v_x = aAe^{z/4}\cos\left(\frac{2\omega}{c_s} - \frac{2\omega}{v_A} + \frac{1}{\omega}\left(k_x c_s^2 \tanh^{-1}\left(\frac{v_A}{c_s}\right) + \frac{v_A}{16} - k_x^2 v_A\right)\right), \\
& v_z = -aA\frac{k_x c_s^2 v_A e^{z/4}}{\omega\left(v_A^2 - c_s^2\right)}\sin\left(\frac{2\omega}{c_s} - \frac{2\omega}{v_A} + \frac{1}{\omega}\left(k_x c_s^2 \tanh^{-1}\left(\frac{v_A}{c_s}\right) + \frac{v_A}{16} - k_x^2 v_A\right)\right),
\end{aligned}$$

where $a = e^{-z_m/2}$, and A and B are as defined by Equations (3.86) and (3.89).

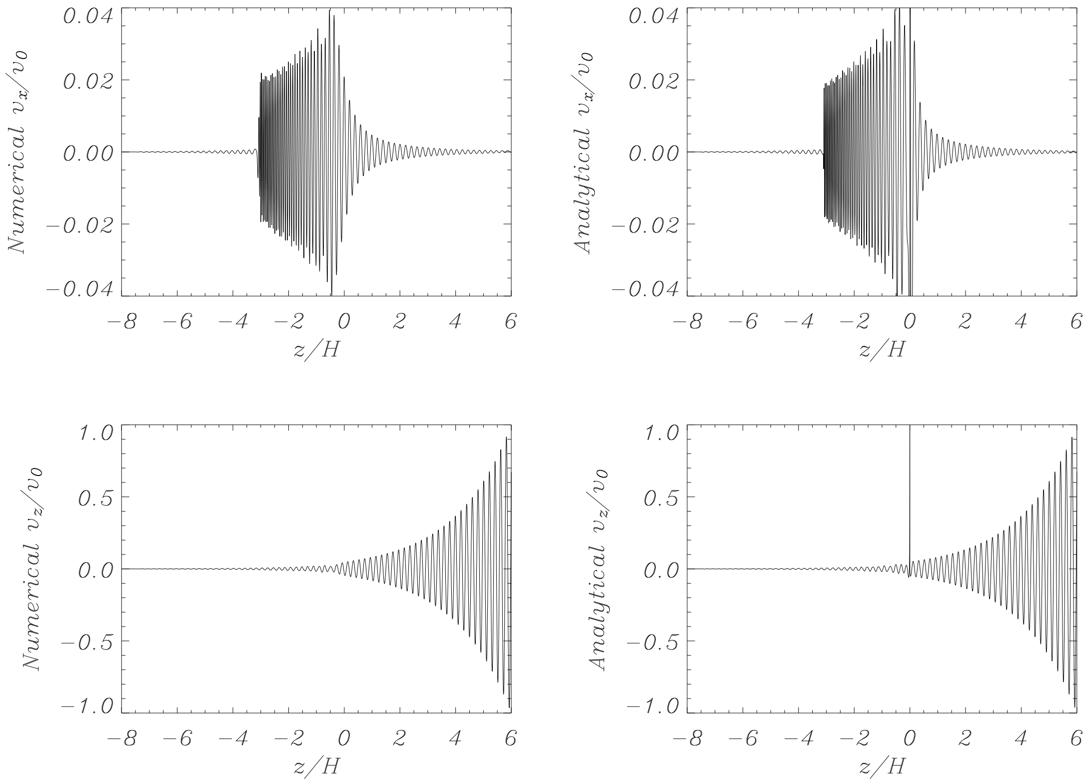

Figure 3.14: The numerical and analytical horizontal velocity and the numerical and analytical vertical velocity respectively from top left to bottom right. In all plots $\omega = 4\pi\sqrt{6}$, $k_x = \pi$ and $t = 13.5$ Alfvén times.

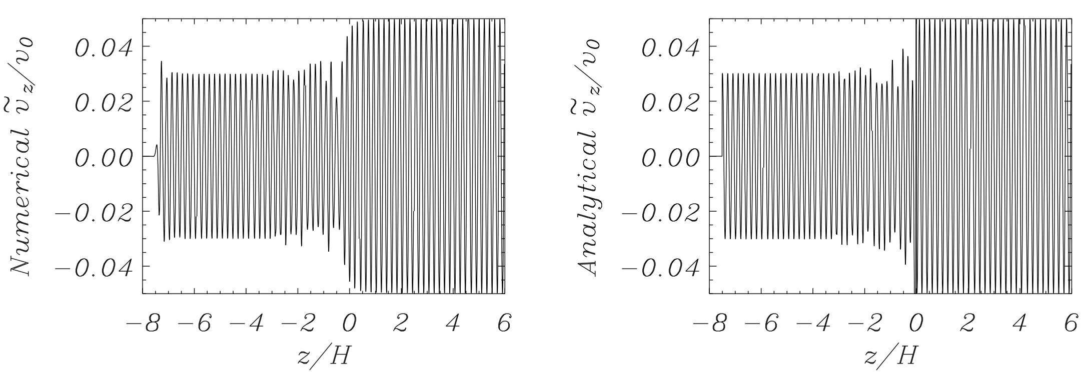

Figure 3.15: The numerical and analytical transformed vertical velocity for $\omega = 4\pi\sqrt{6}$, $k_x = \pi$ and $t = 13.5$ Alfvén times.

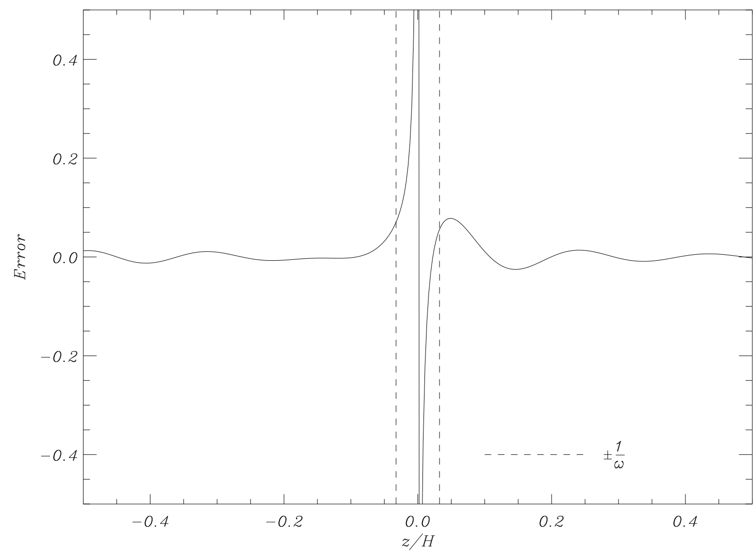

Figure 3.16: The absolute error between the results of the WKB analysis and the numerical simulations zoomed in around $z = 0$ (where $c_s = v_A$). The dashed line shows $z = \pm 1/\omega$ demonstrating that the WKB analysis only breaks down very close to the conversion region.

In Figure 3.14 we have used the above information, along with the knowledge of the positions of the various wavefronts from Equations (3.43) and (3.45), to construct analytical plots of the horizontal and vertical velocity (right-hand side). These are shown next to plots of the equivalent numerical simulations (left-hand side). The agreement between these plots is excellent, although the strong exponential nature in the plots of the vertical velocity could disguise any deviation in the results. To ensure this is not the case we also checked the agreement in the absence of the exponential (Figure 3.15).

Using the WKB method to find the wave behaviour away from the conversion region and then matching the amplitudes across this region using the method developed by Cairns and Lashmore-Davies has been very successful. The WKB analysis has predicted the phase and amplitude behaviour accurately, and using the transmission and conversion coefficients we have been able to predict the correct amplitudes for the different modes. The only place where the analytical prediction suffers is at the mode-conversion point, $z = 0$, as $c_s = v_A$ and the transmitted v_x and converted v_z both have a zero in the denominator and thus grow very large. However the effect of this singularity is restricted to a very small area. This is because the singularity is multiplied by a factor of $1/\omega$ in all cases and as ω is assumed to be large the effect of the singularity is thus reduced. This is clear in Figure 3.16 which shows the difference between the WKB and numerical results. The error clearly grows at the mode-conversion region, but at a distance of only $1/\omega$ from this point it has reduced back to its previous magnitude.

It is fairly straightforward to show how the results of this section link in with those of Section 3.4.1 as the mode-conversion region is approached. We may do this by assuming z is small and expanding about the mode-conversion region, so $z = \xi$ and v_A is as defined in Equation (3.55). Remembering that $v_z \approx e^{z/2} V_z$

the transmitted wave may be written

$$V_z \approx B \exp\left(\frac{i\omega}{c_s}\xi + \frac{ik_x^2 c_s}{2\omega}\ln\xi\right), \tag{3.127}$$

where small terms have been omitted. This may also be written

$$V_z \approx B\xi^{ik_x^2 c_s/(2\omega)} \exp\left(\frac{i\omega}{c_s}\xi\right). \tag{3.128}$$

Following the same process for the converted wave

$$V_z \approx -\frac{k_x c_s}{\omega\xi} A \exp\left(\frac{i\omega}{c_s}\xi - \frac{i\omega}{4c_s}\xi^2 + \frac{ik_x^2 c_s}{2\omega}\ln\xi^{-1}\right), \tag{3.129}$$

or

$$V_z \approx -\frac{k_x c_s}{\omega} A\xi^{-ik_x^2 c_s/(2\omega)-1} \exp\left(\frac{i\omega}{c_s}\xi - \frac{i\omega}{4c_s}\xi^2\right). \tag{3.130}$$

Adding Equations (3.128) and (3.130) we obtain

$$V_z \approx B\xi^{ik_x^2 c_s/(2\omega)} \exp\left(\frac{i\omega}{c_s}\xi\right) - \frac{k_x c_s}{\omega} A\xi^{-ik_x^2 c_s/(2\omega)-1} \exp\left(\frac{i\omega}{c_s}\xi - \frac{i\omega}{4c_s}\xi^2\right), \tag{3.131}$$

and we have obtained the same result found in Equation (3.85), so we can see how these two solutions match onto each other at the conversion region.

3.5 Conclusions

In this chapter we have considered the downward propagation of linear waves through an isothermal atmosphere permeated by a vertical background magnetic field, shown in Figure 3.1. More specifically we concentrated on the region where the wave passes from a low-β to a high-β plasma. As expected the simulations show mode conversion occurring as the wave passes through this region at the point where the sound and Alfvén speeds are equal (Figure 3.2), but this behaviour is masked by the strongly exponential nature of the variables. This may be removed by making a simple transformation, and the conversion across $c_s = v_A$ is then much clearer (Figure 3.3). In this figure we can see the transmitted fast wave propagating out in front of the converted slow wave, which has a decreasing wavelength. In Section 3.3.1 we also calculated the exact position of the various wavefronts using the fact that in the high-β plasma the fast wave propagates at approximately c_s and the slow wave approximately v_A. We then looked at what happens when we vary the free parameters in the model individually, beginning with the horizontal wavenumber k_x. Figure 3.5 shows that k_x has a strong effect on the amount of mode conversion. For $k_x = 0$ the two modes are completely decoupled and no conversion occurs. Then as k_x increases so does the degree of mode conversion. In Sections 3.4.1 and 3.4.2 we investigated what happens in the limit of small and large k_x respectively. The second free parameter is the driving frequency ω. The effect of varying this parameter is shown in Figure 3.6. Here we note that the amount of conversion decreases with increasing ω, in agreement with

Cally (2005).

In the limit of small k_x we used a method developed by Cairns and Lashmore-Davies (1983) to find that the velocity may be modelled by Parabolic Cylinder functions. These have links to Hypergeometric functions (see Abramowitz and Stegun (1964)) which have been used previously in mode-conversion problems by Zhugzhda (1979); Zhugzhda and Dzhalilov (1982a); and Cally (2001). The asymptotic behaviour of these Parabolic Cylinder functions was then used to find transmission and conversion coefficients valid for small k_x. The transmission and conversion coefficients, given by Equations (3.86) and (3.89), back up the observations from the simulations that the extent of conversion will increase with increasing wavenumber and decreasing driving frequency. The equations do suggest that k_x has the stronger effect of the two parameters. The amplitude of the transmitted wave predicted from Equation (3.86) also agrees very well with the numerical data (Figure 3.8).

For large k_x we followed an analysis carried out by Roberts (2006). From this we found a WKB solution for v_z valid for large ω (Equation (3.102)). This in turn was used to find an analytical solution for v_x using Equation (3.92). Figure 3.11 suggests that we have good agreement between the analytical and numerical results for v_z; however once we remove the exponential behaviour we can see that as z decreases the fit of the analytical approximation worsens, particularly past the conversion point (Figure 3.12). Figure 3.13 shows that this is also the case for the horizontal velocity. The fit does improve as k_x increases, but it is still not significantly better even for very large k_x.

Finally we performed a WKB analysis to find the behaviour in low- and high-β plasmas. These solutions were then matched across the conversion region using the transmission and conversion coefficients (3.86) and (3.89) which were calculated in Section 3.4.1. Using this method we managed to create a highly accurate replica of the numerical results, shown in Figure 3.14. As can be seen we have managed to capture both changes to the phase and the amplitude as the wavefront propagates across the mode-conversion region, even though the WKB approximation does not hold at the location where $c_s = v_A$.

A thorough investigation of this very simple one-dimensional model has yielded some very interesting results, giving us some insight into the mode-conversion problem. We have been able to accurately predict how the phase and amplitude change as a slow wave propagates down from low to high β, and also to isolate the behaviour of the transmitted fast wave and the converted slow wave. In the next chapter we extend this model to include a non-isothermal atmosphere. We use a realistic profile which mimics the steep gradient of the transition region. The methods used in this chapter are applied to this more complex model and give some interesting results.

Chapter 4

MHD Mode Conversion in a Stratified Non-Isothermal Atmosphere

4.1 Introduction

We expand on the work in Chapter 3 by allowing for the inclusion of a variable temperature profile. By using analytical approximations to model the behaviour both at, and distant from, the mode-conversion region combined with numerical simulations, we may compare the results directly with those for the isothermal atmosphere. Some of the results in this chapter have been published in McDougall and Hood (2008).

4.2 Non-Isothermal Model

We work with the same general set up as Chapter 3 (as shown in Figure 3.1). Since variations are now allowed in the temperature profile things are complicated slightly as both the sound and Alfvén speeds will now vary with height. As before we begin with the Ideal MHD equations.

4.2.1 Ideal MHD Equations

The Ideal MHD equations are as given by Equations (1.28) – (1.35).

$$\frac{\partial \rho}{\partial t} + \nabla \cdot (\rho \mathbf{v}) = 0, \tag{4.1}$$

$$\rho \left(\frac{\partial}{\partial t} + \mathbf{v} \cdot \nabla \right) \mathbf{v} = -\nabla p + \mathbf{j} \times \mathbf{B} + \rho \mathbf{g}, \tag{4.2}$$

$$\frac{\partial \mathbf{B}}{\partial t} = \nabla \times (\mathbf{v} \times \mathbf{B}), \tag{4.3}$$

$$\left(\frac{\partial}{\partial t} + \mathbf{v} \cdot \nabla \right) p = \frac{\gamma p}{\rho} \left(\frac{\partial}{\partial t} + \mathbf{v} \cdot \nabla \right) \rho, \tag{4.4}$$

$$p = R \rho \frac{T}{\widetilde{\mu}}, \tag{4.5}$$

$$\mathbf{j} = \frac{1}{\mu} (\nabla \times \mathbf{B}), \tag{4.6}$$

$$\nabla \cdot \mathbf{B} = 0, \tag{4.7}$$

where ρ is the mass density, $\mathbf{v}$ the fluid velocity, p the gas pressure, j the current density, $\mathbf{B}$ the magnetic induction, $\mathbf{g}$ the gravitational acceleration and T the temperature.

4.2.2 Equilibrium

We now consider the equilibrium conditions for a gravitationally-stratified atmosphere permeated by a uniform, vertical magnetic field with a non-isothermal temperature profile. The equilibrium Momentum Equation is

$$\frac{\mathrm{d}p_0}{\mathrm{d}z} = -\rho_0 g, \tag{4.8}$$

and from the equilibrium Ideal Gas Law

$$p_0 = R\rho_0 \frac{T_0}{\widetilde{\mu}}, \tag{4.9}$$

this can be written

$$\frac{\mathrm{d}p_0}{\mathrm{d}z} = -\frac{\tilde{\mu} p_0}{RT_0} g. \tag{4.10}$$

Note that the temperature is now a function of height and so the scale height will also vary with height. We define this as

$$\Lambda\left(z\right) = \frac{RT_0}{\tilde{\mu} g} = \frac{p_0}{g\rho_0}. \tag{4.11}$$

Thus

$$\frac{\mathrm{d}p_0}{\mathrm{d}z} = -\frac{p_0}{\Lambda}, \tag{4.12}$$

which may be solved to give

$$p_0\left(z\right) = p_0\left(0\right) \exp\left(-\int \frac{1}{\Lambda} \mathrm{d}z\right). \tag{4.13}$$

Defining

$$n\left(z\right) = \int_0^z \frac{\mathrm{d}z'}{\Lambda\left(z'\right)}, \tag{4.14}$$

this may be written as

$$p_0\left(z\right) = p_0\left(0\right) e^{-n(z)}. \tag{4.15}$$

Using the equilibrium Ideal Gas Law (4.9), $\rho_0\left(z\right)$ is then

$$\rho_0\left(z\right) = \frac{p_0\left(0\right)}{g\Lambda\left(z\right)}e^{-n(z)}, \tag{4.16}$$

or

$$\rho_0\left(z\right) = \rho_0\left(0\right)\frac{\Lambda\left(0\right)}{\Lambda\left(z\right)}e^{-n(z)}. \tag{4.17}$$

4.2.3 Linearised MHD Equations

The MHD Equations (4.1) – (4.7) may be linearised about the equilibrium by adding a small perturbation (denoted by subscript 1) to each term

$$\mathbf{B} = \mathbf{B}_0 + \mathbf{B}_1\left(x,z,t\right), \quad \mathbf{v} = \mathbf{v}_1\left(x,z,t\right), \quad p = p_0 + p_1\left(x,z,t\right),$$

$$\rho = \rho_0 + \rho_1\left(x,z,t\right), \quad T = T_0 + T_1(x,z,t). \tag{4.18}$$

Substituting these back into the MHD equations and neglecting small quantities we find the Linearised MHD equations:

$$\frac{\partial \rho_1}{\partial t} + \nabla\cdot\left(\rho_0\mathbf{v}_1\right) = 0, \tag{4.19}$$

$$\rho_0\frac{\partial \mathbf{v}_1}{\partial t} = -\nabla p_1 + \frac{1}{\mu}\left(\nabla\times\mathbf{B}_1\right)\times\mathbf{B}_0 + \rho_1\mathbf{g}, \tag{4.20}$$

$$\frac{\partial \mathbf{B}_1}{\partial t} = \nabla\times\left(\mathbf{v}_1\times\mathbf{B}_0\right), \tag{4.21}$$

$$\frac{\partial p_1}{\partial t} + \left(\mathbf{v}_1\cdot\nabla\right)p_0 = \frac{\gamma p_0}{\rho_0}\left(\frac{\partial \rho_1}{\partial t} + \left(\mathbf{v}_1\cdot\nabla\right)\rho_0\right), \tag{4.22}$$

$$\frac{p_1}{p_0} = \frac{\rho_1}{\rho_0} + \frac{T_1}{T_0}, \tag{4.23}$$

$$\nabla\cdot\mathbf{B}_1 = 0. \tag{4.24}$$

We may now drop the subscripts on perturbed variables and assume that we are working with the linearised equations from this point.

Assuming that all perturbations vary in x, z and t alone the Linearised MHD Equations (4.19) – (4.22) reduce to

$$\frac{\partial \rho}{\partial t} + \rho_0\frac{\partial v_x}{\partial x} + \rho_0\frac{\partial v_z}{\partial z} + v_z\frac{\mathrm{d}\rho_0}{\mathrm{d}z} = 0, \tag{4.25}$$

$$\rho_0\frac{\partial v_x}{\partial t} = -\frac{\partial p}{\partial x} + \frac{B_0}{\mu}\left(\frac{\partial B_x}{\partial z} - \frac{\partial B_z}{\partial x}\right), \tag{4.26}$$

$$\rho_0\frac{\partial v_z}{\partial t} = -\frac{\partial p}{\partial z} - \rho g, \tag{4.27}$$

$$\frac{\partial B_x}{\partial t} = B_0 \frac{\partial v_x}{\partial z}, \tag{4.28}$$

$$\frac{\partial B_z}{\partial t} = -B_0 \frac{\partial v_x}{\partial x}, \tag{4.29}$$

$$\frac{\partial p}{\partial t} + v_z \frac{\mathrm{d}p_0}{\mathrm{d}z} = c_s^2\left(z\right)\left(\frac{\partial \rho}{\partial t} + v_z \frac{\mathrm{d}\rho_0}{\mathrm{d}z}\right), \tag{4.30}$$

where

$$c_s^2 = \frac{\gamma p_0\left(z\right)}{\rho_0\left(z\right)} = \frac{\gamma p_0\left(0\right)}{\rho_0\left(0\right)\Lambda\left(0\right)}\Lambda\left(z\right). \tag{4.31}$$

As can be seen from the above equation the squared sound speed is proportional to the scale height, which is in turn proportional to the temperature.

This set of equations may be combined to give a pair of wave equations

$$\frac{\partial^2 v_x}{\partial t^2} = \left(c_s^2 + v_A^2\right)\frac{\partial^2 v_x}{\partial x^2} + c_s^2 \frac{\partial^2 v_z}{\partial x \partial z} + v_A^2 \frac{\partial^2 v_x}{\partial z^2} - g\frac{\partial v_z}{\partial x}, \tag{4.32}$$

$$\frac{\partial^2 v_z}{\partial t^2} = c_s^2\left(\frac{\partial^2 v_x}{\partial x \partial z} + \frac{\partial^2 v_z}{\partial z^2}\right) - \left(\gamma - 1\right) g\frac{\partial v_x}{\partial x} - \gamma g\frac{\partial v_z}{\partial z}, \tag{4.33}$$

where $v_A^2 = B_0^2/\left(\mu\rho_0\right)$ is the square of the Alfvén speed. As expected these are identical to those listed in Equations (3.18) and (3.19), which are valid for a general temperature profile $T\left(z\right)$ (Ferraro and Plumpton, 1958).

4.2.3.1 x-Dependence

To reduce these equations from two dimensions to one dimension, we assume that the x-dependence has a trigonometric form depending on the horizontal wavenumber k_x:

$$\begin{aligned}
\mathbf{v} &= \left(v_x\left(z,t\right)\sin k_x x,\ 0,\ v_z\left(z,t\right)\cos k_x x\right), \\
\mathbf{B} &= \left(B_x\left(z,t\right)\sin k_x x,\ 0,\ B_z\left(z,t\right)\cos k_x x\right), \\
\rho &= \rho\left(z,t\right)\cos k_x x, \\
p &= p\left(z,t\right)\cos k_x x.
\end{aligned} \tag{4.34}$$

Noting that $n'\left(z\right) = 1/\Lambda\left(z\right)$,

$$\frac{\mathrm{d}p_0}{\mathrm{d}z} = -\frac{p_0}{\Lambda}, \tag{4.35}$$

and

$$\frac{\mathrm{d}\rho_0}{\mathrm{d}z} = -\rho_0\left(0\right)\Lambda\left(0\right)\frac{e^{-n(z)}}{\Lambda\left(z\right)}\left(n'\left(z\right) + \frac{\Lambda'\left(z\right)}{\Lambda\left(z\right)}\right), \tag{4.36}$$

or

$$\frac{\mathrm{d}\rho_0}{\mathrm{d}z} = -\frac{\rho_0(z)}{\Lambda(z)}\left(1+\Lambda'(z)\right). \tag{4.37}$$

We may then use the above information to rewrite the Linearised MHD equations:

$$\rho_0\frac{\partial v_x}{\partial t} - \frac{B_0}{\mu}\frac{\partial B_x}{\partial z} = k_x p + k_x\frac{B_0}{\mu}B_z, \tag{4.38}$$

$$\rho_0\frac{\partial v_z}{\partial t} + \frac{\partial p}{\partial z} = -\rho g, \tag{4.39}$$

$$\frac{\partial B_x}{\partial t} - B_0\frac{\partial v_x}{\partial z} = 0, \tag{4.40}$$

$$\frac{\partial B_z}{\partial t} = -k_x B_0 v_x, \tag{4.41}$$

$$\frac{\partial p}{\partial t} + \gamma p_0\frac{\partial v_z}{\partial z} = \rho_0 g v_z - \gamma p_0 k_x v_x, \tag{4.42}$$

$$\frac{\partial \rho}{\partial t} + \rho_0\frac{\partial v_z}{\partial z} = \frac{\rho_0}{\Lambda}\left(1+\Lambda'\right)v_z - k_x\rho_0 v_x. \tag{4.43}$$

As before these may be combined to give a pair of wave equations

$$\frac{\partial^2 v_x}{\partial t^2} = v_A^2\frac{\partial^2 v_x}{\partial z^2} - c_s^2 k_x\frac{\partial v_z}{\partial z} - \left(c_s^2+v_A^2\right)k_x^2 v_x + k_x g v_z, \tag{4.44}$$

$$\frac{\partial^2 v_z}{\partial t^2} = c_s^2\frac{\partial^2 v_z}{\partial z^2} + c_s^2 k_x\frac{\partial v_x}{\partial z} - \gamma g\frac{\partial v_z}{\partial z} - (\gamma-1)\,g k_x v_x, \tag{4.45}$$

which are dependent only on z and t. To make these equations easier to model numerically they are made dimensionless.

4.2.3.2 Non-Dimensionalisation

We set $\mathbf{v} = v_0\bar{\mathbf{v}}$, $\mathbf{B} = B_0\bar{\mathbf{B}}$, $p = p_{00}\bar{p}$, $\rho = \rho_{00}\bar{\rho}$, $T_0 = T_{00}\bar{\Lambda}$, $p_0 = p_{00}\bar{p}_0$, $\rho_0 = \rho_{00}\bar{\rho}_0$, $z = L\bar{z}$, $t = \tau\bar{t}$, and $k_x = \bar{k_x}/L$. Under this system a bar denotes dimensionless quantities and the constants v_0, B_0, p_{00}, ρ_{00}, T_{00}, L and τ have the dimensions of the quantity that they are scaling.

Choosing $p_{00} = p_0(0)$ and $\rho_{00} = \rho_0(0)$ we find

$$\bar{p}_0 = \exp\left(-\frac{L}{H}\int\frac{\mathrm{d}\bar{z}}{\bar{\Lambda}}\right), \tag{4.46}$$

and

$$\bar{\rho}_0 = \frac{1}{\bar{\Lambda}}\exp\left(-\frac{L}{H}\int\frac{\mathrm{d}\bar{z}}{\bar{\Lambda}}\right) = \frac{\bar{p}_0}{\bar{\Lambda}}, \tag{4.47}$$

where $H = RT_{00}/(\mu g) = \Lambda(0)$ and $\Lambda = H\bar{\Lambda}$.

We may then consider the sound and Alfvén speeds. Setting $c_{s0}^2 = \gamma p_{00}/\rho_{00}$ we have

$$\bar{c}_s^2 = \bar{\Lambda}, \tag{4.48}$$

and $v_{A0}^2 = B_0^2/\left(\mu\rho_{00}\right)$ gives

$$\bar{v}_A^2 = \frac{1}{\bar{\rho}_0}. \tag{4.49}$$

The plasma β may then be written as

$$\beta = \frac{2c_s^2}{\gamma v_A^2} = \beta_0\bar{\beta}, \tag{4.50}$$

where $\beta_0 = 2c_{s0}^2/\left(\gamma v_{A0}^2\right)$ and $\bar{\beta} = \bar{p}_0$. At this point we may choose to set $v_0 = v_{A0} = 1$, giving $c_{s0}^2 = \gamma\beta_0/2$.

If we wish to set the region where the sound and Alfvén speeds are equal to lie at $z = 0$ then the following relation must be satisfied

$$\bar{\rho}_0\big|_{z=0} = \frac{\gamma\beta_0}{2}. \tag{4.51}$$

Note that this is dependent on the chosen temperature profile and so the chosen value for β_0 will differ from case to case.

The linearised dimensionless equations are given by

$$\bar{\rho}_0\frac{\partial\bar{v}_x}{\partial\bar{t}} - \frac{\partial\bar{B}_x}{\partial\bar{z}} = \frac{\beta_0}{2}\bar{k}_x\bar{p} + \bar{k}_x\bar{B}_z, \tag{4.52}$$

$$\bar{\rho}_0\frac{\partial\bar{v}_z}{\partial\bar{t}} + \frac{\beta_0}{2}\frac{\partial\bar{p}}{\partial\bar{z}} = -\frac{L}{H}\frac{\beta_0}{2}\bar{\rho}, \tag{4.53}$$

$$\frac{\partial\bar{B}_x}{\partial\bar{t}} - \frac{\partial\bar{v}_x}{\partial\bar{z}} = 0, \tag{4.54}$$

$$\frac{\partial\bar{B}_z}{\partial\bar{t}} = -\bar{k}_x\bar{v}_x, \tag{4.55}$$

$$\frac{1}{\bar{p}_0}\frac{\partial\bar{p}}{\partial\bar{t}} + \gamma\frac{\partial\bar{v}_z}{\partial\bar{z}} = \frac{L}{H}\frac{\bar{v}_z}{\bar{\Lambda}} - \gamma\bar{k}_x\bar{v}_x, \tag{4.56}$$

$$\frac{1}{\bar{\rho}_0}\frac{\partial\bar{\rho}}{\partial\bar{t}} + \frac{\partial\bar{v}_z}{\partial\bar{z}} = \frac{\bar{v}_z}{\bar{\Lambda}}\left(\frac{L}{H} + \bar{\Lambda}'\right) - \bar{k}_x\bar{v}_x, \tag{4.57}$$

where it has been noted that $g = c_{s0}^2/\gamma H$. These may then be combined to give the wave equations

$$\left(\bar{v}_A^2\frac{\partial^2}{\partial\bar{z}^2} - \left(\frac{\gamma\beta_0}{2}\bar{c}_s^2 + \bar{v}_A^2\right)\bar{k}_x^2 - \frac{\partial^2}{\partial\bar{t}^2}\right)\bar{v}_x = \frac{\gamma\beta_0}{2}\bar{k}_x\left(\bar{c}_s^2\frac{\partial}{\partial\bar{z}} - \frac{L}{\gamma H}\right)\bar{v}_z, \tag{4.58}$$

$$\left(\frac{\gamma\beta_0}{2}\bar{c}_s^2\frac{\partial^2}{\partial\bar{z}^2} - \frac{L}{H}\frac{\gamma\beta_0}{2}\frac{\partial}{\partial\bar{z}} - \frac{\partial^2}{\partial\bar{t}^2}\right)\bar{v}_z = -\frac{\gamma\beta_0}{2}\bar{k}_x\left(\bar{c}_s^2\frac{\partial}{\partial\bar{z}} - \frac{L}{\gamma H}\left(\gamma - 1\right)\right)\bar{v}_x. \tag{4.59}$$

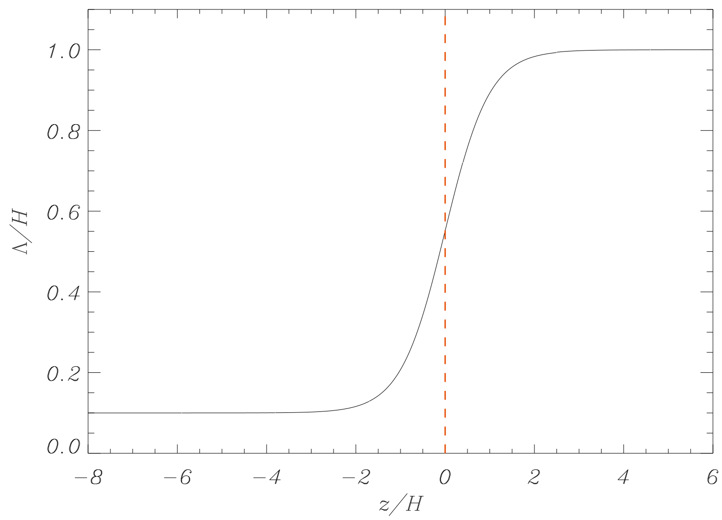

Figure 4.1: The chosen temperature profile has the form $\Lambda = a + b\tanh(dz/H)$ and is chosen to mimic the steep gradient of the transition region. Here we have set $a = 0.55$, $b = 0.45$ and $d = 1.0$. The dashed line indicates where $c_s = v_A$.

Henceforth the bars on normalised values are dropped and it is assumed that we are working with dimensionless quantities unless otherwise stated.

4.2.4 Temperature Profile

The temperature profile that we use is a $\tanh$ profile, given by

$$\Lambda = a + b\tanh(dz). \tag{4.60}$$

This is chosen because of its steep temperature gradient reflective of that seen in the transition region. As shown in Figure 4.1, away from the gradient the temperature is constant. So in these regions the results would be the same as for an isothermal atmosphere. For this reason we choose to set the region where the sound and Alfvén speeds are equal at $z = 0$ in the centre of the steep gradient. In order to do this we need to know the value of p_0. For this we require the expression

$$\int \frac{\mathrm{d}z}{\Lambda} = \frac{\ln(\tanh(dz)+1)}{2d(a-b)} - \frac{\ln(\tanh(dz)-1)}{2d(a+b)} - \frac{b\ln(a+b\tanh(dz))}{d(a^2-b^2)}. \tag{4.61}$$

Noting that

$$\tanh(dz) = \frac{e^{2dz}-1}{e^{2dz}+1}, \tag{4.62}$$

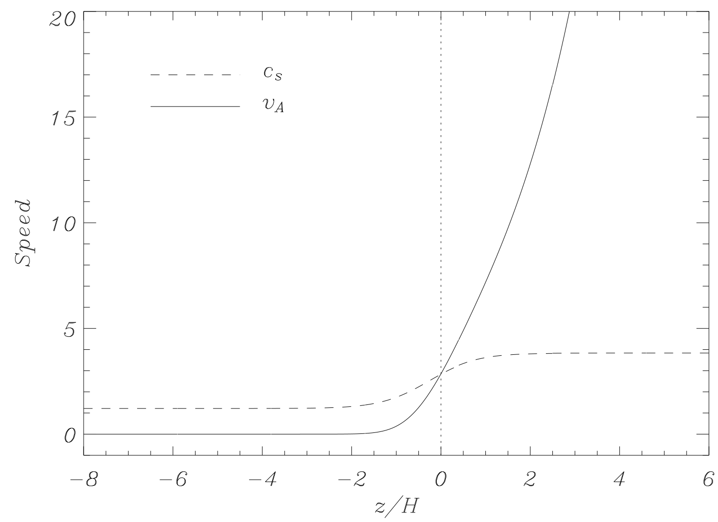

Figure 4.2: This plot shows how the sound and Alfvén speeds vary across the computational domain. The mode-conversion region lies at $z = 0$ where these speeds are equal.

this may be written

$$\int \frac{\mathrm{d}z}{\Lambda} = \frac{b}{d\,(a^2 - b^2)} \ln\left(\frac{2}{(a+b)\,e^{2dz} + (a-b)}\right) + \frac{z}{(a-b)}. \tag{4.63}$$

From Equation (4.46) this gives p_0 as

$$p_0 = \left(\frac{(a+b)\,e^{2dz} + (a-b)}{2}\right)^{\frac{Lb}{Hd(a^2-b^2)}} \exp\left(-\frac{Lz}{H\,(a-b)}\right), \tag{4.64}$$

and to satisfy the condition $c_s = v_A$ at $z = 0$ (Equation (4.51)) we require

$$\beta_0 = \frac{2}{\gamma} a^{-\frac{Lb}{Hd(a^2-b^2)}}. \tag{4.65}$$

The mode-conversion region will then lie at $z = 0$, as shown in Figure 4.2, and we are free to define $\gamma = 5/3$ and $L = H$. So, as for the isothermal case, L is equal to the scale height H defined at $z = 0$. We also set $a = 0.55$ and $b = 0.45$ leaving the parameter d free to vary the steepness of the slope.

4.3 Numerical Simulations

Equations (4.52) – (4.57) are solved numerically using the MacCormack method as was done in Chapter 3. As described in Section 2.3.8 the MacCormack method is a finite difference scheme which uses a predictor and corrector step to advance the solution. Either forward/backward or backward/forward differencing may be chosen for the predictor and corrector steps respectively. We choose to use forward differencing for the predictor steps and backward differencing for the corrector steps. This means that we are using the more accurate corrected values on the upper boundary where a slow wave is driven. The lower boundary is less important as the simulation is terminated before this boundary is reached to eliminate reflection effects. The boundary conditions are given by

$$B_x = -\frac{1}{k_x}\frac{\partial B_z}{\partial z}, \quad \frac{\partial B_z}{\partial t} = -k_x v_x, \quad \frac{\partial p}{\partial z} = 0, \quad \frac{\partial \rho}{\partial z} = 0. \tag{4.66}$$

In addition to these we have the conditions on the velocity which vary on the upper and lower boundaries.

$$\text{Upper Boundary:} \quad v_x = 0, \quad v_z = \sin \omega t. \tag{4.67}$$

$$\text{Lower Boundary:} \quad \frac{\partial v_x}{\partial z} = 0, \quad v_z = 0. \tag{4.68}$$

As for the isothermal case, by driving v_z on the upper boundary we are predominantly driving a slow wave. There will be a small component of the fast wave introduced because we have set $v_x = 0$, but we need not worry about this as the fast wave is evanescent in the low-β plasma. The simulations are run for $-8 \leq z \leq 6$ and $0 \leq t \leq 7.2$ with $\delta z = 0.003$ and $\delta t = 0.0013$, where the end time is chosen just prior to the wavefront hitting the lower boundary. We are then free to choose the values of the parameters d, which varies the steepness of the slope of the temperature profile, and the parameters ω and k_x which will alter the driving frequency and wavenumber respectively. The slow wave is driven on the upper boundary for frequencies of $\omega = 2\pi\sqrt{\gamma\beta_0/2}$, $2\pi\sqrt{6}\sqrt{\gamma\beta_0/2}$ and $4\pi\sqrt{6}\sqrt{\gamma\beta_0/2}$ which correspond in real terms to frequencies of 0.20 s^{-1}, 0.49 s^{-1} and 0.98 s^{-1} and periods of 31.3 s, 12.8 s and 6.4 s respectively. In calculating these values we have assumed a typical lengthscale of 6 Mm and sound speed of 50 km s^{-1} in the transition region. Using $\Omega_{ac} = \gamma g/2c_s$ (Roberts, 2004) the acoustic cutoff frequency is given by $\Omega_{ac} = 0.004$ s^{-1}, which is much smaller than the driving frequencies.

4.3.1 Wave Properties

As we are driving a slow wave on the upper boundary we would expect to see similar behaviour to that demonstrated in the isothermal case. Thus, in the absence of any mode conversion ($k_x = 0$) the low-β slow wave should propagate as a fast wave once it crosses into the high-β plasma. For $k_x \neq 0$ some mode conversion will occur, and we would expect some component of the slow mode to be visible in the high-β plasma. At this point we also note that as the wavelength is given by

$$\lambda = \frac{2\pi}{\omega}\sqrt{\frac{\gamma\beta_0}{2}}c_s, \tag{4.69}$$

which varies with the sound speed, we would expect the wavelength of the incident wave to vary as it crosses the steep temperature gradient at $z = 0$.

Figure 4.3 shows the horizontal and vertical velocity, horizontal and vertical magnetic field, pressure and density resulting from the numerical simulation with $d = 1$, $\omega = 2\pi\sqrt{6}\sqrt{\gamma\beta_0/2}$ and $k_x = \pi$ at $t = 7.2$ Alfvén times. There does appear to be some mode conversion occurring; this is clearest in the plots of horizontal velocity and the horizontal and vertical magnetic field, where a change in behaviour is seen in the amplitude. As in the isothermal case this is masked by a strong amplitude variation. By using the WKB

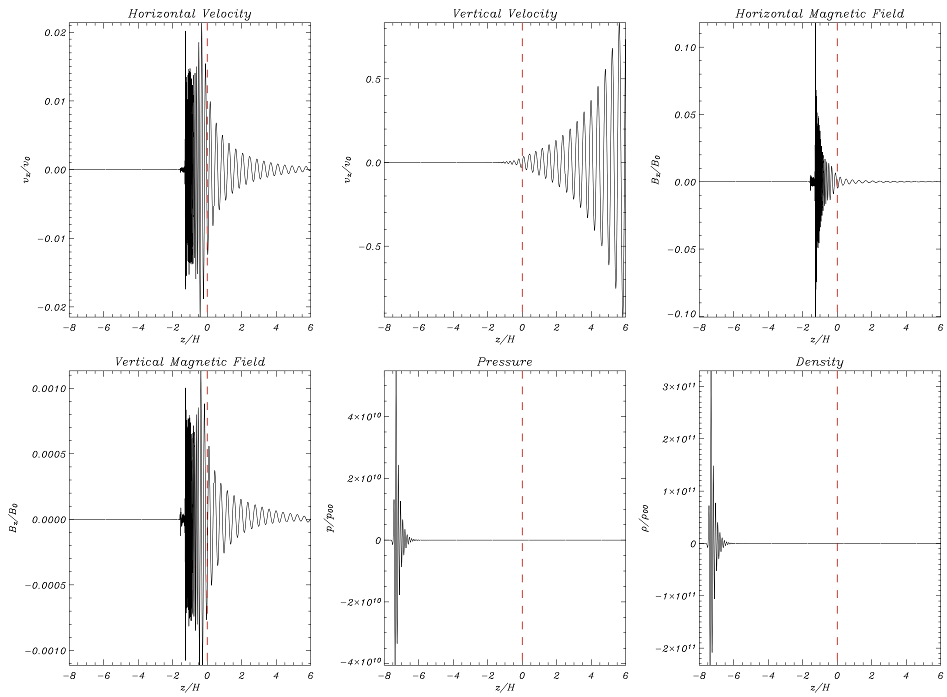

Figure 4.3: Results of the numerical simulation with $\omega = 2\pi\sqrt{6}\sqrt{\gamma\beta_0/2}$ and $k_x = \pi$ at $t = 7.2$ Alfvén times. The plots show the horizontal and vertical velocity, the horizontal and vertical magnetic field, pressure and density respectively from top left to bottom right. The red dashed line indicates where $c_s = v_A$.

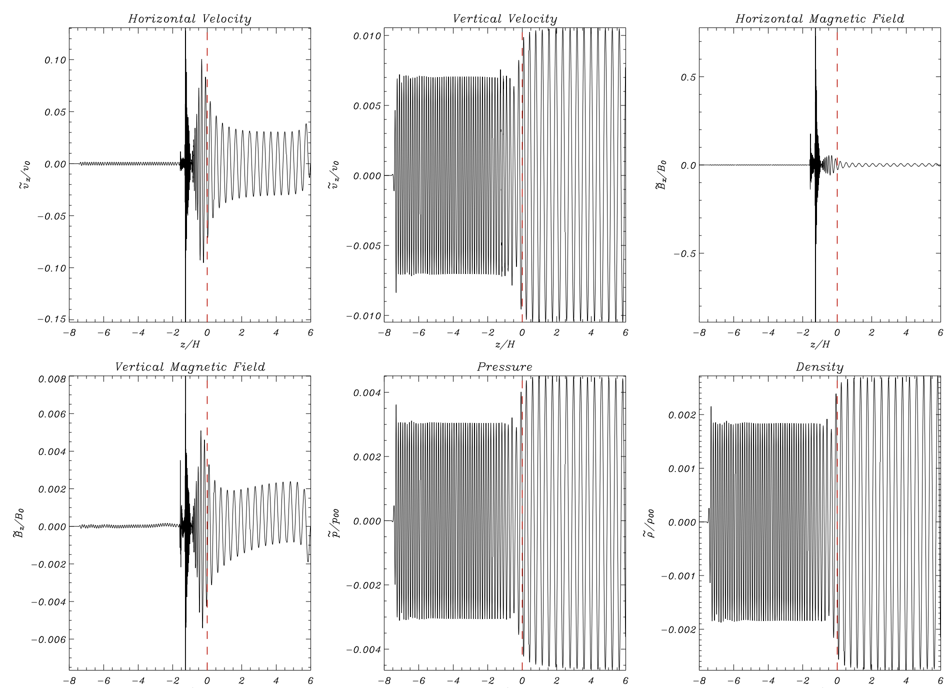

Figure 4.4: Results of the numerical simulation with $\omega = 2\pi\sqrt{6}\sqrt{\gamma\beta_0/2}$ and $k_x = \pi$ at $t = 7.2$ Alfvén times. The plots show a transformation of the horizontal and vertical velocity, the horizontal and vertical magnetic field, pressure and density respectively from top left to bottom right. The red dashed line indicates where $c_s = v_A$.

method as shown in Section 4.4.2 it is possible to find a transformation which will give a constant amplitude for the incident and transmitted waves. These transformations are given by

$$v_x \to \tilde{v}_x \frac{c_s^3 \Lambda^{1/4}}{\left(v_A^2 - c_s^2\right) p_0^{1/2}}, \quad B_x \to \tilde{B}_x \frac{c_s^3 \Lambda^{1/4}}{\left(v_A^2 - c_s^2\right) p_0^{1/2}}, \quad B_z \to \tilde{B}_z \frac{c_s^3 \Lambda^{1/4}}{\left(v_A^2 - c_s^2\right) p_0^{1/2}},$$

$$v_z \to \tilde{v}_z \frac{\Lambda^{1/4}}{p_0^{1/2}}, \quad p \to \tilde{p} \frac{p_0^{1/2}}{\Lambda^{1/4}}, \quad \rho \to \tilde{\rho} \frac{p_0^{1/2}}{\Lambda^{5/4}}. \tag{4.70}$$

The plots resulting from these transformations are shown in Figure 4.4. The conversion is now much clearer across the $c_s = v_A$ layer (indicated by the red dashed line). The vertical velocity, pressure and density show the transmitted wave propagating out ahead, which has a shorter wavelength as predicted. The converted wave is present behind as interference to the left of the red dashed line, and is also visible in the plots of horizontal velocity, and horizontal and vertical magnetic field.

It is possible to calculate exactly how these wavefronts will progress with time. The position of the acoustic wave is given by

$$\frac{\mathrm{d}z}{\mathrm{d}t} = -c_s = -\sqrt{\frac{\gamma\beta_0}{2}} \sqrt{a + b\tanh\left(dz\right)}. \tag{4.71}$$

Making the substitution

$$u = \sqrt{a + b\tanh\left(dz\right)}, \tag{4.72}$$

this may be written

$$\frac{2b}{d} \int \frac{\mathrm{d}u}{\left(b^2 - \left(u^2 - a\right)^2\right)} = -\sqrt{\frac{\gamma\beta_0}{2}} t + C. \tag{4.73}$$

Solving using partial fractions along with the initial condition $t = 0$, $z = 6$ gives

$$t = \frac{1}{d}\sqrt{\frac{2}{\gamma\beta_0}} \left[\frac{1}{\sqrt{a+b}} \tanh^{-1}\left(\frac{\sqrt{a + b\tanh\left(6d\right)}}{\sqrt{a+b}}\right) - \frac{1}{\sqrt{a-b}} \coth^{-1}\left(\frac{\sqrt{a + b\tanh\left(6d\right)}}{\sqrt{a-b}}\right) - \right.$$
$$\left. - \frac{1}{\sqrt{a+b}} \tanh^{-1}\left(\frac{\sqrt{a + b\tanh\left(dz\right)}}{\sqrt{a+b}}\right) + \frac{1}{\sqrt{a-b}} \coth^{-1}\left(\frac{\sqrt{a + b\tanh\left(dz\right)}}{\sqrt{a-b}}\right) \right]. \tag{4.74}$$

From this we can see that at $t = 7.2$ Alfvén times the acoustic wave will have reached $z \approx -7.5$.

The position of the magnetic and slow modes are given by

$$\frac{\mathrm{d}z}{\mathrm{d}t} = -v_A = -\frac{1}{\rho_0}, \tag{4.75}$$

and

$$\frac{\mathrm{d}z}{\mathrm{d}t} = -c_T = -\frac{c_s v_A}{\sqrt{c_s^2 + v_A^2}}, \tag{4.76}$$

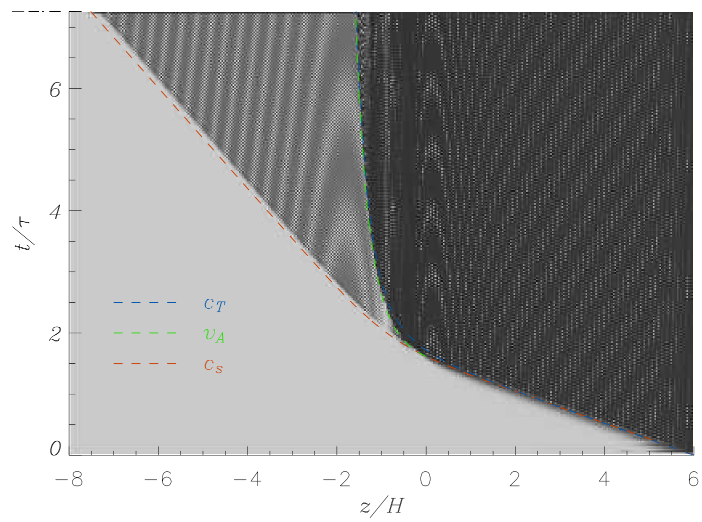

Figure 4.5: Surface plot of the transformed horizontal velocity for $\omega = 2\pi\sqrt{6}\sqrt{\gamma\beta_0/2}$, $k_x = \pi$ and $d = 1$. The red dashed line shows the position of the acoustic mode, the green dashed line the position of the magnetic mode, and the blue dashed line the position of the slow mode.

respectively. These are not easily solved analytically but a numerical solution may be found using a fourth order Runge-Kutta method. The slow mode solution is solved under the initial condition that $z = 6$ at $t = 0$. The magnetic mode is not present until the slow mode has passed through the conversion region. Using Equation (4.74) we find that this occurs at $t \approx 1.6$ Alfvén times, and so the initial condition for the magnetic mode is given by $z = 0$ at $t = 1.6$. The results of these calculations are shown in Figure 4.5. In this figure the transformed horizontal velocity is viewed from above, and overplotted are the paths predicted by Equations (4.74), (4.75) and (4.76). The acoustic mode gives the path of the slow wave in the low-β plasma and the fast wave in the high-β plasma. The magnetic mode is only present in the high-β plasma and gives the position of the slow wave in this region. The solution to Equation (4.76) gives the path of the slow mode and is valid as it passes from the low- to high-β plasma.

4.3.2 Effect of Varying the Model Parameters

We now investigate the effect of varying the three free parameters d, k_x and ω on mode conversion, and compare this to the results of the previous chapter.

4.3.2.1 Varying the Slope

By varying the value of the parameter d we may vary the steepness of the slope representing the transition region. To do this we fix the driving frequency to be $\omega = 2\pi\sqrt{6}\sqrt{\gamma\beta_0/2}$ and the wavenumber to be $k_x = \pi$. The time at which to stop each simulation was calculated using Equation (4.74), and the plots in Figure 4.6 are shown for $t = 1.8$, 7.2, and 11.5 Alfvén times respectively from left to right. So, the steeper the slope

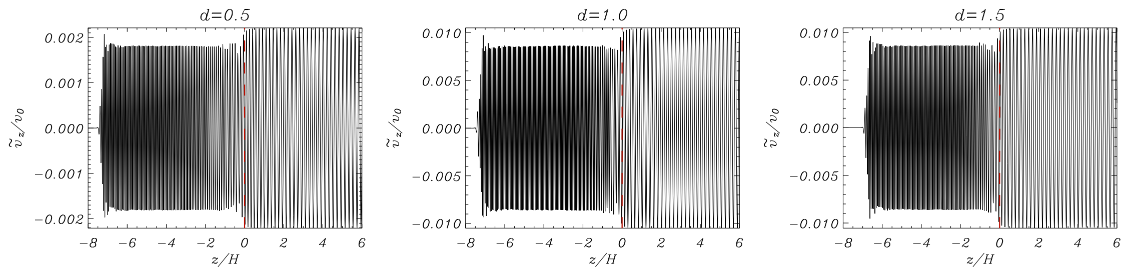

Figure 4.6: Transformed vertical velocity for $\omega = 2\pi\sqrt{6}\sqrt{\gamma\beta_0/2}$ and $k_x = \pi$. The plots show $d = 0.5$, 1 and 1.5 respectively from left to right. The dashed red line indicates where $c_s = v_A$.

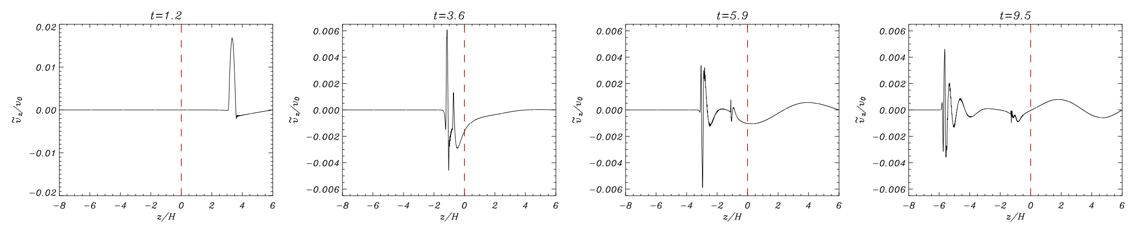

Figure 4.7: The transformed vertical velocity for $\omega = 2\pi\sqrt{\gamma\beta_0/2}$, $k_x = \pi$ and $d = 1.5$. The plots show $t = 1.2$, 3.6, 5.9 and 9.5 Alfvén times respectively from left to right. The red dashed line denotes where $c_s = v_A$.

the longer it takes for the wavefront to reach the left hand boundary. Although the timescale is affected by the slope the mode conversion seems to be unchanged. Each plot in Figure 4.6 shows the same proportion of the incident wave being transmitted across the $c_s = v_A$ layer.

It should be noted that the value of ω is chosen as it gives a wavelength of $\lambda \approx 0.2$ in the low-β plasma. This is much smaller than the width of the gradient in the temperature profile in all three cases. If this is not the case then some of the incident wave will be reflected back into the low-β plasma from the conversion region. This is demonstrated in Figure 4.7, which shows a slow mode pulse being driven on the upper boundary with frequency $\omega = 2\pi\sqrt{\gamma\beta_0/2}$ (giving a wavelength $\lambda = 1$ in the low-β plasma), wavenumber $k_x = \pi$ and slope $d = 1.5$. The incident pulse is clearly seen approaching the $c_s = v_A$ layer, denoted by the dashed red line. As this wave crosses the mode-conversion layer it splits into a converted and transmitted wave. But as these travel through the high-β plasma, another wave can be seen in the low-β plasma to the right of the dashed red line. This wave has been reflected due to the slope of the temperature profile. As we are not concerned with the reflection, we ensure that a high enough driving frequency is chosen to give a wavelength much smaller than the width of the temperature gradient. This does limit the applicability of the model as it has been shown that reflection is important for typical frequencies (Fedun et al., 2009).

4.3.2.2 Varying the Wavenumber

From Chapter 3 we would expect the amount of mode conversion to increase as the wavenumber k_x increases. We examine the same range of values for k_x, Figure 4.8 shows $k_x = 0$, 0.25, $\pi/10$, 1, $\pi/2$, 2, π, 5 and 7 respectively from top left to bottom right. In all cases the slope is fixed at $d = 1$, the driving frequency at $\omega = 2\pi\sqrt{6}\sqrt{\gamma\beta_0/2}$, and the time is $t = 7.2$ Alfvén times. As we had expected, the mode conversion increases and the transmission decreases as the value of the wavenumber increases; just as it did in the isothermal case. For $k_x = 0$ there is no mode conversion. Whilst k_x remains small the amount of mode conversion is negligible and cannot be seen in the plots representing $k_x = 0.25$, $\pi/10$, 1 or $\pi/2$. Once k_x grows beyond this point, the mode conversion can be seen in the plots clearly as the amount of transmission decreases. If we compare these plots to those shown in Section 3.3.2 we can see that the increase in mode conversion is slower in this case. Due to the similarities in behaviour we would expect to find similar equations to those found in Section 3.4.1 to describe the transmission and conversion.

4.3.2.3 Varying the Driving Frequency

The final free parameter left for us to examine is the driving frequency. From the work done by Cally (2005) and from Section 3.3.2 we expect the mode conversion to decrease with increasing frequency. We examine the frequencies $\omega = 2\pi\sqrt{\gamma\beta_0/2}$, $\omega = 2\pi\sqrt{6}\sqrt{\gamma\beta_0/2}$ and $\omega = 4\pi\sqrt{6}\sqrt{\gamma\beta_0/2}$. These are shown from left to right in Figure 4.9, in which the slope is given by $d = 1$ and the wavenumber by $k_x = \pi$ at $t = 7.2$ Alfvén times. The transmission clearly increases as the frequency increases and therefore the conversion decreases, as we suspected it should.

4.4 Analytical Approximations

As was done in Chapter 3 these predictions from the numerical simulations can be backed up using analytical techniques. We use the Cairns and Lashmore-Davies (1983) method and the WKB method to describe the wave behaviour across the domain.

4.4.1 Small k_x Limit

First we use the method by Cairns and Lashmore-Davies (1983) to find the behaviour at the mode-conversion region itself. Beginning with Equations (4.58) and (4.59) we assume that the time dependence has the form $e^{i\omega t}$ so that $\partial/\partial t = i\omega$

$$\left(v_A^2\frac{\mathrm{d}^2}{\mathrm{d}z^2} - \left(\frac{\gamma\beta_0}{2}c_s^2 + v_A^2\right)k_x^2 + \omega^2\right)v_x = \frac{\gamma\beta_0}{2}k_x\left(c_s^2\frac{\mathrm{d}}{\mathrm{d}z} - \frac{1}{\gamma}\right)v_z, \tag{4.77}$$

$$\left(\frac{\gamma\beta_0}{2}c_s^2\frac{\mathrm{d}^2}{\mathrm{d}z^2} - \frac{\gamma\beta_0}{2}\frac{\mathrm{d}}{\mathrm{d}z} + \omega^2\right)v_z = -\frac{\gamma\beta_0}{2}k_x\left(c_s^2\frac{\mathrm{d}}{\mathrm{d}z} - \frac{1}{\gamma}(\gamma-1)\right)v_x. \tag{4.78}$$

Making the substitution

$$v_z = i\frac{v_A}{c_s}\sqrt{\frac{2}{\gamma\beta_0}}V_z, \tag{4.79}$$

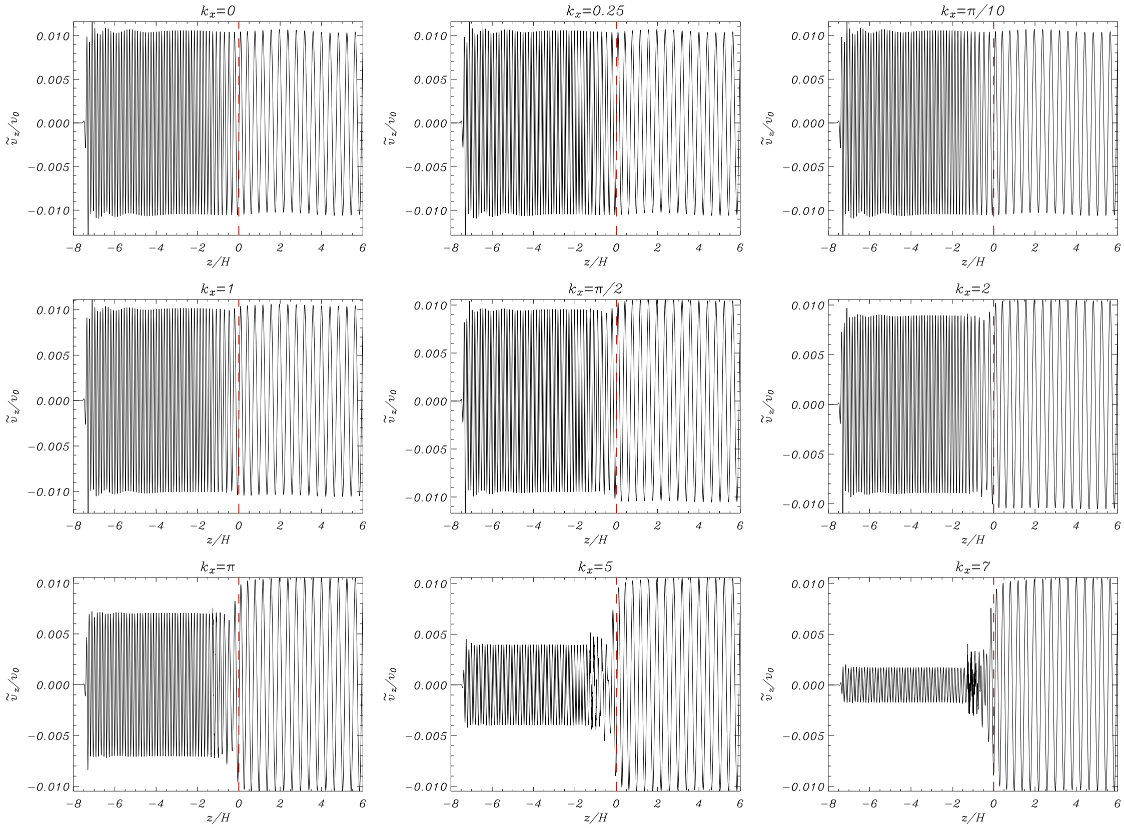

Figure 4.8: Transformed vertical velocity for $d = 1$ and $\omega = 2\pi\sqrt{6}\sqrt{\gamma\beta_0/2}$ at $t = 7.2$ Alfvén times. The plots show the results for $k_x = 0$, 0.25, $\pi/10$, 1, $\pi/2$, 2, π, 5 and 7 respectively from top left to bottom right. The dashed red line indicates where $c_s = v_A$.

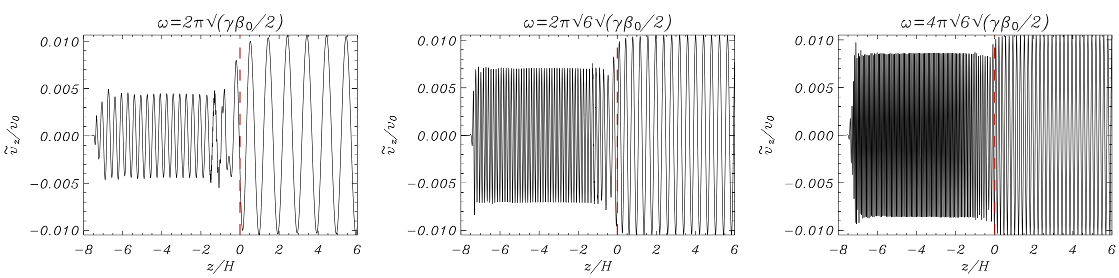

Figure 4.9: Transformed vertical velocity for $d = 1$ and $k_x = \pi$ at $t = 7.2$ Alfvén times. The plots show $\omega = 2\pi\sqrt{\gamma\beta_0/2}$, $2\pi\sqrt{6}\sqrt{\gamma\beta_0/2}$ and $4\pi\sqrt{6}\sqrt{\gamma\beta_0/2}$ respectively from left to right. The dashed red line indicates where $c_s = v_A$.

and assuming that $k_x \ll \omega/c_s$ and that variables may be neglected in comparison to their derivatives, these equations become

$$\left(v_A^2 \frac{\mathrm{d}^2}{\mathrm{d}z^2} + \omega^2\right) v_x = i\frac{\gamma\beta_0}{2} v_A c_s k_x \frac{\mathrm{d}V_z}{\mathrm{d}z}, \tag{4.80}$$

$$\left(\frac{\gamma\beta_0}{2} c_s^2 \frac{\mathrm{d}^2}{\mathrm{d}z^2} + \omega^2\right) V_z = i\left(\frac{\gamma\beta_0}{2}\right)^{3/2} \frac{c_s^3}{v_A} k_x \frac{\mathrm{d}v_x}{\mathrm{d}z}. \tag{4.81}$$

The wave equations then reduce down to

$$\left(\frac{\mathrm{d}}{\mathrm{d}z} + i\frac{\omega}{v_A}\right)\left(\frac{\mathrm{d}}{\mathrm{d}z} - i\frac{\omega}{v_A}\right) v_x = i\sqrt{\frac{\gamma\beta_0}{2}} \frac{c_s}{v_A} k_x \frac{\mathrm{d}V_z}{\mathrm{d}z}, \tag{4.82}$$

$$\left(\frac{\mathrm{d}}{\mathrm{d}z} + i\sqrt{\frac{2}{\gamma\beta_0}}\frac{\omega}{c_s}\right)\left(\frac{\mathrm{d}}{\mathrm{d}z} - i\sqrt{\frac{2}{\gamma\beta_0}}\frac{\omega}{c_s}\right) V_z = i\sqrt{\frac{\gamma\beta_0}{2}} \frac{c_s}{v_A} k_x \frac{\mathrm{d}v_x}{\mathrm{d}z}. \tag{4.83}$$

Written in this form each wave equation separates the upward and downward travelling waves. Note that although we drive only V_z on the upper boundary, this in turn drives the right-hand side of the wave equation for v_x. At the mode-conversion layer we have $v_A = \sqrt{\gamma\beta_0/2}c_s$ and there is a resonance between the downward propagating waves. This is what allows energy to transfer from one wave mode to another.

Expanding about the mode-conversion region by setting $z = 0 + \xi + \ldots$ we have $\mathrm{d}/\mathrm{d}z = \mathrm{d}/\mathrm{d}\xi$. Then taking a linear expansion of Λ we have

$$\Lambda \approx a + bd\xi, \tag{4.84}$$

so

$$p_0 = (a + bd\xi)^{-1/bd}. \tag{4.85}$$

Note that letting $a \to 1$ and $b \to 0$ and using the limit definition of the exponential function ($e^x = \lim_{n\to\infty}(1 + x/n)^n$) we return to the isothermal case.

This means that

$$\frac{\gamma\beta_0}{2} = a^{-1/bd}, \tag{4.86}$$

and we may write

$$\frac{1}{v_A} \approx \sqrt{\frac{2}{\gamma\beta_0}}\frac{1}{c_s}\left(1 - \frac{\xi}{2a}\right). \tag{4.87}$$

For the waves travelling upwards, away from the mode-conversion region, we may simply set $\mathrm{d}/\mathrm{d}z = i\sqrt{2/\gamma\beta_0}\omega/c_s$. Equations (4.82) and (4.83) then become

$$\frac{\mathrm{d}v_x}{\mathrm{d}\xi} - i\left(\sqrt{\frac{2}{\gamma\beta_0}}\frac{\omega}{c_s} - \sqrt{\frac{2}{\gamma\beta_0}}\frac{\omega}{2ac_s}\xi\right) v_x = \frac{ik_x}{2} V_z, \tag{4.88}$$

$$\frac{\mathrm{d}V_z}{\mathrm{d}\xi} - i\sqrt{\frac{2}{\gamma\beta_0}}\frac{\omega}{c_s}V_z = \frac{ik_x}{2}v_x. \tag{4.89}$$

Equations (4.88) and (4.89) may be shown to satisfy energy conservation. If we multiply Equation (4.88) by its complex conjugate to give

$$\bar{v}_x\frac{\mathrm{d}v_x}{\mathrm{d}\xi} - i\left(\sqrt{\frac{2}{\gamma\beta_0}}\frac{\omega}{c_s} - \sqrt{\frac{2}{\gamma\beta_0}}\frac{\omega}{2ac_s}\xi\right)\bar{v}_x v_x = \frac{ik_x}{2}\bar{v}_x V_z, \tag{4.90}$$

and taking its complex conjugate

$$v_x\frac{\mathrm{d}\bar{v}_x}{\mathrm{d}\xi} + i\left(\sqrt{\frac{2}{\gamma\beta_0}}\frac{\omega}{c_s} - \sqrt{\frac{2}{\gamma\beta_0}}\frac{\omega}{2ac_s}\xi\right)v_x\bar{v}_x = -\frac{ik_x}{2}v_x\bar{V}_z. \tag{4.91}$$

Adding these together gives

$$\frac{\mathrm{d}}{\mathrm{d}\xi}\left(|v_x|^2\right) = \frac{ik_x}{2}\left(\bar{v}_x V_z - v_x\bar{V}_z\right). \tag{4.92}$$

The same process may be performed on Equation (4.89) giving

$$\bar{V}_z\frac{\mathrm{d}V_z}{\mathrm{d}\xi} - i\sqrt{\frac{2}{\gamma\beta_0}}\frac{\omega}{c_s}\bar{V}_z V_z = \frac{ik_x}{2}\bar{V}_z v_x, \tag{4.93}$$

and

$$V_z\frac{\mathrm{d}\bar{V}_z}{\mathrm{d}\xi} + i\sqrt{\frac{2}{\gamma\beta_0}}\frac{\omega}{c_s}V_z\bar{V}_z = -\frac{ik_x}{2}V_z\bar{v}_x, \tag{4.94}$$

which may be added to give

$$\frac{\mathrm{d}}{\mathrm{d}\xi}\left(|V_z|^2\right) = \frac{ik_x}{2}\left(\bar{V}_z v_x - V_z\bar{v}_x\right). \tag{4.95}$$

Taking Equation (4.92) and adding it to Equation (4.95) we obtain

$$\frac{\mathrm{d}}{\mathrm{d}\xi}\left(|v_x|^2 + |V_z|^2\right) = 0, \tag{4.96}$$

and so we see that energy is indeed conserved.

Looking back to Equations (4.88) and (4.89) v_x may be eliminated to give a second-order differential equation for V_z

$$\frac{\mathrm{d}^2V_z}{\mathrm{d}\xi^2} + i\sqrt{\frac{2}{\gamma\beta_0}}\frac{\omega}{c_s}\left(\frac{\xi}{2a} - 2\right)\frac{\mathrm{d}V_z}{\mathrm{d}\xi} + \left(\frac{2\omega^2}{\gamma\beta_0 c_s^2}\left(\frac{\xi}{2a} - 1\right) + \frac{k_x^2}{4}\right)V_z = 0. \tag{4.97}$$

To eliminate the first derivative term we make the substitution

$$V_z(\xi) = \exp\left(-i\sqrt{\frac{2}{\gamma\beta_0}}\frac{\omega}{2}\int\frac{1}{c_s}\left(\frac{\xi}{2a} - 2\right)\mathrm{d}\xi\right)\psi(\xi), \tag{4.98}$$

treating the sound speed as constant at the mode-conversion region, this gives

$$\frac{\mathrm{d}^2\psi}{\mathrm{d}\xi^2} + \left(\frac{2\omega^2}{16a^2\gamma\beta_0 c_s^2}\xi^2 - i\sqrt{\frac{2}{\gamma\beta_0}}\frac{\omega}{4ac_s} + \frac{k_x^2}{4}\right)\psi = 0. \tag{4.99}$$

Making a second substitution

$$\zeta = \left(\sqrt{\frac{2}{\gamma\beta_0}}\frac{\omega}{2ac_s}\right)^{1/2} e^{3i\pi/4}\xi, \tag{4.100}$$

the second-order differential equation may be written

$$\frac{\mathrm{d}^2\psi}{\mathrm{d}\zeta^2} - \left(\frac{\zeta^2}{4} - \frac{1}{2} - i\sqrt{\frac{\gamma\beta_0}{2}}\frac{k_x^2 ac_s}{2\omega}\right)\psi = 0. \tag{4.101}$$

The advantage to writing the equation in this form is that the solution is known in terms of the Parabolic Cylinder function $U\left(f,\,\zeta\right)$, where

$$f = -\frac{1}{2} - i\sqrt{\frac{\gamma\beta_0}{2}}\frac{k_x^2 ac_s}{2\omega}. \tag{4.102}$$

A full description of these functions and their behaviour may be found in Abramowitz and Stegun (1964).

On comparison with the results in Cairns and Lashmore-Davies (1983) we may write down the asymptotic behaviour in the low-β plasma ($\xi > 0$)

$$\begin{aligned} V_z \sim \left(\sqrt{\frac{2}{\gamma\beta_0}}\frac{\omega}{2ac_s}\right)^{i\sqrt{\gamma\beta_0/2}k_x^2 ac_s/(4\omega)} \exp\left(\sqrt{\frac{\gamma\beta_0}{2}}\frac{\pi k_x^2 ac_s}{8\omega}\right)\xi^{i\sqrt{\gamma\beta_0/2}k_x^2 ac_s/(2\omega)} \times \\ \times \exp\left(i\sqrt{\frac{2}{\gamma\beta_0}}\frac{\omega}{c_s}\xi\right), \end{aligned} \tag{4.103}$$

and in the high-β plasma ($\xi < 0$)

$$\begin{aligned} V_z \sim \left(\sqrt{\frac{2}{\gamma\beta_0}}\frac{\omega}{2ac_s}\right)^{i\sqrt{\gamma\beta_0/2}k_x^2 ac_s/(4\omega)} \exp\left(-\sqrt{\frac{\gamma\beta_0}{2}}\frac{3\pi k_x^2 ac_s}{8\omega}\right)|\xi|^{i\sqrt{\gamma\beta_0/2}k_x^2 ac_s/(2\omega)} \times \\ \times \exp\left(i\sqrt{\frac{2}{\gamma\beta_0}}\frac{\omega}{c_s}\xi\right) - \frac{(2\pi)^{1/2}}{\Gamma\left(-i\sqrt{\frac{\gamma\beta_0}{2}}\frac{k_x^2 ac_s}{2\omega}\right)}\exp\left(-\sqrt{\frac{\gamma\beta_0}{2}}\frac{\pi k_x^2 ac_s}{8\omega}\right) \times \\ \times \left(\sqrt{\frac{2}{\gamma\beta_0}}\frac{\omega}{2ac_s}\right)^{-\left(i\sqrt{\gamma\beta_0/2}k_x^2 ac_s/(4\omega)\right)-1/2} |\xi|^{-\left(i\sqrt{\gamma\beta_0/2}k_x^2 ac_s/(2\omega)\right)-1} \times \\ \times \exp\left(i\sqrt{\frac{2}{\gamma\beta_0}}\frac{\omega}{c_s}\xi - i\sqrt{\frac{\gamma\beta_0}{2}}\frac{\omega}{4ac_s}\xi^2 - \frac{3i\pi}{4}\right). \end{aligned} \tag{4.104}$$

To find an expression for the transmission and conversion coefficients from these equations we use the WKB method. Assuming that v_x is small in comparison to V_z will give us information about the transmitted wave. So we set

$$v_x = \frac{V_{x0}}{\omega}\exp\left(\omega\phi_0 + \frac{\phi_1}{\omega}\right), \tag{4.105}$$

$$V_z = B\exp\left(\omega\phi_0 + \frac{\phi_1}{\omega}\right), \tag{4.106}$$

where $\omega\phi_0 \gg \phi_1/\omega,\ V_{x0}/\omega$. Substituting these into Equations (4.88) and (4.89) we find

$$\left(\phi_0' - i\sqrt{\frac{2}{\gamma\beta_0}}\frac{1}{c_s}\left(1-\frac{\xi}{2a}\right)\right)V_{x0} + \frac{V_{x0}'}{\omega} + \frac{V_{x0}}{\omega}\phi_1' = \frac{ik_x}{2}B, \tag{4.107}$$

$$\omega\left(\phi_0' B - i\sqrt{\frac{2}{\gamma\beta_0}}\frac{B}{c_s}\right) + \frac{\phi_1'}{\omega}B = \frac{ik_x}{2}\frac{V_{x0}}{\omega}. \tag{4.108}$$

Equating the various powers of ω we find

$$\phi_0 = \frac{i}{c_s}\sqrt{\frac{2}{\gamma\beta_0}}\xi, \quad V_{x0} = \sqrt{\frac{\gamma\beta_0}{2}}\frac{k_x a c_s}{\xi}B, \quad \phi_1 = i\sqrt{\frac{\gamma\beta_0}{2}}\frac{k_x^2 a c_s}{2}\ln\xi, \tag{4.109}$$

where c_s has been treated as a constant. This assumption is valid as we are only concerned with the mode-conversion region at $z = 0$ where $c_s = \sqrt{0.55}$. These give the transmitted component as

$$V_z = B\xi^{i\sqrt{\gamma\beta/2}k_x^2 a c_s/(2\omega)}\exp\left(i\sqrt{\frac{\gamma\beta_0}{2}}\frac{\omega}{c_s}\xi\right). \tag{4.110}$$

To find an expression for the converted component of V_z we follow the same process, this time assuming that V_z is small in comparison to v_x

$$v_x = A\exp\left(\omega\phi_0 + \frac{\phi_1}{\omega}\right), \tag{4.111}$$

$$V_z = \frac{V_{z0}}{\omega}\exp\left(\omega\phi_0 + \frac{\phi_1}{\omega}\right), \tag{4.112}$$

where $\omega\phi_0 \gg \phi_1/\omega,\ V_{z0}/\omega$. Substituting these into Equations (4.88) and (4.89) yields

$$\omega\left(\phi_0' A - i\sqrt{\frac{2}{\gamma\beta_0}}\frac{A}{c_s}\left(1-\frac{\xi}{2a}\right)\right) + \frac{\phi_1'}{\omega}A = \frac{ik_x}{2\omega}V_{z0}. \tag{4.113}$$

Equating powers of ω we find

$$\phi_0 = \frac{i}{c_s}\sqrt{\frac{2}{\gamma\beta_0}}\left(\xi - \frac{\xi^2}{4a}\right), \quad V_{z0} = -\sqrt{\frac{\gamma\beta_0}{2}}\frac{k_x a c_s}{\xi}A, \quad \phi_1 = -i\sqrt{\frac{\gamma\beta_0}{2}}\frac{k_x^2 a c_s}{2}\ln\xi, \tag{4.114}$$

where c_s has again been assumed constant. The converted component is then

$$V_z = -\sqrt{\frac{\gamma\beta_0}{2}}\frac{k_x a c_s}{\omega}A\xi^{-\left(i\sqrt{\gamma\beta_0/2}k_x^2 a c_s/(2\omega)\right)-1}\exp\left(i\sqrt{\frac{2}{\gamma\beta_0}}\frac{\omega}{c_s}\left(\xi - \frac{\xi^2}{4a}\right)\right). \tag{4.115}$$

Equations (4.110) and (4.115) may be added together to give

$$V_z \sim B\xi^{i\sqrt{\gamma\beta_0/2}k_x^2 ac_s/(2\omega)} \exp\left(i\sqrt{\frac{2}{\gamma\beta_0}}\frac{\omega}{c_s}\xi\right) -$$

$$-\sqrt{\frac{\gamma\beta_0}{2}}\frac{k_x a c_s}{\omega} A\xi^{-\left(i\sqrt{\gamma\beta_0/2}k_x^2 ac_s/(2\omega)\right)-1} \exp\left(i\sqrt{\frac{2}{\gamma\beta_0}}\frac{\omega}{c_s}\left(\xi - \frac{\xi^2}{4a}\right)\right). \tag{4.116}$$

Comparing this to Equations (4.103) and (4.104) we may deduce the values of the conversion and transmission coefficients, A and B. Dividing the high-β equation by the low-β equation and comparing the result to Equation (4.116) gives

$$B = \exp\left(-\sqrt{\frac{\gamma\beta_0}{2}}\frac{\pi k_x^2 ac_s}{2\omega}\right), \tag{4.117}$$

$$A = \frac{2\,(2\pi)^{1/2}}{k_x \Gamma\left(-i\sqrt{\frac{\gamma\beta_0}{2}}\frac{k_x^2 ac_s}{2\omega}\right)}\left(\sqrt{\frac{2}{\gamma\beta_0}}\frac{\omega}{2ac_s}\right)^{1/2} \exp\left(-\sqrt{\frac{\gamma\beta_0}{2}}\frac{\pi k_x^2 ac_s}{4\omega}\right), \tag{4.118}$$

where imaginary terms have been neglected as these influence only the phase, not the amplitude. Noting that

$$|\Gamma\,(iy)|^2 = |\Gamma\,(-iy)|^2 = \frac{\pi}{y \sinh(\pi y)}, \tag{4.119}$$

(Gradshteyn and Ryzhik, 1981) the conversion coefficient simplifies to

$$A = \sqrt{1 - \exp\left(-\sqrt{\frac{\gamma\beta_0}{2}}\frac{\pi k_x^2 ac_s}{\omega}\right)}. \tag{4.120}$$

Equations (4.117) and (4.120) tell us what proportion of the incident wave we would expect to be transmitted and converted across the mode-conversion region. Substituting these coefficients back into Equation (4.116) we have a description of the vertical velocity across the domain. This is shown in Figure 4.10 for $\omega = 4\pi\sqrt{6}\sqrt{\gamma\beta_0/2}$ and $k_x = \pi$. Overplotted on this figure is the amplitude we would expect to see for the incident wave once the amplitude dependence is removed, and to the left of the red dashed line the amplitude predicted for the transmitted wave by Equation (4.117). We may compare this result to the numerical simulations by taking the ratio of the transmitted wave to the incident wave for various values of k_x. The results of this are shown in Figure (4.11).

In Figure 4.11 we can see excellent agreement between the analytical prediction for the transmission (solid line) and the numerical simulations (stars). As for the isothermal case this is true even as the horizontal wavenumber becomes large, violating the assumptions. When taking the logarithm of the amplitude ratio (shown on the right-hand side) the numerical results can be seen to deviate away from the numerical prediction as k_x becomes large. However this deviation is small, and Equation (4.117) gives an excellent prediction for the amount of transmission. It is more difficult to make a direct comparison for the conversion coefficient due to the interference of the fast wave. It is easily shown that $A^2 + B^2 = 1$ however, and so we can also have confidence in the values predicted from Equation (4.120).

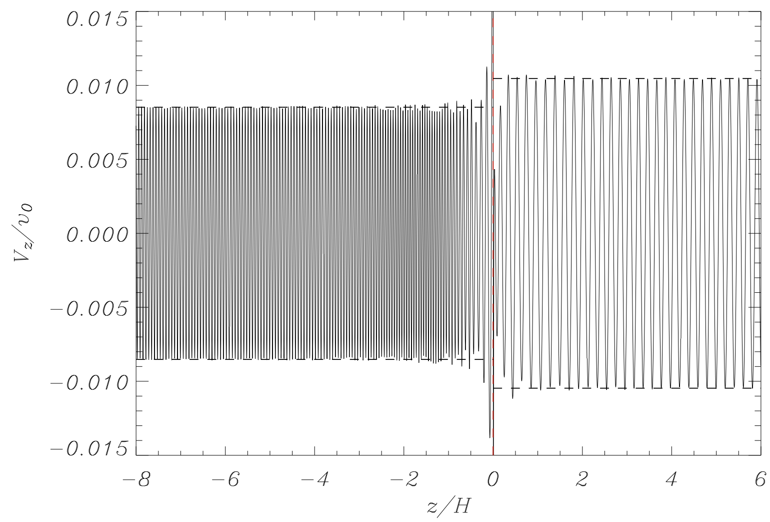

Figure 4.10: Vertical velocity as predicted by Equation (4.116) with $\omega = 4\pi\sqrt{6}\sqrt{\gamma\beta_0/2}$ and $k_x = \pi$. The vertical red dashed line denotes where $c_s = v_A$; the horizontal dashed lines to the right of this show the predicted amplitude of the incident wave, and those to the left the predicted amplitude of the transmitted wave.

The transmission and conversion coefficients are dependent on both the horizontal wavenumber (k_x) and the driving frequency (ω). Their variation with these parameters is shown in Figure 4.12. As for the isothermal case the amount of conversion increases with increasing k_x, and decreases with increasing ω; hence the transmission will decrease or increase respectively. This result is in agreement with Section 4.3.2 and we can see that the variation with the horizontal wavenumber is the stronger effect.

Looking back to the transmission and conversion coefficients found in the isothermal case, Equations (3.86) and (3.89), we can see that the inclusion of a non-isothermal temperature profile has no effect as long as reflection effects may be neglected. To retrieve the isothermal results we simply need to set $a = 1$ and $b = 0$ in the expression for Λ and take $\gamma\beta_0/2 = 1$. In the more general form that we have here in Equations (4.117) and (4.120) the transmission and conversion coefficients may be found for any temperature profile.

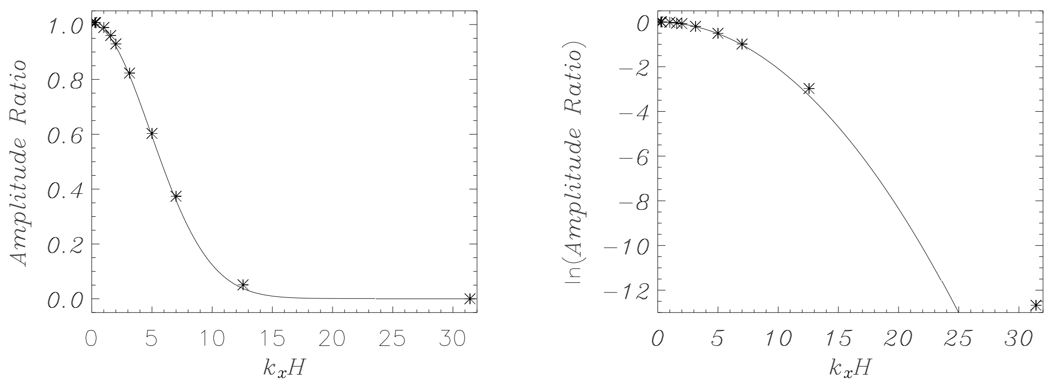

Figure 4.11: *Left:* Ratio of the transmitted and incident wave amplitudes.
Right: Logarithm of the ratio of the transmitted and incident wave amplitudes.
In both cases $\omega = 4\pi\sqrt{6}\sqrt{\gamma\beta_0/2}$ and the solid line is that predicted by Equation (4.117) and the stars are the values calculated from the numerical data.

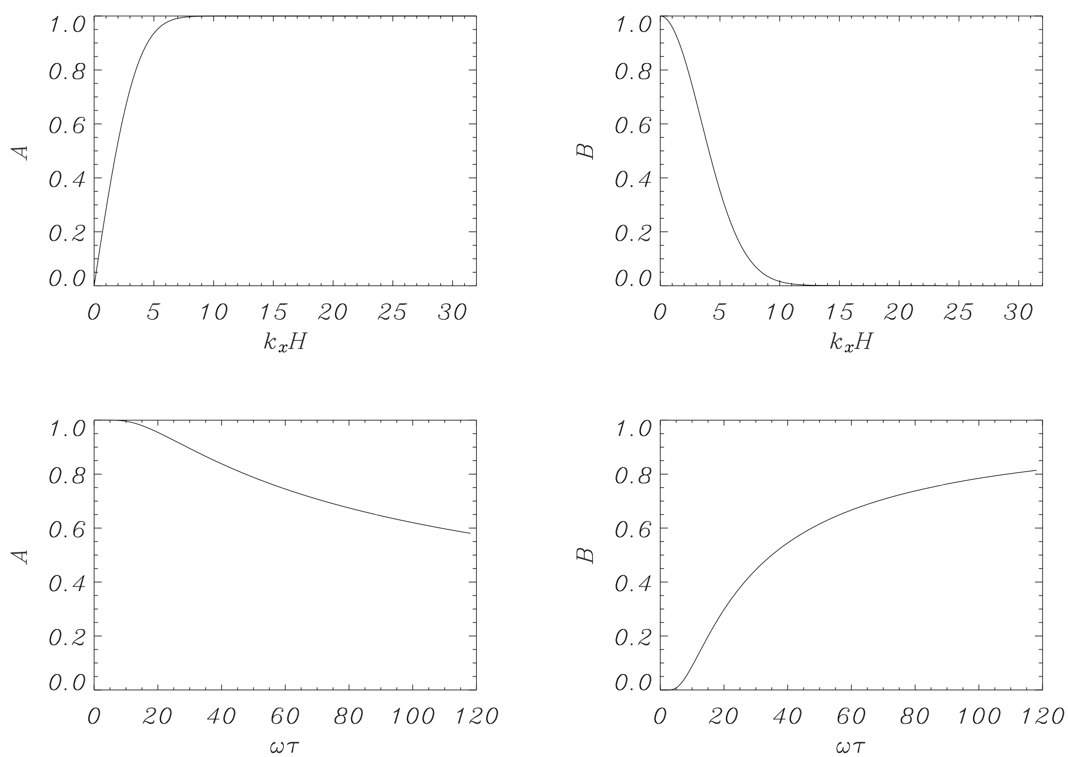

Figure 4.12: *Top Left:* The variation of A with k_x for $\omega = 2\pi\sqrt{6}\sqrt{\gamma\beta_0/2}$.
Top Right: The variation of B with k_x for $\omega = 2\pi\sqrt{6}\sqrt{\gamma\beta_0/2}$.
Bottom Left: The variation of A with ω for $k_x = \pi$.
Bottom Right: The variation of B with ω for $k_x = \pi$.

4.4.2 WKB Analysis away from the Conversion Region

The small k_x approximation gives the wave behaviour at the mode-conversion region. To study the behaviour away from this region we use the WKB method. This works under the assumption that ω is large, and will give the amplitude dependence and phase in both the high- and low-β plasma.

We begin with the wave equations (4.58) and (4.59) with $\partial/\partial t = i\omega$

$$\left(v_A^2\frac{\partial^2}{\partial z^2} - \left(\frac{\gamma\beta_0}{2}c_s^2 + v_A^2\right)k_x^2 + \omega^2\right)v_x = \frac{\gamma\beta_0}{2}k_x\left(c_s^2\frac{\partial}{\partial z} - \frac{1}{\gamma}\right)v_z, \tag{4.121}$$

$$\left(\frac{\gamma\beta_0}{2}c_s^2\frac{\partial^2}{\partial z^2} - \frac{\gamma\beta_0}{2}\frac{\partial}{\partial z} + \omega^2\right)v_z = -\frac{\gamma\beta_0}{2}k_x\left(c_s^2\frac{\partial}{\partial z} - \frac{1}{\gamma}(\gamma-1)\right)v_x. \tag{4.122}$$

Assuming that $\omega \gg k_x c_s$ we may expand the horizontal and vertical velocities, v_x and v_z, in inverse powers of ω. In order to find equations describing the incident and transmitted waves we make the assumption that v_x is small in comparison to v_z.

$$v_x = \frac{V_{x0}}{\omega}\exp\left(\omega\phi_0 + \phi_1 + \frac{\phi_2}{\omega}\right), \tag{4.123}$$

$$v_z = \exp\left(\omega\phi_0 + \phi_1 + \frac{\phi_2}{\omega}\right), \tag{4.124}$$

where $\omega\phi_0 \gg \phi_1 \gg \phi_2/\omega,\ V_{x0}/\omega$.

Substituting these into the wave equations we obtain

$$\begin{aligned}
&\omega\left(V_{x0}\left(\phi_0'\right)^2 v_A^2 + V_{x0}\right) + v_A^2\left(2V_{x0}'\phi_0' + V_{x0}\phi_0'' + 2V_{x0}\phi_0'\phi_1'\right) + \\
&+\frac{1}{\omega}\left(v_A^2V_{x0}'' + 2v_A^2V_{x0}'\phi_1' + v_A^2V_{x0}\phi_1'' + 2v_A^2V_{x0}\phi_0'\phi_2' + v_A^2V_{x0}\left(\phi_1'\right)^2 - \right.\\
&\left.-\left(\frac{\gamma\beta_0}{2}c_s^2 + v_A^2\right)k_x^2V_{x0}\right) = \omega\frac{\gamma\beta_0}{2}k_xc_s^2\phi_0' + \left(\frac{\gamma\beta_0}{2}k_xc_s^2\phi_1' - \frac{\beta_0}{2}k_x\right) + \\
&\qquad +\frac{1}{\omega}\frac{\gamma\beta_0}{2}k_xc_s^2\phi_2' + \mathcal{O}\left(\frac{1}{\omega^2}\right),
\end{aligned} \tag{4.125}$$

and

$$\begin{aligned}
&\omega^2\left(\frac{\gamma\beta_0}{2}c_s^2\left(\phi_0'\right)^2 + 1\right) + \omega\left(\frac{\gamma\beta_0}{2}c_s^2\left(\phi_0'' + 2\phi_0'\phi_1'\right) - \frac{\gamma\beta_0}{2}\phi_0'\right) + \\
&+\left(\frac{\gamma\beta_0}{2}c_s^2\left(\phi_1'' + 2\phi_0'\phi_2' + \left(\phi_1'\right)^2\right) - \frac{\gamma\beta_0}{2}\phi_1'\right) = -\frac{\gamma\beta_0}{2}k_xc_s^2V_{x0}\phi_0' + \mathcal{O}\left(\frac{1}{\omega}\right),
\end{aligned} \tag{4.126}$$

where $' = \mathrm{d}/\mathrm{d}z$.

From the $\mathcal{O}\left(\omega^2\right)$ terms we find

$$\phi_0' = i\sqrt{\frac{2}{\gamma\beta_0}}\frac{1}{c_s}, \tag{4.127}$$

so

$$\phi_0 = i\sqrt{\frac{2}{\gamma\beta_0}}\int\frac{\mathrm{d}z}{c_s}, \qquad \phi_0'' = -i\sqrt{\frac{2}{\gamma\beta_0}}\frac{c_s'}{c_s^2}. \tag{4.128}$$

Substituting these values back into the $\mathcal{O}(\omega)$ terms we find

$$V_{x0} = -ik_x\left(\frac{\gamma\beta_0}{2}\right)^{3/2}\frac{c_s^3}{(v_A^2-\gamma\beta_0/2c_s^2)}, \tag{4.129}$$

and

$$\phi_1 = \ln\left|\frac{\Lambda^{1/4}}{p_0^{1/2}}\right|. \tag{4.130}$$

These may then be substituted into the $\mathcal{O}(1)$ equations giving

$$\phi_2' = i\frac{k_x^2}{2}\left(\frac{\gamma\beta_0}{2}\right)^{3/2}\frac{c_s^3}{(v_A^2-\gamma\beta_0/2c_s^2)} + \frac{i}{4}\sqrt{\frac{\gamma\beta_0}{2}}c_s'' - \frac{i}{8}\sqrt{\frac{\gamma\beta_0}{2}}\frac{1}{c_s^3} - \frac{i}{8}\sqrt{\frac{\gamma\beta_0}{2}}\left(\frac{c_s'}{c_s}\right)^2 - \\ -\frac{i}{2}\sqrt{\frac{\gamma\beta_0}{2}}\frac{c_s'}{c_s^2}, \tag{4.131}$$

but due to the fact that c_s is dependent on z this is very messy to integrate analytically. It is possible, however, to solve for this value numerically using a fourth order Runge-Kutta scheme.

Returning to Equations (4.123) and (4.124) we have

$$v_x = -ik_x\left(\frac{\gamma\beta_0}{2}\right)^{3/2}\frac{c_s^3}{\omega\,(v_A^2-\gamma\beta_0/2c_s^2)}\exp\left(i\omega\sqrt{\frac{2}{\gamma\beta_0}}\int\frac{\mathrm{d}z}{\Lambda^{1/2}} + \ln\left|\frac{\Lambda^{1/4}}{p_0^{1/2}}\right| + \frac{\phi_2}{\omega}\right), \tag{4.132}$$

$$v_z = \exp\left(i\omega\sqrt{\frac{2}{\gamma\beta_0}}\int\frac{\mathrm{d}z}{\Lambda^{1/2}} + \ln\left|\frac{\Lambda^{1/4}}{p_0^{1/2}}\right| + \frac{\phi_2}{\omega}\right), \tag{4.133}$$

which may alternatively be written in trigonometric form as

$$v_x = -k_x\left(\frac{\gamma\beta_0}{2}\right)^{3/2}\frac{c_s^3\Lambda^{1/4}}{\omega\,(v_A^2-\gamma\beta_0/2c_s^2)\,p_0^{1/2}}\cos\left(\omega\sqrt{\frac{2}{\gamma\beta_0}}\int\frac{\mathrm{d}z}{\Lambda^{1/2}} + \frac{\phi_2}{\omega}\right), \tag{4.134}$$

$$v_z = \frac{\Lambda^{1/4}}{p_0^{1/2}}\sin\left(\omega\sqrt{\frac{2}{\gamma\beta_0}}\int\frac{\mathrm{d}z}{\Lambda^{1/2}} + \frac{\phi_2}{\omega}\right). \tag{4.135}$$

Equations (4.134) and (4.135) represent the incident wave in the low-β plasma and the transmitted wave in the high-β plasma. The transmitted wave will be multiplied by a constant, which may be calculated from Equation (4.117), telling us the proportion of the incident wave that has passed into the high-β plasma.

It then remains to find equations describing the converted wave. To do this we assume that v_z is small in comparison to v_x by setting

$$v_x = \exp\left(\omega\phi_0 + \phi_1 + \frac{\phi_2}{\omega}\right), \tag{4.136}$$

$$v_z = \frac{V_{z0}}{\omega}\exp\left(\omega\phi_0 + \phi_1 + \frac{\phi_2}{\omega}\right), \tag{4.137}$$

where, as before, $\omega\phi_0 \gg \phi_1 \gg \phi_2/\omega,\ V_{z0}/\omega$. On substitution into Equations (4.58) and (4.59) we find

$$\begin{aligned}\omega^2\left(v_A^2\left(\phi_0'\right)^2+1\right)+\omega v_A^2\left(\phi_0''+2\phi_0'\phi_1'\right)+\Big(v_A^2\phi_1''+2v_A^2\phi_0'\phi_2'+v_A^2\left(\phi_1'\right)^2-\\-\left(\frac{\gamma\beta_0}{2}c_s^2+v_A^2\right)k_x^2\Big)=\frac{\gamma\beta_0}{2}k_xc_s^2V_{z0}\phi_0'+\mathcal{O}\left(\frac{1}{\omega}\right),\end{aligned} \tag{4.138}$$

and

$$\begin{aligned}\omega\left(\frac{\gamma\beta_0}{2}c_s^2V_{z0}\left(\phi_0'\right)^2+V_{z0}\right)+\left(\frac{\gamma\beta_0}{2}c_s^2\left(2V_{z0}'\phi_0'+V_{z0}\phi_0''+2V_{z0}\phi_0'\phi_1'\right)-\frac{\gamma\beta_0}{2}V_{z0}\phi_0'\right)=\\=-\frac{\gamma\beta_0}{2}k_xc_s^2\omega\phi_0'+\frac{\gamma\beta_0}{2}k_x\left(\frac{1}{\gamma}\left(\gamma-1\right)-c_s^2\phi_1'\right)+\mathcal{O}\left(\frac{1}{\omega}\right).\end{aligned} \tag{4.139}$$

The $\mathcal{O}\left(\omega^2\right)$ terms give

$$\phi_0' = \frac{i}{v_A}, \tag{4.140}$$

which may be solved to give

$$\phi_0 = i\int\frac{\mathrm{d}z}{v_A}, \quad \phi_0'' = -i\frac{v_A'}{v_A^2}. \tag{4.141}$$

Substituting these values into the $\mathcal{O}\left(\omega\right)$ equations we find

$$V_{z0} = -ik_x\frac{\gamma\beta_0}{2}\frac{c_s^2v_A}{\left(v_A^2-\gamma\beta_0/2c_s^2\right)}, \tag{4.142}$$

and

$$\phi_1 = \frac{1}{2}\ln\left|v_A\right|. \tag{4.143}$$

Finally to find a value for ϕ_2 we turn to the $\mathcal{O}\left(1\right)$ equations.

$$\phi_2' = -i\frac{k_x^2}{2v_A}\left(\frac{\gamma\beta_0}{2}\right)^2\frac{c_s^4}{\left(v_A^2-\gamma\beta_0c_s^2/2\right)}-i\frac{k_x^2}{2v_A}\left(\frac{\gamma\beta_0}{2}c_s^2+v_A^2\right)+\frac{i}{4}v_A''-\frac{i}{8}\frac{\left(v_A'\right)^2}{v_A}. \tag{4.144}$$

Again, this is not easy to solve analytically but may be found numerically using a fourth order Runge-Kutta scheme.

Putting these values back into Equations (4.136) and (4.137) we find

$$v_x = v_A^{1/2} \exp\left(i\omega \int \frac{\mathrm{d}z}{v_A} + \frac{\phi_2}{\omega}\right), \tag{4.145}$$

$$v_z = -ik_x \frac{\gamma\beta_0}{2} \frac{c_s^2 v_A^{3/2}}{\omega\left(v_A^2 - \gamma\beta_0 c_s^2/2\right)} \exp\left(i\omega \int \frac{\mathrm{d}z}{v_A} + \frac{\phi_2}{\omega}\right). \tag{4.146}$$

These may also be written

$$v_x = v_A^{1/2} \cos\left(\omega \int \frac{\mathrm{d}z}{v_A} + \frac{\phi_2}{\omega}\right), \tag{4.147}$$

$$v_z = -k_x \frac{\gamma\beta_0}{2} \frac{c_s^2 v_A^{3/2}}{\omega\left(v_A^2 - \gamma\beta_0 c_s^2/2\right)} \sin\left(\omega \int \frac{\mathrm{d}z}{v_A} + \frac{\phi_2}{\omega}\right). \tag{4.148}$$

Equations (4.147) and (4.148) describe the converted slow wave in the high-β plasma. These equations need to be multiplied by a constant, given by Equation (4.120), which describes the proportion of the incident wave which is converted. In the low-β plasma these equations will be zero as the fast wave is evanescent in that region.

In summary we have

$$\begin{aligned}
\text{Low } \beta\text{:} \quad \text{Inc.} \quad & v_x = -\alpha k_x \left(\frac{\gamma\beta_0}{2}\right)^{3/2} \frac{c_s^3 \Lambda^{1/4}}{\omega\left(v_A^2 - \gamma\beta_0 c_s^2/2\right) p_0^{1/2}} \cos\left(\omega \sqrt{\frac{2}{\gamma\beta_0}} \int \frac{\mathrm{d}z}{\Lambda^{1/2}} + \frac{\phi_2}{\omega}\right), \\
& v_z = \alpha \frac{\Lambda^{1/4}}{p_0^{1/2}} \sin\left(\omega \sqrt{\frac{2}{\gamma\beta_0}} \int \frac{\mathrm{d}z}{\Lambda^{1/2}} + \frac{\phi_2}{\omega}\right), \\
\text{High } \beta\text{:} \quad \text{Trans.} \quad & v_x = -\alpha B k_x \left(\frac{\gamma\beta_0}{2}\right)^{3/2} \frac{c_s^3 \Lambda^{1/4}}{\omega\left(v_A^2 - \gamma\beta_0 c_s^2/2\right) p_0^{1/2}} \cos\left(\omega \sqrt{\frac{2}{\gamma\beta_0}} \int \frac{\mathrm{d}z}{\Lambda^{1/2}} + \frac{\phi_2}{\omega}\right), \\
& v_z = \alpha B \frac{\Lambda^{1/4}}{p_0^{1/2}} \sin\left(\omega \sqrt{\frac{2}{\gamma\beta_0}} \int \frac{\mathrm{d}z}{\Lambda^{1/2}} + \frac{\phi_2}{\omega}\right), \\
\text{Conv.} \quad & v_x = \alpha A v_A^{1/2} \cos\left(\omega \int \frac{\mathrm{d}z}{v_A} + \frac{\phi_2}{\omega}\right), \\
& v_z = -\alpha A k_x \frac{\gamma\beta_0}{2} \frac{c_s^2 v_A^{3/2}}{\omega\left(v_A^2 - \gamma\beta_0 c_s^2/2\right)} \sin\left(\omega \int \frac{\mathrm{d}z}{v_A} + \frac{\phi_2}{\omega}\right),
\end{aligned}$$

where A and B are as defined by Equations (4.120) and (4.117) and

$$\alpha = \left.\frac{p_0^{1/2}}{\Lambda^{1/4}}\right|_{z=z_m}. \tag{4.149}$$

From Equations (4.74) and (4.75) we know that at $t = 7.2$ Alfvén times the fast wave will have reached $z \approx -7.5$ and the slow wave will have reached $z \approx -1.6$. Using this information along with the above equations and the transmission and conversion coefficients calculated from Equations (4.117) and (4.120), we may create analytical predictions of how the horizontal and vertical velocity behave across the domain. The results of this are shown in Figure 4.13 which shows the numerical simulations alongside for com-

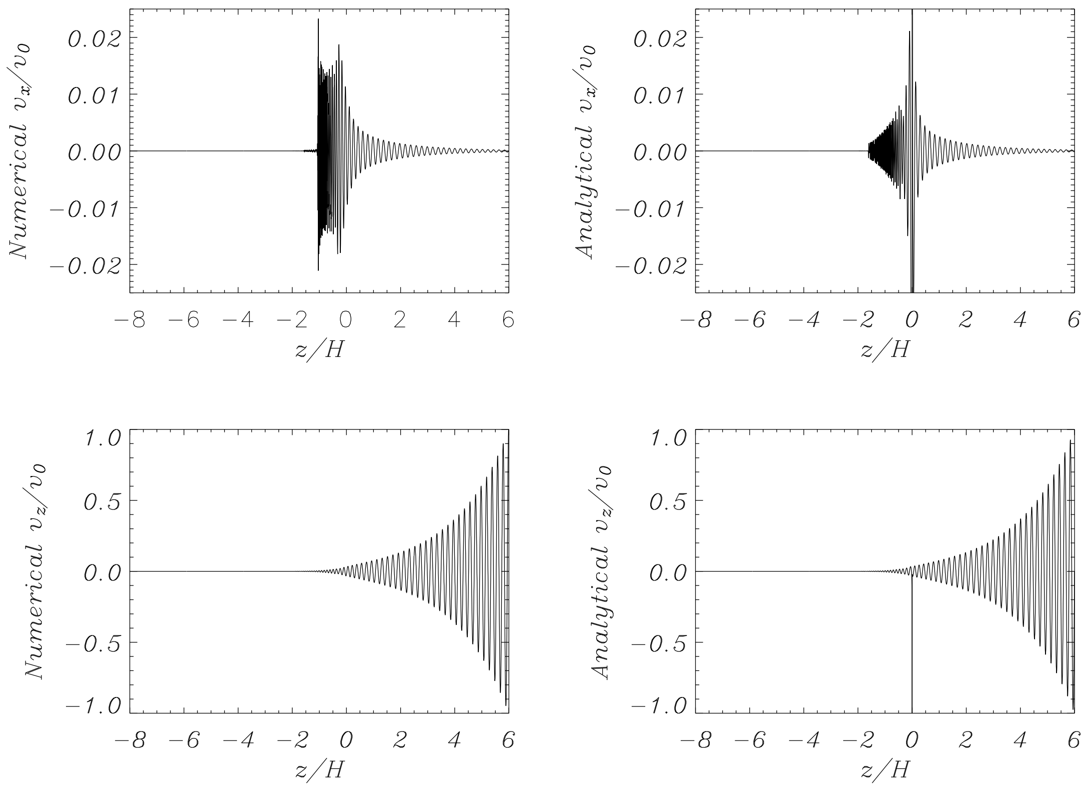

Figure 4.13: The numerical and analytical horizontal velocity and the numerical and analytical vertical velocity respectively from top left to bottom right. In all plots $\omega = 4\pi\sqrt{6}\sqrt{\gamma\beta_0/2}$, $k_x = \pi$ and $t = 7.2$ Alfvén times.

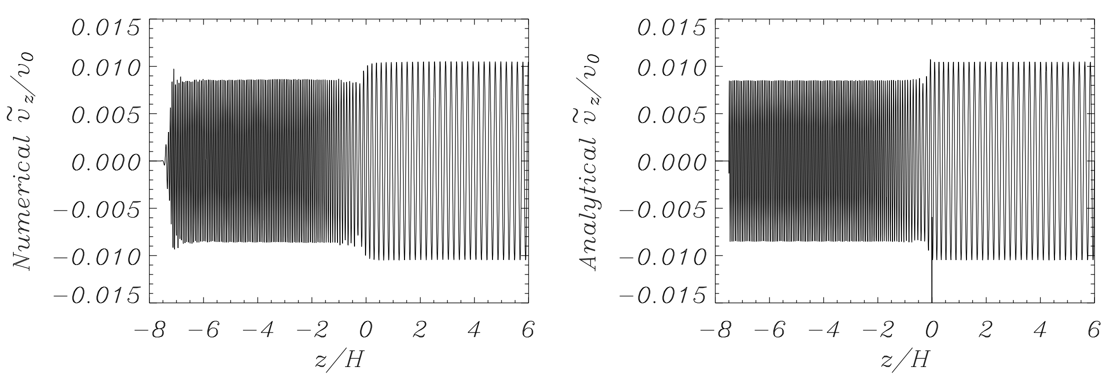

Figure 4.14: The numerical and analytical transformed vertical velocity for $\omega = 4\pi\sqrt{6}\sqrt{\gamma\beta_0/2}$, $k_x = \pi$ and $t = 7.2$ Alfvén times.

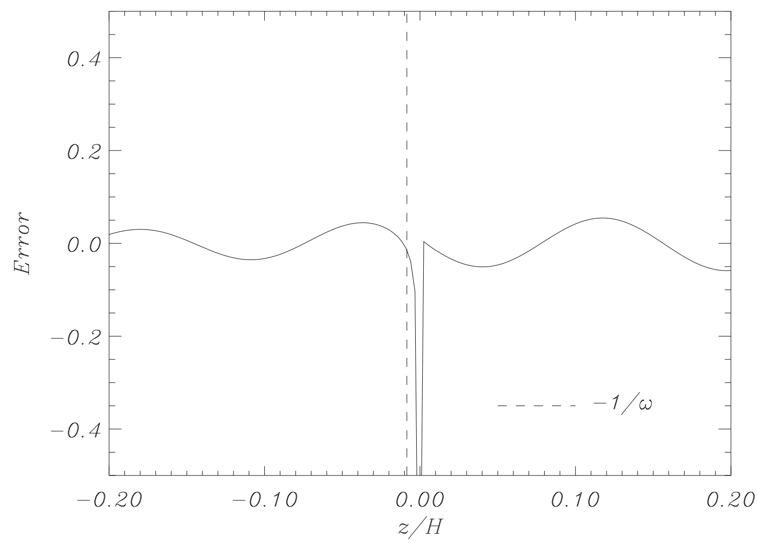

Figure 4.15: The absolute error between the results of the WKB analysis and the numerical simulations zoomed in around $z = 0$ (where $c_s = v_A$). The dashed line shows $z = -1/\omega$ demonstrating that the WKB analysis only breaks down very close to the conversion region.

parison. The analytical prediction for the converted wave does not quite capture the correct amplitude dependence, although the phase looks to be in good agreement. The predicted vertical velocity is in excellent agreement with the numerical simulations, which is even clearer when looking at the transformed vertical velocity shown in Figure 4.14. The analytical prediction has captured both the change in amplitude and phase across the mode-conversion region.

The analytical predictions do break down at $z = 0$ as there is a singularity in the equations for the incident and transmitted horizontal velocities, and the converted vertical velocity at this point. These terms are multiplied by a factor of $1/\omega$ and, as ω is assumed to be large, the singularity does not have a strong effect on the results. In fact looking at Figure 4.15, which shows the difference between the analytical and numerical velocities, we see that outwith $1/\omega$ of $z = 0$ the effects of the singularity are gone. So, using a combination of the Cairns and Lashmore-Davies method and the WKB method we have a good description of the wave behaviour across the domain.

4.5 Conclusions

In this chapter we have extended upon the model used in Chapter 3 by allowing for the inclusion of a temperature profile that varies with height. Apart from this the set-up remained the same as for the previous chapter, and so we examined the downward propagation of a slow magnetoacoustic wave through a gravitationally stratified atmosphere permeated by a uniform, vertical magnetic field (Figure 3.1). For the temperature a $\tanh$ profile was chosen as it reflects the steep gradient found at the transition region (Figure 4.1). To ensure that the model was sufficiently different from that of the previous chapter the $c_s = v_A$

layer, where mode conversion occurs, was placed in the centre of this gradient. Away from this region the temperature becomes constant and we would expect to find the same results as for the isothermal model. As demonstrated in Figure 4.2 the inclusion of a non-isothermal temperature profile complicates matters as both the sound and Alfvén speeds now vary with height.

This process was simulated numerically using a MacCormack finite difference scheme, the results of which are shown in Figure 4.3. As before the waves have a strong amplitude dependence that masks what is happening at the mode-conversion region. Using the WKB method we uncovered the nature of this amplitude dependence (Section 4.4.2) allowing it to be removed. The mode conversion is then much clearer (Figure 4.4). The plots of the vertical velocity, the pressure and the density all show a decrease in amplitude of the wave transmitted across the $c_s = v_A$ layer. The converted slow wave is visible in the plots of the horizontal velocity, and the horizontal and vertical magnetic field behind the transmitted fast wave. In Section 4.3.1 we calculated exactly how the positions of the various wavefronts vary with time, given by Equations (4.74) and (4.75), and shown in Figure 4.5. There were three free parameters in the numerical simulations: the slope d, the horizontal wavenumber k_x, and the driving frequency ω. In Section 4.3.2 we studied the effect of varying these model parameters. The steepness of the slope was found to have no effect on the conversion as long as the wavelength was sufficiently less than the width of the slope to avoid reflection. The effects of varying the wavenumber and the horizontal driving frequency were found to be the same as for the isothermal case. For a horizontal wavenumber of $k_x = 0$ there is no mode conversion and the incident wave is fully transmitted across the $c_s = v_A$ layer. As the value of k_x increases, the conversion increases and less of the incident wave is simply transmitted into the high-β plasma (Figure 4.8). Varying the frequency has the opposite effect; as the driving frequency increases the conversion decreases (Figure 4.9).

In Section 4.4 we used analytical techniques to derive transmission and conversion coefficients and to determine the wave behaviour throughout the domain. We began by looking at the method developed by Cairns and Lashmore-Davies (1983) which is valid for small k_x. This method is only valid at the mode-conversion region and uses the local dispersion relations to find differential equations describing the coupled mode amplitudes. This results in a solution given in terms of Parabolic Cylinder functions (see Abramowitz and Stegun (1964)) which are linked to the Meijer-G and Hypergeometric functions that have previously been used to describe mode conversion (Zhugzhda, 1979; Zhugzhda and Dzhalilov, 1982a; Cally, 2001). This method has the advantage that an exact analytical solution need not be known in order to determine the transmission and conversion coefficients, given by Equations (4.117) and (4.120) respectively. From these we can see that the dependence on k_x and ω is as we predicted in Section 4.3.2 and the effect of the horizontal wavenumber is dominant (Figure 4.12). In Figure 4.11 we can see that the agreement between the numerical simulations and the analytical prediction for the transmission is excellent. So good that no difference may be seen between the two without taking the logarithm of the amplitude ratio. In doing this we see that the prediction does deviate from the numerical solution as k_x becomes large.

A WKB analysis was used to find the wave behaviour in the low- and high-β plasma away from the conversion region. These solutions were then matched across the mode-conversion region using the transmission and conversion coefficients calculated in Section 4.4.1. As seen in Figure 4.13 the analytical predictions reproduce the results of the numerical simulations well. The amplitude dependence of the converted slow wave does not agree with the numerical simulation, and there is a small discrepancy at $z = 0$

where the WKB method breaks down. However this is only the case over a very small area, as shown in Figure 4.15. It is easier to see just how well the analytical and numerical simulations agree when the transformed vertical velocity is examined (Figure 4.14). Here we see that the WKB method has captured the phase and amplitude dependence excellently.

Having studied mode conversion in a non-isothermal atmosphere we have found that we obtain the same behaviour as in the isothermal case. In fact, we may return to this case simply by setting $\Lambda = 1$ and letting $\gamma\beta_0/2 = 1$. Thus the temperature profile itself does not effect the mode-conversion process. Next we shall investigate a more complex two-dimensional model with an expanding magnetic field, representative of a coronal hole.

Chapter 5

MHD Mode Conversion in a Coronal Hole

5.1 Introduction

As a starting point for investigating mode conversion in a two-dimensional model we look at a radially-expanding magnetic field. As with the previous chapters a combination of analytical and numerical techniques are used to capture the wave behaviour at the mode-conversion region and also in the rest of the domain. The same techniques are utilised as in Chapters 3 and 4, but these have been extended to cope with a two-dimensional problem.

5.2 Zero Gravity Model

The expanding field model is illustrated in Figure 5.1 and is representative of a coronal hole. Due to the geometry of the set up we use spherical coordinates, (r, θ, ϕ) - see Schey (2005). To reduce the problem to two dimensions all variables are assumed invariant in ϕ. Gravity is taken to be zero. A slow wave driven at the surface, located at $r = 1$, will propagate upwards passing from low- to high-β plasma as it does so. When it crosses the layer where the sound and Alfvén speeds are equal, indicated by the dashed line, the slow wave will undergo mode conversion. Some proportion of the incident wave will be transmitted into the high-β plasma as a fast wave and any remainder will be converted into a slow wave.

5.2.1 Ideal MHD Equations

We use the ideal form of the MHD equations

$$\rho\left(\frac{\partial}{\partial t}+\mathbf{v}\cdot\nabla\right)\mathbf{v}=-\nabla p+\frac{1}{\mu}\left(\nabla\times\mathbf{B}\right)\times\mathbf{B}, \tag{5.1}$$

$$\frac{\partial\rho}{\partial t}+\nabla\cdot\left(\rho\mathbf{v}\right)=0, \tag{5.2}$$

$$\frac{\partial\mathbf{B}}{\partial t}=\nabla\times\left(\mathbf{v}\times\mathbf{B}\right), \tag{5.3}$$

$$\left(\frac{\partial}{\partial t}+\mathbf{v}\cdot\nabla\right)p=\frac{\gamma p}{\rho}\left(\frac{\partial}{\partial t}+\mathbf{v}\cdot\nabla\right)\rho, \tag{5.4}$$

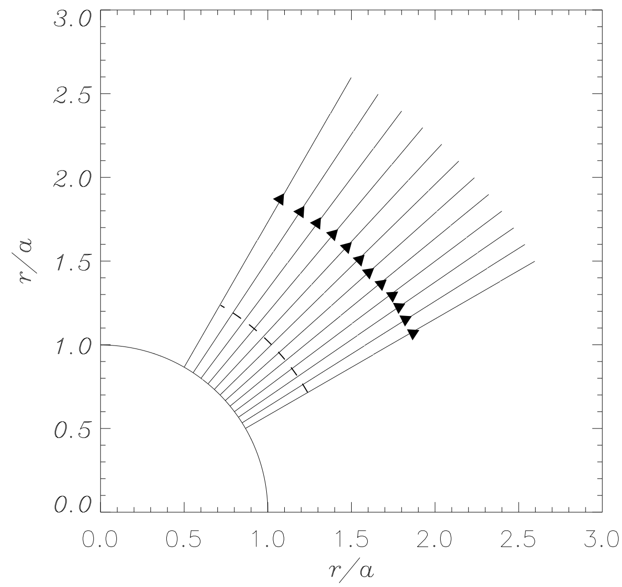

Figure 5.1: Image of the equilibrium magnetic field. The field lines fan out radially from the surface located at $r = 1$. A wave driven at the surface will propagate upwards passing from low- to high-β plasma. The mode-conversion region where $c_s = v_A$ is indicated by a dashed line.

$$p = R\rho\frac{T}{\widetilde{\mu}}, \tag{5.5}$$

$$\nabla \cdot \mathbf{B} = 0, \tag{5.6}$$

where ρ is the mass density, $\mathbf{v}$ is the fluid velocity, p is the gas pressure, μ is the magnetic permeability, **B** is the magnetic induction, R is the universal gas constant, T is the temperature and $\widetilde{\mu}$ is the mean molecular weight.

5.2.2 Equilibrium

If we consider the equilibrium conditions of a radially-expanding magnetic field, $\mathbf{B}_0 = \left(B_0 a^2/r^2, 0, 0\right)$, in an isothermal atmosphere Equation (5.1) gives

$$\nabla p_0 = 0, \tag{5.7}$$

and Equation (5.5) gives

$$p_0 = R\rho_0\frac{T_0}{\widetilde{\mu}}. \tag{5.8}$$

Thus the equilibrium pressure is constant. As we are assuming the equilibrium temperature is isothermal Equation (5.5) tells us that the equilibrium density must also be constant.

5.2.3 Linearised MHD Equations

Equations (5.1) – (5.6) may be linearised by adding a small perturbation to the variables

$$\rho = \rho_0 + \rho_1 \left(r, \theta, t\right), \quad \mathbf{v} = \mathbf{v}_1 \left(r, \theta, t\right), \quad p = p_0 + p_1 \left(r, \theta, t\right),$$

$$\mathbf{B} = \mathbf{B}_0 + \mathbf{B}_1 \left(r, \theta, t\right), \quad T = T_0 + T_1 \left(r, \theta, t\right), \tag{5.9}$$

where the subscript 0 denotes an equilibrium value and subscript 1 denotes a perturbation. To complete the linearisation process these are substituted into the Ideal MHD equations and products of perturbed values are neglected

$$\rho_0 \frac{\partial \mathbf{v}_1}{\partial t} = -\nabla p_1 + \frac{1}{\mu} \left(\nabla \times \mathbf{B}_1\right) \times \mathbf{B}_0, \tag{5.10}$$

$$\frac{\partial \rho_1}{\partial t} + \nabla \cdot \left(\rho_0 \mathbf{v}_1\right) = 0, \tag{5.11}$$

$$\frac{\partial \mathbf{B}_1}{\partial t} = \nabla \times \left(\mathbf{v}_1 \times \mathbf{B}_0\right), \tag{5.12}$$

$$\frac{\partial p_1}{\partial t} = -\left(\mathbf{v}_1 \cdot \nabla\right) p_0 - \gamma p_0 \left(\nabla \cdot \mathbf{v}_1\right), \tag{5.13}$$

$$\frac{p_1}{p_0} = \frac{\rho_1}{\rho_0} + \frac{T_1}{T_0}, \tag{5.14}$$

$$\nabla \cdot \mathbf{B}_1 = 0. \tag{5.15}$$

From this point on the subscripts on the perturbed terms are dropped and it is assumed that we are working with the linearised equations.

The Linearised MHD equations, under the assumption that $\partial / \partial \phi = 0$, then reduce to

$$\rho_0 \frac{\partial v_r}{\partial t} = -\frac{\partial p}{\partial r}, \tag{5.16}$$

$$\rho_0 \frac{\partial v_\theta}{\partial t} = -\frac{1}{r} \frac{\partial p}{\partial \theta} + \frac{B_{r0}}{\mu r} \frac{\partial \left(r B_\theta\right)}{\partial r} - \frac{B_{r0}}{\mu r} \frac{\partial B_r}{\partial \theta}, \tag{5.17}$$

$$\rho_0 \frac{\partial v_\phi}{\partial t} = \frac{B_{r0}}{\mu r} \frac{\partial \left(r B_\phi\right)}{\partial r}, \tag{5.18}$$

$$\frac{\partial B_r}{\partial t} = -\frac{B_{r0}}{r \sin \theta} \frac{\partial \left(v_\theta \sin \theta\right)}{\partial \theta}, \tag{5.19}$$

$$\frac{\partial B_\theta}{\partial t} = \frac{1}{r} \frac{\partial \left(r B_{r0} v_\theta\right)}{\partial r}, \tag{5.20}$$

$$\frac{\partial B_\phi}{\partial t} = \frac{1}{r} \frac{\partial \left(r B_{r0} v_\phi\right)}{\partial r}, \tag{5.21}$$

$$\frac{\partial p}{\partial t} = -\frac{\gamma p_0}{r^2} \frac{\partial \left(r^2 v_r\right)}{\partial r} - \frac{\gamma p_0}{r \sin \theta} \frac{\partial \left(v_\theta \sin \theta\right)}{\partial \theta}, \tag{5.22}$$

$$\frac{\partial \rho}{\partial t} = -\frac{\rho_0}{r^2} \frac{\partial \left(r^2 v_r\right)}{\partial r} - \frac{\rho_0}{r \sin \theta} \frac{\partial \left(v_\theta \sin \theta\right)}{\partial \theta}. \tag{5.23}$$

It should be noted that none of Equations (5.16) – (5.22) are dependent on ρ, thus Equation (5.23) may be considered separately. The remaining equations may be combined to give wave equations by differentiating Equations (5.16) – (5.18) with respect to t and substituting from the remaining equations. This results in the equations

$$\frac{\partial^2 v_r}{\partial t^2} = c_s^2 \frac{\partial}{\partial r}\left(\frac{1}{r^2}\frac{\partial\left(r^2 v_r\right)}{\partial r} + \frac{1}{r\sin\theta}\frac{\partial\left(v_\theta \sin\theta\right)}{\partial\theta}\right), \tag{5.24}$$

$$\begin{aligned}\frac{\partial^2 v_\theta}{\partial t^2} &= \frac{c_s^2}{r^2}\frac{\partial}{\partial\theta}\left(\frac{1}{r}\frac{\partial\left(r^2 v_r\right)}{\partial r} + \frac{1}{\sin\theta}\frac{\partial\left(v_\theta\sin\theta\right)}{\partial\theta}\right) + \\ &+ \frac{B_{r0}}{\mu\rho_0 r}\left(\frac{\partial^2\left(rB_{r0}v_\theta\right)}{\partial r^2} + \frac{B_{r0}}{r}\frac{\partial}{\partial\theta}\left(\frac{1}{\sin\theta}\frac{\partial\left(v_\theta\sin\theta\right)}{\partial\theta}\right)\right),\end{aligned} \tag{5.25}$$

$$\frac{\partial^2 v_\phi}{\partial t^2} = \frac{B_{r0}}{\mu\rho_0 r}\frac{\partial^2\left(rB_{r0}v_\phi\right)}{\partial r^2}, \tag{5.26}$$

where $c_s^2 = \gamma p_0/\rho_0$ is the square of the sound speed.

Notice that Equation (5.26) is completely decoupled from the other wave equations. This is because it is derived from Equations (5.18) and (5.21), which themselves are independent from the other equations. This describes the Alfvén wave and may be written

$$\frac{\partial^2\left(rB_{r0}v_\phi\right)}{\partial t^2} = v_A^2\frac{\partial^2\left(rB_{r0}v_\phi\right)}{\partial r^2}, \tag{5.27}$$

where $v_A^2 = B_{r0}^2/\left(\mu\rho_0\right)$ is the squared Alfvén speed. Equations (5.24) and (5.25) describe the fast and slow magnetoacoustic waves. As we are only interested in the coupling between the fast and slow waves we shall not consider Equation (5.27) further here.

5.2.3.1 Non-Dimensionalisation

We non-dimensionalise these equations in order to make the numerical simulations easier. This is done by setting $r = a\bar{r}$, $t = \tau\bar{t}$, $\mathbf{v} = v_0\bar{\mathbf{v}}$, $\mathbf{B} = B_0\bar{\mathbf{B}}$, $\mathbf{B}_0 = B_0\bar{\mathbf{B}}_0$, $p = p_0\bar{p}$, $p_0 = \bar{p}_0$, $\rho_0 = \bar{\rho}_0$, and $\theta = \bar{\theta}$. The typical lengthscales against which the variables have been made dimensionless are related by $v_0 = a/\tau$. Note that we have the relations

$$\bar{\mathbf{B}}_0 = \left(\frac{1}{\bar{r}^2}, 0, 0\right), \tag{5.28}$$

and

$$c_s^2 = \frac{\gamma\bar{p}_0}{\bar{\rho}_0}, \qquad v_A^2 = \frac{B_0^2}{\mu\bar{\rho}_0}\frac{1}{\bar{r}^4}. \tag{5.29}$$

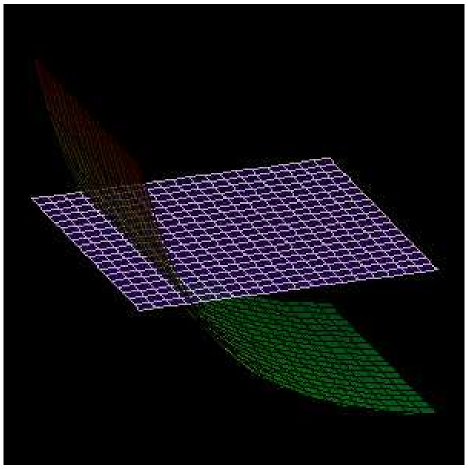

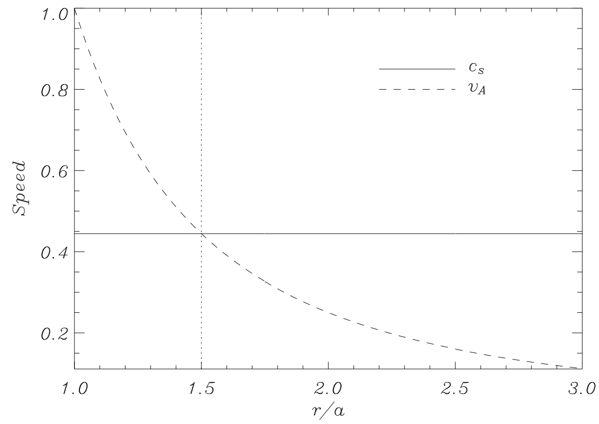

Figure 5.2: These plots show how the sound and Alfvén speeds vary across the numerical domain. In the left-hand plot the variation with both r and θ is shown. The right-hand plot shows a cut taken along constant θ - the $c_s = v_A$ region is denoted by the dotted line, to the left of this the plasma is low β and to the right it is high β.

Defining $c_{s0}^2 = \gamma \bar{p}_0/\bar{\rho}_0$, and $v_0^2 = B_0^2/\left(\mu\bar{\rho}_0\right) = 1$ the dimensionless sound and Alfvén speeds are given by

$$\bar{c}_s^2 = 1, \qquad \bar{v}_A^2 = \frac{1}{\bar{r}^4}. \tag{5.30}$$

The plasma β, which is the ratio of the gas to the magnetic pressure, may be written

$$\beta = \frac{2c_s^2}{\gamma v_A^2}. \tag{5.31}$$

This is non-dimensionalised by setting

$$\beta_0 = \frac{2c_{s0}^2}{\gamma}, \qquad \bar{\beta} = \bar{r}^4. \tag{5.32}$$

The mode-conversion region where the sound and Alfvén speeds are equal is then found where

$$\frac{\gamma\beta_0}{2} = \frac{1}{\bar{r}^4}, \tag{5.33}$$

and we can define the parameter β_0 according to where we wish to locate the mode-conversion region. If we choose to set the mode-conversion region to lie at $r_c = 1.5$, then the sound and Alfvén speeds vary as shown in Figure 5.2.

Under these assumptions the dimensionless equations are

$$\frac{\partial \bar{v}_r}{\partial \bar{t}} = -\frac{\beta_0}{2}\frac{\partial \bar{p}}{\partial \bar{r}}, \tag{5.34}$$

$$\frac{\partial \bar{v}_\theta}{\partial \bar{t}} = -\frac{\beta_0}{2\bar{r}}\frac{\partial \bar{p}}{\partial \bar{\theta}} + \frac{1}{\bar{r}^3}\frac{\partial\left(\bar{r}\bar{B}_\theta\right)}{\partial \bar{r}} - \frac{1}{\bar{r}^3}\frac{\partial \bar{B}_r}{\partial \bar{\theta}}, \tag{5.35}$$

$$\frac{\partial \bar{B}_r}{\partial \bar{t}} = -\frac{1}{\bar{r}^3 \sin\bar{\theta}} \frac{\partial\left(\bar{v}_\theta \sin\bar{\theta}\right)}{\partial\bar{\theta}}, \tag{5.36}$$

$$\frac{\partial \bar{B}_\theta}{\partial \bar{t}} = \frac{1}{\bar{r}} \frac{\partial}{\partial \bar{r}} \left(\frac{\bar{v}_\theta}{\bar{r}}\right), \tag{5.37}$$

$$\frac{\partial \bar{p}}{\partial \bar{t}} = -\frac{\gamma}{\bar{r}^2} \frac{\partial\left(\bar{r}^2 \bar{v}_r\right)}{\partial \bar{r}} - \frac{\gamma}{\bar{r}\sin\bar{\theta}} \frac{\partial\left(\bar{v}_\theta \sin\bar{\theta}\right)}{\partial\bar{\theta}}. \tag{5.38}$$

Equations (5.34) – (5.38) may be combined to give a pair of dimensionless wave equations describing the fast and slow magnetoacoustic waves.

$$\frac{\partial^2 \bar{v}_r}{\partial \bar{t}^2} = c_{s0}^2 \frac{\partial}{\partial \bar{r}} \left(\frac{1}{\bar{r}^2} \frac{\partial\left(\bar{r}^2 \bar{v}_r\right)}{\partial \bar{r}} + \frac{1}{\bar{r}\sin\bar{\theta}} \frac{\partial\left(\bar{v}_\theta \sin\bar{\theta}\right)}{\partial\bar{\theta}}\right), \tag{5.39}$$

$$\frac{\partial^2 \bar{v}_\theta}{\partial \bar{t}^2} = \frac{c_{s0}^2}{\bar{r}^3} \frac{\partial^2\left(\bar{r}^2 \bar{v}_r\right)}{\partial \bar{r}\partial\bar{\theta}} + \bar{r}\bar{v}_A^2 \frac{\partial^2}{\partial \bar{r}^2}\left(\frac{\bar{v}_\theta}{\bar{r}}\right) + \frac{\left(c_{s0}^2 + \bar{v}_A^2\right)}{\bar{r}^2} \frac{\partial}{\partial\bar{\theta}} \left(\frac{1}{\sin\bar{\theta}} \frac{\partial\left(\bar{v}_\theta \sin\bar{\theta}\right)}{\partial\bar{\theta}}\right). \tag{5.40}$$

Henceforth the bars on dimensionless values are dropped and it is assumed that we are working with the dimensionless equations.

5.3 Numerical Simulations

We solve Equations (5.34) – (5.38) numerically using the MacCormack method as was done in Chapters 3 and 4, although here it has been extended to deal with a two-dimensional problem. This works in two steps; the first predicts the solution at the next time step, this is then corrected at the next stage. This predictor/corrector method may use either forward or backward finite differencing. We choose to utilise forward differencing for the predictor steps and backward differencing for the corrector steps. This means that the more accurate, corrected values are being used on the lower radial boundary where a slow wave is driven.

We are driving v_r on the lower boundary in the low-β plasma so this is a slow magnetoacoustic wave. The simulations are run for $1 \leq r \leq 3$, $\pi/6 \leq \theta \leq \pi/3$ and $0 \leq t \leq 4.3$, where $\delta r = \delta\theta = 0.001$ and $\delta t = 0.0002$. The end time is chosen to terminate the simulation just before the transmitted fast wave hits the upper boundary. The free parameters remaining in the model are then given by m and ω. These describe the azimuthal wavenumber and driving frequency respectively, which are introduced through the lower boundary conditions. In a coronal hole the typical lengthscale may be taken as the solar radius, $R_\odot = 696$ Mm, and a typical Alfvén speed in the corona is 1000 km s^{-1}. We drive a slow wave on the lower boundary with frequencies of $\omega = 16\pi$, 24π and 32π which correspond in real terms to frequencies of 0.07 s^{-1}, 0.11 s^{-1} and 0.14 s^{-1} and periods of 87 s, 58 s and 43.5 s respectively. These driving frequencies are much larger than the acoustic cutoff frequency, $\Omega_{ac} = 0.001$ s^{-1} (Roberts, 2004), and so are unaffected by it.

On examining the Wave Equations (5.39) and (5.40) we can see that if $v_\theta = 0$ on the lower boundary, and v_r is independent of θ, then v_θ will remain zero throughout the simulation as the fast and slow magnetoacoustic waves are decoupled. Thus to observe mode conversion v_r must have some θ dependence. So on the lower radial boundary we choose

$$v_r = \sin\omega t \sin\left(m\left[6\theta - \pi\right]\right), \qquad v_\theta = 0, \tag{5.41}$$

where m must be an integer. Thus v_r will be zero on both θ boundaries and the value of m will dictate the number of nodes across the wave. Equation (5.36) would then suggest that $B_r = 0$. The condition for the pressure is given by Equation (5.34)

$$\frac{\partial p}{\partial r} = -\frac{2}{\beta_0}\omega\cos\omega t \sin\left(m\left[6\theta - \pi\right]\right). \tag{5.42}$$

Finally a condition is required for B_θ. If we solely consider the r derivatives in Equation (5.35) then it would suggest that we select

$$\frac{\partial\left(rB_\theta\right)}{\partial r} = 0. \tag{5.43}$$

The boundary conditions on the upper radial boundary are less important as we terminate the simulation before it reaches this point. Thus we simply choose open boundary conditions for all variables on the upper boundary.

As previously mentioned $v_r = 0$ on the θ boundaries. Equation (5.34) then suggests that $p = 0$ which then implies that

$$\frac{\partial\left(v_\theta\sin\theta\right)}{\partial\theta} = 0, \tag{5.44}$$

from Equation (5.38). This in turn gives $B_r = 0$ and it only remains to find a condition for B_θ. Since B_θ is in phase with V_θ we select

$$\frac{\partial\left(B_\theta\sin\theta\right)}{\partial\theta} = 0. \tag{5.45}$$

To summarise the boundary conditions on the lower radial boundary are given by

$$v_r = \sin\omega t \sin\left(m\left[6\theta - \pi\right]\right), \qquad \frac{\partial p}{\partial r} = -\frac{2}{\beta_0}\omega\cos\omega t \sin\left(m\left[6\theta - \pi\right]\right), \tag{5.46}$$

$$v_\theta = 0, \qquad B_r = 0, \qquad \frac{\partial\left(rB_\theta\right)}{\partial r} = 0. \tag{5.47}$$

The side boundary conditions are given by

$$v_r = 0, \qquad B_r = 0, \qquad p = 0, \tag{5.48}$$

$$\frac{\partial\left(v_\theta\sin\theta\right)}{\partial\theta} = 0, \qquad \frac{\partial\left(B_\theta\sin\theta\right)}{\partial\theta} = 0, \tag{5.49}$$

and the upper radial boundary conditions are

$$\frac{\partial v_r}{\partial r} = 0, \qquad \frac{\partial v_\theta}{\partial r} = 0, \qquad \frac{\partial B_r}{\partial r} = 0, \qquad \frac{\partial B_\theta}{\partial r} = 0, \qquad \frac{\partial p}{\partial r} = 0. \tag{5.50}$$

5.3.1 Wave Properties

As for the one-dimensional models we are driving a slow wave from low to high β. In this case that means that we are driving v_r on the lower radial boundary. As noted above, if the slow wave is not θ dependent then there is no coupling between the wave modes and we would not expect to see any mode conversion. The slow wave would then pass from the low-β plasma into the high-β plasma as a fast wave. If v_r does have a θ dependence then some proportion of the incident slow wave will be converted as it passes through the mode-conversion region and propagate as a slow wave in the high-β plasma.

Figure 5.3 shows the radial and azimuthal velocity, the radial and azimuthal magnetic field, and the pressure respectively. These are the results of a numerical simulation with driving frequency $\omega = 16\pi$ and azimuthal wavenumber $m = 3$ at $t = 4.3$ Alfvén times. Evidence of mode conversion can be seen in the plots of the azimuthal velocity, and the radial and azimuthal magnetic field. Once the wave train passes the mode-conversion region, denoted by the red dashed line, a change in the phase and amplitude dependence can be seen. This signifies the converted slow wave. The plots of the azimuthal velocity and magnetic field also show a transmitted fast wave propagating out ahead of the converted wave. This cannot be seen in the plots of the radial velocity or pressure due to the amplitude dependence. It is possible to transform the variables in such a way that the amplitude dependence of the incident wave is removed. The required transformations are calculated using the WKB method, as detailed in Section 5.4, and are given by

$$\begin{aligned} &v_r \to \frac{\tilde{v}_r}{r}, \quad v_\theta \to \frac{\tilde{v}_\theta}{r^2\left(v_A^2 - \gamma\beta_0 c_s^2/2\right)}, \quad B_r \to \frac{\tilde{B}_r}{r^2\left(v_A^2 - \gamma\beta_0 c_s^2/2\right)}, \\ &B_\theta \to \frac{\tilde{B}_\theta}{r^2\left(v_A^2 - \gamma\beta_0 c_s^2/2\right)}, \quad p \to \frac{\tilde{p}}{r}. \end{aligned} \tag{5.51}$$

The plots resulting from these transformations are shown in Figure 5.4. The mode conversion can now clearly be seen in the plots of the transformed radial velocity and pressure. The amplitude of the incident wave decreases when it crosses the mode-conversion region. The transmitted wave also now has a constant amplitude and the converted portion is visible as interference to the right of the dashed line. As before the converted wave may also be seen propagating ahead in the plots of the transformed azimuthal velocity, and the transformed radial and azimuthal magnetic field.

It is possible to calculate the positions of the various wavefronts in the simulation. The position of the acoustic mode, which is the slow wave in low β and the fast wave in high β, is given by the differential equation

$$\frac{\mathrm{d}r}{\mathrm{d}t} = \sqrt{\frac{\gamma\beta_0}{2}}c_s, \tag{5.52}$$

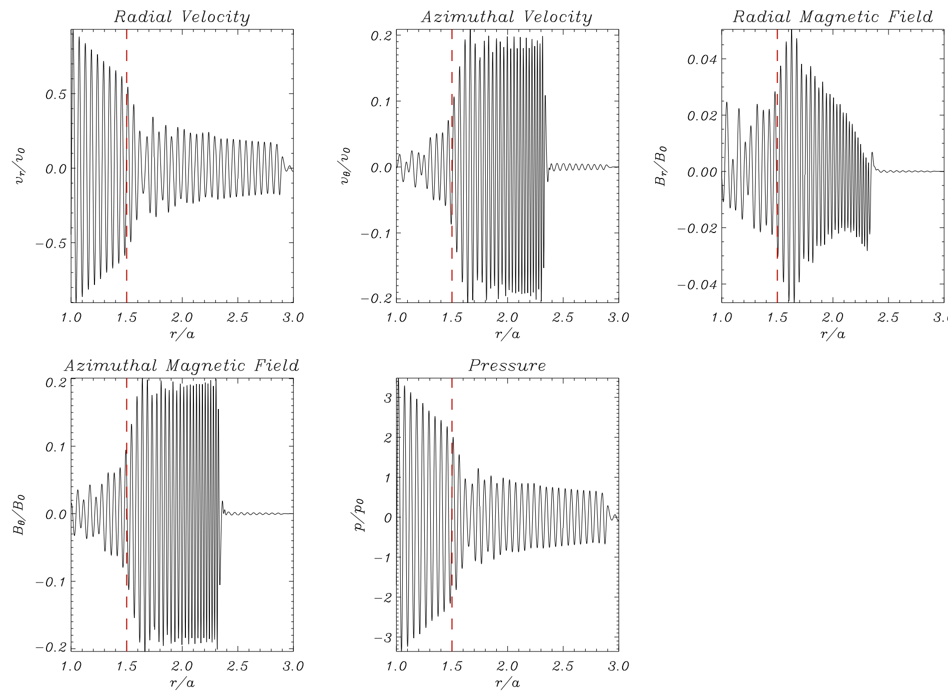

Figure 5.3: Results of the numerical simulation with $\omega = 16\pi$, $m = 3$ and $\theta = \pi/4$ at $t = 4.3$ Alfvén times. The plots show the radial and azimuthal velocity, the radial and azimuthal magnetic field, and the pressure respectively from top left to bottom right. The red dashed line indicates where $c_s = v_A$.

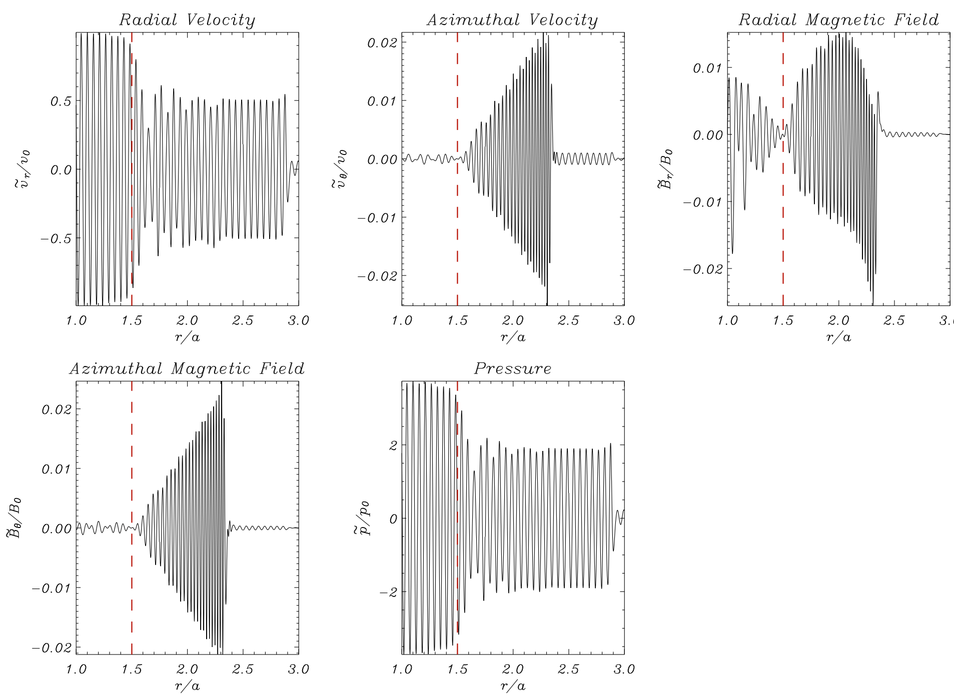

Figure 5.4: Results of the numerical simulation with $\omega = 16\pi$, $m = 3$ and $\theta = \pi/4$ at $t = 4.3$ Alfvén times. The plots show a transformation of the radial and azimuthal velocity, the radial and azimuthal magnetic field, and the pressure respectively from top left to bottom right. The red dashed line indicates where $c_s = v_A$.

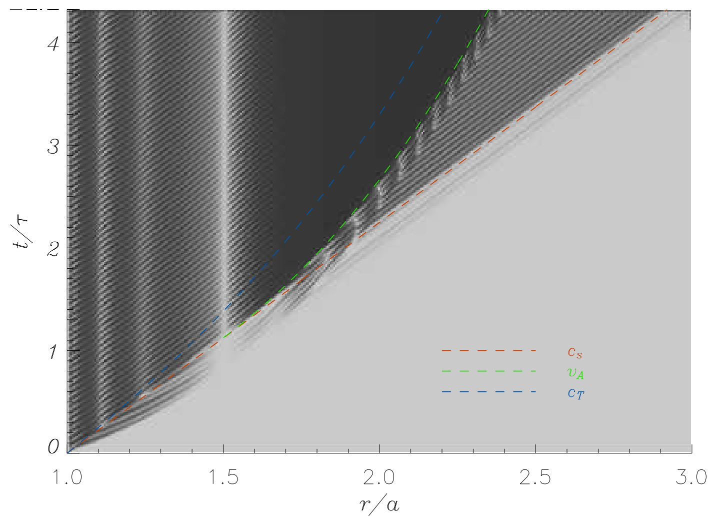

Figure 5.5: Surface plot of the transformed azimuthal velocity along $\theta = \pi/5$ for $\omega = 16\pi$ and $m = 3$. The red dashed line shows the position of the acoustic mode, the green dashed line the position of the magnetic mode, and the blue dashed line the position of the slow mode.

which may be solved to give

$$r = \sqrt{\frac{\gamma\beta_0}{2}}t + 1. \tag{5.53}$$

Thus for $\gamma\beta_0/2 = 16/81$, at $t = 4.3$ Alfvén times, the fast wave will have reached $r \approx 2.9$. Similarly the position of the magnetic mode, which is the slow wave in high β, may be found from the equation

$$\frac{\mathrm{d}r}{\mathrm{d}t} = v_A. \tag{5.54}$$

Using the initial condition $r = 1.5$ at $t = 9/8$ this has the solution

$$r^3 = 3t, \tag{5.55}$$

and so the converted wave will have reached $r \approx 2.35$ when $t = 4.3$ Alfvén times. These predictions are in excellent agreement with the numerical simulations shown in Figures 5.3 and 5.4. To calculate the position of the slow mode throughout the domain the equation

$$\frac{\mathrm{d}r}{\mathrm{d}t} = c_T = \sqrt{\frac{\gamma\beta_0}{2}}\frac{v_A}{\sqrt{\gamma\beta_0/2 + v_A^2}}, \tag{5.56}$$

may be solved. We do this numerically using a fourth-order, Runge-Kutta scheme.

Figure 5.5 shows the transformed azimuthal velocity along $\theta = \pi/5$ for driving frequency $\omega = 16\pi$ and wavenumber $m = 3$. Overplotted are the paths predicted by Equations (5.53), (5.55) and (5.56). The acoustic mode is the slow wave in the low-β plasma and the fast wave in the high-β plasma. The

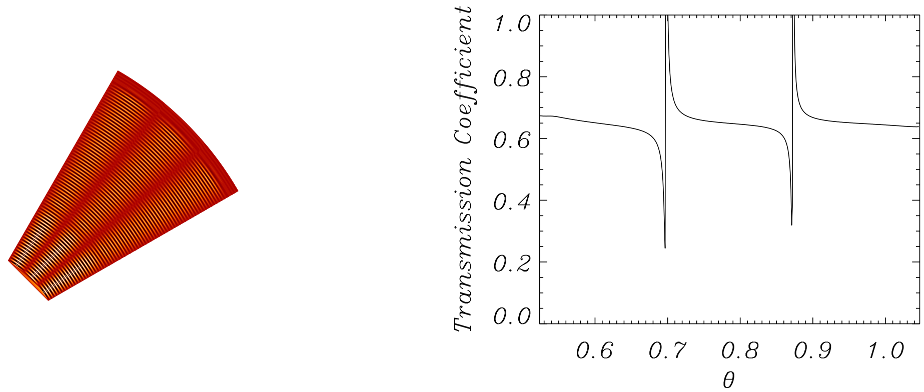

Figure 5.6: *Left:* A contour plot of the radial velocity for $\omega = 32\pi$ and $m = 3$ at $t = 4.3$ Alfvén times. *Right:* The variation of the transmission with θ for a numerical simulation with $\omega = 32\pi$ and $m = 3$.

magnetic mode is only present in the high-β plasma and is the slow wave in this region. The last path is that predicted by the tube speed, c_T, which follows the slow wave throughout the domain. This does not predict the position of the slow wave as well as Equations (5.53) and (5.55).

5.3.2 Effect of Varying the Model Parameters

As previously mentioned there are two free parameters in the numerical simulations: the azimuthal wavenumber (m) and the driving frequency (ω). In this section we examine the effect varying these parameters has on the proportion of the incident wave that is transmitted and converted.

We do this in each case along a fixed value of θ. This is acceptable as the amount of conversion and transmission does not depend on θ. We do not expect it to, since the sound speed is constant and the Alfvén speed varies with r alone. This can be seen in the left-hand plot of Figure 5.6 which shows a contour plot of the radial velocity for $\omega = 32\pi$ and $m = 3$ at $t = 4.3$ Alfvén times. The velocity goes to zero at each of the nodes in the θ-direction, but this does not change the transmission and conversion occurring at $r = 1.5$. This is demonstrated in the right-hand plot of Figure 5.6, which shows the variation of the transmission with θ for a numerical simulation with $\omega = 32\pi$ and $m = 3$. This is calculated by taking the amplitude ratio of the transformed radial velocity in high- and low-β plasma, which is why it grows where the velocity goes to zero at the nodes. Other than this the transmission is fairly constant.

5.3.2.1 Varying the Wavenumber

To examine the effect of varying the azimuthal wavenumber we fix the frequency at $\omega = 16\pi$ and run numerical simulations for different values of m. The results of this are shown in Figure 5.7 where the transformed radial velocity is plotted along $\theta = 11\pi/60$ for $m = 1$, 2, 3, 4, 5, and 6. As we would have expected from the results of the previous chapters the amount of transmission decreases as the azimuthal

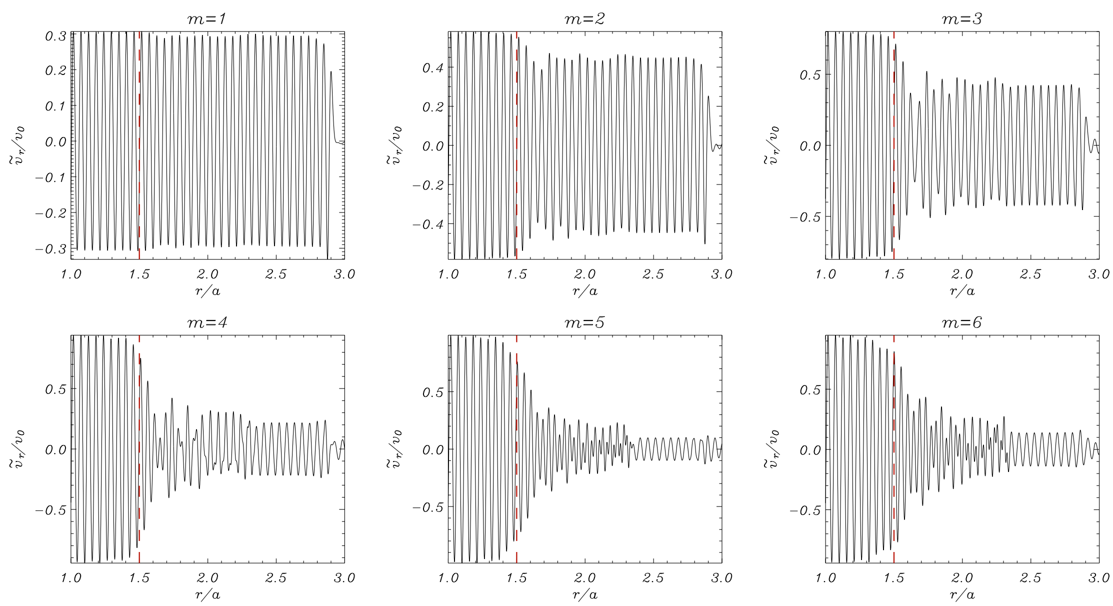

Figure 5.7: Transformed radial velocity along $\theta = 11\pi/60$ for $\omega = 16\pi$ at $t = 4.3$ Alfvén times. The plots show the results for $m = 1$, 2, 3, 4, 5 and 6 respectively from top left to bottom right. The dashed red line indicates where $c_s = v_A$.

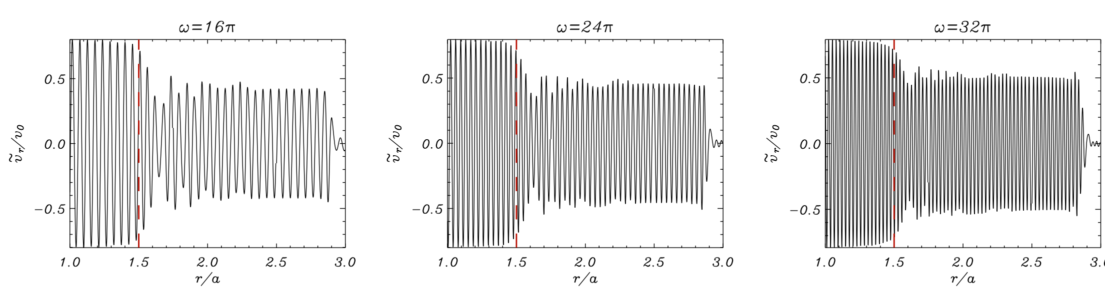

Figure 5.8: Transformed radial velocity along $\theta = 11\pi/60$ for $m = 3$ at $t = 4.3$ Alfvén times. The plots show $\omega = 16\pi$, 24π and 32π respectively from left to right. The dashed red line indicates where $c_s = v_A$.

wavenumber increases. For $m = 1$ there is so little conversion that it is barely visible and the incident wave appears to be fully transmitted into the high-β plasma. As m increases from 2 to 4 the amount of transmission decreases rapidly from plot to plot before levelling off by $m = 6$. Due to the similarities between this figure and Figures 3.5 and 4.8 we would expect to find similar equations describing the transmission and conversion coefficients.

5.3.2.2 Varying the Driving Frequency

Considering these similarities we would also expect the transmission to increase with increasing ω as before. As may be seen in Figure 5.8 this is indeed the case. In these plots we have fixed $m = 3$ and looked at the transformed radial velocity along $\theta = 11\pi/60$ at $t = 4.3$ Alfvén times for driving frequencies of $\omega = 16\pi$, 24π and 32π. This effect is clearly much weaker than that of varying the wavenumber.

5.4 Analytical Approximations

Having seen the similarities between the numerical simulations with a radially-expanding field and those in Chapters 3 and 4, we use the same analytical methods to uncover the behaviour throughout the domain. In Section 5.4.1 the Cairns and Lashmore-Davies (1983) method is used to find transmission and conversion coefficients valid at the conversion region. The WKB method is then used to find the wave behaviour away from the mode-conversion layer in Section 5.4.2.

5.4.1 Limit of $m \ll \partial/\partial r$

As in Chapter 4 we begin with the method by Cairns and Lashmore-Davies (1983) to approximate the behaviour at the mode-conversion region. We begin with the Wave Equations (5.39) and (5.40) written in their expanded form

$$\frac{\partial^2 v_r}{\partial t^2} = \frac{\gamma\beta_0}{2} c_s^2 \left(\frac{\partial^2 v_r}{\partial r^2} + \frac{1}{r}\frac{\partial^2 v_\theta}{\partial r \partial \theta} + \frac{2}{r}\frac{\partial v_r}{\partial r} + \frac{1}{r\tan\theta}\frac{\partial v_\theta}{\partial r} - \frac{1}{r^2}\frac{\partial v_\theta}{\partial \theta} - \frac{2}{r^2} v_r - \frac{1}{r^2 \tan\theta} v_\theta \right), \quad (5.57)$$

$$\begin{aligned} \frac{\partial^2 v_\theta}{\partial t^2} = \frac{\gamma\beta_0}{2}\frac{c_s^2}{r}\frac{\partial^2 v_r}{\partial r \partial \theta} + v_A^2 \frac{\partial^2 v_\theta}{\partial r^2} + \frac{\left(\gamma\beta_0 c_s^2/2 + v_A^2\right)}{r^2}\frac{\partial^2 v_\theta}{\partial \theta^2} + 2\frac{\gamma\beta_0}{2}\frac{c_s^2}{r^2}\frac{\partial v_r}{\partial \theta} + \\ + \left(\left(v_A^2\right)' + 2\frac{v_A^2}{r} \right)\frac{\partial v_\theta}{\partial r} + \frac{\left(\gamma\beta_0 c_s^2/2 + v_A^2\right)}{r^2 \tan\theta}\frac{\partial v_\theta}{\partial \theta} + \\ + \left(\frac{\left(v_A^2\right)'}{r} + B_{r0}B_{r0}'' - \frac{\left(\gamma\beta_0 c_s^2/2 + v_A^2\right)}{r^2 \sin^2\theta} \right) v_\theta. \end{aligned} \quad (5.58)$$

Assuming that $\partial/\partial t = i\omega$, and that derivatives are large, so that v_r and v_θ may be neglected in comparison to their first derivatives and so on, *i.e.* $\partial/\partial\theta \gg 1$, these equations reduce to

$$-\omega^2 v_r = \frac{\gamma\beta_0}{2} c_s^2 \frac{\partial^2 v_r}{\partial r^2} + \frac{\gamma\beta_0}{2}\frac{c_s^2}{r}\frac{\partial^2 v_\theta}{\partial r \partial\theta}, \tag{5.59}$$

$$-\omega^2 v_\theta = \frac{\gamma\beta_0}{2}\frac{c_s^2}{r}\frac{\partial^2 v_r}{\partial r\partial\theta} + v_A^2 \frac{\partial^2 v_\theta}{\partial r^2} + \frac{\left(\gamma\beta_0 c_s^2/2 + v_A^2\right)}{r^2}\frac{\partial^2 v_\theta}{\partial\theta^2}. \tag{5.60}$$

Finally, by making the assumption that $\partial/\partial\theta$ is small, these equations may be written

$$\left(\frac{\partial^2}{\partial r^2} + \frac{2}{\gamma\beta_0}\frac{\omega^2}{c_s^2}\right) v_r = -\frac{1}{r}\frac{\partial^2 v_\theta}{\partial r\partial\theta}, \tag{5.61}$$

$$\left(\frac{\partial^2}{\partial r^2} + \frac{\omega^2}{v_A^2}\right) v_\theta = -\frac{\gamma\beta_0}{2}\frac{c_s^2}{r v_A^2}\frac{\partial^2 v_r}{\partial r\partial\theta}. \tag{5.62}$$

Or alternatively

$$\left(\frac{\partial}{\partial r} + i\sqrt{\frac{2}{\gamma\beta_0}}\frac{\omega}{c_s}\right)\left(\frac{\partial}{\partial r} - i\sqrt{\frac{2}{\gamma\beta_0}}\frac{\omega}{c_s}\right) v_r = -\frac{1}{r}\frac{\partial^2 v_\theta}{\partial r\partial\theta}, \tag{5.63}$$

$$\left(\frac{\partial}{\partial r} + i\frac{\omega}{v_A}\right)\left(\frac{\partial}{\partial r} - i\frac{\omega}{v_A}\right) v_\theta = -\frac{\gamma\beta_0}{2}\frac{c_s^2}{r v_A^2}\frac{\partial^2 v_r}{\partial r\partial\theta}, \tag{5.64}$$

where the brackets on the left-hand side of each equation represent the upward and downward propagating waves respectively.

The next step is to expand about the mode-conversion region for waves travelling up towards this region. We do this by letting

$$r = r_c - \xi + \ldots, \qquad \frac{\partial}{\partial r} = -\frac{\partial}{\partial\xi} + \ldots. \tag{5.65}$$

At the conversion region the sound and Alfvén speeds are equal so

$$\sqrt{\frac{\gamma\beta_0}{2}} c_s = \frac{1}{r_c^2} = v_A\left(r_c\right), \tag{5.66}$$

where r_c is the radius at the mode-conversion region. The Alfvén speed may then be written

$$v_A = \frac{1}{r_c^2\left(1 - 2\xi/r_c + \xi^2/r_c^2\right)} \approx \frac{1}{r_c^2\left(1 - 2\xi/r_c\right)}, \tag{5.67}$$

as $\xi \ll 1$. Thus

$$v_A \approx \sqrt{\frac{\gamma\beta_0}{2}}\frac{c_s}{\left(1 + 2\xi/r_c\right)}. \tag{5.68}$$

Away from the mode-conversion region we simply let

$$\frac{\partial}{\partial r} = -i\sqrt{\frac{2}{\gamma\beta_0}}\frac{\omega}{c_s}. \tag{5.69}$$

Equations (5.63) and (5.64) then become

$$\frac{\partial v_r}{\partial \xi} - i\sqrt{\frac{2}{\gamma\beta_0}}\frac{\omega}{c_s}v_r = \frac{1}{2r_c}\frac{\partial v_\theta}{\partial \theta}, \tag{5.70}$$

$$\frac{\partial v_\theta}{\partial \xi} - i\left(\sqrt{\frac{2}{\gamma\beta_0}}\frac{\omega}{c_s} - \sqrt{\frac{2}{\gamma\beta_0}}\frac{2\omega}{r_c c_s}\xi\right)v_\theta = \frac{1}{2r_c}\frac{\partial v_r}{\partial \theta}. \tag{5.71}$$

Based on the boundary conditions of the numerical simulations, we then let $\partial/\partial\theta = 6im$, giving

$$\frac{\mathrm{d}v_r}{\mathrm{d}\xi} - i\sqrt{\frac{2}{\gamma\beta_0}}\frac{\omega}{c_s}v_r = \frac{3im}{r_c}v_\theta, \tag{5.72}$$

$$\frac{\mathrm{d}v_\theta}{\mathrm{d}\xi} - i\left(\sqrt{\frac{2}{\gamma\beta_0}}\frac{\omega}{c_s} - \sqrt{\frac{2}{\gamma\beta_0}}\frac{2\omega}{r_c c_s}\xi\right)v_\theta = \frac{3im}{r_c}v_r. \tag{5.73}$$

It may be shown that these satisfy the conservation of energy. Multiplying Equation (5.72) by its complex conjugate we obtain

$$\bar{v}_r\frac{\mathrm{d}v_r}{\mathrm{d}\xi} - i\sqrt{\frac{2}{\gamma\beta_0}}\frac{\omega}{c_s}\bar{v}_r v_r = \frac{3im}{r_c}\bar{v}_r v_\theta, \tag{5.74}$$

taking the complex conjugate of this gives

$$v_r\frac{\mathrm{d}\bar{v}_r}{\mathrm{d}\xi} + i\sqrt{\frac{2}{\gamma\beta_0}}\frac{\omega}{c_s}v_r\bar{v}_r = -\frac{3im}{r_c}v_r\bar{v}_\theta. \tag{5.75}$$

Adding these together we are left with

$$\frac{\mathrm{d}}{\mathrm{d}\xi}\left(|v_r|^2\right) = \frac{3im}{r_c}\left(\bar{v}_r v_\theta - v_r\bar{v}_\theta\right). \tag{5.76}$$

Repeating this for Equation (5.73) we may add

$$\bar{v}_\theta\frac{\mathrm{d}v_\theta}{\mathrm{d}\xi} - i\left(\sqrt{\frac{2}{\gamma\beta_0}}\frac{\omega}{c_s} - \sqrt{\frac{2}{\gamma\beta_0}}\frac{2\omega}{r_c c_s}\xi\right)\bar{v}_\theta v_\theta = \frac{3im}{r_c}\bar{v}_\theta v_r, \tag{5.77}$$

and

$$v_\theta\frac{\mathrm{d}\bar{v}_\theta}{\mathrm{d}\xi} + i\left(\sqrt{\frac{2}{\gamma\beta_0}}\frac{\omega}{c_s} - \sqrt{\frac{2}{\gamma\beta_0}}\frac{2\omega}{r_c c_s}\xi\right)v_\theta\bar{v}_\theta = -\frac{3im}{r_c}v_\theta\bar{v}_r, \tag{5.78}$$

to give

$$\frac{\mathrm{d}}{\mathrm{d}\xi}\left(|v_\theta|^2\right) = \frac{3im}{r_c}\left(\bar{v}_\theta v_r - v_\theta\bar{v}_r\right). \tag{5.79}$$

Adding Equations (5.76) and (5.79) we see that energy is conserved

$$\frac{\mathrm{d}}{\mathrm{d}\xi}\left(|v_r|^2 + |v_\theta|^2\right) = 0. \tag{5.80}$$

Returning to Equations (5.72) and (5.73) v_θ may be eliminated to give a second-order, ordinary differential equation for v_r.

$$\frac{\mathrm{d}^2 v_r}{\mathrm{d}\xi^2} + i\sqrt{\frac{2}{\gamma\beta_0}}\frac{\omega}{c_s}\left(\frac{2}{r_c}\xi - 2\right)\frac{\mathrm{d}v_r}{\mathrm{d}\xi} + \left(\frac{9m^2}{r_c^2} - \frac{2}{\gamma\beta_0}\frac{\omega^2}{c_s^2}\left(1 - \frac{2}{r_c}\xi\right)\right)v_r = 0. \tag{5.81}$$

To eliminate the first derivative we make the substitution

$$v_r(\xi) = \exp\left(-i\sqrt{\frac{2}{\gamma\beta_0}}\frac{\omega}{c_s}\left(\frac{\xi^2}{2r_c} - \xi\right)\right)\psi(\xi), \tag{5.82}$$

to give

$$\frac{\mathrm{d}^2\psi}{\mathrm{d}\xi^2} + \left(\frac{2}{\gamma\beta_0}\frac{\omega^2}{c_s^2}\frac{\xi^2}{r_c^2} - i\sqrt{\frac{2}{\gamma\beta_0}}\frac{\omega}{r_c c_s} + \frac{9m^2}{r_c^2}\right)\psi = 0. \tag{5.83}$$

Finally we make the substitution

$$\zeta = \left(\sqrt{\frac{2}{\gamma\beta_0}}\frac{2\omega}{r_c c_s}\right)^{1/2} e^{3i\pi/4}\xi, \tag{5.84}$$

yielding

$$\frac{\mathrm{d}^2\psi}{\mathrm{d}\zeta^2} - \left(\frac{\zeta^2}{4} - \frac{1}{2} - i\sqrt{\frac{\gamma\beta_0}{2}}\frac{9m^2 c_s}{2\omega r_c}\right). \tag{5.85}$$

The advantage of writing the equation in this form is that the solutions are known in terms of the Parabolic Cylinder function $U(a, \zeta)$ where

$$a = -\frac{1}{2} - i\sqrt{\frac{\gamma\beta_0}{2}}\frac{9m^2 c_s}{2\omega r_c}, \tag{5.86}$$

as described in Abramowitz and Stegun (1964). Using the asymptotic expansion, v_r is given in low β $(\xi > 0)$ by

$$v_r \sim \left(\sqrt{\frac{2}{\gamma\beta_0}}\frac{2\omega}{r_c c_s}\right)^{i\sqrt{\gamma\beta_0/2}9m^2 c_s/(4\omega r_c)} \exp\left(\sqrt{\frac{\gamma\beta_0}{2}}\frac{9\pi m^2 c_s}{8\omega r_c}\right)\xi^{i\sqrt{\gamma\beta_0/2}9m^2 c_s/(2\omega r_c)} \times$$
$$\times \exp\left(i\sqrt{\frac{2}{\gamma\beta_0}}\frac{\omega}{c_s}\xi\right), \tag{5.87}$$

and in high β $(\xi < 0)$ by

$$v_r \sim \left(\sqrt{\frac{2}{\gamma\beta_0}}\frac{2\omega}{r_c c_s}\right)^{i\sqrt{\gamma\beta_0/2}9m^2 c_s/(4\omega r_c)} \exp\left(-\sqrt{\frac{\gamma\beta_0}{2}}\frac{27\pi m^2 c_s}{8\omega r_c}\right)|\xi|^{i\sqrt{\gamma\beta_0/2}9m^2 c_s/(2\omega r_c)} \times$$
$$\times \exp\left(i\sqrt{\frac{2}{\gamma\beta_0}}\frac{\omega}{c_s}\xi\right) - \frac{(2\pi)^{1/2}}{\Gamma\left(-i\sqrt{\frac{\gamma\beta_0}{2}}\frac{9m^2 c_s}{2\omega r_c}\right)}\exp\left(-\sqrt{\frac{\gamma\beta_0}{2}}\frac{9\pi m^2 c_s}{8\omega r_c}\right) \times$$

$$\times\left(\sqrt{\frac{2}{\gamma\beta_0}}\frac{2\omega}{r_c c_s}\right)^{-\left(i\sqrt{\gamma\beta_0/2}9m^2c_s/(4\omega r_c)\right)-1/2}|\xi|^{-\left(i\sqrt{\gamma\beta_0/2}9m^2c_s/(2\omega r_c)\right)-1}\times$$
$$\times\exp\left(i\sqrt{\frac{2}{\gamma\beta_0}}\frac{\omega}{c_s}\xi - i\sqrt{\frac{2}{\gamma\beta_0}}\frac{\omega}{r_c c_s}\xi^2 - \frac{3i\pi}{4}\right). \quad (5.88)$$

The WKB method is used to find transmission and conversion coefficients from these equations. We first assume that v_θ is small in comparison to v_r to find an expression for the transmitted component. We let

$$v_r = B\exp\left(\omega\phi_0 + \frac{\phi_1}{\omega}\right), \quad (5.89)$$

$$v_\theta = \frac{V_{\theta 0}}{\omega}\exp\left(\omega\phi_0 + \frac{\phi_1}{\omega}\right), \quad (5.90)$$

where ω is assumed to be large and $\omega\phi_0 \gg V_{\theta 0}/\omega, \phi_1/\omega$. These are substituted into Equations (5.72) and (5.73) to obtain

$$\left(\omega\phi_0' + \frac{\phi_1'}{\omega}\right)B - i\sqrt{\frac{2}{\gamma\beta_0}}\frac{\omega}{c_s}B = \frac{3im}{r_c}\frac{V_{\theta 0}}{\omega}, \quad (5.91)$$

$$\frac{V_{\theta 0}'}{\omega} + V_{\theta 0}\phi_0' + V_{\theta 0}\frac{\phi_1'}{\omega^2} - i\sqrt{\frac{2}{\gamma\beta_0}}\frac{1}{c_s}\left(1 - \frac{2}{r_c}\xi\right)V_{\theta 0} = \frac{3im}{r_c}B. \quad (5.92)$$

By equating the coefficients of ω we find that

$$\phi_0 = i\sqrt{\frac{2}{\gamma\beta_0}}\frac{\xi}{c_s}, \quad V_{\theta 0} = \sqrt{\frac{\gamma\beta_0}{2}}\frac{3mc_s}{2\xi}B, \quad \phi_1 = i\sqrt{\frac{\gamma\beta_0}{2}}\frac{9m^2c_s}{2r_c}\ln\xi. \quad (5.93)$$

These give the transmitted component of v_r as

$$v_r = B\xi^{i\sqrt{\gamma\beta_0/2}9m^2c_s/(2\omega r_c)}\exp\left(i\sqrt{\frac{2}{\gamma\beta_0}}\frac{\omega}{c_s}\xi\right). \quad (5.94)$$

Similarly to find the converted component we assume that v_r is small compared to v_θ by letting

$$v_r = \frac{V_{r0}}{\omega}\exp\left(\omega\phi_0 + \frac{\phi_1}{\omega}\right), \quad (5.95)$$

$$v_\theta = A\exp\left(\omega\phi_0 + \frac{\phi_1}{\omega}\right), \quad (5.96)$$

where $\omega\phi_0 \gg V_{r0}/\omega, \phi_1/\omega$. Substituting these into Equations (5.72) and (5.73) we obtain

$$\frac{V_{r0}'}{\omega} + V_{r0}\phi_0' + V_{r0}\frac{\phi_1'}{\omega} - i\sqrt{\frac{2}{\gamma\beta_0}}\frac{1}{c_s}V_{r0} = \frac{3im}{r_c}A, \quad (5.97)$$

$$\left(\omega\phi_0' + \frac{\phi_1'}{\omega}\right)A - i\sqrt{\frac{2}{\gamma\beta_0}}\frac{\omega}{c_s}\left(1 - \frac{2}{r_c}\xi\right)A = \frac{3im}{r_c}\frac{V_{r0}}{\omega}. \quad (5.98)$$

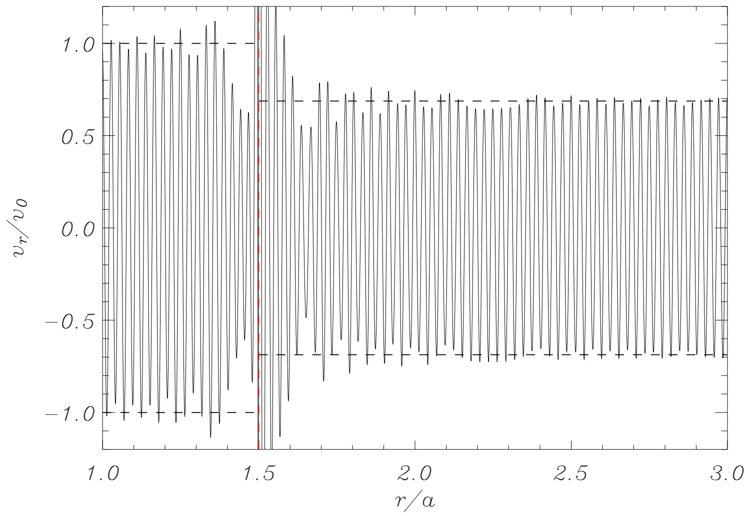

Figure 5.9: Radial velocity as predicted by Equation (5.101) with $\omega = 32\pi$ and $m = 3$ at $\theta = \pi/4$. The vertical red dashed line denotes where $c_s = v_A$; the horizontal lines to the left of this show the predicted amplitude of the incident wave, and those to the right the predicted amplitude of the transmitted wave.

Equating coefficients of ω we find that

$$\phi_0 = i\sqrt{\frac{2}{\gamma\beta_0}}\frac{1}{c_s}\left(\xi - \frac{\xi^2}{r_c}\right), \quad V_{r0} = -\sqrt{\frac{\gamma\beta_0}{2}}\frac{3mc_s}{2\xi}A, \quad \phi_1 = -i\sqrt{\frac{\gamma\beta_0}{2}}\frac{9m^2c_s}{2r_c}\ln\xi. \tag{5.99}$$

These give the converted component as

$$v_r = -\sqrt{\frac{\gamma\beta_0}{2}}\frac{3mc_s}{2\omega}A\xi^{-\left(i\sqrt{\gamma\beta_0/2}9m^2c_s/(2\omega r_c)\right)-1}\exp\left(i\sqrt{\frac{2}{\gamma\beta_0}}\frac{\omega}{c_s}\left(\xi - \frac{\xi^2}{r_c}\right)\right). \tag{5.100}$$

Equations (5.94) and (5.100) may be added together to give

$$\begin{aligned} v_r \sim{}& B\xi^{i\sqrt{\gamma\beta_0/2}9m^2c_s/(2\omega r_c)}\exp\left(i\sqrt{\frac{2}{\gamma\beta_0}}\frac{\omega}{c_s}\xi\right) - \sqrt{\frac{\gamma\beta_0}{2}}\frac{3mc_s}{2\omega}A\times \\ &\times\xi^{-\left(i\sqrt{\gamma\beta_0/2}9m^2c_s/(2\omega r_c)\right)-1}\exp\left(i\sqrt{\frac{2}{\gamma\beta_0}}\frac{\omega}{c_s}\left(\xi - \frac{\xi^2}{r_c}\right)\right). \end{aligned} \tag{5.101}$$

Taking the high-β approximation to v_r, given by Equation (5.88), and dividing by the low-β approximation, Equation (5.87), we may find transmission and conversion coefficients by comparison with Equation (5.101). Doing so we obtain the transmission coefficient

$$B = \exp\left(-\sqrt{\frac{\gamma\beta_0}{2}}\frac{9\pi m^2c_s}{2\omega r_c}\right), \tag{5.102}$$

and the expression

$$A = \frac{r_c (2\pi)^{1/2}}{3m\Gamma\left(-i\sqrt{\frac{\gamma\beta_0}{2}}\frac{9m^2c_s}{2\omega r_c}\right)}\left(\sqrt{\frac{2}{\gamma\beta_0}}\frac{2\omega}{r_c c_s}\right)^{1/2}\exp\left(-\sqrt{\frac{\gamma\beta_0}{2}}\frac{9\pi m^2 c_s}{4\omega r_c}\right), \tag{5.103}$$

for the conversion coefficient. Using the fact that

$$|\Gamma(iy)|^2 = |\Gamma(-iy)|^2 = \frac{\pi}{y\sinh(\pi y)}, \tag{5.104}$$

from Gradshteyn and Ryzhik (1981), the conversion coefficient may be simplified to

$$A = \sqrt{1 - \exp\left(-\sqrt{\frac{\gamma\beta_0}{2}}\frac{9\pi m^2 c_s}{\omega r_c}\right)}. \tag{5.105}$$

Equations (5.102) and (5.105) describe the proportion of the incident wave that is transmitted and converted as it crosses the mode-conversion region. Substituting these values back into Equation (5.101) gives a description of the radial velocity across the mode-conversion region. This is shown in Figure 5.9 for $\omega = 32\pi$, and $m = 3$ at $\theta = \pi/4$. Overplotted on this figure is the amplitude we would expect to see for the incident wave once the amplitude dependence is removed, and to the right of the red dashed line the amplitude predicted for the transmitted wave by Equation (5.102). We may compare this result to the numerical simulations by taking the ratio of the transmitted wave to the incident wave for various values of m. The results of this are shown in Figure 5.10.

In each of the images in Figure 5.10 the driving frequency is $\omega = 16\pi$ and $\theta = 11\pi/60$, the solid line shows the amount of transmission predicted by Equation (5.102) and the stars overplotted are the amount of transmission seen in the numerical simulations. The left-hand image shows good agreement; there is some deviation of the numerical results from the analytical prediction but the points do follow the curve. This small deviation may be attributed to the additional complexity of this model. Taking the logarithm of these values, as shown in the right-hand figure, we can see that the difference between the numerical and analytical results really is small. As expected it does begin to get larger as the value of the azimuthal wavenumber increases in violation of the initial assumptions.

On comparison with Equations (3.86) and (3.89), and (4.117) and (4.120), we see that the form of the coefficients is very similar to those for an isothermal and non-isothermal atmosphere permeated by a uniform vertical magnetic field. As in these previous cases the coefficients are dependent on both the driving frequency and on the azimuthal wavenumber. The nature of this dependence is shown in Figure 5.11. As before the amount of transmission decreases with increasing wavenumber and increases with increasing driving frequency. The opposite is true of the amount of conversion.

Figure 5.12 also shows how the predicted transmission compares to that seen in the numerical simulations. As before the amount of transmission is calculated by taking the ratio of the transmitted to the incident wave. In this case we see how the transmission varies with θ for the azimuthal wavenumber and driving frequency fixed at $m = 3$ and $\omega = 32\pi$ respectively. The dashed line overplotted on this is the

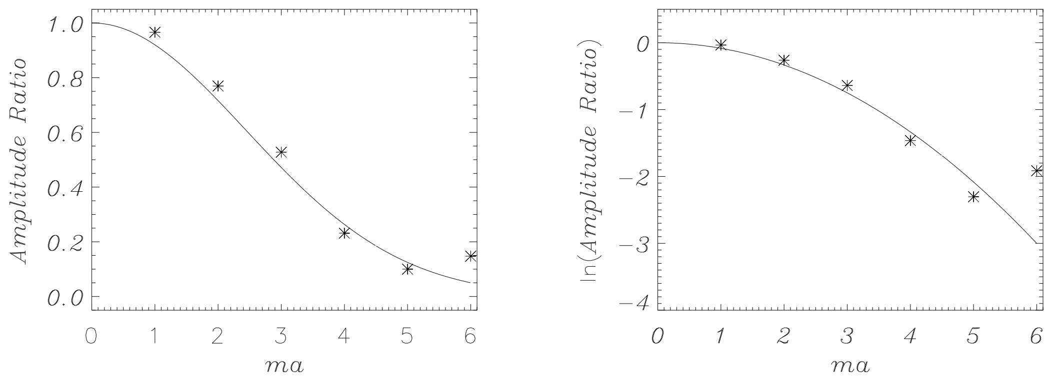

Figure 5.10: *Left:* Ratio of the transmitted and incident wave amplitudes.
Right: Logarithm of the ratio of the transmitted and incident wave amplitudes.
In both cases $\omega = 16\pi$, $\theta = 11\pi/60$, the solid line is that predicted by Equation (5.102) and the stars are the values calculated from the numerical data.

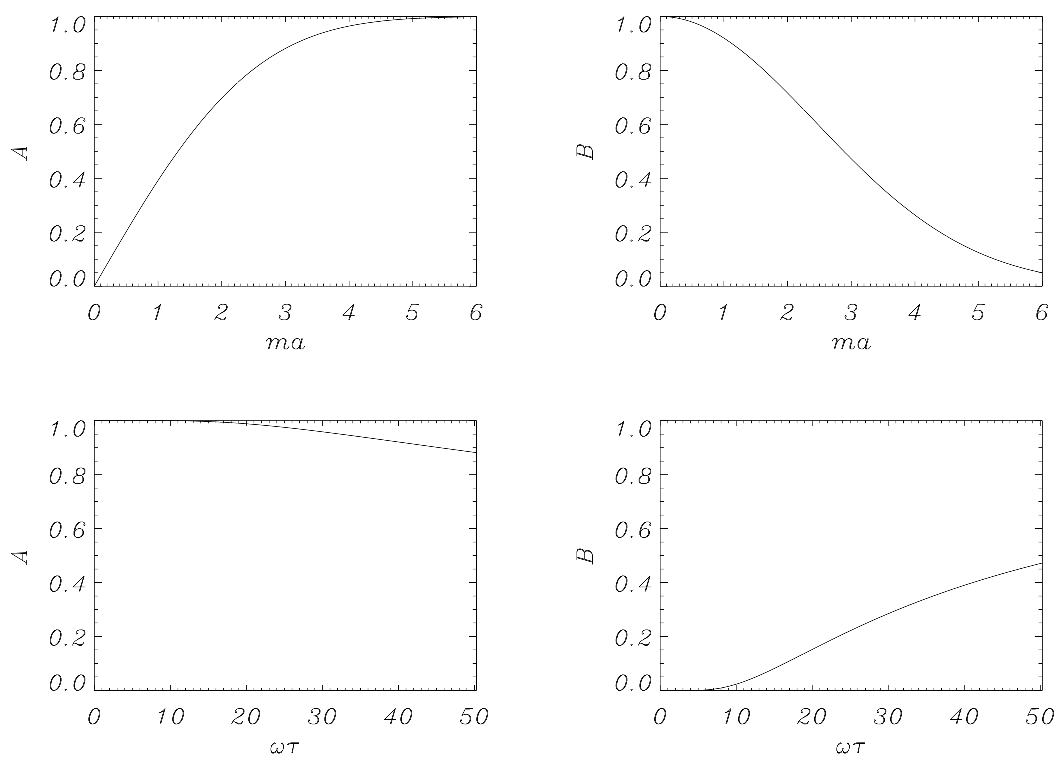

Figure 5.11: *Top Left:* The variation of A with m for $\omega = 16\pi$.
Top Right: The variation of B with m for $\omega = 16\pi$.
Bottom Left: The variation of A with ω for $m = 3$.
Bottom Right: The variation of B with ω for $m = 3$.

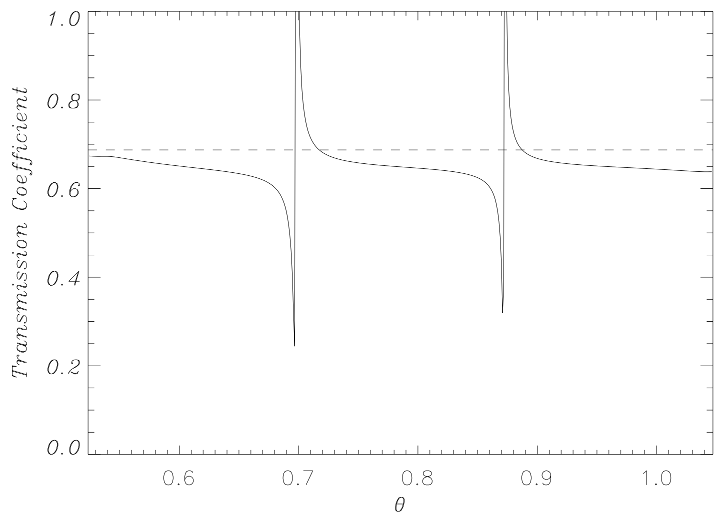

Figure 5.12: The variation of the transmission with θ for a numerical simulation with $\omega = 32\pi$ and $m = 3$. The dashed line overplotted shows the amount of transmission predicted by Equation (5.102).

transmission predicted by Equation (5.102). Ignoring the regions where the radial component goes to zero the transmission is approximately constant and the prediction is a fairly good one.

5.4.2 WKB Analysis away from the Conversion Region

The above method has described the proportion of the incident wave transmitted and converted across the conversion region. It does not, however, tell us about the wave behaviour away from this region. To find this out we use the WKB method, as described in Chapter 2, beginning with the wave equations. Under the assumption that the time dependence may be written $\partial/\partial t = i\omega$ these become

$$\left(\frac{\gamma\beta_0}{2}c_s^2\frac{\partial^2}{\partial r^2} + 2\frac{\gamma\beta_0}{2}\frac{c_s^2}{r}\frac{\partial}{\partial r} - 2\frac{\gamma\beta_0}{2}\frac{c_s^2}{r^2} + \omega^2\right)v_r = \frac{\gamma\beta_0}{2}\frac{c_s^2}{r}\times$$
$$\times\left(-\frac{\partial^2}{\partial r\partial\theta} - \frac{1}{\tan\theta}\frac{\partial}{\partial r} + \frac{1}{r}\frac{\partial}{\partial\theta} + \frac{1}{r\tan\theta}\right)v_\theta, \qquad (5.106)$$

$$\left(v_A^2\frac{\partial^2}{\partial r^2} + \frac{\left(\gamma\beta_0 c_s^2/2 + v_A^2\right)}{r^2}\frac{\partial^2}{\partial\theta^2} + \left(\left(v_A^2\right)' + 2\frac{v_A^2}{r}\right)\frac{\partial}{\partial r} + \frac{\left(\gamma\beta_0 c_s^2/2 + v_A^2\right)}{r^2\tan\theta}\frac{\partial}{\partial\theta} +\right.$$
$$\left. + \left(\frac{\left(v_A^2\right)'}{r} + B_{r0}B_{r0}'' - \frac{\left(\gamma\beta_0 c_s^2/2 + v_A^2\right)}{r^2\sin^2\theta} + \omega^2\right)\right)v_\theta =$$
$$= -\frac{\gamma\beta_0}{2}\frac{c_s^2}{r}\left(\frac{\partial^2}{\partial r\partial\theta} + \frac{2}{r}\frac{\partial}{\partial\theta}\right)v_r. \qquad (5.107)$$

Assuming that $\omega \gg c_s\partial/\partial\theta$ we expand v_r and v_θ in inverse powers of ω. To find equations describing the incident and transmitted waves we assume that v_θ is small in comparison to v_r

$$v_r = \exp\left(\omega\phi_0 + \phi_1\right), \tag{5.108}$$

$$v_\theta = \frac{V_{\theta 0}}{\omega}\exp\left(\omega\phi_0 + \phi_1\right), \tag{5.109}$$

where $\omega\phi_0 \gg \phi_1 \gg V_{\theta 0}/\omega$ and the variables ϕ_0, ϕ_1, and $V_{\theta 0}$ may all be functions of both r and θ.

Substituting these back into Equations (5.106) and (5.107) we may then equate coefficients of ω to solve for the unknowns. The $\mathcal{O}\left(\omega^2\right)$ equations are given by

$$\frac{\gamma\beta_0}{2}c_s^2\left(\frac{\partial\phi_0}{\partial r}\right)^2 + 1 = 0, \tag{5.110}$$

and

$$-\frac{\gamma\beta_0}{2}\frac{c_s^2}{r}\frac{\partial\phi_0}{\partial r}\frac{\partial\phi_0}{\partial\theta} = 0. \tag{5.111}$$

These may be solved to give

$$\phi_0 = i\sqrt{\frac{2}{\gamma\beta_0}}\frac{(r-1)}{c_s}. \tag{5.112}$$

From the $\mathcal{O}\left(\omega\right)$ terms we find the equations

$$\frac{\partial\phi_1}{\partial r} + \frac{1}{r} = 0, \tag{5.113}$$

and

$$v_A^2\left(\frac{\partial\phi_0}{\partial r}\right)^2 V_{\theta 0} + V_{\theta 0} = -\frac{\gamma\beta_0}{2}\frac{c_s^2}{r}\frac{\partial\phi_0}{\partial r}\frac{\partial\phi_1}{\partial\theta}. \tag{5.114}$$

Using the boundary conditions these yield the results

$$\phi_1 = -\ln r + im\left(6\theta - \pi\right), \tag{5.115}$$

and

$$V_{\theta 0} = -6m\left(\frac{\gamma\beta_0}{2}\right)^{3/2}\frac{c_s^3}{r\left(v_A^2 - \gamma\beta_0 c_s^2/2\right)}. \tag{5.116}$$

Substituting these values back into Equations (5.108) and (5.109) we have

$$v_r = \frac{1}{r}\exp\left(i\omega\sqrt{\frac{2}{\gamma\beta_0}}\frac{(r-1)}{c_s} + im\left(6\theta - \pi\right)\right), \tag{5.117}$$

$$v_\theta = -\frac{6m}{\omega}\left(\frac{\gamma\beta_0}{2}\right)^{3/2}\frac{c_s^3}{r^2\left(v_A^2-\gamma\beta_0 c_s^2/2\right)}\exp\left(i\omega\sqrt{\frac{2}{\gamma\beta_0}}\frac{(r-1)}{c_s^2}+im\left(6\theta-\pi\right)\right). \tag{5.118}$$

Alternatively these may be written in trigonometric form

$$v_r = \frac{1}{r}\sin\left(\omega\sqrt{\frac{2}{\gamma\beta_0}}\frac{(r-1)}{c_s}\right)\sin\left(m\left(6\theta-\pi\right)\right), \tag{5.119}$$

$$v_\theta = -\frac{6m}{\omega}\left(\frac{\gamma\beta_0}{2}\right)^{3/2}\frac{c_s^3}{r^2\left(v_A^2-\gamma\beta_0 c_s^2/2\right)}\cos\left(\omega\sqrt{\frac{2}{\gamma\beta_0}}\frac{(r-1)}{c_s}\right)\sin\left(m\left(6\theta-\pi\right)\right). \tag{5.120}$$

Equations (5.119) and (5.120) describe the behaviour of the incident and transmitted waves in the low- and high-β plasma respectively. The transmitted wave must be multiplied by the transmission coefficient found in the previous section to get the correct amplitude.

To find the behaviour of the converted wave we must assume that v_r is small in comparison to v_θ, so we let

$$v_r = \frac{V_{r0}}{\omega}\exp\left(\omega\phi_0+\phi_1\right), \tag{5.121}$$

$$v_\theta = \exp\left(\omega\phi_0+\phi_1\right), \tag{5.122}$$

where, as before, $\omega\phi_0 \gg \phi_1 \gg V_{r0}/\omega$ and ϕ_0, ϕ_1 and V_{r0} are functions of both r and θ.

On substitution into the Wave Equations (5.106) and (5.107) the $\mathcal{O}\left(\omega^2\right)$ terms give

$$-\frac{\gamma\beta_0}{2}\frac{c_s^2}{r}\frac{\partial\phi_0}{\partial r}\frac{\partial\phi_0}{\partial\theta} = 0, \tag{5.123}$$

$$v_A^2\left(\frac{\partial\phi_0}{\partial r}\right)^2+\frac{\left(\gamma\beta_0 c_s^2/2+v_A^2\right)}{r^2}\left(\frac{\partial\phi_0}{\partial\theta}\right)^2+1 = 0. \tag{5.124}$$

It is the $\partial\phi_0/\partial\theta$ term which must be equal to zero in the first equation, thus the second equation gives

$$\phi_0 = i\left(\frac{r^3}{3}-\frac{9}{8}\right). \tag{5.125}$$

We may then look to the $\mathcal{O}\left(\omega\right)$ equations

$$\frac{\gamma\beta_0}{2}c_s^2\left(\frac{\partial\phi_0}{\partial r}\right)^2 V_{r0}+V_{r0} = -\frac{\gamma\beta_0}{2}\frac{c_s^2}{r}\frac{\partial\phi_0}{\partial r}\frac{\partial\phi_1}{\partial\theta}-\frac{\gamma\beta_0}{2}\frac{c_s^2}{r\tan\theta}\frac{\partial\phi_0}{\partial r}, \tag{5.126}$$

$$v_A^2\left(\frac{\partial^2\phi_0}{\partial r^2}+2\frac{\partial\phi_0}{\partial r}\frac{\partial\phi_1}{\partial r}\right)+\left(\left(v_A^2\right)'+2\frac{v_A^2}{r}\right)\frac{\partial\phi_0}{\partial r} = 0. \tag{5.127}$$

These may be solved to give

$$\phi_1 = r^2+\ln r^{-2}+im\left(6\theta-\pi\right), \tag{5.128}$$

and

$$V_{r0} = \frac{\gamma\beta_0}{2}\frac{rc_s^2 v_A^2}{\left(v_A^2 - \gamma\beta_0 c_s^2/2\right)}\left(6m - \frac{i}{\tan\theta}\right). \tag{5.129}$$

Noting that $6m \gg 1/\tan\theta$ the second term in the bracket may be neglected.

Substituting these values into Equations (5.108) and (5.109) the converted component of the wave is described by

$$v_r = \frac{\gamma\beta_0}{2}\frac{6mc_s^2 v_A^2 e^{r^2}}{\omega r\left(v_A^2 - \gamma\beta_0 c_s^2/2\right)}\exp\left(i\omega\left(\frac{r^3}{3} - \frac{9}{8}\right) + im\left(6\theta - \pi\right)\right), \tag{5.130}$$

$$v_\theta = \frac{e^{r^2}}{r^2}\exp\left(i\omega\left(\frac{r^3}{3} - \frac{9}{8}\right) + im\left(6\theta - \pi\right)\right). \tag{5.131}$$

As before these may also be written in trigonometric form

$$v_r = \frac{\gamma\beta_0}{2}\frac{6mc_s^2 v_A^2 e^{r^2}}{\omega r\left(v_A^2 - \gamma\beta_0 c_s^2/2\right)}\sin\left(\omega\left(\frac{r^3}{3} - \frac{9}{8}\right)\right)\sin\left(m\left(6\theta - \pi\right)\right), \tag{5.132}$$

$$v_\theta = \frac{e^{r^2}}{r^2}\cos\left(\omega\left(\frac{r^3}{3} - \frac{9}{8}\right)\right)\sin\left(m\left(6\theta - \pi\right)\right). \tag{5.133}$$

Equations (5.132) and (5.133) describe the converted wave in the high-β plasma. As with the transmitted wave these must be multiplied by the corresponding conversion coefficient from the previous section to get the correct amplitude. The fast wave is negligible in the low-β plasma and so these solutions will be zero in this region.

In summary we have

$$\begin{array}{lll}
\text{Low } \beta & \text{Inc.} & v_r = \dfrac{1}{r}\sin\left(\omega\sqrt{\dfrac{2}{\gamma\beta_0}}\dfrac{(r-1)}{c_s}\right)\sin\left(m\left(6\theta - \pi\right)\right), \\
 & & v_\theta = -\left(\dfrac{\gamma\beta_0}{2}\right)^{3/2}\dfrac{6mc_s^3}{\omega r^2\left(v_A^2 - \gamma\beta_0 c_s^2/2\right)}\cos\left(\omega\sqrt{\dfrac{2}{\gamma\beta_0}}\dfrac{(r-1)}{c_s}\right)\sin\left(m\left(6\theta - \pi\right)\right), \\
\text{High } \beta & \text{Trans.} & v_r = \dfrac{B}{r}\sin\left(\omega\sqrt{\dfrac{2}{\gamma\beta_0}}\dfrac{(r-1)}{c_s}\right)\sin\left(m\left(6\theta - \pi\right)\right), \\
 & & v_\theta = -B\left(\dfrac{\gamma\beta_0}{2}\right)^{3/2}\dfrac{6mc_s^3}{\omega r^2\left(v_A^2 - \gamma\beta_0 c_s^2/2\right)}\cos\left(\omega\sqrt{\dfrac{2}{\gamma\beta_0}}\dfrac{(r-1)}{c_s}\right)\sin\left(m\left(6\theta - \pi\right)\right), \\
 & \text{Conv.} & v_r = A\dfrac{\gamma\beta_0}{2}\dfrac{6mc_s^2 v_A^2 e^{r^2}}{\omega r\left(v_A^2 - \gamma\beta_0 c_s^2/2\right)}\sin\left(\omega\left(\dfrac{r^3}{3} - \dfrac{9}{8}\right)\right)\sin\left(m\left(6\theta - \pi\right)\right), \\
 & & v_\theta = \dfrac{Ae^{r^2}}{r^2}\cos\left(\omega\left(\dfrac{r^3}{3} - \dfrac{9}{8}\right)\right)\sin\left(m\left(6\theta - \pi\right)\right),
\end{array}$$

where A and B are as defined by Equations (5.102) and (5.105).

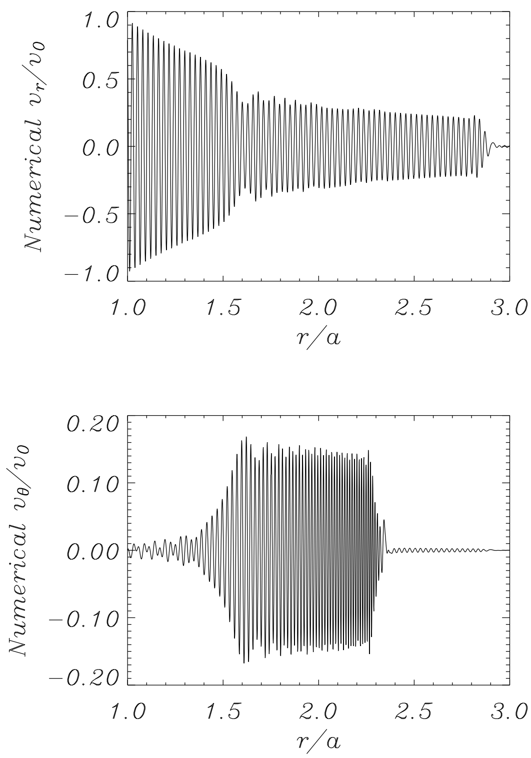

Figure 5.13: The numerical and analytical radial velocity and the numerical and analytical azimuthal velocity respectively from top left to bottom right. In all plots $\omega = 32\pi$, $m = 3$, $\theta = \pi/5$ and $t = 4.3$ Alfvén times.

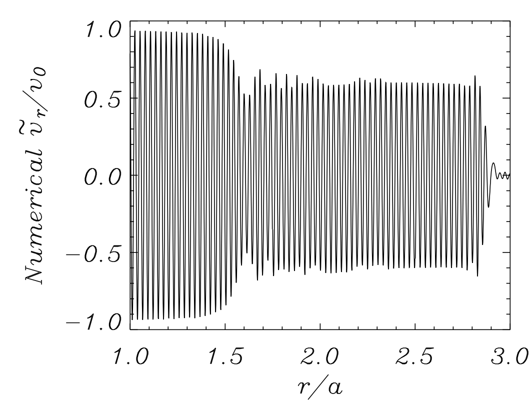

Figure 5.14: The numerical and analytical transformed radial velocity for $\omega = 32\pi$, $m = 3$, $\theta = \pi/5$ and $t = 4.3$ Alfvén times.

We know that the fast wave will have reached $r \approx 2.9$, and the slow wave $r \approx 2.35$, after $t = 4.3$ Alfvén times from Equations (5.53) and (5.55). Along with the transmission and conversion coefficients calculated from Equations (5.102) and (5.105) this information may be used to give analytical predictions of the behaviour of the radial and azimuthal velocities across the computational domain. The results of this are shown in Figure 5.13. On the left-hand side of this figure the numerical simulations for the radial and azimuthal velocity are displayed for frequency $\omega = 32\pi$ and wavenumber $m = 3$ at $\theta = \pi/5$ and $t = 4.3$ Alfvén times. On the right-hand side are the analytical predictions found using the WKB method. It is immediately clear that these predictions are not as accurate as the simpler one-dimensional cases in Chapters 3 and 4. Whilst the transmitted component of the wave seems to agree well with the numerical simulation, the amplitude of the converted component is over estimated. This suggests that energy is not conserved in this case.

This is especially clear once the amplitude dependence is removed from the radial velocity, as shown in Figure 5.14. The amplitude dependence for the incident and transmitted waves is clearly in excellent agreement as both are now constant. It is also clear that the amount of transmission predicted by Equation (5.102) is accurate. Additionally the phase is in good agreement for the incident, transmitted and converted components. However, the predicted amplitude of the converted wave does not agree. This may be due to the fact that the frequency is not sufficiently larger than the wavenumber, in violation of the initial assumptions. Thus combining the Cairns and Lashmore-Davies method and the WKB method models the behaviour of the incident and transmitted wave components well, but does not capture the correct amplitude of the converted wave.

5.5 Conclusions

Building upon the previous chapters we have examined mode conversion in a two-dimensional atmosphere with a radially-expanding magnetic field, representative of a coronal hole. Due to the geometry of the problem spherical coordinates were used and it was assumed that all variables are invariant in the ϕ direction. In the interest of simplicity gravitational acceleration was neglected in the model. This set-up is shown in Figure 5.1. In keeping with the previous studies a slow wave was driven from low- to high-β plasma, thus travelling upwards in this case. As the model is isothermal the sound speed remains constant but the Alfvén speed decreases as the wave propagates away from the surface (Figure 5.2).

The MacCormack method was used to numerically model the wave behaviour, the results of which are shown in Figure 5.3. Mode conversion clearly occurs as the incident wave passes through the region where the sound and Alfvén speeds are equal. Even with the amplitude variation a reduction in the amplitude of the transmitted wave is noticeable in the radial velocity and pressure. The converted component may be seen in the plots of the azimuthal velocity, and radial and azimuthal magnetic field. Using the WKB method (as described in Section 5.4.2) the amplitude dependence of the incident and transmitted waves was eliminated. The results of these transformations are shown in Figure 5.4. The mode conversion is much more obvious in this figure, particularly due to the amplitude decrease across $c_s = v_A$ seen in the plots of the radial velocity and pressure. Again the converted component is seen in the plots of the azimuthal velocity, and the radial and azimuthal magnetic field. In Section 5.3.1 the position of the fast and slow wavefronts was calculated. These are given by Equations (5.53) and (5.55) and are shown against one of the numerical simulations in Figure 5.5. The free parameters in the model are the azimuthal wavenumber m, and the driving frequency ω. The effect of varying these parameters for a fixed value of θ was studied in Section 5.3.2. As shown in Figure 5.6 this is a valid approach as the value of θ has no effect on the mode conversion. When m is small the majority of the incident wave is transmitted into the high-β plasma. As m increases the transmission decreases as more of the incident wave is converted into a high-β slow wave (Figure 5.7). The effect of varying the frequency is much less pronounced (Figure 5.8) and in this case the transmission increases as the frequency increases. These results are as expected based on previous chapters.

Section 5.4 concentrated on the use of analytical methods to find conversion and transmission coefficients and the wave behaviour throughout the domain. Firstly the conversion and transmission coefficients were found using the method developed by Cairns and Lashmore-Davies (1983), valid for small m. This method focuses on the mode-conversion region itself and uses differential equations derived from the local dispersion relations to describe the wave behaviour. The differential equations are combined to give a second-order differential equation, the solutions of which are known in terms of Parabolic Cylinder functions (see Abramowitz and Stegun (1964)). Thus the transmission and conversion coefficients, given by Equations (5.102) and (5.105), can be found without knowing an exact solution. These coefficients are similar in form to those found in Sections 3.4.1 and 4.4.1. In agreement with the numerical simulations these do indeed vary with both m and ω, illustrated in Figure 5.11. The agreement between the numerical simulations and analytical predictions is good, as shown in Figure 5.10. The amount of transmission calculated from the numerical simulations does not sit exactly on the predicted curve but these definitely follow the correct shape as long as m remains small. Looking at the variation of transmission with θ in the numerical simulations we see that the analytical prediction is good excepting the regions where the radial velocity falls to zero (Figure 5.12).

The WKB method was then used to find the wave behaviour away from the conversion region. Using the transmission and conversion coefficients given by Equations (5.102) and (5.105) the WKB solutions were matched across the mode-conversion region, giving a description of the entire domain. Figure 5.13 shows both the numerical and analytical results side by side. From these we can see that the incident and transmitted components of the wave have been captured well by the analytical approximations. But, whilst the phase of the converted component looks good, the amplitude is too large. This is especially clear when the amplitude dependence is removed from the plots of the radial velocity (Figure 5.14). This discrepancy is most likely due to the fact that the frequency is not sufficiently large in comparison to the wavenumber.

All the methods used to investigate mode conversion in one dimension have transferred well to two dimensions, particularly the Cairns and Lashmore-Davies method. We expand on this in the next chapter by looking at the more complex magnetic topology of a two-dimensional magnetic null point.

Chapter 6

MHD Mode Conversion around a 2D Magnetic Null Point

6.1 Introduction

In this chapter we investigate mode conversion in the vicinity of a two-dimensional magnetic null point. This extends the results of the previous chapter as we are looking at a more complex magnetic topology. As before, a combination of analytical approximations and numerical simulations is used. Wave behaviour around a two-dimensional null point has previously been studied by McLaughlin and Hood (2004). In a zero-β plasma a fast wave was driven towards a null point; as the wave approached the null it wrapped around it causing a build up of current. This was extended in McLaughlin and Hood (2006) which included a finite β allowing mode conversion to occur. In this case when driving a fast wave toward the null the effects of refraction and mode conversion were in competition with one another. The smaller the value of β_0 the more dominant the refraction effect. We are interested only in mode conversion, and in this chapter we look at the conversion of both slow and fast magnetoacoustic waves and the behaviour of all wave components is found.

6.2 2D Magnetic Null Point Model

The model atmosphere used for a two-dimensional null point is shown in Figure 6.1. The magnetic field lines are shown in black with the direction indicated on the field lines. The null point lies in the centre of the plot and is denoted by the blue cross. The green circle surrounding this shows where the sound and Alfvén speed are equal. A wave driven on the upper boundary will propagate towards the null point, passing from low- to high-β plasma as it does so. When the wave crosses this boundary mode conversion will take place.

6.2.1 Ideal MHD Equations

We use the ideal form of the MHD equations as given by Equations (1.28) – (1.35)

$$\rho\left(\frac{\partial}{\partial t}+\mathbf{v}\cdot\nabla\right)\mathbf{v}=-\nabla p+\frac{1}{\mu}\left(\nabla\times\mathbf{B}\right)\times\mathbf{B}, \tag{6.1}$$

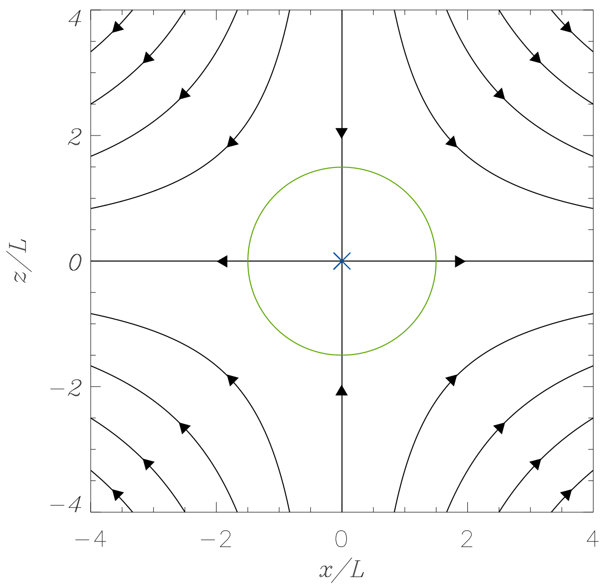

Figure 6.1: The equilibrium magnetic field for the two-dimensional null point model. The null point is depicted by the blue cross in the centre and the green circle shows where the sound and Alfvén speeds are equal. A wave driven on the upper boundary will propagate towards the null point crossing the mode-conversion region as it does so.

$$\frac{\partial \rho}{\partial t} + \nabla \cdot (\rho \mathbf{v}) = 0, \tag{6.2}$$

$$\frac{\partial \mathbf{B}}{\partial t} = \nabla \times (\mathbf{v} \times \mathbf{B}), \tag{6.3}$$

$$\left(\frac{\partial}{\partial t} + \mathbf{v} \cdot \nabla\right) p = \frac{\gamma p}{\rho} \left(\frac{\partial}{\partial t} + \mathbf{v} \cdot \nabla\right) \rho, \tag{6.4}$$

$$p = R\rho \frac{T}{\widetilde{\mu}}, \tag{6.5}$$

$$\nabla \cdot \mathbf{B} = 0, \tag{6.6}$$

where gravity has been neglected for simplicity. In these equations ρ is the mass density, $\mathbf{v}$ is the fluid velocity, p is the gas pressure, μ is the magnetic permeability, $\mathbf{B}$ is the magnetic induction, γ is the ratio of specific heats, R is the universal gas constant, T is the temperature and $\widetilde{\mu}$ is the mean molecular weight.

6.2.2 Equilibrium

The equilibrium magnetic field of a two-dimensional null point is given by $\mathbf{B}_0 = \frac{B_{00}}{L}(x, 0, -z)$ and the pressure and density are taken as constants. Under the equilibrium conditions of $\partial/\partial t = 0$ and $\mathbf{v} = 0$ the Equation of Motion becomes

$$\frac{1}{\mu}\left(\nabla\times\mathbf{B}_0\right)\times\mathbf{B}_0=0. \tag{6.7}$$

Thus the current density is zero and the magnetic field is potential.

6.2.3 Linearised MHD Equations

Equations (6.1) – (6.6) may be linearised about the above equilibrium by adding a small perturbation to each variable

$$\rho=\rho_0+\rho_1\left(x,z,t\right), \quad \mathbf{v}=\mathbf{v}_1\left(x,z,t\right), \quad p=p_0+p_1\left(x,z,t\right),$$

$$\mathbf{B}=\mathbf{B}_0+\mathbf{B}_1\left(x,z,t\right), \quad T=T_0+T_1\left(x,z,t\right), \tag{6.8}$$

where subscript 0 denotes equilibrium values and subscript 1 denotes perturbed values. These may then be substituted into the Ideal MHD equations; neglecting products of perturbed values gives the Linearised MHD equations.

$$\rho_0\frac{\partial\mathbf{v}}{\partial t}=-\nabla p+\frac{1}{\mu}\left(\nabla\times\mathbf{B}\right)\times\mathbf{B}_0, \tag{6.9}$$

$$\frac{\partial\rho}{\partial t}+\nabla\cdot\left(\rho_0\mathbf{v}\right)=0, \tag{6.10}$$

$$\frac{\partial\mathbf{B}}{\partial t}=\nabla\times\left(\mathbf{v}\times\mathbf{B}_0\right), \tag{6.11}$$

$$\frac{\partial p}{\partial t}+\left(\mathbf{v}\cdot\nabla\right)p_0=\frac{\gamma p_0}{\rho_0}\left(\frac{\partial\rho}{\partial t}+\left(\mathbf{v}\cdot\nabla\right)\rho_0\right), \tag{6.12}$$

$$\frac{p_1}{p_0}=\frac{\rho_1}{\rho_0}+\frac{T_1}{T_0}, \tag{6.13}$$

$$\nabla\cdot\mathbf{B}_1=0. \tag{6.14}$$

From this point onwards subscripts on perturbed variables are dropped and it is assumed that we are working with the linearised equations.

Assuming that all variables vary with x, z and t alone, Equations (6.9) – (6.12) may be written

$$\rho_0\frac{\partial v_x}{\partial t}=-\frac{\partial p}{\partial x}-\frac{B_{00}}{\mu L}z\left(\frac{\partial B_x}{\partial z}-\frac{\partial B_z}{\partial x}\right), \tag{6.15}$$

$$\rho_0\frac{\partial v_z}{\partial t}=-\frac{\partial p}{\partial z}+\frac{B_{00}}{\mu L}x\left(\frac{\partial B_z}{\partial x}-\frac{\partial B_x}{\partial z}\right), \tag{6.16}$$

$$\frac{\partial B_x}{\partial t}=-\frac{B_{00}}{L}z\frac{\partial v_x}{\partial z}-\frac{B_{00}}{L}v_x-\frac{B_{00}}{L}x\frac{\partial v_z}{\partial z}, \tag{6.17}$$

$$\frac{\partial B_z}{\partial t}=\frac{B_{00}}{L}x\frac{\partial v_z}{\partial x}+\frac{B_{00}}{L}v_z+\frac{B_{00}}{L}z\frac{\partial v_x}{\partial x}, \tag{6.18}$$

$$\frac{\partial p}{\partial t} = -\gamma p_0 \left(\frac{\partial v_x}{\partial x} + \frac{\partial v_z}{\partial z} \right). \tag{6.19}$$

As none of the above equations depend explicitly on the perturbed density the equation describing the variation of density with respect to time (Equation (6.10)) may be neglected.

The above equations may be combined to give a pair of wave equations by differentiating Equations (6.15) and (6.16) with respect to t and substituting from the remaining equations. This yields the equations

$$\begin{aligned}\frac{\partial^2 v_x}{\partial t^2} = \left(c_s^2 + \frac{B_{00}^2}{\mu\rho_0 L^2} z^2 \right) \frac{\partial^2 v_x}{\partial x^2} + \frac{B_{00}^2}{\mu\rho_0 L^2} z^2 \frac{\partial^2 v_x}{\partial z^2} + \frac{B_{00}^2}{\mu\rho_0 L^2} xz \frac{\partial^2 v_z}{\partial x^2} + c_s^2 \frac{\partial^2 v_z}{\partial x \partial z} + \\ + \frac{B_{00}^2}{\mu\rho_0 L^2} xz \frac{\partial^2 v_z}{\partial z^2} + 2\frac{B_{00}^2}{\mu\rho_0 L^2} z \frac{\partial v_x}{\partial z} + 2\frac{B_{00}^2}{\mu\rho_0 L^2} z \frac{\partial v_z}{\partial x},\end{aligned} \tag{6.20}$$

$$\begin{aligned}\frac{\partial^2 v_z}{\partial t^2} = \frac{B_{00}^2}{\mu\rho_0 L^2} xz \frac{\partial^2 v_x}{\partial x^2} + c_s^2 \frac{\partial^2 v_x}{\partial x \partial z} + \frac{B_{00}^2}{\mu\rho_0 L^2} xz \frac{\partial^2 v_x}{\partial z^2} + \frac{B_{00}^2}{\mu\rho_0 L^2} x^2 \frac{\partial^2 v_z}{\partial x^2} + \\ + \left(c_s^2 + \frac{B_{00}^2}{\mu\rho_0 L^2} x^2 \right) \frac{\partial^2 v_z}{\partial z^2} + 2\frac{B_{00}^2}{\mu\rho_0 L^2} x \frac{\partial v_x}{\partial z} + 2\frac{B_{00}^2}{\mu\rho_0 L^2} x \frac{\partial v_z}{\partial x},\end{aligned} \tag{6.21}$$

where $c_s^2 = \gamma p_0/\rho_0$ is the square of the sound speed.

6.2.3.1 Non-Dimensionalisation

To aid with the numerical simulations the above equations are made dimensionless. This is done by setting $x = L\bar{x}$, $z = L\bar{z}$, $t = \tau\bar{t}$, $\rho_0 = \bar{\rho}_0$, $p_0 = B_{00}^2 \bar{p}_0 / (2\mu)$, $\mathbf{B}_0 = B_{00}\bar{\mathbf{B}}_0$, $p = B_{00}^2 \bar{p} / (2\mu)$, $\mathbf{v} = v_0 \bar{\mathbf{v}}$, and $\mathbf{B} = B_{00}\bar{\mathbf{B}}$. The lengthscales against which the variables have been made dimensionless are related by $v_0 = L/\tau$. Note that we have the relations

$$\bar{\mathbf{B}}_0 = (\bar{x}, 0, -\bar{z}), \tag{6.22}$$

and

$$c_s^2 = \frac{\gamma B_{00}^2}{2\mu\rho_0} \bar{p}_0, \qquad v_A^2 = \frac{B_{00}^2}{\mu\rho_0} \left(\bar{x}^2 + \bar{z}^2 \right). \tag{6.23}$$

Defining $v_0^2 = B_{00}^2 / (\mu\rho_0) = c_{s0}^2$ the dimensionless sound and Alfvén speeds are then given by the equations

$$\bar{c}_s^2 = \frac{\gamma}{2} \bar{p}_0, \qquad \bar{v}_A^2 = \bar{x}^2 + \bar{z}^2. \tag{6.24}$$

The plasma β, given by the ratio of the gas pressure to the magnetic pressure, is then

$$\bar{\beta} = \frac{\bar{p}_0}{(\bar{x}^2 + \bar{z}^2)}. \tag{6.25}$$

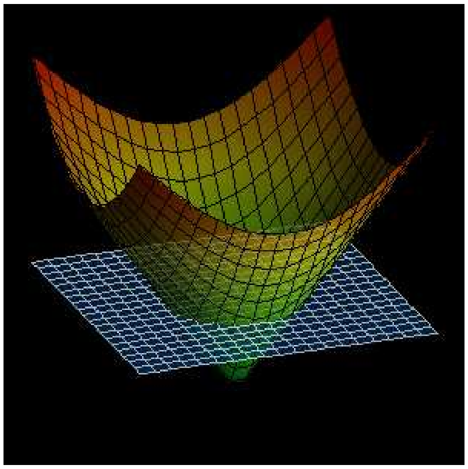

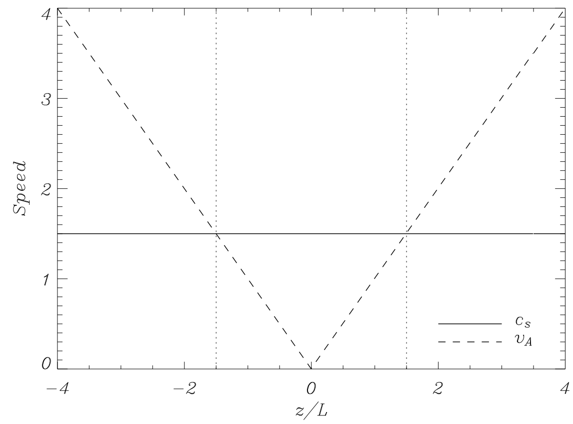

Figure 6.2: These plots show how the sound and Alfvén speeds vary with x and z. The sound speed is constant with x and z, whilst the Alfvén speed varies with position. The left-hand plot shows the speed variation in two dimensions. The right-hand plots takes a cut along $x = 0$ - the $c_s = v_A$ region is denoted by the dotted lines, in between these lines the plasma is high β and outside it is low β.

The sound and Alfvén speeds are equal when $\bar{\beta} = 2/\gamma\,(= 6/5)$ and the radius, $\bar{r}$, at which this occurs may be chosen by setting

$$\bar{p}_0 = \frac{2}{\gamma}\bar{r}^2, \tag{6.26}$$

where $\bar{r}^2 = \bar{x}^2 + \bar{z}^2$. If we choose to set the mode-conversion region at a radius of $r = 1.5$ then the sound and Alfvén speeds vary as shown in Figure 6.2.

Substituting the non-dimensionalised variables into Equations (6.15) – (6.19) the dimensionless, Linearised MHD equations are given by

$$\frac{\partial \bar{v}_x}{\partial \bar{t}} = -\frac{1}{2}\frac{\partial \bar{p}}{\partial \bar{x}} - \bar{z}\left(\frac{\partial \bar{B}_x}{\partial \bar{z}} - \frac{\partial \bar{B}_z}{\partial \bar{x}}\right), \tag{6.27}$$

$$\frac{\partial \bar{v}_z}{\partial \bar{t}} = -\frac{1}{2}\frac{\partial \bar{p}}{\partial \bar{z}} + \bar{x}\left(\frac{\partial \bar{B}_z}{\partial \bar{x}} - \frac{\partial \bar{B}_x}{\partial \bar{z}}\right), \tag{6.28}$$

$$\frac{\partial \bar{B}_x}{\partial \bar{t}} = -\bar{z}\frac{\partial \bar{v}_x}{\partial \bar{z}} - \bar{v}_x - \bar{x}\frac{\partial \bar{v}_z}{\partial \bar{z}}, \tag{6.29}$$

$$\frac{\partial \bar{B}_z}{\partial \bar{t}} = \bar{x}\frac{\partial \bar{v}_z}{\partial \bar{x}} + \bar{v}_z + \bar{z}\frac{\partial \bar{v}_x}{\partial \bar{x}}, \tag{6.30}$$

$$\frac{\partial \bar{p}}{\partial \bar{t}} = -\gamma\bar{p}_0\left(\frac{\partial \bar{v}_x}{\partial \bar{x}} + \frac{\partial \bar{v}_z}{\partial \bar{z}}\right). \tag{6.31}$$

As before, Equations (6.27) – (6.31) may be combined to give a pair of dimensionless wave equations by differentiating Equations (6.27) and (6.28) with respect to t and substituting from the remaining equations.

The dimensionless wave equations are

$$\frac{\partial^2 \bar{v}_x}{\partial \bar{t}^2} = \left(\bar{c}_s^2 + \bar{z}^2\right) \frac{\partial^2 \bar{v}_x}{\partial \bar{x}^2} + \bar{z}^2 \frac{\partial^2 \bar{v}_x}{\partial \bar{z}^2} + \bar{x}\bar{z}\frac{\partial^2 \bar{v}_z}{\partial \bar{x}^2} + \bar{c}_s^2 \frac{\partial^2 \bar{v}_z}{\partial \bar{x}\partial \bar{z}} + \bar{x}\bar{z}\frac{\partial^2 \bar{v}_z}{\partial \bar{z}^2} + 2\bar{z}\frac{\partial \bar{v}_x}{\partial \bar{z}} + 2\bar{z}\frac{\partial \bar{v}_z}{\partial \bar{x}}, \tag{6.32}$$

$$\frac{\partial^2 \bar{v}_z}{\partial \bar{t}^2} = \bar{x}\bar{z}\frac{\partial^2 \bar{v}_x}{\partial \bar{x}^2} + \bar{c}_s^2 \frac{\partial^2 \bar{v}_x}{\partial \bar{x}\partial \bar{z}} + \bar{x}\bar{z}\frac{\partial^2 \bar{v}_x}{\partial \bar{z}^2} + \bar{x}^2 \frac{\partial^2 \bar{v}_z}{\partial \bar{x}^2} + \left(\bar{c}_s^2 + \bar{x}^2\right) \frac{\partial^2 \bar{v}_z}{\partial \bar{z}^2} + 2\bar{x}\frac{\partial \bar{v}_x}{\partial \bar{z}} + 2\bar{x}\frac{\partial \bar{v}_z}{\partial \bar{x}}. \tag{6.33}$$

Henceforth the bars on dimensionless quantities are dropped and it is assumed that we are working with the dimensionless equations.

6.3 Numerical Simulations

Equations (6.27) – (6.31) are solved numerically using the MacCormack method in two dimensions, as was done in Chapter 5. This method uses a combination of predictor and corrector steps; we choose to use backward differencing for the predictor steps and forward differencing for the corrector steps. This ensures that we are using the more accurate corrected values on the upper boundary where the wave is driven into the system.

We drive waves on the upper boundary with frequencies of $\omega = 4\pi$, 10π and 16π which correspond in real terms to frequencies of 0.21 s^{-1}, 0.52 s^{-1} and 0.84 s^{-1} and periods of 30 s, 12 s and 7.5 s respectively. In calculating these values we have assumed the typical lengthscale of 10 Mm to be the distance between the null point and the conversion region and the typical Alfvén speed to be 1000 km s^{-1}. As for the previous chapters the driving frequencies are much larger than the coronal acoustic cutoff frequency, $\Omega_{ac} = 0.001$ s^{-1} (Roberts, 2004), so this does not affect the simulations.

6.3.1 Velocity Parallel and Perpendicular to the Magnetic Field

At this point it is useful to note that in the low-β plasma a slow wave will travel parallel to the magnetic field and a fast wave perpendicular to the magnetic field. Thus, in order to drive a pure slow or fast wave, we need to work with the velocity components parallel and perpendicular to the magnetic field rather than using v_x and v_z. If

$$\mathbf{v} = v_{\|} \left(\frac{\mathbf{B}_0}{\sqrt{\mathbf{B}_0 \cdot \mathbf{B}_0}}\right) - v_{\perp} \left(\frac{\nabla A_0}{\sqrt{\mathbf{B}_0 \cdot \mathbf{B}_0}}\right), \tag{6.34}$$

where $\mathbf{A} = (0, A_0, 0)$ is the vector potential, then $A_0 = -xz$ and the parallel and perpendicular components of the velocity are given by

$$v_{\|} = \frac{xv_x - zv_z}{\sqrt{x^2 + z^2}}, \tag{6.35}$$

and

$$v_{\perp} = \frac{zv_x + xv_z}{\sqrt{x^2 + z^2}}. \tag{6.36}$$

By driving either $v_\parallel$ or $v_\perp$ on the upper boundary we may drive either a slow wave or a fast wave towards the magnetic null point.

It is possible to rewrite Equations (6.27) – (6.31) in terms of the variables $v_\perp$ and $v_\parallel$

$$\frac{\partial v_\parallel}{\partial t} = -\frac{1}{2\sqrt{x^2+z^2}}\left(x\frac{\partial p}{\partial x} + z\frac{\partial p}{\partial z}\right), \tag{6.37}$$

$$\frac{\partial v_\perp}{\partial t} = -\frac{1}{2\sqrt{x^2+z^2}}\left(z\frac{\partial p}{\partial x} + x\frac{\partial p}{\partial z}\right) + \sqrt{x^2+z^2}\left(\frac{\partial B_z}{\partial x} - \frac{\partial B_x}{\partial z}\right), \tag{6.38}$$

$$\frac{\partial B_x}{\partial t} = -\sqrt{x^2+z^2}\frac{\partial v_\perp}{\partial z} - \frac{z}{\sqrt{x^2+z^2}}v_\perp, \tag{6.39}$$

$$\frac{\partial B_z}{\partial t} = \sqrt{x^2+z^2}\frac{\partial v_\perp}{\partial x} + \frac{x}{\sqrt{x^2+z^2}}v_\perp, \tag{6.40}$$

$$\begin{aligned}\frac{\partial p}{\partial t} = -\gamma p_0 \Bigg(&\frac{x}{\sqrt{x^2+z^2}}\frac{\partial v_\parallel}{\partial x} - \frac{z}{\sqrt{x^2+z^2}}\frac{\partial v_\parallel}{\partial z} - \frac{\left(x^2-z^2\right)}{\left(x^2+z^2\right)^{3/2}}v_\parallel + \frac{z}{\sqrt{x^2+z^2}}\frac{\partial v_\perp}{\partial x} + \\ &+ \frac{x}{\sqrt{x^2+z^2}}\frac{\partial v_\perp}{\partial z} - \frac{2xz}{\left(x^2+z^2\right)^{3/2}}v_\perp\Bigg).\end{aligned} \tag{6.41}$$

In terms of the parallel and perpendicular velocity components the wave equations are given by

$$\begin{aligned}\frac{\partial^2 v_\parallel}{\partial t^2} = c_s^2\Bigg(&\frac{x^2}{\left(x^2+z^2\right)}\frac{\partial^2 v_\parallel}{\partial x^2} - \frac{2xz}{\left(x^2+z^2\right)}\frac{\partial^2 v_\parallel}{\partial x\partial z} + \frac{z^2}{\left(x^2+z^2\right)}\frac{\partial^2 v_\parallel}{\partial z^2} - \frac{x\left(x^2-3z^2\right)}{\left(x^2+z^2\right)^2}\frac{\partial v_\parallel}{\partial x} + \\ &+ \frac{z\left(3x^2-z^2\right)}{\left(x^2+z^2\right)^2}\frac{\partial v_\parallel}{\partial z} + \frac{\left(x^4-10x^2z^2+z^4\right)}{\left(x^2+z^2\right)^3}v_\parallel + \frac{xz}{\left(x^2+z^2\right)}\frac{\partial^2 v_\perp}{\partial x^2} + \\ &+ \frac{\left(x^2-z^2\right)}{\left(x^2+z^2\right)}\frac{\partial^2 v_\perp}{\partial x\partial z} - \frac{xz}{\left(x^2+z^2\right)}\frac{\partial^2 v_\perp}{\partial z^2} - \frac{4x^2z}{\left(x^2+z^2\right)^2}\frac{\partial v_\perp}{\partial x} + \\ &+ \frac{4xz^2}{\left(x^2+z^2\right)^2}\frac{\partial v_\perp}{\partial z} + \frac{6xz\left(x^2-z^2\right)}{\left(x^2+z^2\right)^3}v_\perp\Bigg),\end{aligned} \tag{6.42}$$

$$\begin{aligned}\frac{\partial^2 v_\perp}{\partial t^2} = &\frac{c_s^2 xz}{\left(x^2+z^2\right)}\frac{\partial^2 v_\parallel}{\partial x^2} + \frac{c_s^2\left(x^2-z^2\right)}{\left(x^2+z^2\right)}\frac{\partial^2 v_\parallel}{\partial x\partial z} - \frac{c_s^2 xz}{\left(x^2+z^2\right)}\frac{\partial^2 v_\parallel}{\partial z^2} - \frac{2c_s^2 z\left(x^2-z^2\right)}{\left(x^2+z^2\right)^2}\frac{\partial v_\parallel}{\partial x} - \\ &- \frac{2c_s^2 x\left(x^2-z^2\right)}{\left(x^2+z^2\right)^2}\frac{\partial v_\parallel}{\partial z} + \frac{6c_s^2 xz\left(x^2-z^2\right)}{\left(x^2+z^2\right)^3}v_\parallel + \left(\frac{c_s^2 z^2}{\left(x^2+z^2\right)} + v_A^2\right)\frac{\partial^2 v_\perp}{\partial x^2} + \\ &+ \frac{2c_s^2 xz}{\left(x^2+z^2\right)}\frac{\partial^2 v_\perp}{\partial x\partial z} + \left(\frac{c_s^2 x^2}{\left(x^2+z^2\right)} + v_A^2\right)\frac{\partial^2 v_\perp}{\partial z^2} + \left(\frac{c_s^2 x\left(x^2-3z^2\right)}{\left(x^2+z^2\right)^2} + 2x\right)\frac{\partial v_\perp}{\partial x} - \\ &- \left(\frac{c_s^2 z\left(3x^2-z^2\right)}{\left(x^2+z^2\right)^2} - 2z\right)\frac{\partial v_\perp}{\partial z} - \left(\frac{2c_s^2\left(x^4-4x^2z^2+z^4\right)}{\left(x^2+z^2\right)^3} + 1\right)v_\perp.\end{aligned} \tag{6.43}$$

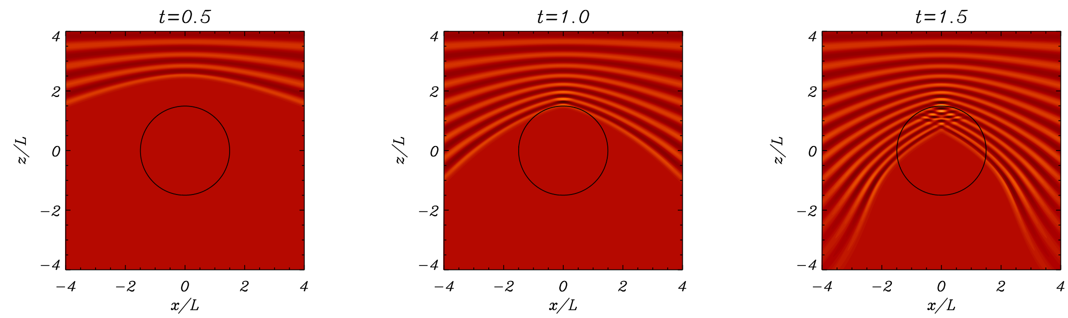

Figure 6.3: Contour plots of the perpendicular velocity component for $\omega = 16\pi$ at $t = 0.5$, 1.0 and 1.5 Alfvén times respectively from left to right. The black circle shows the position where $c_s = v_A$ and the null point lies at the origin in the centre of this circle.

6.3.2 Driving $v_\perp$

To drive the perpendicular velocity component, which is predominantly a fast wave, on the upper boundary we set $v_\perp = \sin\omega t$ and $v_\parallel = 0$. The simulations are run for $-6 \leq x \leq 6$, $-6 \leq z \leq 4$ and $0 \leq t \leq 2.3$ Alfven times, where $\delta x = \delta z = 0.013$ and $\delta t = 0.0005$. The only free parameter in this case is the driving frequency (ω) which is introduced through the conditions on the upper boundary. The boundary conditions on the upper boundary are given by

$$v_x = \frac{z}{\sqrt{x^2+z^2}}\sin\omega t, \quad v_z = \frac{x}{\sqrt{x^2+z^2}}\sin\omega t, \tag{6.44}$$

and using Equations (6.29) – (6.31) the remaining conditions are given by

$$B_x = \frac{z}{\omega\sqrt{x^2+z^2}}\left(\cos\omega t - 1\right), \quad B_z = \frac{x}{\omega\sqrt{x^2+z^2}}\left(1-\cos\omega t\right), \quad p = \frac{2\gamma p_0 xz}{\omega\left(x^2+z^2\right)^{3/2}}. \tag{6.45}$$

For the side boundaries we simply choose to use open boundary conditions

$$\frac{\partial v_x}{\partial x} = 0, \quad \frac{\partial v_z}{\partial x} = 0, \quad \frac{\partial B_x}{\partial x} = 0, \quad \frac{\partial B_z}{\partial x} = 0, \quad \frac{\partial p}{\partial x} = 0. \tag{6.46}$$

The boundary conditions on the lower boundary are less important, as the simulation is terminated before any reflection effects from this boundary can affect the incoming waves. On this boundary the conditions are given by

$$\frac{\partial v_x}{\partial z} = 0, \quad \frac{\partial v_z}{\partial z} = 0, \quad \frac{\partial B_x}{\partial z} = 0, \quad B_z = 0, \quad \frac{\partial p}{\partial z} = 0. \tag{6.47}$$

6.3.2.1 Wave Properties

We are driving a fast wave on the upper boundary which propagates from low- to high-β plasma. As can be seen in Figure 6.3 the wave slows as it approaches the magnetic null point, where the Alfvén speed goes to zero. The edges of the wavefront propagate faster than the centre causing it to wrap around the null

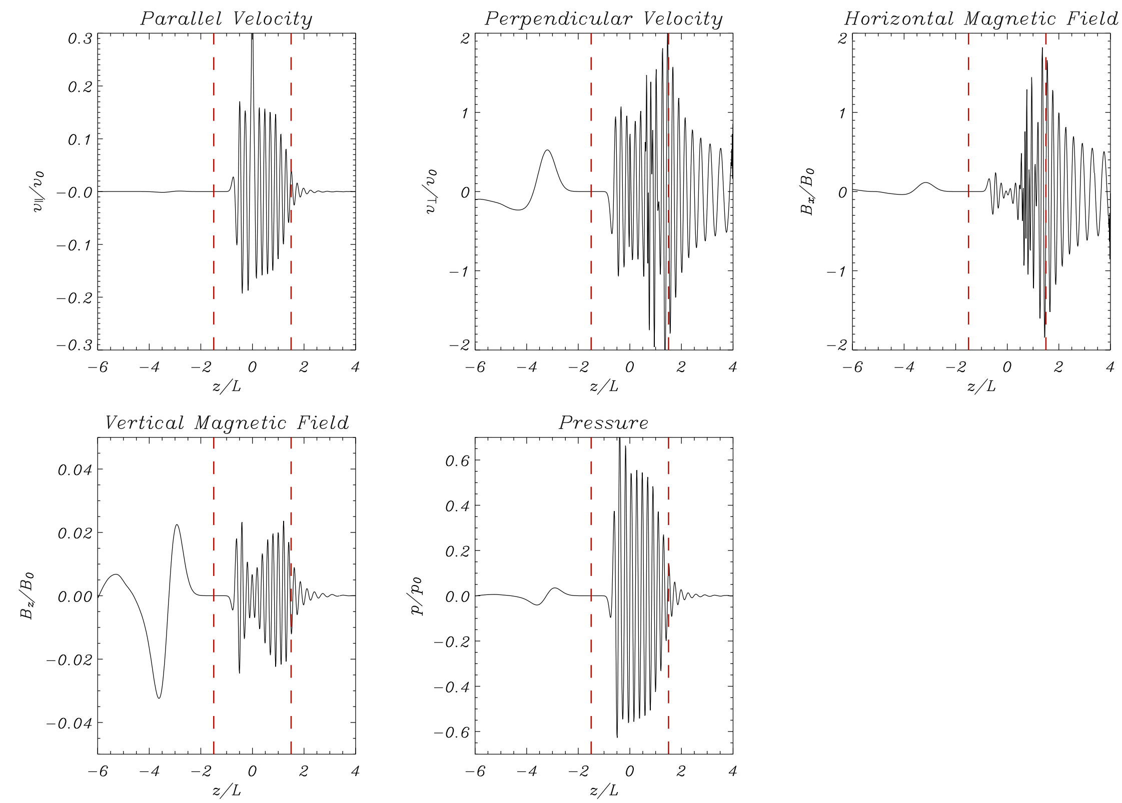

Figure 6.4: Results of the numerical simulation with $\omega = 16\pi$ at $t = 2.3$ Alfvén times for a cut taken along $x = 0$. The plots show the parallel and perpendicular velocity, the horizontal and vertical magnetic field, and the pressure respectively from top left to bottom right. The red dashed line indicates the regions where $c_s = v_A$.

(as found in McLaughlin and Hood (2004)). This means that only a portion of the wavefront will actually cross the mode-conversion region. To observe the mode conversion a cut is taken along $x = 0$ where the wavefront hits the conversion region tangentially.

As the incident fast wave hits the mode-conversion region it will split into a transmitted slow wave and a converted fast wave in the high-β plasma. This is shown in Figure 6.4 where we see the parallel and perpendicular velocity, the horizontal and vertical magnetic field, and the pressure respectively. These are the results of a numerical simulation with driving frequency $\omega = 16\pi$ shown at $t = 2.3$ Alfvén times. In the plots of the perpendicular velocity, and horizontal and vertical magnetic field two distinct waves can be seen in the high-β plasma. The two modes may be distinguished by their different amplitude dependencies and phase behaviour. The mode in front is the converted fast wave component and behind this is the transmitted slow wave. Both waves are also present in the plots of the parallel velocity and pressure, but the slow wave is only visible as interference with the fast wave. There is also a wave seen in the low-β plasma in the left-hand side of each plot. This is has been introduced into the system by boundary effects on the lower boundary and can be ignored as the simulation has been stopped before this causes any interference.

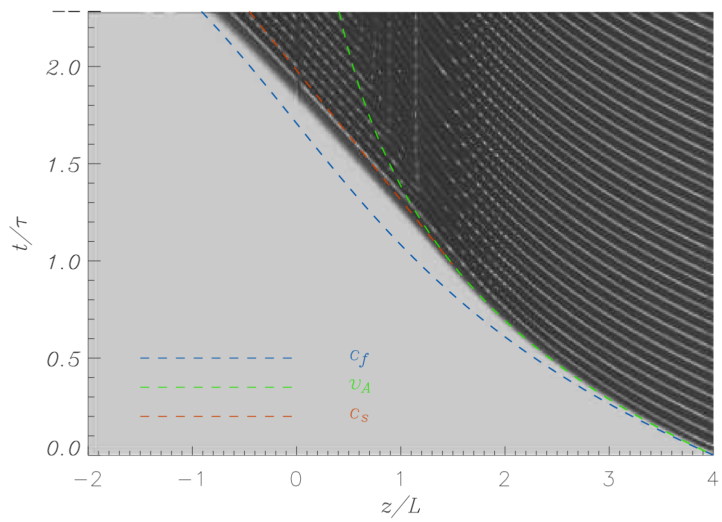

Figure 6.5: Surface plot of the perpendicular velocity for $\omega = 16\pi$ along $x = 0$. The red dashed line shows the position of the acoustic mode, the green dashed line the position of the magnetic mode, and the blue dashed line the position of the fast mode.

It is possible to calculate the position of the various wavefronts in the simulation. In the low-β plasma the fast wave will travel at approximately the Alfvén speed

$$\frac{\mathrm{d}z}{\mathrm{d}t} = -v_A = -\sqrt{x^2 + z^2}. \tag{6.48}$$

Focusing along the cut $x = 0$, this reduces to

$$\frac{\mathrm{d}z}{\mathrm{d}t} = -z. \tag{6.49}$$

Using the initial condition $z = 4$ when $t = 0$ gives the solution

$$z = 4e^{-t}. \tag{6.50}$$

This tells us that the fast wave will reach the mode-conversion region when $t = 1$ Alfvén time, and at $t = 2.3$ Alfvén times the high-β slow wave will have reached $z \approx 0.41$. Similarly the position of the fast wave in the high-β plasma will be given by the equation

$$\frac{\mathrm{d}z}{\mathrm{d}t} = -c_s, \tag{6.51}$$

which has the solution

$$z = c_s \left(\ln \frac{8}{3} - t \right) + 1.5, \tag{6.52}$$

and so the converted wave will have reached $z \approx -0.45$ at $t = 2.3$ Alfvén times. These predictions are in excellent agreement with the numerical simulations shown in Figure 6.4.

To calculate the position of the fast mode throughout the domain we use the equation

$$\frac{\mathrm{d}z}{\mathrm{d}t} = -c_f = -\sqrt{c_s^2 + v_A^2}. \tag{6.53}$$

Along $x = 0$ this simplifies to

$$\frac{\mathrm{d}z}{\mathrm{d}t} = -\sqrt{c_s^2 + z^2}, \tag{6.54}$$

which has the solution

$$t = \ln\left|\frac{4 + \sqrt{c_s^2 + 16}}{z + \sqrt{c_s^2 + z^2}}\right|. \tag{6.55}$$

Figure 6.5 shows the perpendicular velocity for a numerical simulation with driving frequency $\omega = 16\pi$. Overplotted are the paths predicted by Equations (6.50), (6.52) and (6.55). The magnetic mode is the fast wave in the low-β plasma and the slow wave in the high-β plasma. The acoustic mode is only present once the incident wave passes into the high-β plasma and is the fast wave in this region. The final path is that predicted by the fast speed, c_f, which follows the fast wave throughout the domain. The path predicted by the fast speed does not follow the actual wave behaviour as well as those predicted by Equations (6.50) and (6.52).

6.3.2.2 Effect of Varying the Driving Frequency

The only free parameter in the numerical simulation in this case is the driving frequency. In this section we examine the effect that variation of this parameter has on the amount of the incident wave that is transmitted and converted into the high-β plasma. To do this we run the simulation for three different values of ω: 4π, 10π and 16π. The results of these simulations at $t = 2.3$ Alfvén times are shown in Figure 6.6. Without knowing the amplitude dependence of the incoming wave it is difficult to determine the wave behaviour. But the amount of conversion does seem to be decreasing as ω increases suggesting that the transmission is increasing. This agrees with our findings in Chapters 3, 4 and 5.

6.3.3 Driving $v_\|$

Another option is to drive a slow wave on the upper boundary. This can be done by driving the parallel component of the velocity, $v_\| = \sin\omega t$, and setting the perpendicular component to zero, $v_\perp = 0$. As for the previous case the simulations are run for $-6 \le x \le 6$, $-6 \le z \le 4$ and $0 \le t \le 4.6$ Alfvén times. The driving frequency is the only free parameter, which is introduced through the conditions imposed on the upper boundary. These are given by

$$v_x = \frac{x}{\sqrt{x^2 + z^2}}\sin\omega t, \qquad v_z = -\frac{z}{\sqrt{x^2 + z^2}}\sin\omega t, \tag{6.56}$$

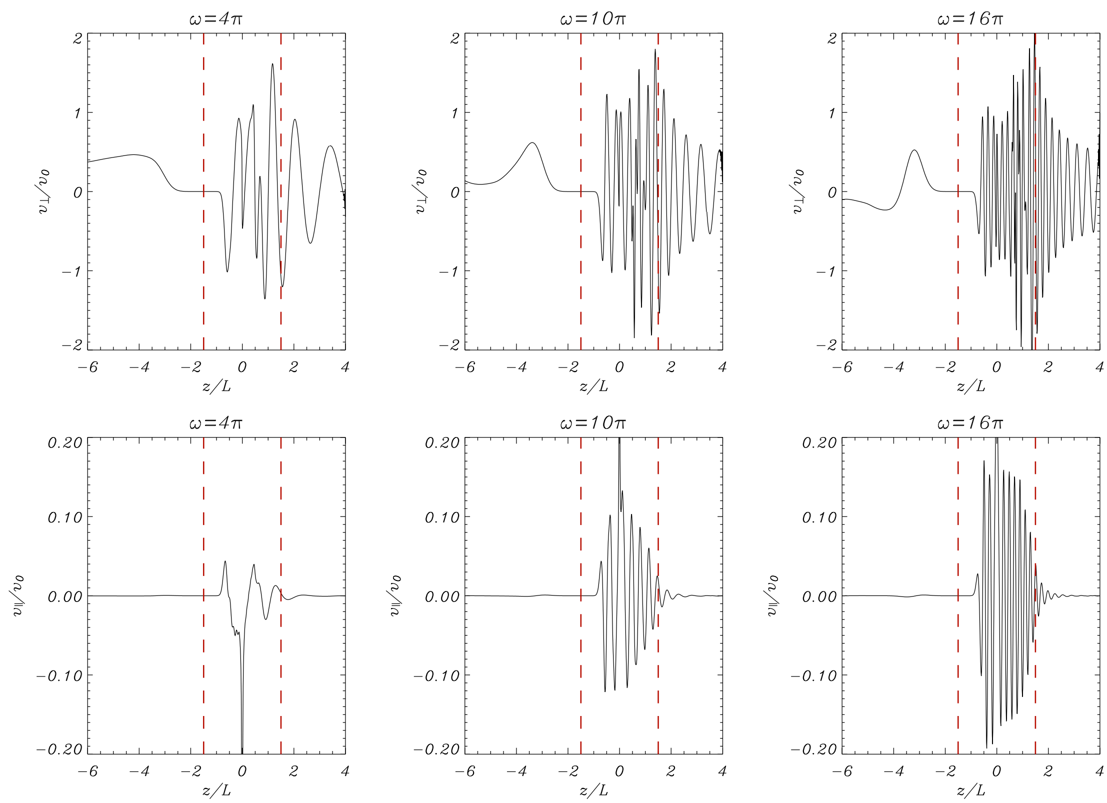

Figure 6.6: *Top*: Perpendicular velocity at $t = 2.3$ Alfvén times for $\omega = 4\pi$, 10π and 16π respectively from left to right.
Bottom: Parallel velocity at $t = 2.3$ Alfvén times for $\omega = 4\pi$, 10π and 16π respectively from left to right. The red dashed lines indicate where $c_s = v_A$.

and through a process of trial and error we choose the remaining boundary conditions to be

$$\frac{\partial B_x}{\partial z} = 0, \qquad B_z = 0, \qquad \frac{\partial p}{\partial z} = 0. \tag{6.57}$$

On the side boundaries we simply choose to use open boundary conditions

$$\frac{\partial v_x}{\partial x} = 0, \qquad \frac{\partial v_z}{\partial x} = 0, \qquad \frac{\partial B_x}{\partial x} = 0, \qquad \frac{\partial B_z}{\partial x} = 0, \qquad \frac{\partial p}{\partial x}. \tag{6.58}$$

The boundary conditions on the lower boundary are less important as the simulation is terminated before the wave reaches this point in order to eliminate reflection effects. On this boundary the conditions are given by

$$\frac{\partial v_x}{\partial z} = 0, \qquad \frac{\partial v_z}{\partial z} = 0, \qquad \frac{\partial B_x}{\partial z} = 0, \qquad B_z = 0, \qquad \frac{\partial p}{\partial z} = 0. \tag{6.59}$$

When driving $v_\parallel$ on the upper boundary components of both the slow and fast wave are introduced, as may be seen in Figure 6.7. This is because the wave driven on the upper boundary does not propagate exactly along the magnetic field lines. In order to drive a pure slow magnetoacoustic wave the wavefront

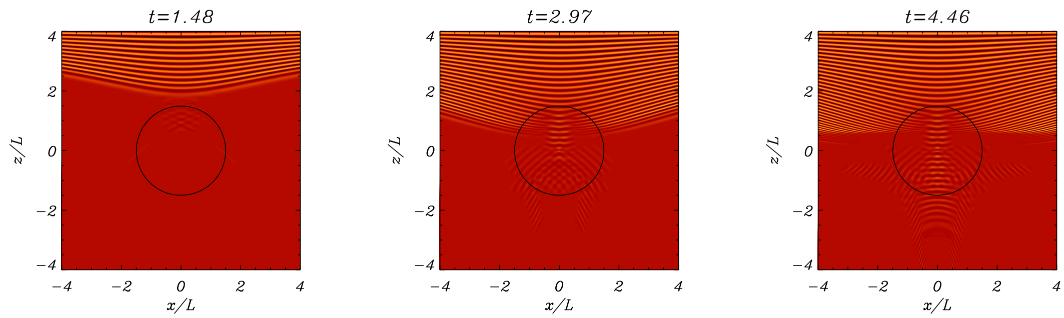

Figure 6.7: Contour plots of the parallel velocity component for $\omega = 16\pi$ at $t = 1.48$, 2.97 and 4.46 Alfvén times respectively from left to right. The black circle shows the position where $c_s = v_A$ and the null point lies at the origin in the centre of this circle.

driven on the upper boundary must be curved, so as to travel along the field lines.

From Section 6.3.1 we know that the magnetic field lines are given by constant values of $A_0 = -xz$. Using the Cauchy-Riemann equations we find that the orthogonal curves to A_0 are given by

$$\phi = -\frac{1}{2}\left(x^2 - z^2\right), \tag{6.60}$$

where ϕ is constant. We know that when $t = 0$ at $x = 0$ we will have $z = 4$, this allows us to calculate $\phi = 8$. Rearranging Equation (6.60) we find an expression for z_0

$$z_0 = \sqrt{16 + x_0^2}. \tag{6.61}$$

If we want to know how a point on the wavefront evolves then it will have a constant value of A_0, thus

$$xz = x_0 z_0. \tag{6.62}$$

In order to drive a wavefront that will pass through $z = 4$ we must have

$$x_0 = \pm 2\sqrt{\sqrt{x^2+4} - 2}. \tag{6.63}$$

To drive a wave which is constant along the field lines we must calculate the time at which $z = 4$ for each value of x_0. This may be done using Charpit's method. This finds a system of ordinary differential equations describing the wave behaviour along the characteristic curve s for the partial differential equation

$$F(\psi, p, q, \omega, x, z, t) = 0, \tag{6.64}$$

where $p = \partial\psi/\partial x$ and $q = \partial\psi/\partial z$, as described in Section 6.4.1. If the parallel and perpendicular wavenumbers are given by

$$k_\parallel = \frac{xp - zq}{\sqrt{x^2+z^2}} \qquad \text{and} \qquad k_\perp = \frac{zp + xq}{\sqrt{x^2+z^2}}, \tag{6.65}$$

we may note that $p^2 + q^2 = k_\parallel^2 + k_\perp^2$ and $xp - zq = v_A k_\parallel$. Letting the perpendicular wavenumber initially be zero Equation (6.80) gives the initial fast wave solution

$$2\omega^2 - \left(c_s^2 + v_{A0}^2\right) k_{\parallel 0}^2 + \sqrt{\left(c_s^2 + v_{A0}^2\right)^2 k_{\parallel 0}^4 - 4c_s^2 v_{A0}^2 k_{\parallel 0}^4} = 0. \tag{6.66}$$

When $s = 0$ we let $t_0 = 0$ and $\psi = 0$ so we have $t = 2\omega s$. The initial conditions for x_0 and z_0 are given by Equations (6.63) and (6.61) and from Equation (6.66) we obtain

$$k_{\parallel 0} = -\sqrt{\frac{2\omega^2}{c_s^2 + x_0^2 + z_0^2 - \sqrt{\left(c_s^2 + x_0^2 + z_0^2\right)^2 - 4c_s^2\left(x_0^2 + z_0^2\right)}}}, \tag{6.67}$$

which gives the initial condition for $k_\parallel$ for a downward propagating wave. The remaining equations must be solved numerically under the above initial conditions using a fourth-order Runge-Kutta scheme.

6.3.3.1 Wave Properties

In Figure 6.8 we can see that by driving the parallel velocity component along the magnetic field lines only a slow wave is initially introduced. This propagates downwards at a constant speed until the front of the wave hits the mode-conversion region. At this point the portion of the wave that crosses into the high-β plasma undergoes mode conversion, and both the transmitted fast wave and a converted slow wave are present. To examine the mode conversion a cut is again taken along $x = 0$ where the wavefront hits the conversion region tangentially.

Figure 6.9 shows the parallel and perpendicular velocity components, the horizontal and vertical magnetic field and the pressure for a cut taken along $x = 0$ at $t = 4.6$ Alfvén times of a numerical simulation with driving frequency $\omega = 16\pi$. In the region to the far right of each plot only the incident slow mode is present. As this wave crosses into the high-β plasma between the red dashed lines some portion of the wave is converted to a slow wave and the rest is transmitted as a fast wave. It is difficult to make out the separate fast and slow wave components in the high-β region due to the interference.

The position of the different wavefronts in time may be calculated analytically. In the low-β plasma the slow wave travels at approximately the sound speed

$$\frac{\mathrm{d}z}{\mathrm{d}t} = -c_s, \tag{6.68}$$

so its position varies according to

$$z = 4 - c_s t. \tag{6.69}$$

The slow wave will therefore reach the mode-conversion region at $z = 1.5$ when $t \approx 1.67$ Alfvén times, and at $t = 4.6$ Alfvén times the high-β fast wave will have passed back into the low-β plasma as a slow wave and reached $z \approx -2.85$.

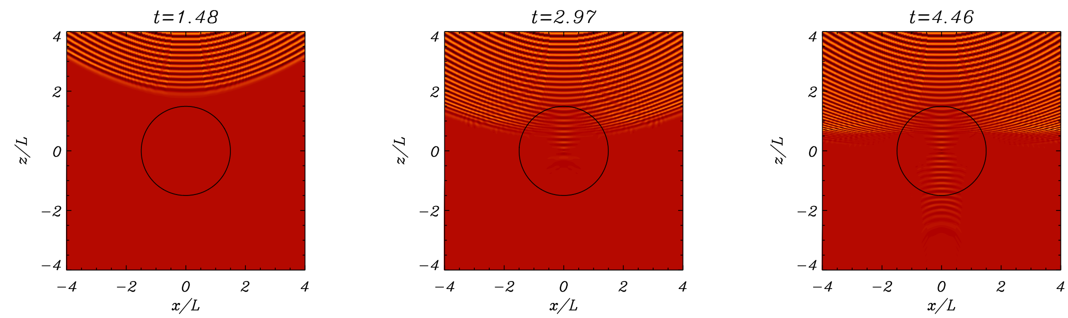

Figure 6.8: Contour plot of the parallel velocity component driven along the magnetic field lines. The plots are shown for a simulation with driving frequency $\omega = 16\pi$ at $t = 1.48$, 2.97 and 4.46 Alfvén times respectively from left to right. The black circle shows the position where $c_s = v_A$ and the null point lies at the origin in the centre of this circle.

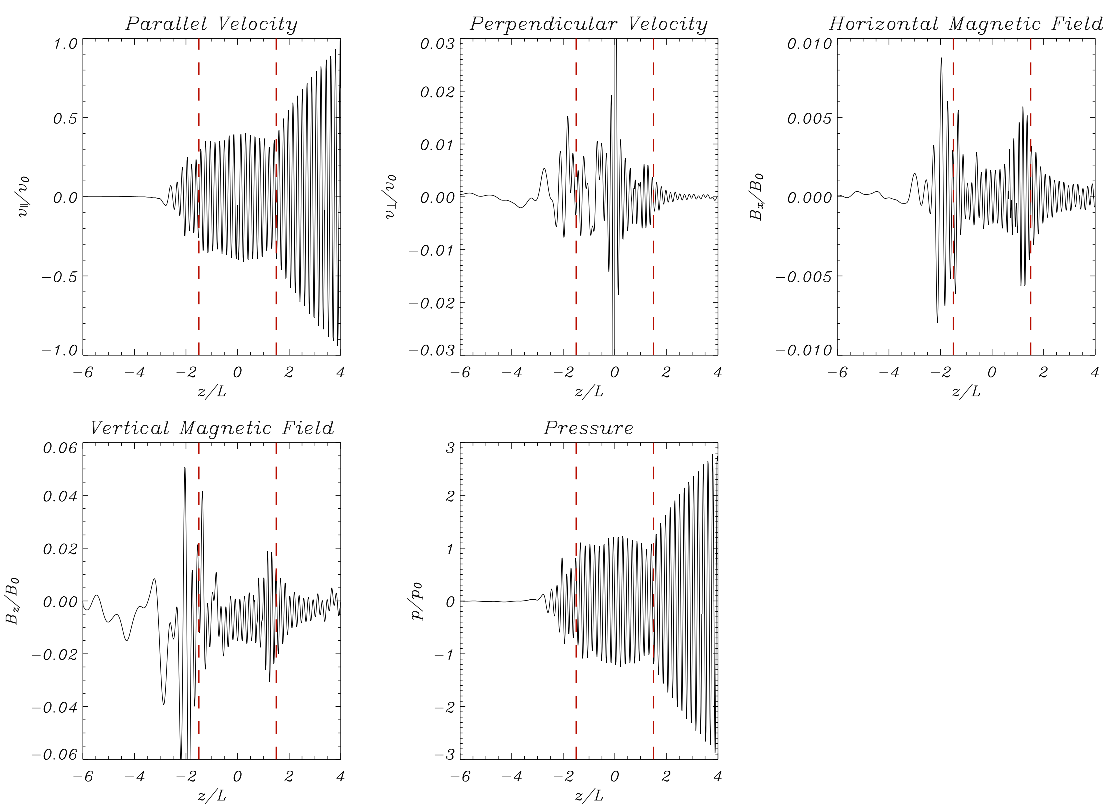

Figure 6.9: Results of driving the parallel velocity along the magnetic field lines with a driving frequency $\omega = 16\pi$ at $t = 4.6$ Alfvén times for a cut taken along $x = 0$. The plots show the parallel and perpendicular velocity, the horizontal and vertical magnetic field, and the pressure respectively from top left to bottom right. The red dashed line indicates the regions where $c_s = v_A$.

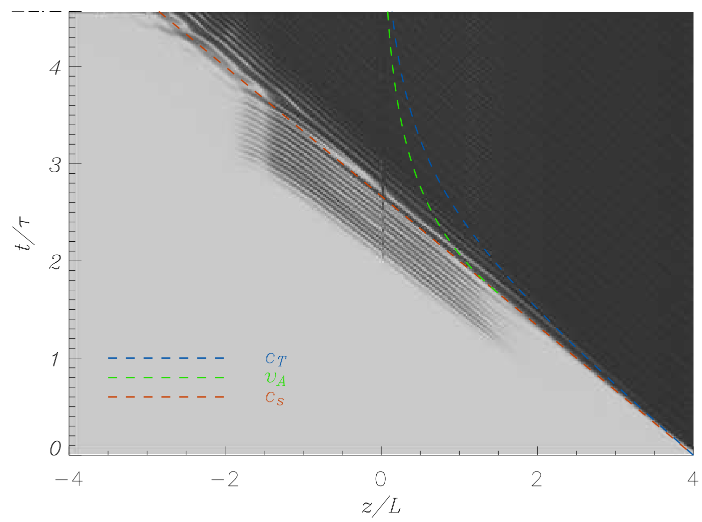

Figure 6.10: Surface plot of the parallel velocity when driven along the magnetic field lines for $\omega = 16\pi$ along $x = 0$. The red dashed line shows the position of the acoustic mode, the green dashed line the position of the magnetic mode, and the blue dashed line the position of the slow mode.

The position of the slow mode in the high-β plasma will be given by the equation

$$\frac{\mathrm{d}z}{\mathrm{d}t} = -v_A = -\sqrt{x^2 + z^2}. \tag{6.70}$$

Along $x = 0$ this reduces to

$$\frac{\mathrm{d}z}{\mathrm{d}t} = -z, \tag{6.71}$$

which, using $z = 3/2$ when $t = 5/3$ from Equation (6.69), has the solution

$$z = \frac{3}{2} e^{5/3} e^{-t}. \tag{6.72}$$

Thus the converted slow mode will only have reached $z \approx 0.08$. The position of the transmitted wave agrees well with the numerical simulations, but it is difficult to see the position of the converted wave in order to compare the results. The position of the slow mode throughout the simulation may be predicted by the tube speed, given by the equation

$$\frac{\mathrm{d}z}{\mathrm{d}t} = -c_T = -\frac{c_s z}{\sqrt{c_s^2 + z^2}}, \tag{6.73}$$

along $x = 0$. This is not easily solved analytically but the fourth-order Runge-Kutta method may be used to find a solution numerically.

Figure 6.10 shows the parallel velocity driven along the magnetic field lines for a numerical simulation with driving frequency $\omega = 16\pi$. Overplotted are the paths predicted by Equations (6.69), (6.72) and (6.73). The acoustic mode is the slow wave in the low-β plasma and the fast mode in the high-β plasma. The

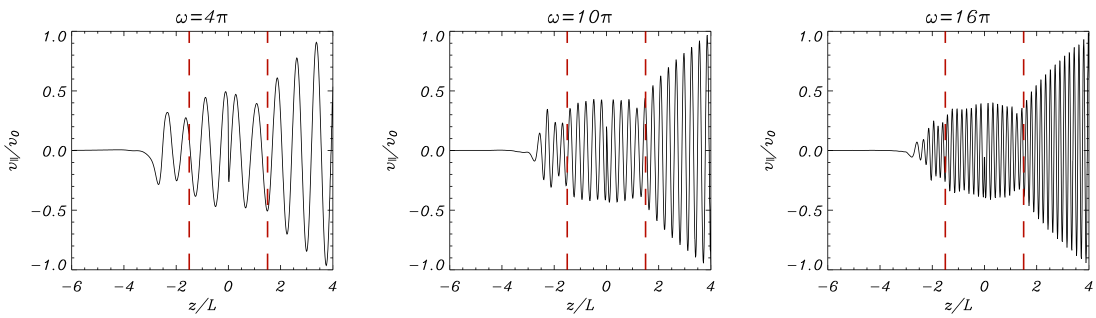

Figure 6.11: Parallel velocity component driven along the magnetic field lines at $t = 4.6$ Alfvén times for $\omega = 4\pi$, 10π and 16π respectively from left to right. The red dashed lines indicate where $c_s = v_A$.

magnetic mode is only present after the incident slow wave crosses into the high-β plasma, and is the slow wave in this region. The third path plotted is that predicted by the tube speed, c_T, which follows the slow mode throughout the domain. This path does not follow the observed wave behaviour as well as those predicted by Equations (6.69) and (6.72) but the agreement is better distant from the conversion region. The ridges appearing ahead of the slow wave are due to a small component of the fast wave being driven on the boundary, but this is effect has been vastly reduced by driving $v_{\|}$ along the magnetic field lines.

6.3.3.2 Effect of Varying the Driving Frequency

Again the only free parameter in the numerical simulation is the driving frequency. In this section we examine the effect that varying this parameter has on the proportion of transmission and conversion observed. Figure 6.11 shows the parallel velocity component at $t = 4.6$ Alfvén times for $\omega = 4\pi$, 10π and 16π respectively from left to right. The converted slow wave cannot be seen below the transmitted fast wave. Although the amplitude dependence of the incident and transmitted waves has not been removed from these plots it can still be seen that the amount of transmission is decreasing as ω increases, in line with the previous chapters.

6.4 Analytical Approximations

In Section 6.3.3 we touched on how Charpit's method could be used to determine when to drive the parallel velocity component on the upper boundary so that it was directed along the magnetic field lines. In this section we look at Charpit's method in more detail and show that it may be used to track the positions of the different wavefronts as they propagate through the domain.

6.4.1 Charpit's Method

Charpit's method results in a system of ordinary differential equations describing the behaviour along a characteristic curve s. To obtain these equations we begin with the wave equations, as given by Equations (6.32) and (6.33)

$$\frac{\partial^2 v_x}{\partial t^2} = \left(c_s^2 + z^2\right)\frac{\partial^2 v_x}{\partial x^2} + z^2\frac{\partial^2 v_x}{\partial z^2} + xz\frac{\partial^2 v_z}{\partial x^2} + c_s^2\frac{\partial^2 v_z}{\partial x \partial z} + xz\frac{\partial^2 v_z}{\partial z^2} + 2z\frac{\partial v_x}{\partial z} + 2z\frac{\partial v_z}{\partial x}, \tag{6.74}$$

$$\frac{\partial^2 v_z}{\partial t^2} = xz\frac{\partial^2 v_x}{\partial x^2} + c_s^2\frac{\partial^2 v_x}{\partial x \partial z} + xz\frac{\partial^2 v_x}{\partial z^2} + x^2\frac{\partial^2 v_z}{\partial x^2} + \left(c_s^2 + x^2\right)\frac{\partial^2 v_z}{\partial z^2} + 2x\frac{\partial v_x}{\partial z} + 2x\frac{\partial v_z}{\partial x}. \tag{6.75}$$

Assuming that we may write the velocity components in terms of their Fourier components, $v_x = ae^{i\psi(x,z,t)}$ and $v_z = be^{i\psi(x,z,t)}$, where $\psi \gg 1$ these equations reduce to

$$\begin{aligned} &\left(\left(\frac{\partial\psi}{\partial t}\right)^2 - \left(c_s^2 + z^2\right)\left(\frac{\partial\psi}{\partial x}\right)^2 - z^2\left(\frac{\partial\psi}{\partial z}\right)^2\right) v_x - \\ &-\left(xz\left(\frac{\partial\psi}{\partial x}\right)^2 + c_s^2\left(\frac{\partial\psi}{\partial x}\right)\left(\frac{\partial\psi}{\partial z}\right) + xz\left(\frac{\partial\psi}{\partial z}\right)^2\right) v_z = 0, \end{aligned} \tag{6.76}$$

$$\begin{aligned} &-\left(xz\left(\frac{\partial\psi}{\partial x}\right)^2 + c_s^2\left(\frac{\partial\psi}{\partial x}\right)\left(\frac{\partial\psi}{\partial z}\right) + xz\left(\frac{\partial\psi}{\partial z}\right)^2\right) v_x + \\ &+\left(\left(\frac{\partial\psi}{\partial t}\right)^2 - x^2\left(\frac{\partial\psi}{\partial x}\right)^2 - \left(c_s^2 + x^2\right)\left(\frac{\partial\psi}{\partial z}\right)^2\right) v_z = 0. \end{aligned} \tag{6.77}$$

For a non-trivial solution we require

$$\begin{aligned} &\left(\frac{\partial\psi}{\partial t}\right)^4 - \left(c_s^2 + v_A^2\right)\left(\left(\frac{\partial\psi}{\partial x}\right)^2 + \left(\frac{\partial\psi}{\partial z}\right)^2\right)\left(\frac{\partial\psi}{\partial t}\right)^2 + c_s^2\left(\left(\frac{\partial\psi}{\partial x}\right)^2 + \left(\frac{\partial\psi}{\partial z}\right)^2\right) \times \\ &\qquad \times \left(x\frac{\partial\psi}{\partial x} - z\frac{\partial\psi}{\partial z}\right)^2 = 0. \end{aligned} \tag{6.78}$$

Letting $\omega = \partial\psi/\partial t$, $p = \partial\psi/\partial x$, and $q = \partial\psi/\partial z$, we may set

$$F\left(\psi, p, q, \omega, x, z, t\right) = \frac{1}{2}\left(\omega^4 - \left(c_s^2 + v_A^2\right)\left(p^2 + q^2\right)\omega^2 + c_s^2\left(p^2 + q^2\right)\left(xp - zq\right)^2\right) = 0. \tag{6.79}$$

This equation can be solved to give

$$2\omega^2 = \left(c_s^2 + v_A^2\right)\left(p^2 + q^2\right) \pm \sqrt{\left(c_s^2 + v_A^2\right)^2\left(p^2 + q^2\right)^2 - 4c_s^2\left(p^2 + q^2\right)\left(xp - zq\right)^2}, \tag{6.80}$$

where the positive root gives the fast wave solution, and the negative root gives the slow wave solution.

Referring to Section 2.2.2 on Charpit's method, the fast wave solution is given by the system of equations

$$\frac{\mathrm{d}\psi}{\mathrm{d}s} = 0, \tag{6.81}$$

$$\frac{\mathrm{d}\omega}{\mathrm{d}s} = 0, \tag{6.82}$$

$$\frac{\mathrm{d}t}{\mathrm{d}s} = 2\omega, \tag{6.83}$$

$$\frac{\mathrm{d}p}{\mathrm{d}s} = x\left(p^2+q^2\right) + \frac{x\left(p^2+q^2\right)^2\left(c_s^2+v_A^2\right) - 2pc_s^2\left(p^2+q^2\right)(xp-zq)}{\sqrt{\left(c_s^2+v_A^2\right)^2\left(p^2+q^2\right)^2 - 4c_s^2\left(p^2+q^2\right)(xp-zq)^2}}, \tag{6.84}$$

$$\frac{\mathrm{d}q}{\mathrm{d}s} = z\left(p^2+q^2\right) + \frac{z\left(p^2+q^2\right)^2\left(c_s^2+v_A^2\right) + 2qc_s^2\left(p^2+q^2\right)(xp-zq)}{\sqrt{\left(c_s^2+v_A^2\right)^2\left(p^2+q^2\right)^2 - 4c_s^2\left(p^2+q^2\right)(xp-zq)^2}}, \tag{6.85}$$

$$\frac{\mathrm{d}x}{\mathrm{d}s} = -p\left(c_s^2+v_A^2\right) - \frac{p\left(p^2+q^2\right)\left(c_s^2+v_A^2\right)^2 - 2pc_s^2(xp-zq)^2 - 2xc_s^2\left(p^2+q^2\right)(xp-zq)}{\sqrt{\left(c_s^2+v_A^2\right)^2\left(p^2+q^2\right)^2 - 4c_s^2\left(p^2+q^2\right)(xp-zq)^2}}, \tag{6.86}$$

$$\frac{\mathrm{d}z}{\mathrm{d}s} = -q\left(c_s^2+v_A^2\right) - \frac{q\left(p^2+q^2\right)\left(c_s^2+v_A^2\right)^2 - 2qc_s^2(xp-zq)^2 + 2zc_s^2\left(p^2+q^2\right)(xp-zq)}{\sqrt{\left(c_s^2+v_A^2\right)^2\left(p^2+q^2\right)^2 - 4c_s^2\left(p^2+q^2\right)(xp-zq)^2}}. \tag{6.87}$$

Similarly the slow wave solution is given by the system of equations

$$\frac{\mathrm{d}\psi}{\mathrm{d}s} = 0, \tag{6.88}$$

$$\frac{\mathrm{d}\omega}{\mathrm{d}s} = 0, \tag{6.89}$$

$$\frac{\mathrm{d}t}{\mathrm{d}s} = 2\omega, \tag{6.90}$$

$$\frac{\mathrm{d}p}{\mathrm{d}s} = x\left(p^2+q^2\right) - \frac{x\left(p^2+q^2\right)^2\left(c_s^2+v_A^2\right) - 2pc_s^2\left(p^2+q^2\right)(xp-zq)}{\sqrt{\left(c_s^2+v_A^2\right)^2\left(p^2+q^2\right)^2 - 4c_s^2\left(p^2+q^2\right)(xp-zq)^2}}, \tag{6.91}$$

$$\frac{\mathrm{d}q}{\mathrm{d}s} = z\left(p^2+q^2\right) - \frac{z\left(p^2+q^2\right)^2\left(c_s^2+v_A^2\right) + 2qc_s^2\left(p^2+q^2\right)(xp-zq)}{\sqrt{\left(c_s^2+v_A^2\right)^2\left(p^2+q^2\right)^2 - 4c_s^2\left(p^2+q^2\right)(xp-zq)^2}}, \tag{6.92}$$

$$\frac{\mathrm{d}x}{\mathrm{d}s} = -p\left(c_s^2+v_A^2\right) + \frac{p\left(p^2+q^2\right)\left(c_s^2+v_A^2\right)^2 - 2pc_s^2(xp-zq)^2 - 2xc_s^2\left(p^2+q^2\right)(xp-zq)}{\sqrt{\left(c_s^2+v_A^2\right)^2\left(p^2+q^2\right)^2 - 4c_s^2\left(p^2+q^2\right)(xp-zq)^2}}, \tag{6.93}$$

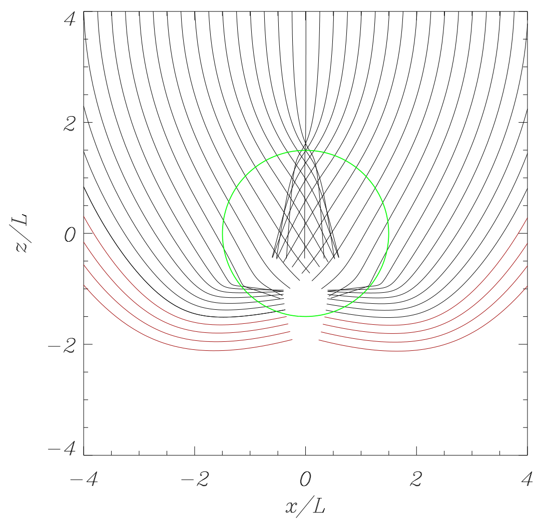

Figure 6.12: The path of the fast wave for various starting points along the x-axis. The green circle denotes where $c_s = v_A$ and the magnetic null point lies at the origin in the centre of this circle. The paths marked in red indicate those paths which do not cross the mode-conversion region during the simulation.

$$\frac{\mathrm{d}z}{\mathrm{d}s} = -q\left(c_s^2 + v_A^2\right) + \frac{q\left(p^2+q^2\right)\left(c_s^2+v_A^2\right)^2 - 2qc_s^2\left(xp-zq\right)^2 + 2zc_s^2\left(p^2+q^2\right)\left(xp-zq\right)}{\sqrt{\left(c_s^2+v_A^2\right)^2\left(p^2+q^2\right)^2 - 4c_s^2\left(p^2+q^2\right)\left(xp-zq\right)^2}}. \tag{6.94}$$

From both sets of equations we can immediately note that ψ and ω are constant, and if $t = 0$ when $s = 0$ then $t = 2\omega s$.

6.4.1.1 Driving $v_\perp$

When driving the perpendicular velocity on the upper boundary the fast wave solution will follow the incident wave in the low-β plasma and the converted wave in the high-β plasma. The initial conditions, taken when $s = 0$, are given by

$$\psi = 0, \qquad t = 0, \qquad x = x_0, \qquad z = 4 \qquad \text{and} \qquad p = 0. \tag{6.95}$$

Thus Equation (6.80) is initially given by

$$2\omega^2 - \left(c_s^2 + x_0^2 + 16\right)q_0^2 + \sqrt{\left(c_s^2 + x_0^2 + 16\right)^2 q_0^4 - 64c_s^2 q_0^4} = 0. \tag{6.96}$$

Solving this for q_0, the positive root will give the downward solution

$$q_0 = \sqrt{\frac{2\omega^2}{c_s^2 + x_0^2 + 16 - \sqrt{\left(c_s^2 + x_0^2 + 16\right)^2 - 64c_s^2}}}. \tag{6.97}$$

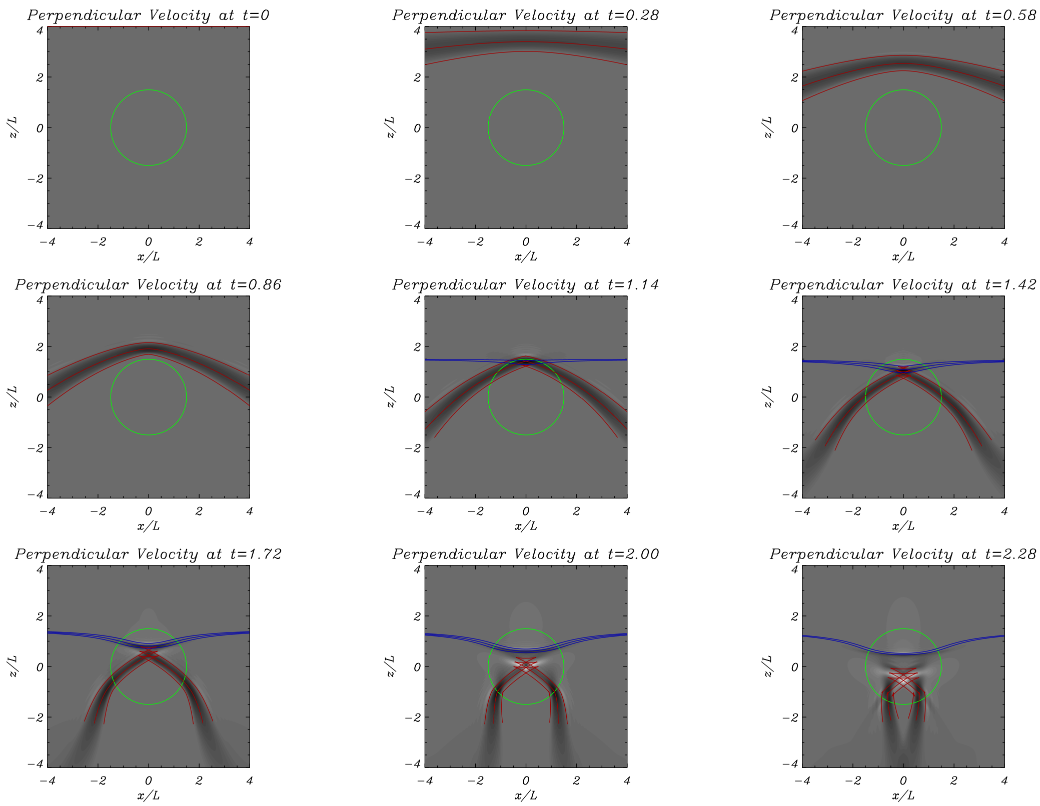

Figure 6.13: Contour plots of the perpendicular velocity for driving frequency $\omega = 4\pi$ at $t = 0$, 0.28, 0.58, 0.86, 1.14, 1.42, 1.72, 2.00 and 2.28 Alfvén times respectively from top left to bottom right. The green circle denotes where $c_s = v_A$ and the magnetic null point lies at the origin in the centre of this circle. The red lines follow the front, middle and back of the fast wave pulse and the blue lines follow the front, middle and back of the slow wave pulse.

Using these initial conditions Equations (6.84) – (6.87) may be solved numerically using the fourth-order Runge-Kutta method to follow the incident and converted waves.

Figure 6.12 shows the characteristic paths of the fast wave for various starting points along the x-axis. This demonstrates the way that the fast wave wraps around the magnetic null point. It is also clear that the edges of the wavefront have travelled further than the centre in the same time, as these are moving faster. The green circle shows where the sound and Alfvén speeds are equal. Not all of the fast wave will cross this mode-conversion region into the high-β region before the end of the simulation. Those paths that remain in the low-β plasma are indicated in red.

To follow the transmitted slow wave the slow wave solution must be used. From Section 6.3.2.1 we know that the incident fast wave will reach the mode-conversion region at $z = 1.5$ when $t = \ln{(8/3)} \approx 0.98$ Alfvén times; therefore these are the initial conditions for the slow wave solution. The conditions for p, q and x are taken to be the same as those for the fast wave solution.

The results of using Charpit's method to follow the fast and slow waves are shown in Figure 6.13. Each plot shows a contour plot of the numerical perpendicular velocity for a driving frequency of $\omega = 4\pi$ as time progresses. Overplotted on these are the position of the front, middle and back of the fast wave pulse in red and the position of the front, middle and back of the slow wave pulse in blue. The green circle shows where the sound and Alfvén speeds are equal. The slow wave solution is introduced at this point as this is where mode conversion occurs. The agreement between the numerical simulations and the analytical predictions is excellent.

Concentrating on the cut along $x = 0$ (with $p = 0$) Equations (6.80), (6.85) and (6.87) reduce down to

$$2\omega^2 = q^2 \left(\left(c_s^2 + z^2 \right) + \left| c_s^2 - z^2 \right| \right), \tag{6.98}$$

$$\frac{\mathrm{d}q}{\mathrm{d}s} = zq^2 \left(1 + \frac{\left(z^2 - c_s^2 \right)}{\left| z^2 - c_s^2 \right|} \right), \tag{6.99}$$

$$\frac{\mathrm{d}z}{\mathrm{d}s} = -q \left(\left(c_s^2 + z^2 \right) + \left| c_s^2 - z^2 \right| \right). \tag{6.100}$$

In the low-β region, where $z^2 > c_s^2$

$$\omega^2 = z^2 q^2, \qquad \frac{\mathrm{d}q}{\mathrm{d}s} = 2zq^2 \qquad \text{and} \qquad \frac{\mathrm{d}z}{\mathrm{d}s} = -2z^2 q, \tag{6.101}$$

which may be solved to find

$$z = 4e^{-t}, \tag{6.102}$$

as predicted by Equation (6.50).
In the high-β region, where $z^2 < c_s^2$

$$\omega^2 = q^2 c_s^2, \qquad \frac{\mathrm{d}q}{\mathrm{d}s} = 0 \qquad \text{and} \qquad \frac{\mathrm{d}z}{\mathrm{d}s} = -2qc_s^2, \tag{6.103}$$

which may be solved to find

$$z = C - c_s t. \tag{6.104}$$

From Equation (6.102) we know that $t = \ln(8/3)$ at $z = 1.5$, so this may be written

$$z = 1.5 + c_s \left(\ln \left(\frac{8}{3} \right) - t \right), \tag{6.105}$$

as predicted by Equation (6.52).

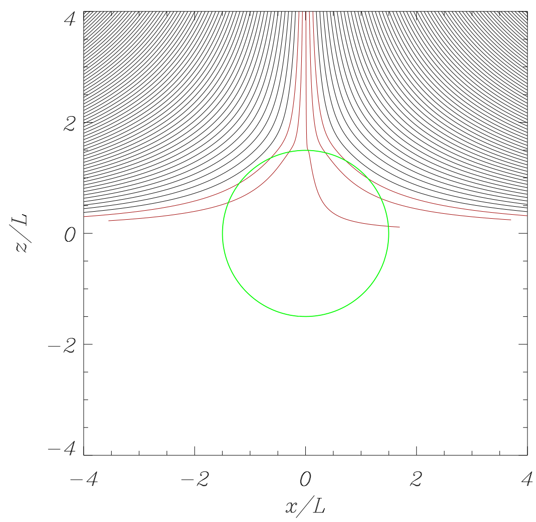

Figure 6.14: The path of the slow wave for various starting points along the x-axis. The green circle denotes where $c_s = v_A$ and the magnetic null point lies at the origin in the centre of the circle. The paths marked in red indicate those paths which do cross the mode-conversion region.

6.4.1.2 Driving $v_{\|}$

We may do the same thing for the simulations driving the parallel velocity component along the magnetic field lines. The slow wave solution will then follow the incident wave in the low-β plasma, and the converted wave in the high-β plasma. The initial conditions, taken when $s = 0$, are

$$\psi = 0, \qquad t = 0, \qquad x_0 = \pm 2\sqrt{\sqrt{x^2+4}-2}, \qquad z_0 = \sqrt{16 + x_0^2}, \qquad k_\perp = 0, \tag{6.106}$$

and from Equation (6.67)

$$k_{\|0} = -\sqrt{\frac{2\omega^2}{c_s^2 + x_0^2 + z_0^2 - \sqrt{\left(c_s^2 + x_0^2 + z_0^2\right)^2 - 4c_s^2\left(x_0^2 + z_0^2\right)}}}. \tag{6.107}$$

The values for p and q may be found from Equation (6.65). Using these initial conditions Equations (6.91) – (6.94) may be solved numerically using the fourth-order Runge-Kutta method to follow the incident and converted waves.

Figure 6.14 shows the path of the slow wave for various starting points along the x-axis. From this we can see that the slow wave follows the magnetic field lines and the wave stretches out away from the magnetic null point. Due to this only a small portion of the wavefront will cross the mode-conversion layer. This part of the wave is located in the centre of the wavefront and is depicted in the figure by the red paths. For this reason the fast wave is only introduced along those points where the slow wave enters the high-β region.

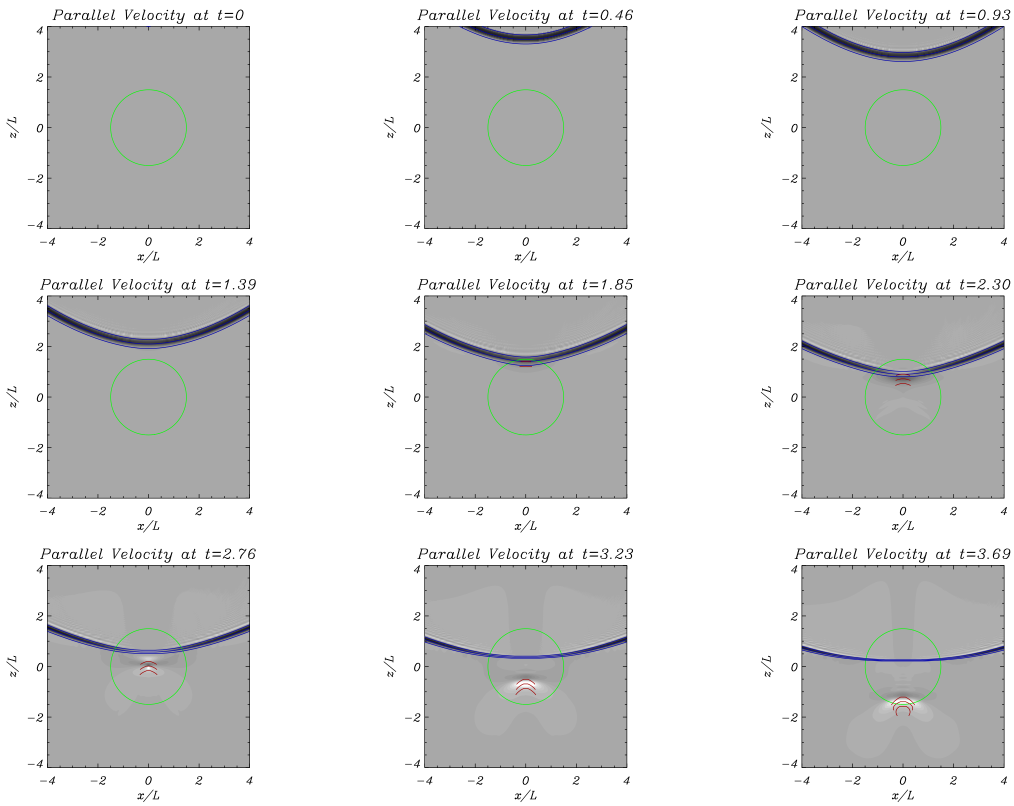

Figure 6.15: Contour plots of the parallel velocity driven along the magnetic field lines with driving frequency $\omega = 4\pi$ at $t = 0$, 0.46, 0.93, 1.39, 1.85, 2.30, 2.76, 3.23 and 3.69 Alfvén times respectively from top left to bottom right. The green circle denotes where $c_s = v_A$ and the magnetic null point lies at the origin in the centre of this circle. The blue lines follow the front, middle and back of the slow wave pulse and the red lines follow the front, middle and back of the fast wave pulse.

To follow the transmitted fast wave Equations (6.84) – (6.87) must be used. From Section 6.3.3.1 we know that the incident slow wave will reach the mode-conversion region at $z = 1.5$ when $t = 5/3 \approx 1.67$ Alfvén times. These are used as the initial conditions for the fast wave solution. The x-position is taken from a cut along constant $z = 1.5$, and p and q are taken to be equal to the values of the slow wave solution.

The results of using Charpit's method to follow the slow and fast waves are shown in Figure 6.15. Each plot shows a contour plot of the numerical parallel velocity driven along the magnetic field lines with a frequency $\omega = 4\pi$ as time progresses. Overplotted on these are the positions of the front, middle and back of the slow wave pulse in blue and the positions of the front, middle and back of the fast wave pulse in red. The green circle shows where the sound and Alfvén speeds are equal and mode conversion takes place so the fast wave solution is introduced here. The agreement between the numerical simulations and the analytical predictions is excellent, although the simulation is stopped before the fast wave leaves the high-β region as the behaviour changes again at this point.

Concentrating on the cut along $x = 0$ (with $p = 0$) Equations (6.80), (6.92) and (6.94) reduce down to

$$2\omega^2 = q^2 \left(\left(c_s^2 + z^2 \right) - \left| c_s^2 - z^2 \right| \right) , \tag{6.108}$$

$$\frac{\mathrm{d}q}{\mathrm{d}s} = zq^2 \left(1 - \frac{\left(z^2 - c_s^2 \right)}{\left| z^2 - c_s^2 \right|} \right) , \tag{6.109}$$

$$\frac{\mathrm{d}z}{\mathrm{d}s} = -q \left(\left(c_s^2 + z^2 \right) - \left| c_s^2 - z^2 \right| \right) . \tag{6.110}$$

In the low-β region, where $z^2 > c_s^2$

$$\omega^2 = q^2 c_s^2, \qquad \frac{\mathrm{d}q}{\mathrm{d}s} = 0 \qquad \text{and} \qquad \frac{\mathrm{d}z}{\mathrm{d}s} = -2qc_s^2, \tag{6.111}$$

which may be solved to find

$$z = 4 - c_s t, \tag{6.112}$$

as predicted by Equation (6.69).
In the high-β plasma, where $z^2 < c_s^2$

$$\omega^2 = q^2 z^2, \qquad \frac{\mathrm{d}q}{\mathrm{d}s} = 2zq^2 \qquad \text{and} \qquad \frac{\mathrm{d}z}{\mathrm{d}s} = -2qz^2, \tag{6.113}$$

which may be solved to find

$$z = Ae^{-t}. \tag{6.114}$$

From Equation (6.112) we know that $t = 5/3$, so this may be written

$$z = 1.5e^{5/3}e^{-t}, \tag{6.115}$$

as predicted by Equation (6.72).

The results of this section have been published in McDougall and Hood (2009).

6.5 Conclusions

This chapter has looked at MHD mode conversion of fast and slow magnetoacoustic waves in the vicinity of a two-dimensional null point (Figure 6.1). At the null point the Alfvén speed goes to zero so a wave propagating towards the null passes from low- to high-β plasma, as demonstrated in Figure 6.2. For simplicity gravitational acceleration was neglected.

In Section 6.3 we used the MacCormack method to simulate a wave propagating towards the null point. In order to drive fast and slow waves the velocity components perpendicular and parallel to the magnetic field were calculated. To drive a fast wave the perpendicular velocity component was driven on the upper boundary whilst the parallel component was held at zero. The results of this are shown in Figure 6.3. As mentioned by McLaughlin and Hood (2004) as the fast wave propagates downwards the centre of the wavefront slows and the wave wraps around the magnetic null point. Looking at a cut of the numerical simulation, taken along $x = 0$, evidence of mode conversion may be seen as the incident fast wave crosses $c_s = v_A$ (Figure 6.4). This is especially clear in the plot of the horizontal magnetic field, in which the converted slow wave can be observed propagating out ahead of the transmitted slow wave. In Section 6.3.2.1 the variation of the position of the wavefronts in time was calculated using the characteristic speeds. These positions are given by Equations (6.50) and (6.52) and are shown against one of the numerical simulations in Figure 6.5. The only free parameter in these numerical simulations was the driving frequency (ω). The effect of varying the driving frequency is small and difficult to see without first removing the amplitude dependence. It is possible, however, to note that the amount of conversion decreases with increasing frequency, and so the amount of transmission must subsequently increase (Figure 6.6) as expected based on the previous chapters.

In Section 6.3.3 we ran similar numerical simulations, this time driving a slow wave on the upper boundary. In order to do this the velocity component parallel to the magnetic field was driven on the upper boundary whilst the perpendicular component was held at zero. When driving $v_{\|}$ straight across the upper boundary some component of the fast wave is also introduced resulting in interference between the two modes (Figure 6.7). To avoid this $v_{\|}$ was driven along the magnetic field lines where the time at which to start the wave was calculated using Charpit's method. Figure 6.8 shows that this stops any component of the fast wave being introduced on the upper boundary. As the slow wave propagates downwards it is curved along the magnetic field lines. When it hits the $c_s = v_A$ layer the incident slow wave is transmitted through the high-β plasma as a fast wave. This may also be seen when a cut of the numerical simulations is taken along $x = 0$ (Figure 6.9). It is difficult to make out the converted slow wave in these simulations as it is masked by the transmitted fast wave. In Section 6.3.3.1 the position of the wavefronts in time was calculated using the characteristic wave speeds. These are given by Equations (6.69) and (6.72) and are shown against one of the numerical simulations in Figure 6.10. Finally the effect of varying the driving frequency was investigated (Figure 6.11). Although the amplitude dependence has not been removed it is clear that the amount of transmission decreases as the frequency increases, and thus the conversion must decrease. Again this agrees with previous results.

In Section 6.4 we looked back at Charpit's method, which was briefly touched upon during the previous section. This was used to describe the behaviour of the fast and slow magnetoacoustic waves along a characteristic curve s. The systems of ordinary differential equations resulting from this were then solved to find how the waves travel throughout the domain. Figure 6.12 shows the how the position of the fast wavefront varies with time for different starting points in the x-direction. This captures the way that the fast wave slows as it approaches the magnetic null point, causing the wavefront to wrap around the null. Charpit's method was then used to predict the position of the fast wave as it propagates downwards (as in McLaughlin and Hood (2006)) and additionally the slow wave from the mode-conversion region (Figure 6.13). These were plotted over one of the numerical simulations in order to compare the results, which are in excellent agreement. By concentrating on the cut along $x = 0$ it was shown that Charpit's method predicted the same wave positions as Equations (6.50) and (6.52).

Charpit's method was then used to examine the wave positions when driving the parallel velocity component along the magnetic field lines in Section 6.4.1.2. Figure 6.14 demonstrates that the slow wave stretches out along the magnetic field lines as it propagates downwards and only a small proportion of the wavefront passes into the mode-conversion region. The position of the slow wave and the transmitted fast wave were calculated and compared to the numerical simulations (Figure 6.15). As only a small section of the slow wave passes into the high-β plasma the fast wave is only modelled along this section. These predictions agree very well with the numerical simulations. As for Section 6.4.1.1, the positions predicted using Charpit's method were shown to agree with those found by Equations (6.69) and (6.72) along $x = 0$.

In this chapter we have developed a good understanding of how fast and slow magnetoacoustic waves behave in the region of a two-dimensional magnetic null point. Using a combination of analytical and numerical techniques we have shown that mode conversion is present when driving both a slow and fast wave toward the null point. In all cases it has been possible to track the incident wave up to the mode-conversion region, and the transmitted and converted components of this wave after it passed into the high-β plasma.

Chapter 7

Conclusions

7.1 Overview of Thesis

This thesis has investigated the mode conversion of fast and slow magnetoacoustic waves in the solar corona. Mode conversion occurs when a resonance between the two wave modes is present, allowing energy to be transferred between the different waves. This results in the amplitude of one wave mode increasing whilst the other decreases. Mode conversion between fast and slow magnetoacoustic waves takes place when their respective characteristic speeds are equal in size. This occurs in regions where the plasma β (the ratio of the gas pressure to the magnetic pressure) is approximately unity.

Throughout this thesis a combination of analytical techniques and numerical methods have been used in conjunction with one another. These methods are described fully in Chapter 2. Mode conversion was modelled numerically by the MacCormack method; a two-step, predictor-corrector finite-difference scheme using both forward and backward differencing. Conversion and transmission coefficients describing the amount of mode conversion were calculated using a method developed by Cairns and Lashmore-Davies (1983) and the behaviour distant from the mode-conversion region was described using a WKB analysis. Each of these methods complements and supports the others, allowing a full description of the mode-conversion process to be built up.

Each chapter has examined mode conversion in a different model atmosphere. Throughout all of the research chapters mode conversion was studied for a wave propagating from low- to high-β plasma. In each case the magnetic topology of the model progressively increased in complexity.

7.2 Summary of Results

In Chapter 3 we investigated mode conversion using a very simple, one-dimensional model. This consisted of a uniform, vertical magnetic field within an isothermal atmosphere. Gravitational stratification was also included in order to ensure that mode conversion took place. As mentioned above the focus was on propagation from low- to high-β plasma and thus the waves were travelling downwards towards the solar surface. This could be representative of a flare-induced blast wave, for example. A slow wave was driven on the upper boundary. No component of the fast wave was introduced because this is evanescent in the low-β plasma. As the slow wave crosses the mode-conversion region the transmitted component takes the form of a fast wave and the converted component takes the form of a slow wave.

Following on from this, Chapter 4 examined mode conversion in the same model. A uniform, background magnetic field was present and gravitational stratification was included, but the conditions were relaxed to allow for a non-isothermal atmosphere. This meant that both the sound and Alfvén speeds varied with height. A $\tanh$ profile was chosen for the temperature as this mimics the steep temperature gradient which is found at the transition region. As before a slow wave was driven on the upper boundary, propagating downwards from low- to high-β plasma and crossing the mode-conversion region as it does so. The transmitted component of the wave is a fast wave in the high-β plasma and the converted component a slow wave.

In Chapter 5 a more complex two-dimensional model was examined. The main feature of this model was a radially-expanding magnetic field which is representative of a coronal hole. Due to the geometry of this model spherical coordinates were used in this chapter. For simplicity gravitational acceleration was neglected, meaning that the background pressure was constant. In addition, the atmosphere was taken to be isothermal so the background density was constant. Thus the sound speed in the model was constant whilst the Alfvén speed varied with radial position. To investigate mode conversion a slow wave was driven on the lower boundary propagating upwards from low- to high-β plasma.

Finally in Chapter 6 mode conversion was investigated in the vicinity of a two-dimensional magnetic null point. At the null point the magnetic field goes to zero and so the wave propagating towards the null passes from a low- to high-β plasma. As for the previous chapter the sound speed was constant while the Alfvén speed varied with height. Mode conversion was investigated when driving both a fast wave and a slow wave on the upper boundary.

In all of the above chapters the process was simulated numerically using the MacCormack finite-difference scheme. In Chapter 5 some θ dependence had to be included in the incoming wave, otherwise the modes would be completely decoupled and no mode conversion would take place. The fast and slow waves in Chapter 6 were introduced by driving the velocity components perpendicular and parallel to the magnetic field. As predicted evidence of mode conversion was observed when the incident wave crossed the conversion region where the sound and Alfvén speeds are equal. In Chapters 3 – 5 the amplitude dependence of the incoming wave was removed, making the conversion much clearer and allowing the amount of transmission in the simulations to be quantified. In these simulations only one wave is present in the low-β region, and after the wave has passed into the high-β plasma both the transmitted and converted components are present. There is a clear drop in amplitude between the incident and transmitted waves, and the converted wave can be identified where there is interference with the transmitted wave.

Using the characteristic wave speeds it was possible to track the positions of the various waves in time. It was found that paths predicted by the sound and Alfvén speeds were in much better agreement with the numerical simulations than those found by the tube speed and the fast speed. However it was noted that although c_T and c_f did not give good agreement at the mode-conversion region, they did tend to the solutions given by c_s and v_A away from this area.

The parameter ω, representing the driving frequency, was a free parameter in all of the numerical simulations. Running the numerical simulations for a range of values of ω we found that the amount of transmission decreases as the driving frequency increases, in agreement with Cally (2005). In Chapters 3 – 5 the wavenumber was also a free parameter. When the wavenumber was equal to zero the fast and slow waves were completely decoupled and no conversion occurred. Comparing the simulations for varying values of the wavenumber the transmission was seen to increase with increasing wavenumber. Additionally, this effect was much stronger than that of varying the driving frequency. Chapter 4 has an additional free parameter, d, which varies the slope of the $\tanh$ temperature profile. Provided that the wavelength of the incoming wave is small in comparison to the width of the temperature gradient the slope has no effect on mode conversion. If this is not the case a proportion of the incident wave will be reflected back into the low-β plasma. The simulations in Chapter 5 were two dimensional, but the value of θ did not influence the mode conversion.

The results from the above numerical simulations were also combined with a number of predictions on the wave behaviour found using various analytical techniques. Cairns and Lashmore-Davies (1983) developed a method of quantifying mode conversion. This uses differential equations derived from the local dispersion relations at the mode-conversion region to describe the wave behaviour. Combining these gives a single differential equation for which the solution in known in terms of the Parabolic Cylinder function (see Abramowitz and Stegun (1964)). This solution may then be used to find coefficients describing the amount of transmission and conversion that takes place. It was shown that the coefficients calculated satisfy the conservation of energy. The advantage of this method is that an exact solution does not need to be known in order to obtain the coefficients, unlike that used in Zhugzhda and Dzhalilov (1982a). This method was used in Chapters 3 – 5 to find transmission and conversion coefficients. In concurrence with the numerical simulations these show that the amount of transmission and conversion depends on the square of the wavenumber and inversely on the driving frequency. Comparing the amount of transmission predicted with that observed in the numerical simulations showed excellent agreement, even when the value of the wavenumber grew large in violation of the assumptions used.

In Chapter 3 a method described in Roberts (2006) was used to find the wave behaviour in the limit of a large wavenumber. This method uses scaling of the variables to find a description of the slow mode in terms of the Klein-Gordon equation. This was then solved using the WKB method. This agreed well with the numerical simulations to start with, but then deviated from the numerical simulation as $z \to -\infty$. This is because the assumptions are no longer valid in this region. Due to this fact the method was not applied in any of the later chapters.

To find the behaviour of the various wave components away from the mode-conversion region the WKB method was used in Chapters 3 – 5. This allowed the amplitude dependence and phase behaviour of the different wave modes to be found. To obtain a full description of the wave behaviour throughout the domain these solutions were then matched across the mode-conversion region using the transmission and conversion coefficients found using the Cairns and Lashmore-Davies (1983) method. In Chapter 3 these analytical descriptions are in near perfect agreement with the numerical simulations capturing both the amplitude and phase behaviour. The amplitude dependence of the converted wave does not agree as well with the numerical simulations in Chapter 4, but the remaining elements of the prediction are in excellent agreement. Unfortunately, in Chapter 5 these predictions are not in such good agreement. Both the transmission and conversion coefficients appear to have been overestimated, suggesting that energy is not conserved in this case. However the amplitude and phase behaviour predicted by the WKB method do look correct.

In Chapter 6 Charpit's method was used to solve the WKB equations to find the behaviour of the fast and slow waves along a characteristic curve. This resulted in two sets of ordinary differential equations which were solved numerically using a fourth-order Runge-Kutta scheme. This allowed the path of incoming wave to be found for various starting points along the x-axis. In line with the numerical simulations these showed that the fast wave slows as it approaches the magnetic null point, causing the edges of the wave to refract around the null point (in agreement with McLaughlin and Hood (2004)). Conversely the slow wave was shown to stretch out along the magnetic field lines as it approaches the null point, meaning that only a small section of the wave actually enters the mode-conversion region. The solutions found using Charpit's method were also used to predict the position of the incoming fast wave (as done in McLaughlin and Hood (2006)) and slow wave, and to predict the position of the transmitted wave from the mode-conversion region. These are in excellent agreement with the numerical simulations. It was also shown that when taking a cut along $x = 0$ these predictions are identical to those found using the characteristic wave speeds.

In Chapters 3 and 4 the one-dimensional model with a uniform, background magnetic field was used as a first step in building up to examine the two-dimensional coronal null point problem. In reality, the mode-conversion region in this type of set-up is unlikely to lie in the corona where the plasma β is typically very low ($\mathcal{O}\left(10^{-4}\right)$) and is more likely to lie in the chromosphere or strong field regions in the photosphere. In Chapter 5 a two-dimensional model representative of a coronal hole was studied. This is more physically realistic than the model used in previous chapters, however its applicability is limited due to the fact that gravitational acceleration was neglected. For this type of magnetic field structure the region where $\beta \approx 1$ will be situated at a height of 1.2 – 1.4 $R_{\odot}$ (Gary, 2001). Chapter 6 concentrated on mode conversion in the vicinity of a magnetic null point. In this situation the mode-conversion layer may be found much lower in the corona at heights of 0.2 – 0.3 $R_{\odot}$ (Gary, 2001). This gives an indication of where mode conversion may occur for different magnetic topologies in the solar atmosphere.

7.3 Future Work

There are numerous ways in which the work in this thesis could be extended. Due to time constraints we were unable to apply the WKB method in Chapter 6. This method could be applied to the parallel and perpendicular velocity components using the derivatives parallel and perpendicular to the magnetic field. This would allow the amplitude and phase behaviour for the different wave modes to be found. This information could then be used to remove the amplitude dependence from the incoming wave, as was done in Chapters 3 – 5, allowing the amount of transmission to be quantified. Ideally this would then be compared to transmission and conversion coefficients found using the Cairns and Lashmore-Davies (1983) method. As it currently stands, the Cairns and Lashmore-Davies (1983) method may only be applied to one-dimensional problems. As such this would need to be extended in order to cope with two dimensions.

In all cases the incoming wave is driven along the magnetic field lines. An interesting problem may be to investigate the effect of driving a wave at an angle to the magnetic field. Other authors have found that the angle at which the incoming wave hits the mode-conversion layer does have an affect on mode conversion, Carlsson and Bogdan (2006) for example. It would be interesting to see whether this effect could be quantified using the techniques utilised in this thesis.

Another obvious extension would be to consider mode conversion in a three-dimensional model. This would be much more realistic than the one- and two-dimensional models. In three dimensions Alfvén waves will also be present in addition to the fast and slow magnetoacoustic waves. This introduces the possibility of coupling between all three modes. In order to find transmission and conversion coefficients, the Cairns and Lashmore-Davies (1983) method would have to be expanded again to deal with three-dimensions.

Bibliography

M. Abramowitz and I. A. Stegun, editors. *Handbook of Mathematical Functions*. National Bureau of Standards, Washington, 1964.

H. Alfvén. Existence of Electromagnetic-Hydrodynamic Waves. *Nature*, 150:405 – 406, 1942.

H. Alfvén. On the Existence of Electromagnetic-Hydrodynamic Waves. *Arkiv f. Mat., Astron. o. Fys.*, 29: 1 – 7, 1943.

M. J. Aschwanden. *Physics of the Solar Corona: An Introduction*. Praxis Publishing Ltd, Chichester, 2004.

C. M. Bender and S. A. Orszag. *Advanced Mathematical Methods for Scientists and Engineers*. McGraw-Hill Book Co., Singapore, 1978.

D. S. Bloomfield, R. T. J. McAteer, M. Mathioudakis, and F. P. Keenan. The Influence of Magnetic Field on Oscillations in the Solar Chromosphere. *ApJ*, 652:812 – 819, 2006.

T. J. Bogdan, M. Carlsson, V. Hansteen, A. McMurray, C. S. Rosenthal, M. Johnson, S. Petty-Powell, E. J. Zita, R. F. Stein, S. W. McIntosh, and Å. Nordlund. Waves in the Magnetised Solar Atmosphere. II. Waves from Localised Sources in Magnetic Flux Concentrations. *ApJ*, 599:626 – 660, 2003.

T. J. M. Boyd and J. J. Sanderson. *Plasma Dynamics*. Nelson, London, 1969.

T. J. M. Boyd and J. J. Sanderson. *The Physics of Plasmas*. Cambridge University Press, Cambridge, 2003.

R. J. Bray and R. E. Loughhead. *Sunspots*. Chapman and Hall Ltd, London, 1964.

L. Brillouin. La méchanique ondulatoire de Schrödinger; une méthode générale de resolution par approximations successives. *C. R. Acad. Sci. Paris*, 183:24 – 26, 1926.

R. A. Cairns and V. Fuchs. Mode Conversion and Dissipation of the Fast Alfvén Wave in Ion Cyclotron Heating. *Phys. Fluids B*, 1:350 – 357, 1989.

R. A. Cairns and C. N. Lashmore-Davies. A Unified Theory of a Class of Mode Conversion Problems. *Phys. Fluids*, 26:1268 – 1274, 1983.

R. A. Cairns and C. N. Lashmore-Davies. Mode Conversion of a Propagating to Nonpropagating Wave. *Phys. Fluids*, 29:3639 – 3642, 1986.

P. S. Cally. Note on an Exact Solution for Magnetoatmospheric Waves. *ApJ*, 548:473 – 481, 2001.

P. S. Cally. Local Magnetohelioseismology of Active Regions. *MNRAS*, 358:353 – 362, 2005.

P. S. Cally. Dispersion Relations, Rays and Ray Splitting in Magnetohelioseismology. *Phil. Trans. R. Soc. A*, 364:333 – 349, 2006.

P. S. Cally and T. J. Bogdan. Simulation of f- and p-mode Interactions with a Stratified Magnetic Field Concentration. *ApJ*, 486:L67 – L70, 1997.

M. Carlsson and T. J. Bogdan. Numerical Modelling of MHD Waves in the Solar Chromosphere. *Phil. Trans. R. Soc. A*, 364:395 – 404, 2006.

J. G. Charney, R. Fjørtoft, and J. von Neumann. Numerical Integration of the Barotropic Vorticity Equation. *Tellus*, 2:237 – 254, 1950.

C. R. Chester. *Techniques in Partial Differential Equations*. McGraw-Hill Book Company, New York, 1971.

J. Crank and P. Nicolson. A Practical Method for Numerical Evaluation of Solutions of Partial Differential Equations of Heat Conduction Type. *Proc. Camb. Phil. Soc.*, 43:50 – 67, 1947.

J. Evershed. Radial Movement in Sun-Spots. *Mon. Not. R. Astron. Soc.*, 69:454 – 457, 1909.

V. Fedun, R. Erdélyi, and S. Shelyag. Oscillatory Response of the 3D Solar Atmosphere to the Leakage of Photospheric Motion. *Sol. Phys.*, 258:219 – 241, 2009.

V. C. A. Ferraro and C. Plumpton. Hydromagnetic Waves in a Horizontally Stratified Atmosphere. *ApJ*, 127:459 – 476, 1958.

G. Fruit and I. J. D. Craig. Visco-resistive Shear Wave Dissipation in Magnetic X-points. *A&A*, 448: 753 – 761, 2006.

G. A. Gary. Plasma Beta above a Solar Active Region: Rethinking the Paradigm. *Sol. Phys.*, 203:71 – 86, 2001.

J. P. Goedbloed and S. Poedts. *Principles of Magnetohydrodynamics*. Cambridge University Press, Cambridge, UK, 2004.

L. Golub and J. M. Pasachoff. *Nearest Star: The Surprising Science of Our Sun*. Harvard University Press, Cambridge, Massachusetts, 2001.

I. S. Gradshteyn and I. M. Ryzhik. *Table of Integrals, Series, and Products*. Academic Press, New York, 1981.

G. Green. On the Motion of Waves in a Variable Canal of Small Depth and Width. *Trans. Cambridge Philos. Soc.*, 6:457 – 462, 1837.

G. E. Hale and S. B. Nicholson. The Law of Sun-Spot Polarity. *ApJ*, 62:270 – 300, 1925.

G. E. Hale, F. Ellerman, S. B. Nicholson, and A. H. Joy. The Magnetic Polarity of Sun-Spots. *ApJ*, 49: 153 – 185, 1919.

J. Heyvaerts and E. R. Priest. Coronal Heating by Phase-Mixed Shear Alfvén Waves. *A&A*, 117:220 – 234, 1983.

K. A. Hoffman and S. T. Chiang. *Computational Fluid Dynamics for Engineers - Volume I*. Engineering Education System, Kansas, 1993.

H. Jeffreys. On Certain Approximate Solutions of Linear Differential Equations of the Second Order. *Proc. London Math. Soc.*, 23:428 – 436, 1924.

E. Khomenko and M. Collados. Numerical Modelling of Magnetohydrodynamic Wave Propagation and Refraction in Sunspots. *ApJ*, 653:739 – 755, 2006.

H. A. Kramers. Wellenmechanik und halbzahlige Quantisierung. *Zeit. f. Phys.*, 39:828 – 840, 1926.

K. R. Lang. *The Cambridge Encyclopedia of the Sun*. Cambridge University Press, Cambridge, 2001.

P. D. Lax. Weak Solutions of Nonlinear Hyperbolic Equations and their Numerical Computation. *Comm. Pure Appl. Math.*, 7:159 – 193, 1954.

P. D. Lax and R. D. Richtmyer. Survey of the Stability of Linear Finite Difference Equations. *Comm. Pure Appl. Math.*, 9:267 – 293, 1956.

P. D. Lax and B. Wendroff. Systems of Conservation Laws. *Comm. Pure Appl. Math.*, 13:217 – 237, 1960.

J. Liouville. Sur la Classification des Transcendants et sur l'imposibilité d'exprimer les racines des certaines équations en fonction finie explicite des coefficients. Part 1. *J. Math. Pure Appl.*, 2:56 – 105, 1837.

B. Lyot. The Study of the Solar Corona without an Eclipse. *JRASC*, 27:225 – 234, 1933.

R. W. MacCormack. The Effect of Viscosity in Hypervelocity Impact Cratering. *AIAA Paper No. 69-354*, 1969.

A. M. D. McDougall and A. W. Hood. A New Look at Mode Conversion in a Stratified Isothermal Atmosphere. *Sol. Phys.*, 246:259 – 271, 2007.

A. M. D. McDougall and A. W. Hood. MHD Mode Conversion in a Stratified Atmosphere. In R. Erdélyi and C. A. Mendoza-Briceño, editors, *Proceedings of the International Astronomical Union, Waves & Oscillations in the Solar Atmosphere: Heating and Magneto-Seismology*, volume 247, pages 296 – 302, 2008.

A. M. D. McDougall and A. W. Hood. MHD Mode Conversion around a 2D Magnetic Null Point. In *15th Cambridge Workshop on Cool Stars, Stellar Systems, and the Sun*, volume 1094, pages 752 – 755, 2009.

J. A. McLaughlin and A. W. Hood. MHD Wave Propagation in the Neighbourhood of a Two-Dimensional Null Point. *A&A*, 420:1129 – 1140, 2004.

J. A. McLaughlin and A. W. Hood. MHD Wave Propagation in the Neighbourhood of Two Null Points. *A&A*, 435:313 – 325, 2005.

J. A. McLaughlin and A. W. Hood. MHD Mode Coupling in the Neighbourhood of a 2-D Null Point. *A&A*, 459:641 – 649, 2006.

R. Muller. Eťude Morphologique et Cinématique des Structures Fines d'une Tache Solaire. *Sol. Phys.*, 29: 55 – 73, 1973.

A. H. Nayfeh. *Introduction to Perturbation Techniques*. John Wiley & Sons, New York, 1981.

E. N. Parker. Dynamics of the Interplanetary Gas and Magnetic Fields. *ApJ*, 128:664 – 676, 1958.

E. N. Parker. The Solar-Flare Phenomenon and the Theory of Reconnection and Annihilation of Magnetic Fields. *Ap. J. Suppl.*, 8:177 – 211, 1963.

H. T. H. Piaggio. *An Elementary Treatise on Differential Equations and their Applications*. G. Bell and Sons, Ltd, London, 1942.

L. J. Porter, J. A. Klimchuk, and P. A. Sturrock. The Possible Role of High-Frequency Waves in Heating Solar Coronal Loops. *ApJ*, 435:502 – 514, 1994.

E. R. Priest. *Solar Magnetohydrodynamics*. D. Reidel Publishing Company, Holland, 1982.

E. R. Priest and T. G. Forbes. New Models for Fast Steady State Magnetic Reconnection. *J. Geophys. Res.*, 91:5579 – 5588, 1986.

Rayleigh. On the Propagation of Waves through a Stratified Medium, with Special Reference to the Question of Reflection. *Proc. R. Soc. London A*, 86:207 – 226, 1912.

P. J. Roache. *Fundamentals of Computational Fluid Dynamics*. Hermosa Publishers, New Mexico, 1998.

B. Roberts. *Solar System Magnetic Fields*, chapter Magnetohydrodynamic Waves. D. Reidel Publishing Company, Holland, 1985.

B. Roberts. MHD Waves in the Solar Atmosphere. In *SOHO13: Waves, Oscillations and Small Scale Events in the Solar Atmosphere. A Joint View from SOHO and TRACE*, volume ESA SP-547, pages 1 – 15, 2004.

B. Roberts. Slow Magnetohydrodynamic Waves in the Solar Atmosphere. *Phil. Trans. R. Soc. A*, 364: 447 – 460, 2006.

B. Roberts and A. R. Webb. Vertical Motions in an Intense Magnetic Flux Tube. *Sol. Phys.*, 56:5 – 35, 1978.

C. S. Rosenthal, T. J. Bogdan, M. Carlsson, S. B. F. Dorch, V. Hansteen, S. W. McIntosh, A. McMurray, Å. Nordlund, and R. F. Stein. Waves in the Magnetized Solar Atmosphere. I. Basic Processes and Internetwork Oscillations. *ApJ*, 564:508 – 524, 2002.

H. M. Schey. *Div, grad, curl, and all that*. W. W. Norton & Co., New York, 2005.

H. Schunker and P. S. Cally. Magnetic Field Inclination and Atmospheric Oscillations above Solar Active Regions. *Mon. Not. R. Astron. Soc.*, 372:551 – 564, 2006.

S. H. Schwabe. Die Sonne. *Astron. Nachr.*, 20:283 – 288, 1843.

R. F. Stein. Reflection, Refraction, and Coupling of MHD Waves at a Density Step. *Ap. J. Suppl.*, 22: 419 – 444, 1971.

P. A. Sweet. The Neutral Point Theory of Solar Flares. In B. Lehnert, editor, *Electromagnetic Phenomena in Cosmical Physics*, volume 6 of *IAU Symposium*, pages 123 – 134, 1958.

E. Tandberg-Hanssen. *Solar Prominences*. D. Reidel Publishing Company, Holland, 1974.

G. Wentzel. Eine Verallegmeinerung der Quantenbedingungen für die Zwecke der Wellenmechanik. *Zeit. f.Phys.*, 38:519 – 529, 1926.

R. B. White. *Asymptotic Analysis of Differential Equations*. Imperial College Press, London, 2005.

A. Wilson and N. Maskelyne. Observations on the Solar Spots. By Alexander Wilson, M. D. Professor of Practical Astronomy in the University of Glasgow. Communicated by the Rev. Neill Maskelyne, Astronomer Royal. *Phil. Trans. Series I*, 64:1 – 30, 1774.

Y. D. Zhugzhda. Magnetogravity Waves in an Isothermal Conductive Atmosphere. *Sov. Astron.*, 23:42 – 47, 1979.

Y. D. Zhugzhda. Seismology of Sunspot Atmosphere: from Chromospheric Resonance to Nonlinear Antireflection. In F. Kneer, K. G. Puschmann, and A. D. Wittmann, editors, *Modern Solar Facilities - Advanced Solar Science*, pages 1 – 4. Universitätsverlag Göttingen, 2007.

Y. D. Zhugzhda and N. S. Dzhalilov. Conversion of Magnetogravitational Waves in the Solar Atmosphere. *Sov. Astron.*, 25:477 – 482, 1981.

Y. D. Zhugzhda and N. S. Dzhalilov. Transformation of Magnetogravitational Waves in the Solar Atmosphere. *A&A*, 112:16 – 23, 1982a.

Y. D. Zhugzhda and N. S. Dzhalilov. Linear Conversion of Magnetogravity Waves in an Exponential Atmosphere. *Sov. J. Plasma Phys.*, 8:558 – 562, 1982b.

Y. D. Zhugzhda and N. S. Dzhalilov. Linear Conversion of Magnetoacoustogravity Waves in an Oblique Magnetic Field. *Sov. J. Plasma Phys.*, 9:587 – 591, 1983.

Y. D. Zhugzhda and N. S. Dzhalilov. Magneto-acoustic-gravity Waves on the Sun. I. Exact Solution for an Oblique Magnetic Field. *A&A*, 132:45 – 51, 1984a.

Y. D. Zhugzhda and N. S. Dzhalilov. Magneto-acoustic-gravity Waves on the Sun. II. Transformation and Propagation. *A&A*, 132:52 – 57, 1984b.

Y. D. Zhugzhda and N. S. Dzhalilov. Magneto-acoustic-gravity Waves on the Sun. III. The Theory of Running Penumbral Waves. *A&A*, 133:333 – 340, 1984c.

Y. D. Zhugzhda and N. S. Dzhalilov. Magneto-Acoustic-Gravity Waves in the Horizontal Magnetic Field. *Geophys. Astrophys. Fluid Dynamics*, 35:131 – 156, 1986.